

Electronic Thesis and Dissertation Repository

8-23-2024 10:30 AM

The Characterization and Electrochemistry of Natural Uranium Dioxide Under Long-Term Disposal Conditions

Martin D. M. Badley, *The University of Western Ontario*

Supervisor: Noël, James J., *The University of Western Ontario*

A thesis submitted in partial fulfillment of the requirements for the Doctor of Philosophy degree in Chemistry

© Martin D. M. Badley 2024

Follow this and additional works at: <https://ir.lib.uwo.ca/etd>

 Part of the [Analytical Chemistry Commons](#)

Recommended Citation

Badley, Martin D. M., "The Characterization and Electrochemistry of Natural Uranium Dioxide Under Long-Term Disposal Conditions" (2024). *Electronic Thesis and Dissertation Repository*. 10327.
<https://ir.lib.uwo.ca/etd/10327>

This Dissertation/Thesis is brought to you for free and open access by Scholarship@Western. It has been accepted for inclusion in Electronic Thesis and Dissertation Repository by an authorized administrator of Scholarship@Western. For more information, please contact wlsadmin@uwo.ca.

Abstract

This thesis describes the studies performed on a number of natural uranium dioxide (UO_2) specimens to determine a range of reactivities. This work will support the safety case for the long-term disposal of spent nuclear fuel in Canada. Under relevant long-term disposal conditions, water radiolysis could produce oxidizing conditions at the surface of the fuel, potentially leading to fuel corrosion and the release of radionuclides into the groundwater. The rate of such a process would be determined by the radiation dose rate from the fuel and the reactivity of the fuel, which will be determined by its composition, in particular by the degree of non-stoichiometry and the concentration of fission products.

For undoped UO_2 (i.e., in the absence of fission products), the reactivity has been shown to be very dependent on the degree of non-stoichiometry (x in UO_{2+x}). The conductivity of natural UO_2 specimens fabricated between 1965 and 2017 was characterized using several surface analytical and electrochemical methods. The reactivity of the characterized specimens in H_2O_2 -containing environments was subsequently found to be only loosely related to the measured resistivities (conductivity). However, most of the H_2O_2 consumed on the surface of the UO_2 electrode was consumed by H_2O_2 decomposition rather than surface oxidation.

In the absence of H_2 , the peroxide oxidized the surface to $\text{U}^{\text{IV}}_{1-2x}\text{U}^{\text{V}}_{2x}\text{O}_{2+x}$ with x varying with H_2O_2 concentration and eventually achieving a composition of $\text{U}^{\text{IV}}_{0.34}\text{U}^{\text{V}}_{0.66}\text{O}_{2.33}$. At this surface composition, the surface becomes unstable with respect to dissolution, but the dominant reaction is H_2O_2 decomposition. In the presence of H_2 , the initial oxidation of the $\text{U}^{\text{IV}}\text{O}_2$ when H_2O_2 was added was reversed by the ability of H_2 to scavenge the OH^\bullet with the H^\bullet radicals formed. This led to a reduction of the oxidized surface. The efficiency of this process is determined by the relative concentrations of H_2O_2 and H_2 .

Keywords

Uranium Dioxide, Characterization, Corrosion, Electrochemistry, Hydrogen Peroxide, Hydrogen, Dissolution, Decomposition

Summary for Lay Audience

Uranium dioxide (UO_2) is an extremely energy-dense material that produces reliable, low-carbon-emitting power. The waste produced from this power generation is a stable ceramic material but is highly radioactive, requiring hundreds of thousands of years to return to its natural radiation levels. The internationally accepted solution for the long-term disposal of this waste is to contain and isolate the UO_2 in corrosion-resistant containers within a deep geological repository. While there is extensive research to support the durability of these containers until the UO_2 returns to its natural radiation levels, it is necessary to evaluate the potential consequences of a failed container filled with groundwater.

A series of UO_2 pellets fabricated between 1965 and 2017 were characterized to determine a range of reactivities under potential long-term disposal conditions. The primary oxidant of concern is hydrogen peroxide (H_2O_2), produced naturally as water reacts with alpha radiation from the spent fuel. However, despite initial suggestions of a large range of reactivities, this work found that most of the H_2O_2 that reacts on the surface of the spent fuel results in the decomposition of H_2O_2 rather than the oxidation of the spent fuel, regardless of the suggested reactivity.

Further studies in the presence of H_2 , which has been shown to scavenge H_2O_2 on simulated nuclear fuel samples, suggested that even on natural UO_2 samples, H_2 can suppress corrosion under expected disposal conditions and, in some cases, reverse surface oxidation.

Co-Authorship Statement

This thesis includes published data in Chapter 5.

Chapter 5 contains contributions from Dr. James Noël and Dr. David Shoesmith, who assisted with editing.

Dedication

This thesis is dedicated to my parents,
Robert and Joyce Badley

Table of Contents

Abstract	ii
Summary for Lay Audience	iii
Co-Authorship Statement	iv
Dedication	v
Table of Contents	vi
List of Figures	xii
List of Symbols and Acronyms	xxi
1. Introduction and Literature Review	1
1.1. Nuclear Waste Disposal in Canada	1
1.1.1. Nuclear Power and Current Waste Storage	1
1.1.2. The Multi-Barrier System	2
1.2. Basic Properties of Uranium Dioxide	4
1.3. Properties of Used Fuel	7
1.4. Matrix Corrosion and Radionuclide Release Under Disposal Conditions	14
1.4.1. The Instant Release Fraction (IRF)	15
1.4.2. The Influence of Redox Conditions	15

1.4.3. Oxidation of the Uranium Dioxide Surface	19
1.4.4. Reactivity of the Uranium Dioxide Surface	20
1.4.5. The Influence of Non-Stoichiometry	21
1.4.6. The Influence of Lattice Dopants	26
1.4.7. The Influence of Surface Composition	27
1.4.8. The Influence of Groundwater Species	30
1.4.9. Potential Oxidants (Oxygen and Hydrogen Peroxide).....	32
1.4.10. The Consequences of Hydrogen Peroxide Decomposition.....	35
1.5. The Influence of Redox Scavengers on Fuel Corrosion	41
1.5.1. Ferrous Ions	41
1.5.2. Hydrogen (H ₂)	42
1.6. Chemical Dissolution Under Anoxic Conditions	45
1.7. Thesis Goals and Outline.....	46
1.8. References.....	47
2. Experimental Techniques and Details	63
2.1. Experimental Design	63
2.2. UO ₂ Material.....	63
2.3. Electrochemical Experimental Techniques	63

2.3.1. Electrochemical Cell and Instrumentation	63
2.3.1.1. Three-Compartment Cell	63
2.3.1.2. Single-Compartment Cell.....	64
2.3.2. Electrode Preparation	65
2.3.3. Solution Preparation	67
2.4. Electrochemical Techniques.....	67
2.4.1. Corrosion Potential (E_{CORR}) Measurements	67
2.4.2. Linear Polarization Resistance (LPR) Measurements.....	68
2.4.3. Cyclic Voltammetry (CV) Measurements.....	68
2.4.4. Potentiostatic Polarization (PSP) Measurements	68
2.4.5. Electrochemical Impedance Spectroscopy (EIS)	69
2.5. Surface Analysis Techniques	70
2.5.1. Raman Spectroscopy	70
2.5.2. Scanning Electron Microscopy	71
2.5.3. X-ray Photoelectron Spectroscopy.....	73
2.6. Solution Analysis Techniques	75
2.6.1. Inductively Coupled Plasma-Mass Spectrometry	75
2.6.2. Ultraviolet-Visible Spectroscopy	76

2.7. References.....	78
3. Characterizing Natural Uranium Dioxide Specimens	79
3.1. Introduction	79
3.2. Experimental.....	80
3.2.1. Electrode Materials and Preparation	80
3.2.2. Resistance Measurements.....	80
3.2.3. Raman Spectroscopy	81
3.2.4. Scanning Electron Microscopy (SEM)	81
3.2.5. Electrochemical Cell and Equipment.....	81
3.2.6. Electrochemical Techniques.....	83
3.3. Results and Discussion	83
3.4. Summary and Conclusions	95
3.5. Acknowledgements	96
3.6. References.....	97
4. Influence of Resistivity on the Dissolution of Uranium Dioxide in Peroxide-Containing Environments	101
4.1. Introduction	101
4.2. Experimental.....	103

4.2.1. Electrode Materials and Preparation	103
4.2.2. Solution Preparation	104
4.2.3. Electrochemical Cell and Equipment	104
4.2.4. Electrochemical Techniques.....	104
4.2.5. Ultraviolet-Visible Spectroscopy (UV-vis).....	105
4.2.6. Inductively Coupled Plasma-Mass Spectrometry (ICP-MS)	105
4.2.7. Scanning Electron Microscopy (SEM)	105
4.3. Results and Discussion	105
4.4. Summary and Conclusions	125
4.5. Acknowledgements	125
4.6. References.....	126
5. Effect of Hydrogen on the Dissolution of Uranium Dioxide in Peroxide-Containing Environments	131
5.1. Introduction	131
5.2. Experimental.....	132
5.2.1. Electrode Materials and Preparation	132
5.2.2. Solution Preparation	133
5.2.3. Electrochemical Cell and Equipment.....	133

5.2.4. Electrochemical Techniques.....	133
5.2.5. X-ray Photoelectron Spectroscopy.....	134
5.2.6. Raman Analyses	134
5.3. Results and Discussion	135
5.4. Summary and Conclusions	150
5.5. Acknowledgements	151
5.6. References.....	152
6. Conclusions and Future Work	156
6.1. Conclusions	156
6.2. Future Work.....	157
Appendix A	159
Appendix B	160

List of Figures

Figure 1-1. Radiation dose rates as a function of time since discharge from reactor to a layer of H ₂ O in contact with a CANDU fuel bundle with a burnup of 220 MWh/kg uranium [5]. ...	2
Figure 1-2. Schematic of the deep geological repository (DGR) concept with the associated barriers [8].....	3
Figure 1-3. Cubic fluorite lattice structure adopted by actinide dioxides. ● Uranium, ▲ Oxygen, □ Cubically coordinated empty interstitial sites.....	4
Figure 1-4. Schematic energy level diagram for UO ₂ derived from spectroscopic and electrochemical data (expressed on the Standard Hydrogen Electrode (SHE) scale). The filled valence band has predominantly O 2p character, and the empty conduction band consists mainly of U5f, 6d, and 7s states. The U5f band contains two electrons per U atom [24].	5
Figure 1-5. Solubilities of UO ₂ and Schoepite (UO ₃ ·2H ₂ O) as a function of pH [24].	6
Figure 1-6. Schematic illustration of a 37-element CANDU fuel bundle [43].....	8
Figure 1-7. SEM Micrographs of UO ₂ fuel: (a) unirradiated UO ₂ , (b) fuel irradiated at high burnup (770 MWh/kgU) with key features of unirradiated fuel and in-reactor irradiation noted, respectively. Features of irradiated fuel noted in brown and blue can be simulated in unirradiated UO ₂ , while those in green (in panel b) cannot [44].	8
Figure 1-8. Schematic illustration showing the conceptual distribution of fission and activation products within a spent fuel element [43].	11
Figure 1-9. Conceptual illustration of the three categories of radionuclide within a spent fuel element [56].	12
Figure 1-10. Radioactivity of reference CANDU used fuel (220 MWh/kgU burnup) as a function of time after discharge from reactor [47].	14

Figure 1-11. Illustration demonstrating the thermodynamic driving force for fuel corrosion in an aqueous solution containing oxidants: E_{CORR} is the corrosion potential at which the overall corrosion process occurs on the fuel surface [70].....16

Figure 1-12. Alpha (α), beta (β) and gamma (γ) dose rates as a function of time for a layer of water in contact with a CANDU fuel bundle with a reference burnup of 220 MWh/kgU [74].
.....17

Figure 1-13. Illustration showing the two corrosion fronts existing within a failed groundwater-flooded waste container. One front is on the fuel surface, established by reactions with radiolytic oxidants, and the second is on the steel surface, established by reactions with H_2O [79].....18

Figure 1-14. The fractions of various oxidation states of U in a 1.5 at% SIMFUEL electrode surface as a function of applied electrochemical potential. The electrode was anodically oxidized at each potential for 1 hour in 0.1 mol/L NaCl (pH = 9.5) solution and then analyzed by X-ray photoelectron spectroscopy (XPS) [80].....19

Figure 1-15. SEM image of a typical surface morphology observed on a UO_2 specimen with a nominal stoichiometry of $UO_{2.1}$. (A) A smooth, flat grain with an approximate O/U ratio of 2.01; (B) A grain with a very shallow stepped pattern with a slightly hyperstoichiometric composition of ~ 2.15 ; (C) A grain with a pronounced stepped pattern of ridges oriented horizontally along the X-Y plain with a composition of ~ 2.22 ; (D) A highly non-stoichiometric spiral-like grain with a composition of ~ 2.31 [99].22

Figure 1-16. Raman spectra recorded on the four types of grains (A) to (D) shown and described in Figure 1 15. The O/U ratios are ~ 2.01 (A), ~ 2.15 (B), ~ 2.22 (C), ~ 2.31 (D) [99].
.....23

Figure 1-17. The relationships between the intensities of the band at 445 cm^{-1} (T_{2g}) and the bands at 1150 cm^{-1} and 155 cm^{-1} based on Raman spot analyses. A-D correlate to similar degrees of non-stoichiometry to those labelled in Figure 1 15. The vertical lines indicate the transitions between defect structures. The compositions indicate the degree of non-stoichiometry at which the transitions occur [99].....24

Figure 1-18. Voltammograms recorded on four hyperstoichiometric electrodes in 0.1 mol/L NaCl solution (pH 9.5) at a scan rate of 5 mV/s. The threshold is that established for the onset of oxidation [43].25

Figure 1-19. Dissolution charges calculated for four UO₂ materials from voltammograms recorded in 0.1 mol/L NaCl solution containing 0.01 mol/L [CO₃]_{total}. Dy-UO₂ (12.9 wt% Dy₂O₃); Gd-UO₂ (6.0 wt% Gd₂O₃); 1.5 at% SIMFUEL; Undoped UO_{2.002} [109].27

Figure 1-20. Relative fractions of U oxidation states as a function of applied potential, recorded on Dy-UO₂ (12.9 wt% Dy) after 1 hour of oxidation in 0.1 mol/L NaCl + 0.05 mol/L [CO₃]_{total} solution. The dashed line shows the fraction of U^{IV} recorded on a freshly polished Dy-UO₂ surface [109].28

Figure 1-21. Schematic illustrating the influence of major tetragonal distortions leading to the extensive formation of cuboctahedral clusters and the onset of dissolution [109].29

Figure 1-22. Cyclic voltammograms recorded on a rotating (16.7 Hz) Dy-UO₂ (12.9 wt% Dy) electrode in an Ar-purged 0.1 mol/L NaCl solution containing various [CO₃]_{total} at a scan rate of 10 mV/s [109].31

Figure 1-23. Reduction of O₂ at donor-acceptor relay (DAR) sites on a U^{IV}_{1-2x}U^V_{2x}O_{2+x} surface [3].33

Figure 1-24. O₂ reduction currents recorded on various SIMFUEL electrodes in a 0.1 mol/L NaCl (pH 9.5) solution purged with air ([O₂] = 2.5 x 10⁻⁴ mol/L): (○) Fission product-doped UO₂ containing no ε-particles; (▲) 1.5 at% SIMFUEL; (□) 3 at% SIMFUEL; (●) 6 at% SIMFUEL; (x) 3 at% SIMFUEL Containing ε-particles but No Fission Products. Line (1) is drawn with a slope of 90 mV/decade of current, the slope expected on noble metals [117]. .34

Figure 1-25. Schematic illustration showing that the reduction of H₂O₂ can occur on either the catalytic U^{IV}_{1-2x}U^V_{2x}O_{2+x} surface or on ε-particles and couple to either UO₂ or H₂O₂ oxidation [119].36

Figure 1-26. Uranium release into solution (A) and H₂O₂ consumption on UO₂ (B) during three consecutive exposures to a deaerated 1 x 10⁻³ mol/L HCO₃⁻ solution [142].38

Figure 1-27. Percentage of U oxidation states in a 3 at% SIMFUEL surface after exposure to a 10^{-2} mol/L H_2O_2 solution. Values obtained by deconvolution of the U 4f7/2 peaks in XPS spectra [148].....39

Figure 1-28. Illustration of the H_2O_2 decomposition (reactions 1.1 and 1.2) and UO_2 corrosion reaction (reactions 1.3, 1.4, 1.5) occurring on a $U^{IV}_{1-2x}U^V_{2x}O_{2+x}$ surface layer on UO_2 [148].40

Figure 1-29. Illustration showing the two corrosion fronts within a groundwater-containing failed container [70].....41

Figure 1-30. Schematic illustrating the possible reaction pathways for the scavenging of H_2O_2 by reaction with H_2 on a 1.5 at% SIMFUEL surface by (a) reaction on ϵ -particles; (b) by H_2 oxidation on ϵ -particles galvanically coupled to the reduction of H_2O_2 on the oxide surface [140].....45

Figure 2-1. Schematic illustrating a 1 L, three-compartment electrochemical cell.64

Figure 2-2. Schematic illustration of the 50 mL, small electrochemical cell used in H_2O_2 decomposition experiments.65

Figure 2-3. Schematic illustration of the experimental setup used to electroplate one side of a UO_2 disk with Cu [2].66

Figure 2-4. Schematic of the potential perturbation applied during an EIS experiment and the resulting AC current response [5]. The change in the phase angle is represented by θ69

Figure 2-5. Schematic illustration of the experimental setup used to measure the resistivity of a UO_2 disk.70

Figure 2-6. Schematic illustrating the energy level diagram of the states involved in a Raman signal. The signal strength from the described energy transitions is qualitatively represented by the line thickness.....71

Figure 2-7. Schematic illustration of the possible interactions between a primary electron beam and a sample surface [7].	72
Figure 2-8. Schematic illustration of the excitation of a core level electron by an X-ray beam and the subsequent generation of a photoelectron.	74
Figure 2-9. Schematic illustration of a quadrupole mass filter [9].	75
Figure 2-10. Schematic illustration of a diode array UV-Vis spectrophotometer.	77
Figure 3-1. Bode plot collected for a UO ₂ disk. The dashed line represents a phase angle of 0, where Z(ω) represents the resistance of the UO ₂ disk.	82
Figure 3-2. Measured resistivities for un-doped UO ₂ samples manufactured between 1965 and 2017. Individual resistivity measurements are shown for each sample.	84
Figure 3-3. Measured resistivities with respect to individual slices from un-doped UO ₂ pellets manufactured between 1965 and 2017. The schematic represents the numbering format used for slices from a single pellet.	85
Figure 3-4. The deconvoluted Raman spectrum of an un-doped UO ₂ sample demonstrates the peak deconvolution into contributions from bands at ~ 445 cm ⁻¹ , 575 cm ⁻¹ , and 630 cm ⁻¹	86
Figure 3-5. Raman spectra, collected across the sample surface, show defect distortion distribution across the sample surfaces. The peak at 445 cm ⁻¹ was normalized to 1 to compare the intensity of lattice distortions at 630 cm ⁻¹ . Samples were manufactured in (a) 2017, (b) 1992, (c) 1990, (d) 1977, and (e) 1965.	87
Figure 3-6. Optical images (a) to (e) of the UO ₂ surface, with the area of analysis highlighted (green rectangle). Raman mapping (f) to (j) of the UO ₂ surface with the overlay of the T _{2g} (red) and A _{1g} (blue) distribution across the sample surface. The samples were manufactured in 2017 (a and f), 1990 (b and g), 1992 (c and h), 1977 (d and i), and 1965 (e and j).	89

Figure 3-7. SEM micrographs showing different grain morphology of UO ₂ samples with varying measured resistivities. Samples were manufactured in (a) 2017, (b) 1992, (c) 1990, (d) 1977, and (e) 1965.	91
Figure 3-8. Cyclic voltammogram recorded on a UO ₂ electrode manufactured in 1990 with a resistivity of 10 kΩ.cm, in Ar-purged 0.1 mol.L ⁻¹ NaCl + 0.05 mol.L ⁻¹ HCO ₃ ⁻ /CO ₃ ²⁻ solution adjusted to pH 9.5. Arrows represent the scan direction.	92
Figure 3-9. Cyclic voltammogram recorded on a UO ₂ electrode manufactured in 1977 with a resistivity of 50 kΩ.cm, in Ar-purged 0.1 mol.L ⁻¹ NaCl + 0.05 mol.L ⁻¹ HCO ₃ ⁻ /CO ₃ ²⁻ solution adjusted to pH 9.5.	94
Figure 3-10. Cyclic voltammogram recorded on a UO ₂ electrode manufactured in 2017 with a resistivity of 2500 kΩ.cm, in Ar-purged 0.1 mol.L ⁻¹ NaCl + 0.05 mol.L ⁻¹ HCO ₃ ⁻ /CO ₃ ²⁻ solution adjusted to pH 9.5.	95
Figure 4-1. Schematic illustration of the possible reactions of H ₂ O ₂ on a UO ₂ surface, showing that the H ₂ O ₂ oxidation reaction can be catalyzed by U ^{IV} /U ^V donor-acceptor sites [19].	102
Figure 4-2. E _{CORR} (line) and R _P (squares) measurements as a function of time with various [H ₂ O ₂] _i . Recorded on a natural UO ₂ electrode with (a) high resistivity, 2500 kΩ.cm, (b) low resistivity, 10 kΩ.cm, or (c) mid resistivity, 50 kΩ.cm, in 0.1 mol L ⁻¹ NaCl + 0.05 mol L ⁻¹ HCO ₃ ⁻ /CO ₃ ²⁻ solution adjusted to pH 9.5.	107
Figure 4-3. Measured [H ₂ O ₂] remaining in solution as a function of time for [H ₂ O ₂] _i ranging from 1-20 mmol.L ⁻¹ . Recorded on a natural UO ₂ electrode with high resistivity, 2500 kΩ.cm (a), low resistivity, 10 kΩ.cm (b), or mid resistivity, 50 kΩ.cm (c), in 0.1 mol L ⁻¹ NaCl + 0.05 mol L ⁻¹ HCO ₃ ⁻ /CO ₃ ²⁻ solution adjusted to pH 9.5.....	109
Figure 4-4. The remaining [H ₂ O ₂], taken after 1, 2, 6, 12, 20, and 24 hours of immersion, with respect to measured E _{CORR} . Recorded on a natural UO ₂ electrode with high resistivity, 2500 kΩ.cm (square), low resistivity, 10 kΩ.cm (circle), or mid resistivity, 50 kΩ.cm (triangle), in 0.1 mol L ⁻¹ NaCl + 0.05 mol L ⁻¹ HCO ₃ ⁻ /CO ₃ ²⁻ solution adjusted to pH 9.5.	110

Figure 4-5. Total amount of H ₂ O ₂ consumed at the UO ₂ surface over 24 hours as a function [H ₂ O ₂] _i . Recorded on a natural UO ₂ electrode with high resistivity, 2500 kΩ.cm (a), low resistivity, 10 kΩ.cm (b), or mid resistivity, 50 kΩ.cm (c), in 0.1 mol L ⁻¹ NaCl + 0.05 mol L ⁻¹ HCO ₃ ⁻ /CO ₃ ²⁻ solution adjusted to pH 9.5.	113
Figure 4-6. Amount of dissolved U in solution with respect to [H ₂ O ₂] _i after 24 hours of immersion.	115
Figure 4-7. Calculated dissolution yield with respect to [H ₂ O ₂] _i after 24 hours immersion.	116
Figure 4-8. Amount of dissolved U in solution with respect to time for electrodes with (a) high resistivity, 2500 kΩ.cm, and (b) mid resistivity, 50 kΩ.cm.	118
Figure 4-9. Calculated dissolution yield with respect to time for electrodes with (a) high resistivity, 2500 kΩ.cm, and (b) mid resistivity, 50 kΩ.cm.	120
Figure 4-10. SEM of the high-resistivity sample (2017, 2500 kΩ.cm) (a) before immersion, and after 24 hours immersion at various [H ₂ O ₂] _i (b) 1 mM, (c) 5 mM, (d) 10 mM, and (e) 20 mM.	122
Figure 4-11. SEM of the mid-resistivity sample (1977, 50 kΩ.cm) (a) before immersion, and after 24 hours immersion at various [H ₂ O ₂] _i (b) 1 mM, (c) 5 mM, (d) 10 mM, and (e) 20 mM.	123
Figure 4-12. SEM of the low-resistivity sample (1990, 10 kΩ.cm) (a) and (b) before immersion, or (c) and (d) after all immersion experiments. Micro-indentations created on the surface are indicated with red arrows and a natural crack along the surface indicated with a yellow arrow.	124
Figure 5-1. Cyclic voltammogram recorded on a UO ₂ electrode in Ar-purged 0.1 mol.L ⁻¹ NaCl + 0.05 mol.L ⁻¹ HCO ₃ ⁻ /CO ₃ ²⁻ solution adjusted to pH 9.5. The vertical dashed line at ~ -400 mV (vs SCE) indicates the thermodynamic threshold for matrix oxidation.	136
Figure 5-2. Raman spectra recorded across the surface of an unoxidized UO ₂ specimen.	136

Figure 5-3. E_{CORR} as a function of time with sequential additions of $[H_2O_2]$, recorded on a natural UO_2 electrode in $0.1 \text{ mol.L}^{-1} \text{ NaCl} + 0.05 \text{ mol.L}^{-1} \text{ HCO}_3^-/\text{CO}_3^{2-}$ solution adjusted to pH 9.5 with (a) Ar, or (b) 5% $H_2/95\%$ Ar purge gas. The values show the actual concentration of H_2O_2 during that measurement period.139

Figure 5-4. Final E_{CORR} values from Figure 5-3, as a function of total $[H_2O_2]$. The horizontal arrow indicates the range in which E_{CORR} is sensitive to the presence of H_2140

Figure 5-5. E_{CORR} as a function of time before and after individual additions of H_2O_2 (indicated by arrows) prior to XPS analyses. The purge gas was either (a) Ar or (b) 5% $H_2/95\%$ Ar...143

Figure 5-6. Surface compositions recorded on a natural UO_2 electrode as a function of the final measured E_{CORR} in a solution purged with either (a) Ar or (b) 5% $H_2/95\%$ Ar (from Figure 5-5). The horizontal dashed line refers to the composition of U^{IV} (green) and $U^V + U^{VI}$ (magenta) after experiments with no H_2O_2 added.144

Figure 5-7. Comparison of $(U^V + U^{VI})/U_{total}$ ratio as a function of potential. The solid circles were measured on a Gd- UO_2 electrode in Ar-purged $0.1 \text{ mol.L}^{-1} \text{ NaCl} + 0.05 \text{ mol.L}^{-1} \text{ HCO}_3^-/\text{CO}_3^{2-}$ solution⁶⁰145

Figure 5-8. E_{CORR} as a function of time in a solution purged with 5% $H_2/95\%$ Ar. The arrow indicates the time at which the electrode was potentiostatically polarized to either 100 mV (blue) or -100 mV (red). XPS was performed immediately after polarization (dashed) or after 4 days of allowing the system to return to a steady state (solid).147

Figure 5-9. Surface compositions recorded as a function of the polarization potential from Figure 5-8. XPS was performed immediately after polarization (open points) or after 4 days of allowing the system to return to a steady state (solid points). The horizontal dashed line refers to the composition of U^{IV} (green) and $U^V + U^{VI}$ (magenta) after experiments with no H_2O_2 added.148

Figure 5-10. E_{CORR} as a function of time in a solution purged with 5% $H_2/95\%$ Ar. The arrows indicate the time at which H_2O_2 was added. Electrodes were removed for XPS analysis at either

the peak potential (dashed lines) or after the eventual achievement of a steady state (solid lines).
.....149

Figure 5-11. Comparison of $(U^V + U^{VI})/U_{\text{total}}$ ratio as a function of potential. XPS analysis was performed after the immersion experiment (Figure 5-10) at peak potential (open points) or after returning to a steady state (solid points).150

List of Symbols and Acronyms

Symbols

A	Absorbance
ω	Angular Frequency
α	Alpha Radiation
at%	Atomic Percent
β	Beta Radiation
E_b	Binding Energy
E_{CORR}	Corrosion Potential
E^e	Equilibrium Potential
γ	Gamma Radiation
O_I	Interstitial Oxygen
E_K	Kinetic Energy
ϵ	Molar Absorption Coefficient
R_P	Polarization Resistance
RE^{III}	Rare Earth
$E_{Red/Ox}$	Redox Potential
E_h	Redox Potential
Φ	Work Function

Acronyms

AECL	Atomic Energy of Canada Limited
APM	Adaptive Phased Management
AC	Alternating Current
BE	Binding Energy
BWR	Boiling Water Reactor
BWXT	BWX Technologies
CANDU	Canadian Deuterium Uranium
CNL	Canadian Nuclear Laboratories
CE	Counter Electrode
CS-AFM	Current Sensing Atomic Force Microscopy
CV	Cyclic Voltammetry
DGR	Deep Geological Repository
DC	Direct Current
DAR	Donor-Acceptor Relay
EIS	Electrochemical Impedance Spectroscopy
ICP-MS	Inductively Coupled Plasma-Mass Spectrometry
IRF	Instant Release Fraction
LWR	Light Water Reactor
LPR	Linear Polarization Resistance

MOX	Mixed Oxide
ϵ-particles	Noble Metal Particle
NWMO	Nuclear Waste Management Organization
OCP	Open Circuit Potential
PSP	Potentiostatic Polarization
RE	Reference Electrode
SCE	Saturated Calomel Electrode
SECCM	Scanning Electrochemical Cell Microscopy
SECM	Scanning Electrochemical Microscopy
SEM	Scanning Electron Microscopy
SIMFUEL	Simulated Nuclear Fuel
SHE	Standard Hydrogen Electrode
UHP	Ultra-High Purity
UV-vis	Ultraviolet-Visible Spectroscopy
WE	Working Electrode
XRD	X-ray Diffraction
XPS	X-ray Photoelectron Spectroscopy

Chapter 1

1. Introduction and Literature Review

1.1. Nuclear Waste Disposal in Canada

1.1.1. Nuclear Power and Current Waste Storage

Nuclear power generation is relied upon worldwide as a leading low-carbon power generation source. Within Canada, nuclear power provided 14.6% of the total energy generated in 2020, with Ontario relying on nuclear for 56.8% of its total power generation [1]. While nuclear power produces 40 to 60 times less CO₂ eq/kWh than coal and fossil fuels, respectively, it comes with the additional responsibility of safely managing the waste forms [2]. The dominant form of high-level nuclear waste is the spent fuel bundles discharged from reactors [3]. If disposed of improperly, long-lived radionuclides released from the fuel matrix may enter the surrounding environment.

As of June 2020, there are approximately 3 million spent fuel bundles in either wet or dry storage in Canada [4]. These interim storage phases provide sufficient time and suitable environments for spent fuel from Canada's Canadian Deuterium Uranium (CANDU) reactors before permanent disposal. Upon removal from the reactors, spent fuel bundles are housed in water pools for 7 to 10 years to provide cooling and shielding while the radiation fields are particularly intense. After wet storage, the spent fuel bundles are transferred to dry storage containers designed with a minimum lifetime of 50 years. However, the radiation fields associated with radionuclide decay will remain significant for up to 10⁵ years, Figure 1.

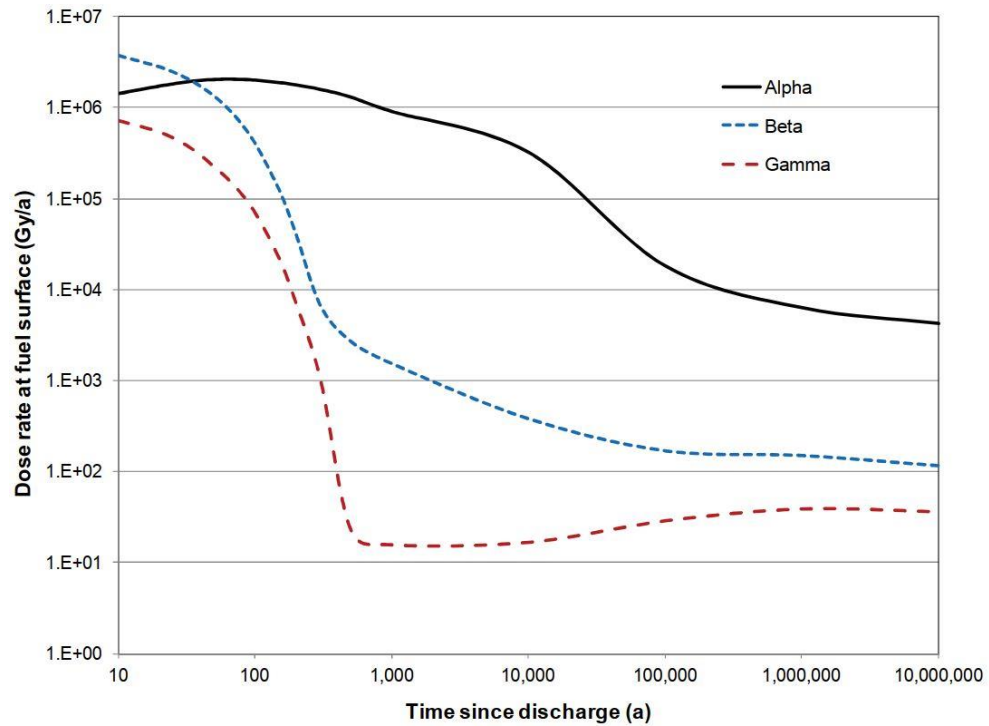


Figure 1-1. Radiation dose rates as a function of time since discharge from reactor to a layer of H₂O in contact with a CANDU fuel bundle with a burnup of 220 MWh/kg uranium [5].

1.1.2. The Multi-Barrier System

Several countries are developing adaptive phased management (APM) disposal procedures for high-level nuclear waste, with the internationally accepted approach being the burial of the fuel bundles in a deep geological repository. Canada's program, under development by the Nuclear Waste Management Organization (NWMO), is deep geologic disposal in either granitic rock or sedimentary rock [6]. This process involves sealing the spent fuel bundles inside a carbon steel vessel protected against corrosion by a corrosion-resistant copper coating. This container would then be placed in a deep geological repository (DGR) at a depth of approximately 500 m within a stable geological formation and surrounded by highly compacted bentonite clay, Figure 2 [7, 8].

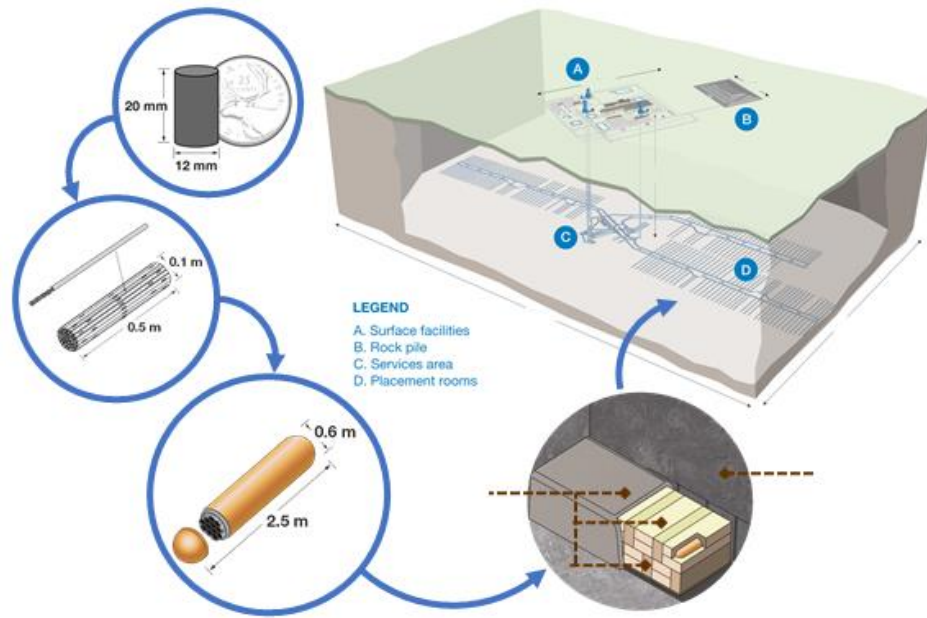


Figure 1-2. Schematic of the deep geological repository (DGR) concept with the associated barriers [8].

While the container will provide long-term containment [9], it is necessary to consider the consequences of its failure, which could lead to fuel exposure to groundwater. Since the fuel contains radioactive fission and activation products, its behaviour in contact with groundwater provides the critical radioactivity source term in the assessment of DGR safety [10].

Over the past few decades, a substantial international effort has been expended to determine the behaviour of spent fuel under a range of proposed DGR conditions [10-23]. This report will review the present understanding of fuel corrosion/dissolution leading to the release of radionuclides.

1.2. Basic Properties of Uranium Dioxide

The common commercial nuclear fuel form is uranium dioxide close to stoichiometric (UO_{2+x} with $0.001 \geq x \geq 0.0001$). As with other actinide oxides, UO_2 adopts a cubic fluorite structure with each U atom surrounded by 8 equivalent nearest neighbour O atoms (Figure 1-3). An important feature of the lattice is the large, cubically coordinated interstitial sites, which can accommodate additional interstitial O atoms (O_i). In the stoichiometric form, UO_2 can be considered a Mott-Hubbard insulator with electronic conductivity requiring the promotion of electrons from the fully occupied 5f level to the conduction band (Figure 1-4), a strongly activated process with an extremely low probability at room temperature.

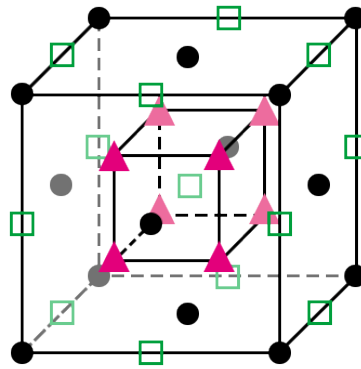


Figure 1-3. Cubic fluorite lattice structure adopted by actinide dioxides. ● Uranium, ▲ Oxygen, □ Cubically coordinated empty interstitial sites.

The conductivity of UO_2 can be increased by either the introduction of O_i atoms into the many available lattice locations, as indicated in Figure 1-3, or by replacing a fraction of U^{IV} atoms in the matrix with lower valent species, which creates holes in the 5f band. To maintain charge balance, an equivalent concentration of U^{V} atoms is created [24]. Since spent nuclear fuel contains significant quantities of lower valent dopants (in particular, rare earth (RE^{III}) atoms) and the O potential of the fuel increases with burnup, both these changes would lead to

an increase in the electrical conductivity of the fuel. This would facilitate the coupling of the anodic and cathodic sites required to support corrosion. Since metallic alloys are also formed in-reactor, this enhanced conductivity will allow the coupling to the fuel matrix as catalytic anodes or cathodes depending on the redox conditions to which the fuel is exposed.

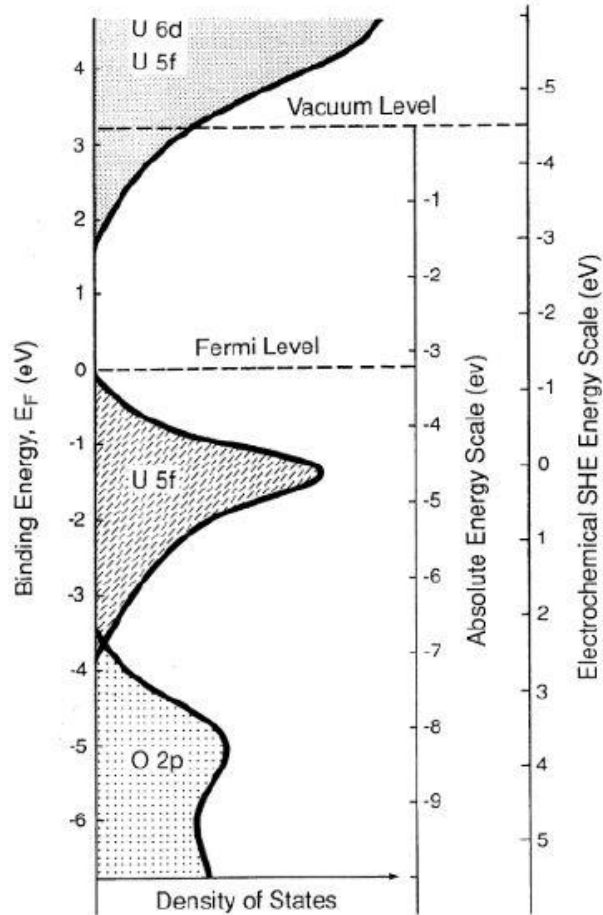


Figure 1-4. Schematic energy level diagram for UO_2 derived from spectroscopic and electrochemical data (expressed on the Standard Hydrogen Electrode (SHE) scale). The filled valence band has predominantly O 2p character, and the empty conduction band consists mainly of U5f, 6d, and 7s states. The U5f band contains two electrons per U atom [24].

The theoretical solubility of crystalline UO_2 , calculated from thermodynamic data, is extremely low [25]. However, measurements [26-34] yield values on the order of $\sim 10^{-9.5}$ mol/L for $\text{pH} > 4$ since the solid is generally not in the perfect crystalline form. Above $\text{pH} \sim 4$, the solubility is insensitive to pH , Figure 1-5.

Under oxidizing conditions, UO_2 can be oxidized to U^{VI} , e.g., as $\text{U}^{\text{VI}}\text{O}_2^{2+}$, and dissolve, since the solubility of U^{VI} is many orders of magnitude greater than that of U^{IV} , as shown for the common phase schoepite ($\text{U}^{\text{VI}}\text{O}_3 \cdot 2\text{H}_2\text{O}$) in Figure 1-5. This renders the fuel susceptible to oxidative dissolution (corrosion) when oxidants are present. Within the pH range anticipated in a DGR (~ 5.5 to 9.5), the common groundwater anions would be expected to increase the solubility of U^{VI} by the formation of soluble complexes but not that of U^{IV} which does not form anion-stabilized complexes [24, 35-38].

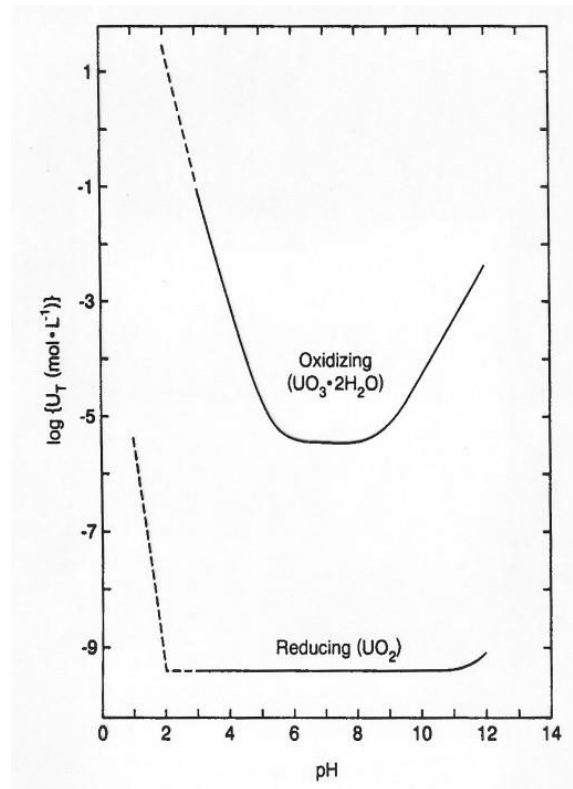


Figure 1-5. Solubilities of UO_2 and Schoepite ($\text{UO}_3 \cdot 2\text{H}_2\text{O}$) as a function of pH [24].

1.3. Properties of Used Fuel

UO₂ is fabricated as ceramic pellets (94% to 97% of theoretical density) for use in a reactor. While CANDU (Canada Deuterium Uranium) fuel is unenriched (0.72% ²³⁵U), light water reactor (LWR) fuel is enriched up to 5% ²³⁵U. Some LWR fuel is mixed oxide (MOX) fuel consisting of UO₂ blended with up to 5% PuO₂. CANDU fuel pellets are sealed within Zircaloy tubes and collected in multi-element fuel bundles (Figure 1-6). CANDU fuel is typically exposed in-reactor to burnups of 8.3-9.2 GWd/tU (200-220 MWh/kgU) [39]. LWR fuels operate to a higher burnup of about 50 GWd/tU because of their enrichment.

In-reactor burnup leads to complex changes in the properties of the fuel [11, 40]. Changes in fuel density occur as fabrication sintering porosity is eliminated, and the generation of fission gas bubbles expands the lattice with bubbles interlinking to form grain boundary tunnels [11, 40, 41]. At higher linear power ratings, grain growth occurs, and thermal stresses lead to cracking [11]. Collision cascades initiated by fission and alpha particle recoil events create a large number of atomic defects, with the final number of defects limited by thermal annealing [42]. Inhomogeneity arises at microscopic and macroscopic levels because of temperature and neutron flux gradients within the fuel. The key features of this evolution in the microstructure relevant to the present discussion are illustrated in Figure 1-7.

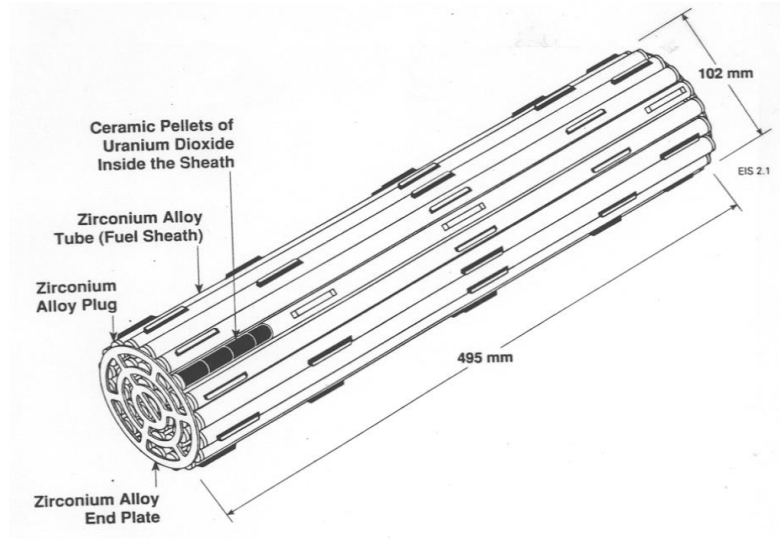


Figure 1-6. Schematic illustration of a 37-element CANDU fuel bundle [43].

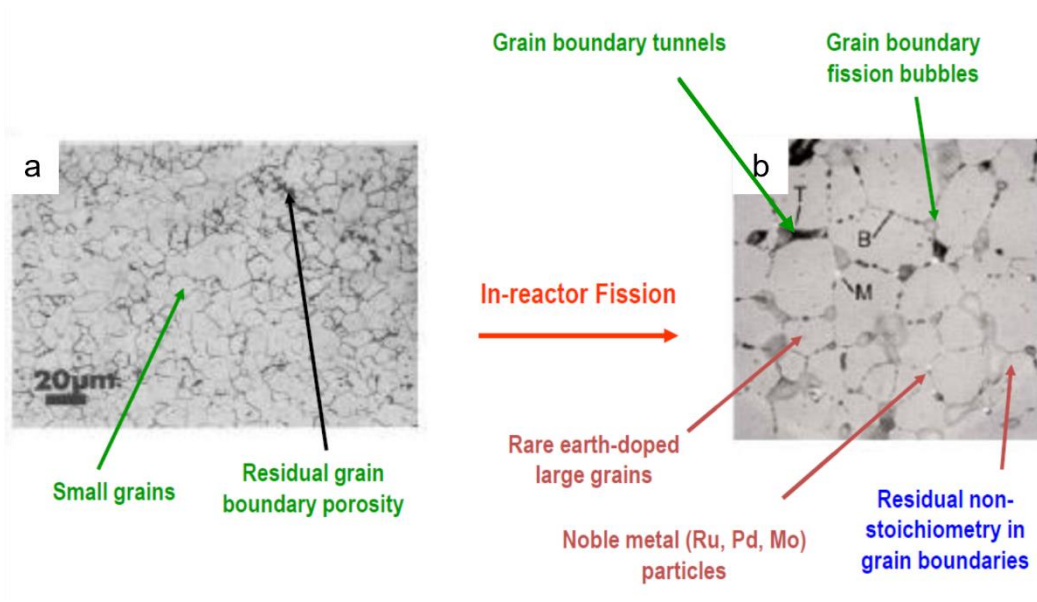


Figure 1-7. SEM Micrographs of UO_2 fuel: (a) unirradiated UO_2 , (b) fuel irradiated at high burnup (770 MWh/kgU) with key features of unirradiated fuel and in-reactor irradiation noted, respectively. Features of irradiated fuel noted in brown and blue can be simulated in unirradiated UO_2 , while those in green (in panel b) cannot [44].

For CANDU fuel, the radial variation in grain size and porosity is small. Besides physical changes, in-reactor irradiation leads to the formation of a wide range of radionuclides as a result of fission reactions, e.g.,



neutron capture, e.g.,



and, to a lesser extent, activation, e.g.,



where n denotes a neutron. Freshly discharged CANDU used fuel contains numerous radionuclides, many of which decay quickly. Analyses are available that list the radionuclide inventories [45, 46] and identify those deemed important under disposal conditions [47].

The chemical composition and microstructure of spent nuclear fuel have been studied in detail [11, 46, 48-50]. These studies show that, while the majority (> 90%) of fission and activation products remain at the location where they were formed, the high reactor operating temperatures lead to some redistribution. The species produced can be grouped according to their chemical behaviour.

(a) Gaseous or volatile species, such as He, Kr, Cs, and I, have relatively high diffusion coefficients under in-reactor conditions and can migrate within the fuel. Small amounts of these species are expressed from the grains into cracks and voids in the fuel and the fuel-cladding gap. Slightly larger amounts become trapped at grain boundaries, while the majority remain as bubbles in the lattice.

(b) Fission products which can form stable oxides incompatible with the UO₂ matrix (e.g., Rb, Cs, Ba, Zr, Nb, Mo, Tc, Sr) can separate into segregated oxides which adopt a perovskite structure with the general composition ABO₃ (A = Ba, Sr, Cs; B = Zr, Mo, U, Pu, rare earths).

(c) Non-volatile species unstable as oxides (e.g., Mo, Ru, Pd) can diffuse within the fuel at high temperatures to form metallic alloy phases commonly referred to as noble metal (ϵ) particles.

(d) Many elements, including actinides (including Np, Am, Pu, Cm), rare earths (including La, Ce, Pr, Nd, Pm, Sm, Eu, Gd, Y) and Sr, Zr, Ba, Te and Nb can remain as ion substitutes in the fuel matrix, within the limits of their solubility to the extent they have not precipitated as ABO_3 phases.

Two fission products exert additional influences on the fuel. Mo can coexist in the metallic and oxide forms and, hence, can maintain the fuel close to stoichiometry. Zr, which can be segregated to the ABO_3 phases, can also be retained by the fuel matrix, within which it can exert an influence on the lattice dimensions. Finally, neutron capture within the fuel cladding can form small inventories of activation products. Figure 1-8 summarizes this distribution of fission products and actinides within the spent fuel matrix [11].

The key thermodynamic factor that influences the chemical state of many fission products in the fuel is the O potential, which is initially very low since the used fuel is stoichiometric [51]. However, burnup raises the ratio of O to U because the O released cannot be completely bonded by the generated fission products, many of which either possess lower oxidation states than IV or are stabilized in the metallic form [52]. Much of this O is neutralized by the formation of ZrMo oxide and reaction with the inner surface of the Zircaloy cladding [53, 54]. For CANDU fuel, the approximate change in fuel stoichiometry has been calculated to range from $UO_{2.001}$ to $UO_{2.007}$ [55].

The irradiation history of spent fuel is characterized by its power rating and burnup, with the radionuclide inventory at the time of emplacement in the DGR depending on how long the spent fuel has been discharged from the reactor. The age of the fuels to be placed in a Canadian DGR will vary, with the earliest dating back to the 1950s for some research fuels. Because the DGR will not open before 2040, the fuel age will range from 10 to > 60 years. The power rating and burnup history of CANDU fuel is known [39], and the used fuel radionuclide inventories for CANDU fuel of various burnups have been calculated [45].

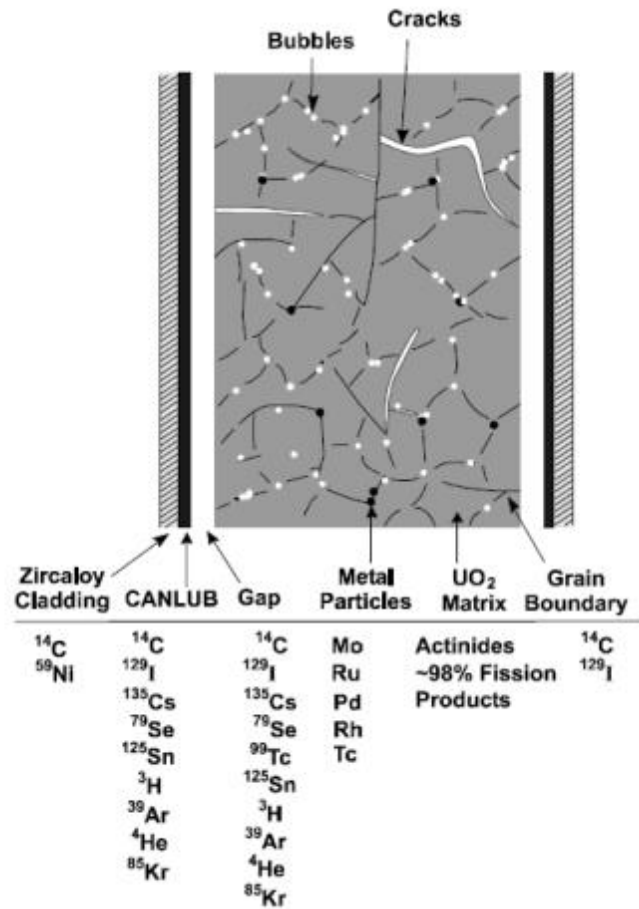


Figure 1-8. Schematic illustration showing the conceptual distribution of fission and activation products within a spent fuel element [43].

Based on these studies, three radionuclide inventories can be defined, as illustrated in Figure 1-9.

- (i) The gap inventory comprises volatile radionuclides accumulated in the fuel-cladding gap. These radionuclides would be expected to be readily soluble and, hence, be rapidly released on contact with groundwater.

- (ii) The inventory of radionuclides which have segregated to grain boundaries within the fuel. Their release will depend on their chemical nature and the chemical and physical properties of their location and could require a protracted period of groundwater exposure.
- (iii) The matrix inventory of radionuclides retained within the fuel grains whose release would be controlled by the corrosion/dissolution of the UO_2 matrix.

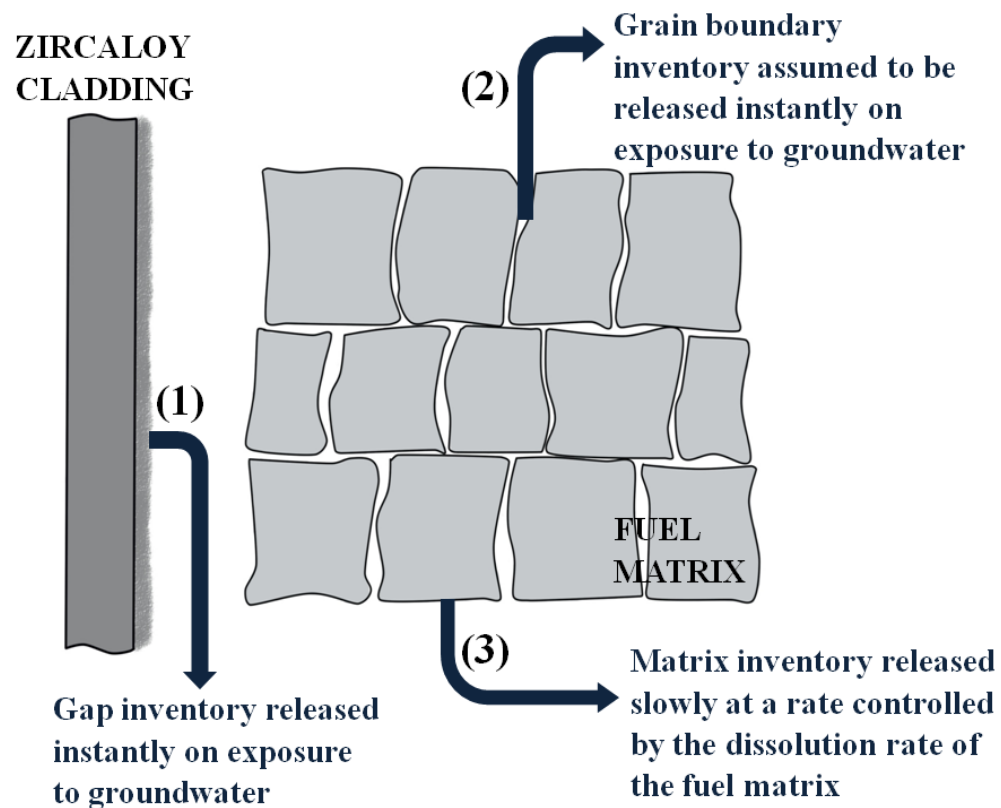


Figure 1-9. Conceptual illustration of the three categories of radionuclide within a spent fuel element [56].

Of these inventories, (i) and (iii) have been extensively studied. Determining the grain boundary inventory (ii) is more difficult to assess despite considerable recent efforts [21]. As a consequence, when assessing radionuclide release, only two release fractions are considered: (a) an instant release fraction (IRF) comprising inventories (i) and (ii), and a matrix dissolution fraction comprising inventory (iii).

The fuel is highly radioactive on discharge from the reactor, but its activity decreases quickly with time. The overall radioactivity for CANDU spent fuel decreases to ~ 0.01% of its value on discharge after ~ 10 years. The evolution in radioactivity beyond 10 years is shown for a reference CANDU fuel (220 MWh/kgU burnup) in Figure 1-10. The basis for choosing this reference value has been discussed elsewhere [45]. For a presently uncertain time up to, or possibly longer than, 100 years, the fuel will be in dry storage.

A majority of the gamma (γ) emitting fission products and activated impurities within the cladding will decay within the first 100 years (Figure 1-10), beyond which the decay will be dominated by α -particle emission predominantly from the actinide content. Since radioactivity is related to the behaviour of specific radionuclides, both the overall decreases in activity level and the radionuclide composition of the fuel are important.

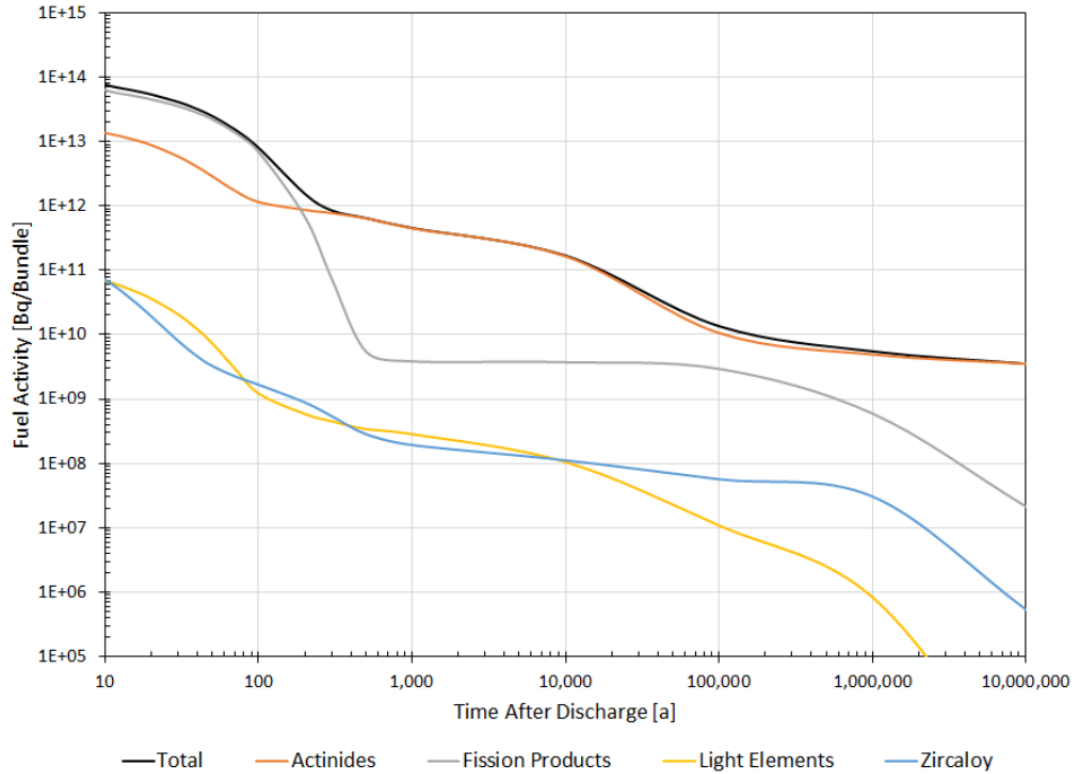


Figure 1-10. Radioactivity of reference CANDU used fuel (220 MWh/kgU burnup) as a function of time after discharge from reactor [47].

1.4. Matrix Corrosion and Radionuclide Release Under Disposal Conditions

Determining the behaviour of used nuclear fuel under disposal conditions requires the consideration of two radionuclide release processes on contact with groundwater, assuming container failure has occurred: (i) the IRF and (ii) the matrix corrosion/dissolution fraction. Since > 90% of radionuclides are contained within the solid-state matrix of the used fuel, the matrix corrosion/dissolution fraction would be expected to be dominant.

1.4.1. The Instant Release Fraction (IRF)

Determination of the IRF requires knowledge of the radionuclide inventories, the half-lives and decay sequences of the individual radionuclides, and analytical measurements of the gap and grain boundary inventories. The half-lives of most radionuclides are known and tabulated [57], and radionuclide inventories can be determined using well-developed codes. These measurements and calculations have been described in detail for various types of fuel [58-61] including CANDU fuel [62-66], and thoroughly reviewed [11, 21, 67, 68].

1.4.2. The Influence of Redox Conditions

The release of > 90% of radionuclides contained within the fuel matrix (the matrix inventory (iii)) will be governed by the corrosion/dissolution of the fuel. The rate of this process will be related to, but not necessarily directly proportional to, the solubility of uranium in the groundwater (Section 1.3). At DGR depths, groundwaters are O₂-free. All O₂ introduced during the construction and operation phases of the DGR, prior to sealing, will have been relatively rapidly consumed by mineral and biochemical reactions in the clays surrounding the emplaced waste container, and by corrosion of the container materials [9, 69].

While groundwater entering a failed container may be anoxic, its radiolysis due to radioactive decay processes within the fuel will produce a variety of chemical species, including oxidants, which can oxidize the UO₂ to the more soluble U^{VI}O₂²⁺ state (Figure 1-5), a process which can be considered a corrosion reaction. The thermodynamic driving force for a corrosion process is illustrated in Figure 1-11. The redox potential of the groundwater (E_{Red/Ox}, commonly termed E_h) must be greater than the equilibrium potential for fuel oxidative dissolution, (E^e)_{UO₂/(UO₂)₂₊}, with the driving force for corrosion being the potential difference, (E^e)_{Red/Ox} - (E^e)_{UO₂/(UO₂)₂₊}. Under these conditions, the fuel will establish a corrosion potential (E_{CORR}) at which the anodic dissolution rate and the cathodic reagent reduction rate are equal, with the overall corrosion reaction being



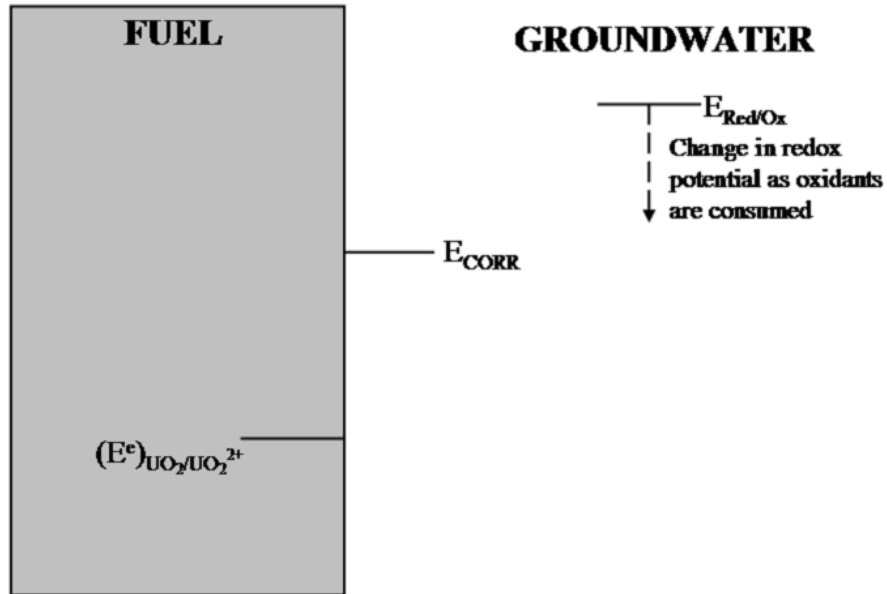


Figure 1-11. Illustration demonstrating the thermodynamic driving force for fuel corrosion in an aqueous solution containing oxidants: E_{CORR} is the corrosion potential at which the overall corrosion process occurs on the fuel surface [70].

Early studies demonstrate that the rate of this reaction is dependent on the redox conditions established inside a container containing groundwater, with corrosion rates determined by the available radiolytic oxidants [13, 25, 71-73]. Since radiation fields decay with time (Figure 1-12), the corrosion rate will decrease as the radiolytically-established redox conditions change with time.

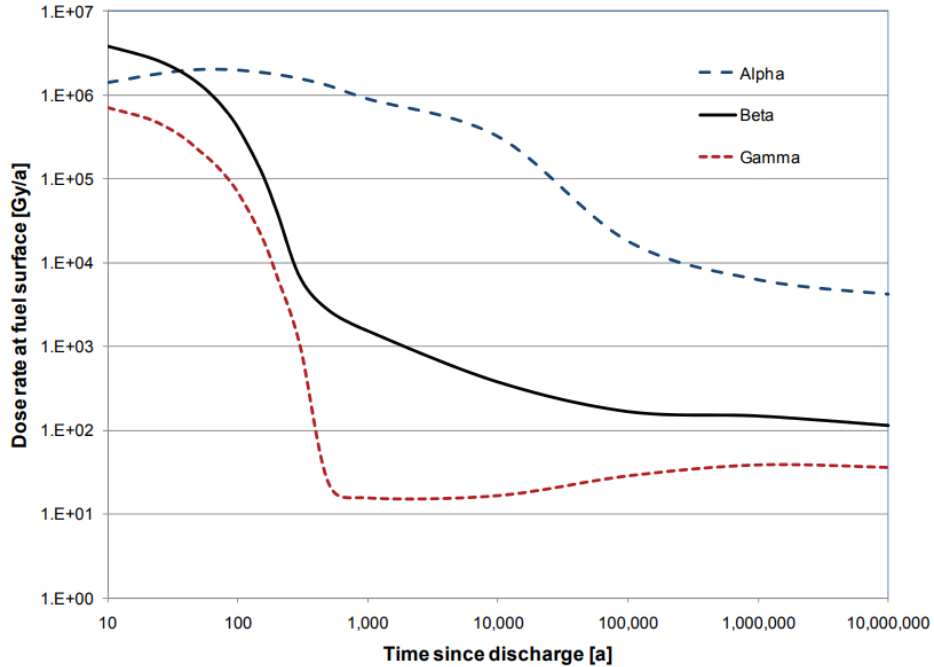


Figure 1-12. Alpha (α), beta (β) and gamma (γ) dose rates as a function of time for a layer of water in contact with a CANDU fuel bundle with a reference burnup of 220 MWh/kgU [74].

Two corrosion fronts will exist within a failed container: one on the fuel surface driven by radiolytic oxidants and the second on the steel surface sustained by H_2O reduction producing the potential redox scavengers Fe^{2+} and H_2 . Under the assumption that the used fuel containers (UFC) will remain unbreached over a period of at least a few 100 years, when γ/β radiation fields are significant (Figure 1-12), only α -radiolysis is considered as a source of oxidants. Among the α -radiolysis products, only molecular oxidants, such as H_2O_2 [75], are expected to be important. Radical oxidants have short lifetimes and steady-state concentrations orders of magnitude lower than those of molecular products [76]. Figure 1-13 shows the equilibrium potentials (E°) for the coupled anodic and cathodic reactions on the two surfaces and the respective E_{CORR} values adopted by the two surfaces in the neutral to slightly alkaline conditions anticipated under disposal conditions [3, 77, 78]. The zone marked E_h indicates the

redox condition possible at high α dose rates. The redox gradient between the two corroding surfaces is apparent in the difference in established E_{CORR} values.

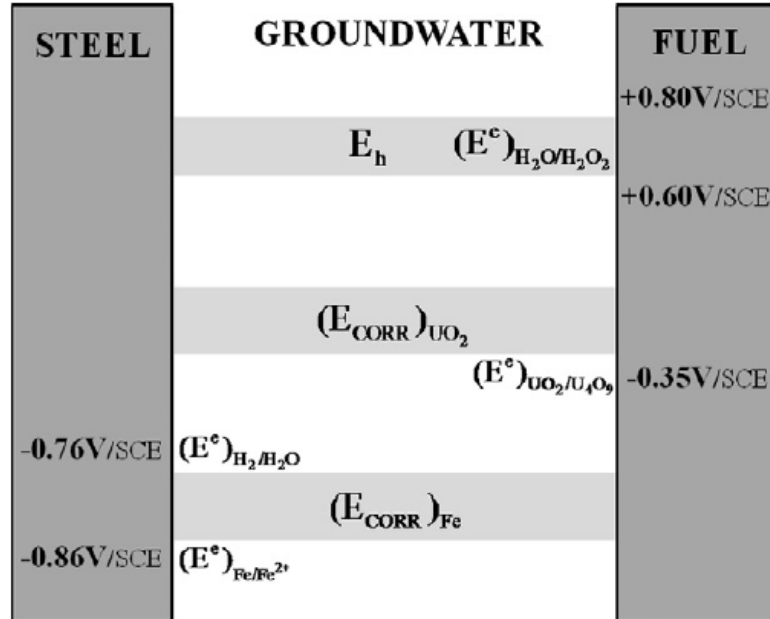


Figure 1-13. Illustration showing the two corrosion fronts existing within a failed groundwater-flooded waste container. One front is on the fuel surface, established by reactions with radiolytic oxidants, and the second is on the steel surface, established by reactions with H_2O [79].

As α -radiation fields evolve with time (Figure 1-12), both $(E^c)_{H_2O/H_2O_2}$ and E_{CORR} on the UO_2 surface will decrease as the driving force for corrosion decreases. If E_{CORR} decreased to or below $(E^c)_{UO_2/U_4O_9}$, the corrosion driving force would disappear and the fuel become electrochemically stable. If fuel degradation were to continue, it would have to be by chemical dissolution (as U^{4+}), not corrosion as $U^{VI}O_2^{2+}$. Calculations based on available thermodynamic data [27, 36, 37] show that E_h would need to be ≤ -0.35 V (vs SCE) for this condition to apply.

1.4.3. Oxidation of the Uranium Dioxide Surface

Uranium generally exists in one of three oxidation states, $U^{IV/V/VI}$, but is effectively only soluble as U^{VI} [27, 34]. Applying electrochemical methods and subsequently analyzing the surface by X-ray photoelectron spectroscopy (XPS), the composition of a $U^{IV}O_2$ surface has been deconvoluted as a function of the potential applied to the surface. Figure 1-14 shows the increasingly oxidized state of the surface as the applied potential is increased from a value of -0.5 V (vs SCE), which is below the potential at which the oxidation of UO_2 should commence (as discussed in Section 1.5.2), to a value of +0.5 V (vs SCE), which is well above any E_{CORR} achievable under open-circuit corrosion conditions in a DGR [80]. The relative amounts of the three oxidation states observed at the lowest potential are indistinguishable from those measured on surfaces strongly reduced at -1.5 V (vs SCE), making them representative of the unoxidized $U^{IV}O_2$ surface. The procedures used to deconvolute spectra into contributions from U^{IV} , U^V and U^{VI} have been described [81-84].

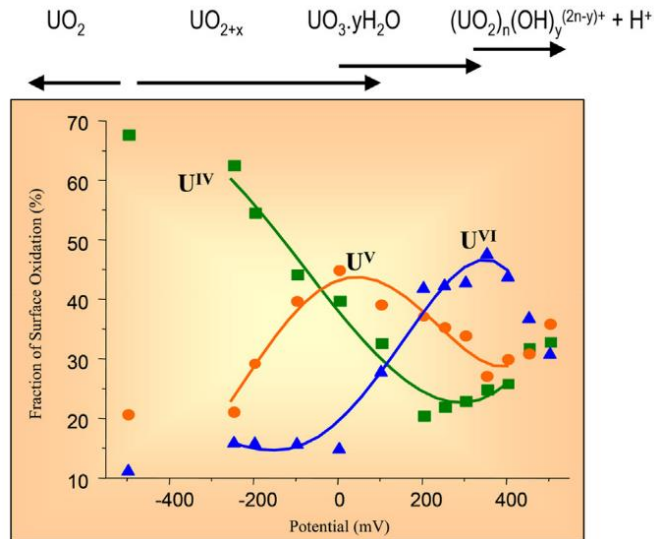
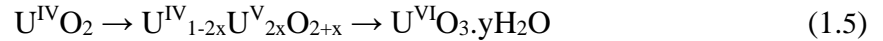
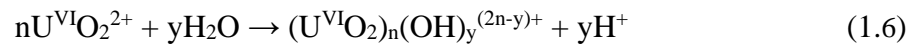


Figure 1-14. The fractions of various oxidation states of U in a 1.5 at% SIMFUEL electrode surface as a function of applied electrochemical potential. The electrode was anodically oxidized at each potential for 1 hour in 0.1 mol/L NaCl (pH = 9.5) solution and then analyzed by X-ray photoelectron spectroscopy (XPS) [80].

All three oxidation states can be detected with the extent of oxidation proceeding through the compositional sequence indicated in Figure 1-14 [80, 85-87]. Oxidation occurs in a two-step process,



The first step involves the injection of O^{II} into vacant interstitial lattice sites (Figure 1-3) to form a thin (≤ 5 nm) $\text{U}^{\text{IV}}/\text{U}^{\text{V}}$ surface layer. As the potential increases, the outer regions of this layer are converted to a U^{VI} alteration product, which can dissolve as $\text{U}^{\text{VI}}\text{O}_2^{2+}$. For high applied potentials, this alteration layer can dissolve more extensively at surface sites where the hydrolysis of already dissolved $\text{U}^{\text{VI}}\text{O}_2^{2+}$ leads to acidification,



and an increase in solubility (Figure 1-5). This hydrolysis/acidification process leads to a decrease in U^{VI} , which exposes the underlying $\text{U}^{\text{IV}}/\text{U}^{\text{V}}$ layer (Figure 1-14).

1.4.4. Reactivity of the Uranium Dioxide Surface

Attempts to measure fuel corrosion rates show a wide variation in fuel reactivity [24, 88, 89] although it is often unclear whether these differences are attributable to real differences in reactivity, or differences in experimental conditions, specimen treatment, or analytical measurements. Photothermal deflection spectroscopy measurements [90], performed on undoped UO_2 in solutions not containing known complexants for UO_2^{2+} detected anodic dissolution at potentials as low as -0.3 V (vs SCE). This suggests the release could commence as soon as the oxidation of the matrix became thermodynamically possible. It was speculated, but not demonstrated, that dissolution at such low potentials could be due to the preferential oxidation and dissolution of non-stoichiometric grain boundaries. Early studies report a difference between the measured dissolution currents (in electrochemical measurements) [91] for single crystals and sintered discs by a factor of 10^3 , and between the dissolution rates (measured chemically) for UO_2 and natural uraninite specimens containing ill-defined

impurities [92]. This indicates that defects and impurities could significantly affect fuel corrosion rates. These observations suggest that in-reactor burnup, leading to lattice doping with fission products and the formation of noble metal (ϵ) particles, will influence fuel corrosion rates.

1.4.5. The Influence of Non-Stoichiometry

As previously noted, the approximate change in fuel stoichiometry for CANDU fuel has been calculated to range from $\text{UO}_{2.001}$ to $\text{UO}_{2.007}$, while the higher burnup LWR/BWR fuels exhibit only marginal oxidation. As indicated in Figure 1-3, the face-centred cubic UO_2 lattice contains a large number of octahedral vacant sites, which allows the lattice to accommodate large amounts of O_I to form hyperstoichiometric $\text{U}^{\text{IV}}_{1-2x}\text{U}^{\text{V}}_{2x}\text{O}_{2+x}$. Incorporation of O occurs readily since the energy of formation for O_I is negative [93-97]. This, and the ability of U to form multiple oxidation states (U^{IV} , U^{V} , U^{VI}), allows the formation of a complex family of binary metal oxides within the range from UO_2 to U_3O_7 [98]. As noted above, this increases the electrical conductivity and provides donor-acceptor relay sites in the surface of the oxide, which can catalyze oxidant reduction reactions.

By studying a range of stoichiometries that extend to higher values, three aspects of the corrosion process can be investigated: (i) the composition (UO_{2+x}) at which the surface becomes unstable and susceptible to dissolution can be identified; (ii) the influence of surface composition on the kinetics of the cathodic reactions supporting corrosion can be determined; and (iii) the importance of surface composition on the kinetics of radiolytically-produced H_2O_2 decomposition can be evaluated.

The changes in the properties of the oxide and their influence on the reactivity of UO_2 have been characterized by Raman spectroscopy using a specimen with a nominal stoichiometry of $\text{UO}_{2.1}$ [99]. Figure 1-15 shows the surface of a specimen exhibiting four distinct features which can be distinguished according to the relationship between their topography and composition. The Raman spectra recorded on such locations, Figure 1-16, show that the relative decrease in intensity of the peak at 445 cm^{-1} (indicative of the undisturbed fluorite lattice) is accompanied by a relative increase in the peaks within the band between 500 cm^{-1} and 700 cm^{-1} (indicative

of the increasingly disturbed lattice as non-stoichiometry increases). A small peak at 155 cm^{-1} (indicating the onset of tetragonal lattice distortions) is also observed at higher degrees of non-stoichiometry.

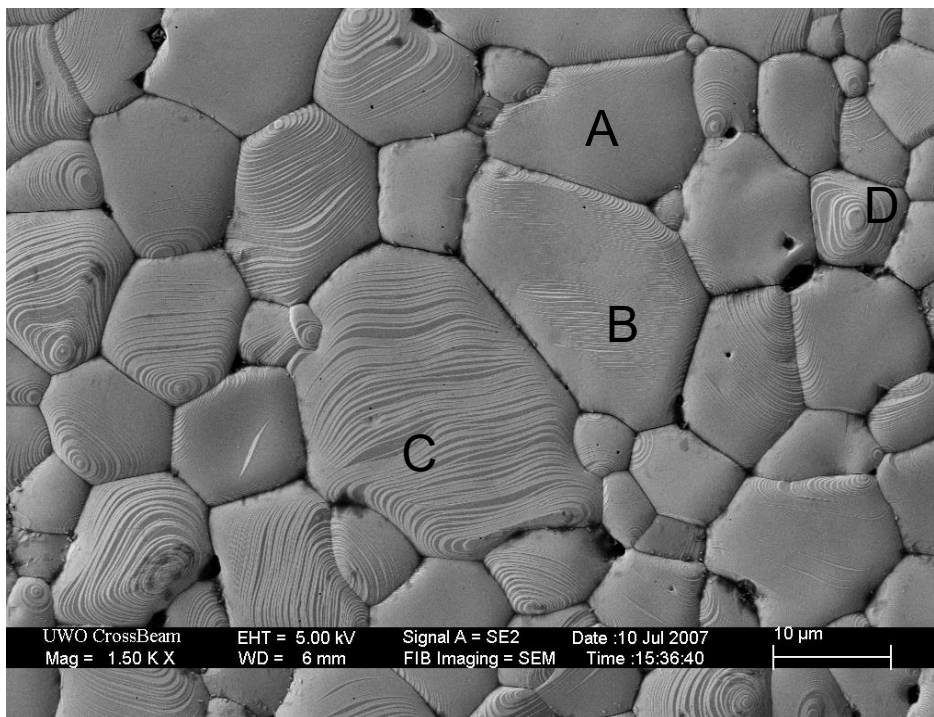


Figure 1-15. SEM image of a typical surface morphology observed on a UO_2 specimen with a nominal stoichiometry of $\text{UO}_{2.1}$. (A) A smooth, flat grain with an approximate O/U ratio of 2.01; (B) A grain with a very shallow stepped pattern with a slightly hyperstoichiometric composition of ~ 2.15 ; (C) A grain with a pronounced stepped pattern of ridges oriented horizontally along the X-Y plain with a composition of ~ 2.22 ; (D) A highly non-stoichiometric spiral-like grain with a composition of ~ 2.31 [99].

An extensive series of Raman spot analyses and an accompanying XRD analysis yielded a relationship between the various Raman peaks and their connection to lattice composition and structure. Interpretation of these changes [99] are indicated in Figure 1-17:

- For relatively low degrees of non-stoichiometry, the number of randomly distributed O_I increases.
- For $x > 0.05$, further increases in non-stoichiometry lead to the association of defects into clusters.
- For a sufficiently high degree of non-stoichiometry ($x > 0.15$), the generation of large cuboctahedral clusters leads to a major loss of cubic symmetry with the observance of a band at 155 cm^{-1} indicating the onset of a cubic to tetragonal structural transition.

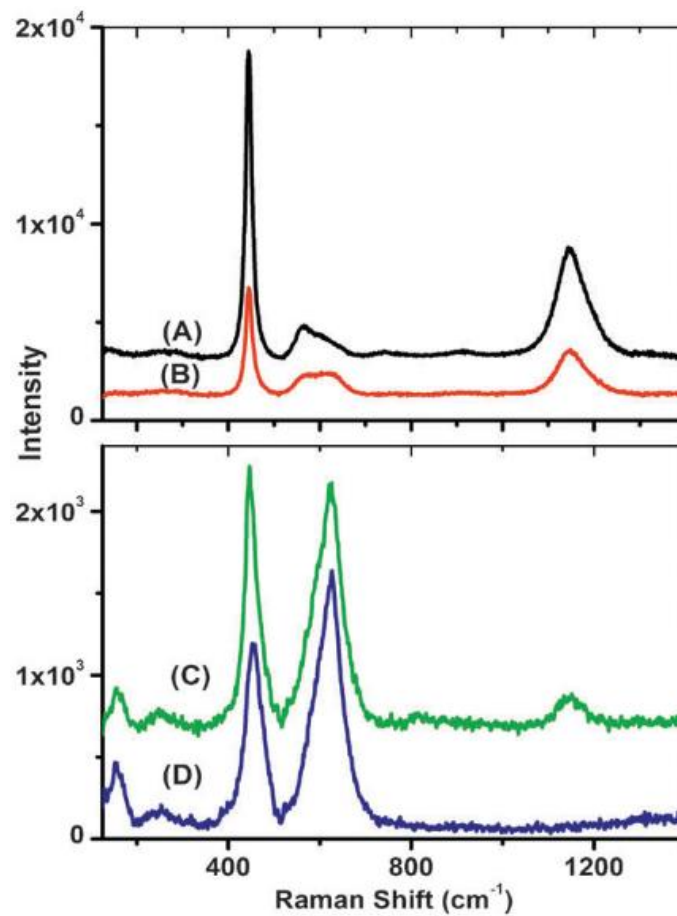


Figure 1-16. Raman spectra recorded on the four types of grains (A) to (D) shown and described in Figure 1-15. The O/U ratios are ~ 2.01 (A), ~ 2.15 (B), ~ 2.22 (C), ~ 2.31 (D) [99].

The cuboctahedral cluster is the most densely packed defect cluster, which minimizes the damage to the UO_2 lattice induced by the incorporation of excess O by optimizing the spatial distribution of vacancies and interstitials [100, 101]. These observations are consistent with published literature [100, 102-104]. As the degree of non-stoichiometry increases, the surface oxidation progresses deeper into the UO_2 matrix. This is demonstrated in a series of voltammetric experiments on UO_{2+x} specimens with nominal compositions of $\text{UO}_{2.002}$, $\text{UO}_{2.011}$, $\text{UO}_{2.05}$ and $\text{UO}_{2.1}$. These specimens have been extensively characterized [99, 105-108] and shown to range from a specimen almost uniformly stoichiometric ($\text{UO}_{2.002}$) to one comprised of individual grains ranging from stoichiometric to extremely non-stoichiometric ($\text{UO}_{2.1}$), as shown in Figure 1-15.

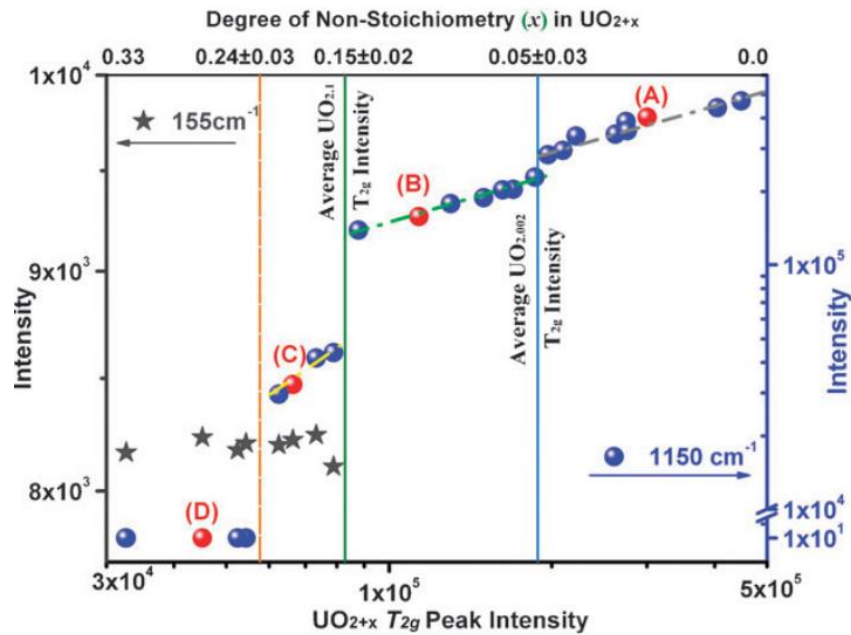


Figure 1-17. The relationships between the intensities of the band at 445 cm^{-1} (T_{2g}) and the bands at 1150 cm^{-1} and 155 cm^{-1} based on Raman spot analyses. A-D correlate to similar degrees of non-stoichiometry to those labelled in Figure 1-15. The vertical lines indicate the transitions between defect structures. The compositions indicate the degree of non-stoichiometry at which the transitions occur [99].

Figure 1-18 shows voltammograms recorded on these four specimens with anodic currents indicating the extent of oxidation on the forward potential scan (from negative to positive potentials) and cathodic currents the extent of reduction of the anodically oxidized surface on the reverse potential scan.

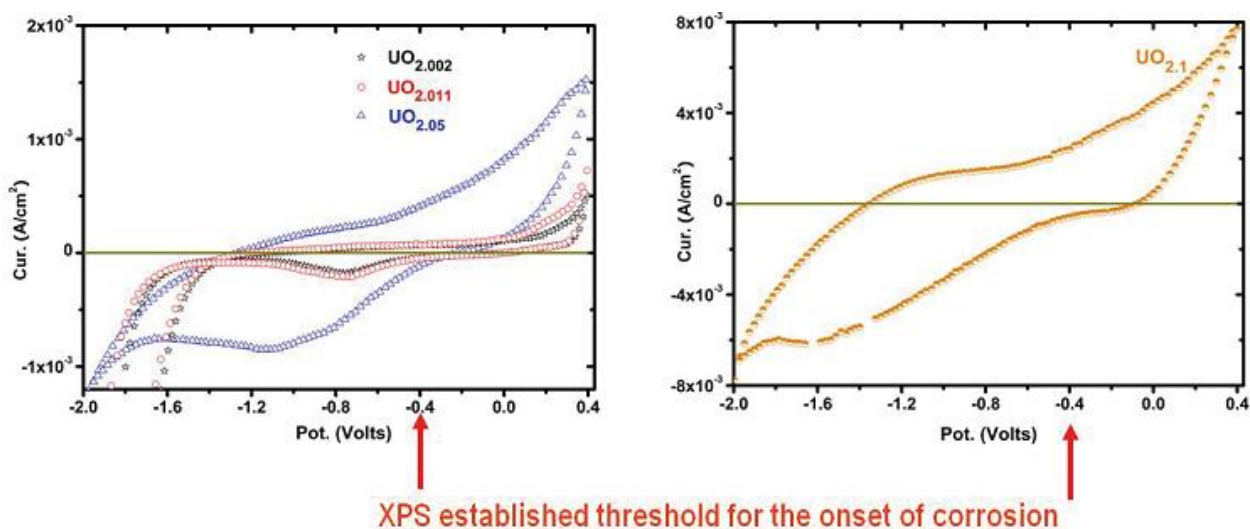


Figure 1-18. Voltammograms recorded on four hyperstoichiometric electrodes in 0.1 mol/L NaCl solution (pH 9.5) at a scan rate of 5 mV/s. The threshold is that established for the onset of oxidation [43].

For the two specimens closest to stoichiometric, anodic oxidation currents were low. The reduction current peak (between -0.7 V and -0.9 V) indicated only a thin oxide surface layer was formed on the forward scan. The very low currents (UO_{2.002}, UO_{2.011}) recorded at potentials below the threshold, indicate minimal sub-thermodynamic oxidation as expected and are consistent with Raman spectroscopic measurements [99, 106, 107]. As the degree of non-stoichiometry increases to UO_{2.05} and UO_{2.1}, the anodic current both below and above the threshold increases markedly, indicating the facile and more extensive oxidation of non-

stoichiometric regions of the surface with the large reduction current on the reverse scan confirming the formation (on the forward scan) of a much more extensively oxidized surface. A combination of SEM and SECM measurements confirms that oxidation occurs preferentially on non-stoichiometric grains [105-107].

1.4.6. The Influence of Lattice Dopants

Figure 1-19 compares the dissolution charges (extent of dissolution measured electrochemically in voltammetric experiments) [109] for a UO_2 specimen close to stoichiometric ($\text{UO}_{2.002}$), 1.5 at% simulated spent fuel (SIMFUEL), and two RE^{III} -doped UO_2 specimens with stoichiometric compositions. For $\text{UO}_{2.002}$, minor dissolution commenced at potentials as low as -0.7 V (vs SCE), which is well below the thermodynamic threshold for the oxidation of UO_2 (\sim -0.4 V vs SCE). Current sensing atomic force microscopy (CS-AFM) indicates this could be due to the presence of non-stoichiometric surface locations in the vicinity of the grain boundaries [109], consistent with the claims of Rudnicki, et al. [90] based on photothermal deflection spectroscopic measurements. The extent of dissolution (Figure 1-19) decreased in the order:



demonstrating the influence of RE^{III} -doping in decreasing the reactivity of the UO_2 surface.

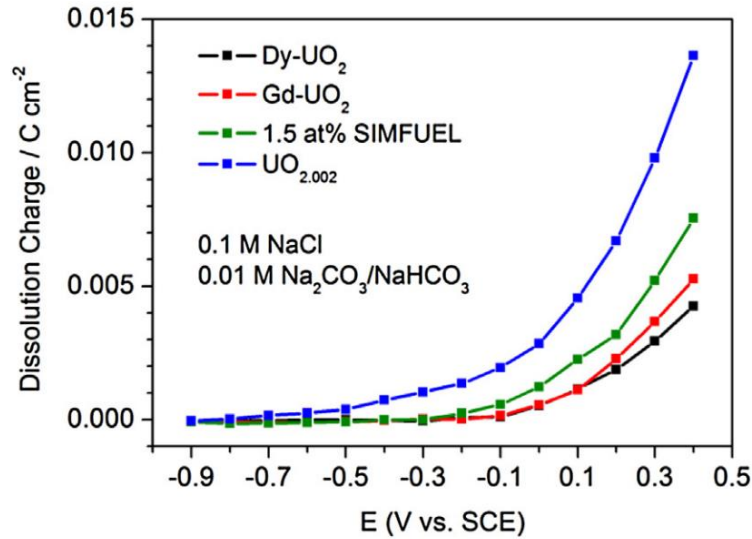


Figure 1-19. Dissolution charges calculated for four UO₂ materials from voltammograms recorded in 0.1 mol/L NaCl solution containing 0.01 mol/L [CO₃]_{total}. Dy-UO₂ (12.9 wt% Dy₂O₃); Gd-UO₂ (6.0 wt% Gd₂O₃); 1.5 at% SIMFUEL; Undoped UO_{2.002} [109].

1.4.7. The Influence of Surface Composition

This influence of surface stoichiometry can be appreciated by reconsidering the results in Figure 1-19 for the Dy-UO₂ specimen. These experiments were conducted in carbonate-containing solutions to stimulate dissolution rather than the retention of U^{VI} in alteration phases on the UO₂ surface. This procedure enabled XPS analyses of the surface to detect changes in composition in the U^{IV}_{1-2x}U^V_{2x}O_{2+x} layer unobscured by U^{VI} deposits (Figure 1-20). Over the potential range from -0.2 V (vs SCE) to 0.1 V (vs SCE), the extent of surface oxidation increases markedly, as indicated by the more rapid increase in U^V content with potential, with the results in Figure 1-19 showing this increase is accompanied by the onset of dissolution. Since the surface content of U^{VI} changed only marginally, this enhanced oxidation can be attributed to the thickening of the U^{IV}_{1-2x}U^V_{2x}O_{2+x} layer.

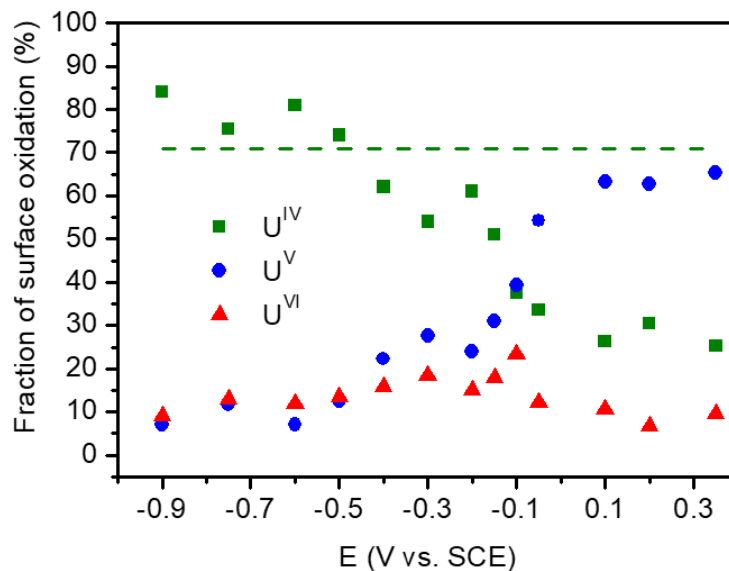


Figure 1-20. Relative fractions of U oxidation states as a function of applied potential, recorded on Dy-UO₂ (12.9 wt% Dy) after 1 hour of oxidation in 0.1 mol/L NaCl + 0.05 mol/L [CO₃]_{total} solution. The dashed line shows the fraction of U^{IV} recorded on a freshly polished Dy-UO₂ surface [109].

This change occurred at a surface composition of $\sim \text{U}^{\text{IV}}_{0.7}\text{U}^{\text{V}}_{0.3}\text{O}_{2.15}$, a composition around which Raman spectroscopy first detects the onset of the distortion of the cubic lattice to a tetragonal structure (Figure 1-17) (i.e., the appearance of the band at 155 cm^{-1}) [99]. This is consistent with SECM measurements, which show that beyond an intermediate composition in this range, the rate and depth of anodic oxidation increased markedly [106]. These coincidences and their consistency with the phase transformations occurring during oxidation demonstrate that the onset of tetragonal distortions of the cubic lattice leads to dissolution. Raman spectroscopy indicates that this transformation involves a switch from shallow oxidation involving randomly distributed O_I ions to deeper oxidation involving lattice distortions and the formation of cuboctahedral clusters. An attempt to illustrate this change is shown in Figure 1-21 [109].

force microscopy (CS-AFM) demonstrates this could be attributable to surface locations near grain boundaries with a stoichiometry already beyond the threshold of $\text{UO}_{2.15}$ [109].

1.4.8. The Influence of Groundwater Species

The composition of the groundwater entering a failed container will depend on the type of host rock and the interaction between groundwater and the surrounding clay as DGR conditions evolve with time. Groundwater compositions from Canadian sedimentary rocks and crystalline rocks have been measured [111]. The reference groundwater compositions are noted in Hall, et al. [9]. The key groundwater species likely to influence fuel dissolution are the anions Cl^- , SO_4^{2-} and HCO_3^- and the cations, H^+ , Na^+ and Ca^{2+} .

While the concentration of HCO_3^- in the groundwater is expected to be low and controlled by the solubility of carbonate minerals (e.g., calcite (CaCO_3)) in the clay surrounding the container [69] and in the host rock, its ability to complex $\text{U}^{\text{VI}}\text{O}_2^{2+}$ [27, 34-36] makes it the most likely anion to influence the fuel corrosion process. As a consequence, its influence has been extensively studied [112-115].

Figure 1-22 shows a series of voltammograms recorded on Dy-doped UO_2 [109]. A number of features are instructive. The potential at which anodic dissolution commences is -0.2 V (vs SCE) when tetragonal lattice distortions first occur, Figure 1-21. This onset is independent of $[\text{CO}_3]_{\text{total}}$, indicating the lattice is destabilized by the strength of oxidation, not the presence of HCO_3^- . For more positive applied potentials, the current becomes dependent on $[\text{CO}_3]_{\text{total}}$, consistent with the acceleration of dissolution by HCO_3^- . The two small reduction peaks observed on the reverse scan show that a small amount of the anodic current is consumed in the formation of surface films, with current peak 1 attributed to the reduction of the $\text{U}^{\text{IV}}_{1-2x}\text{U}^{\text{V}}_{2x}\text{O}_{2+x}$ layer and peak 2 to the reduction of $\text{U}^{\text{VI}}\text{O}_3 \cdot y\text{H}_2\text{O}$ or $\text{U}^{\text{VI}}\text{O}_2\text{CO}_3$ formed at the oxide/solution interface [109]. The charge associated with these films is reduced as the $[\text{CO}_3]_{\text{total}}$ is increased, confirming that when a sufficient concentration of HCO_3^- is present, deposition of U^{VI} as $\text{U}^{\text{VI}}\text{O}_3 \cdot y\text{H}_2\text{O}$ or $\text{U}^{\text{VI}}\text{O}_2\text{CO}_3$ is prevented and the $\text{U}^{\text{IV}}_{1-2x}\text{U}^{\text{V}}_{2x}\text{O}_{2+x}$ surface layer is thinned.

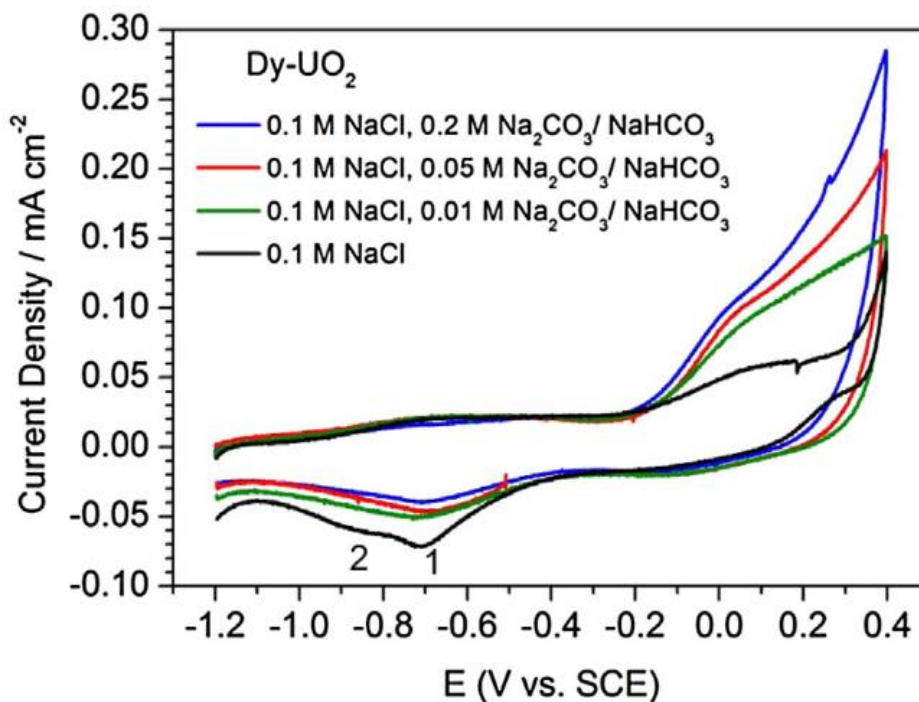
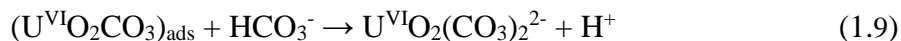
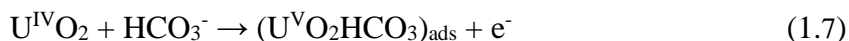


Figure 1-22. Cyclic voltammograms recorded on a rotating (16.7 Hz) Dy-UO₂ (12.9 wt% Dy) electrode in an Ar-purged 0.1 mol/L NaCl solution containing various [CO₃]_{total} at a scan rate of 10 mV/s [109].

The results of a more extensive study on SIMFUELS [115] used electrochemical impedance spectroscopy (EIS) measurements to confirm the overall reaction proceeds via adsorbed U^V and U^{VI} intermediates,



with the first electron transfer step (reaction 1.7) controlling the corrosion rate at low potentials and the chemical dissolution step (reaction 1.9) controlling the rate at high potentials. A similar

switch from control by electron transfer to control by chemical dissolution depending on the $[\text{H}_2\text{O}_2]$ and $[\text{CO}_3]_{\text{total}}$ has been observed in chemical (open circuit) experiments [113, 116], although the kinetics were complicated by studtite ($[\text{UO}_2\text{O}_2(\text{H}_2\text{O})_2](\text{H}_2\text{O})_2$) formation. Under DGR conditions, when oxidant concentrations will be low, reaction 1.7 will be the slow anodic step, with the corrosion rate dictated by the kinetics of the oxidant reduction reaction.

When present at a sufficiently high concentration, HCO_3^- can also influence the kinetics of oxidant reduction reactions. Irrespective of whether O_2 or H_2O_2 is the oxidant, HCO_3^- can suppress the oxidant reduction rate by adsorbing and stabilizing U^{V} surface states, thereby denying $\text{O}_2/\text{H}_2\text{O}_2$ access to the DAR (Donor-Acceptor Relay) sites, which catalyze their reduction [117, 118]. At sufficiently high $[\text{HCO}_3^-]$ and $[\text{H}_2\text{O}_2]$, it has also been proposed, but not analytically demonstrated, that U^{V} -peroxycarbonate species ($\text{U}^{\text{V}}\text{O}_2(\text{HCO}_3)(\text{H}_2\text{O}_2)$) are involved in catalyzing both the anodic and cathodic reactions [114].

More detailed studies [119] also claimed dissolution was accelerated by the formation of soluble peroxycarbonate species ($\text{U}^{\text{VI}}\text{O}_2(\text{O}_2)_x(\text{CO}_3)_y^{2-2x-2y}$). Such species have been shown to accelerate $\text{U}^{\text{IV}}\text{O}_2$ dissolution when $[\text{H}_2\text{O}_2]$ and $[\text{CO}_3]_{\text{total}}$ were higher than those commonly employed in spent fuel studies [120, 121].

1.4.9. Potential Oxidants (Oxygen and Hydrogen Peroxide)

If container failure occurs while γ/β radiation fields are significant, fuel corrosion could be driven by both radical and molecular oxidants [3, 118, 122]. However, while the rate constants for the reaction of radiolytic radicals with the fuel surface have been shown to be large [123], the steady-state radical concentrations are low, and fuel corrosion would be expected to be dominated by reaction with H_2O_2 , which would be present in substantially larger concentrations. If container failure is delayed until γ/β fields are insignificant (after a few hundred years, Figure 1-12) and only α -radiolysis of H_2O is important, H_2O_2 would be the dominant oxidant. However, H_2O_2 decomposition occurs readily on oxides [76, 124-129] to produce the additional oxidant O_2 ,



which reacts over 2 orders of magnitude more slowly with UO_2 than H_2O_2 [76] and fuel corrosion could correspondingly be much slower.

The reduction of O_2 is notoriously slow due to the need to break the strong O-O bond [117, 118]. On UO_2 , the kinetics are accelerated by oxidizing the surface to $\text{U}^{\text{IV}}_{1-2x}\text{U}^{\text{V}}_{2x}\text{O}_{2+x}$, which enables catalysis by mixed oxidation states at donor/acceptor relay (DAR) sites on the oxide surface as illustrated schematically in Figure 1-23 [87].

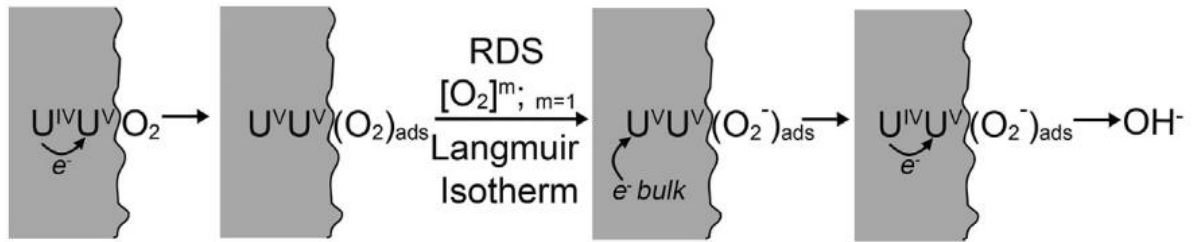


Figure 1-23. Reduction of O_2 at donor-acceptor relay (DAR) sites on a $\text{U}^{\text{IV}}_{1-2x}\text{U}^{\text{V}}_{2x}\text{O}_{2+x}$ surface [3].

The reaction is first order with respect to $[\text{O}_2]$ and appears to initiate by O_2 adsorption under Langmuir isotherm conditions involving the interaction of the π and/or sp^3 orbitals of O_2 with partially filled $\text{U}5f$ orbitals present in $\text{U}^{\text{IV}}_{1-2x}\text{U}^{\text{V}}_{2x}\text{O}_{2+x}$. For highly non-stoichiometric $\text{U}^{\text{IV}}_{1-2x}\text{U}^{\text{V}}_{2x}\text{O}_{2+x}$, O_2 reduction currents are suppressed with a square root dependence on $[\text{O}_2]$ and exhibit large Tafel slopes, suggesting partial chemical control of the first electron transfer step. Although unproven, the tendency of O_1 to form cuboctahedral clusters may deactivate some DAR sites for O_2 reduction by isolating them from the matrix conductive network.

Two possible effects of in-reactor burnup on O_2 reduction can be identified: (i) fission product doping with RE^{III} ions, which will increase the number density of $\text{U}^{\text{IV}}/\text{U}^{\text{V}}$ DAR sites by creating additional U^{V} sites; (ii) the creation of noble metal (ϵ) particles which contain Ru, Rh, and Pd, all of which have been shown to catalyze O_2 reduction [130, 131]. Figure 1-24 shows O_2 reduction currents recorded on SIMFUEL electrodes in air-saturated solutions. RE^{III} -doping alone has only a marginal effect on the kinetics, but an increase in the number density of ϵ -

particles (over the simulated burn-up range 1.5 at% to 6 at%) systematically increases the rate of O₂ reduction. Thus, O₂ reduction in support of UO₂ corrosion would occur preferentially on ε-particles rather than on the UO₂ surface.

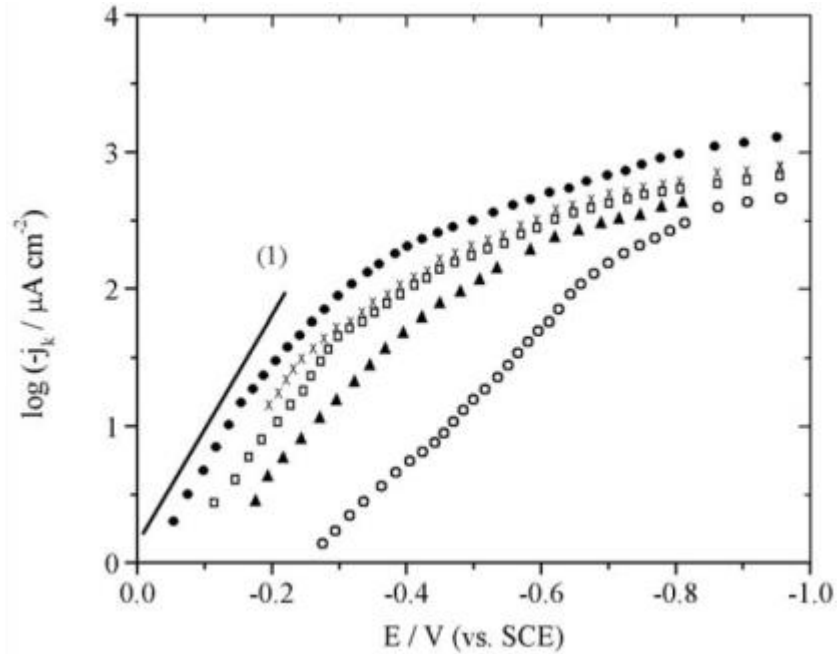


Figure 1-24. O₂ reduction currents recorded on various SIMFUEL electrodes in a 0.1 mol/L NaCl (pH 9.5) solution purged with air ([O₂] = 2.5 x 10⁻⁴ mol/L): (○) Fission product-doped UO₂ containing no ε-particles; (▲) 1.5 at% SIMFUEL; (□) 3 at% SIMFUEL; (●) 6 at% SIMFUEL; (x) 3 at% SIMFUEL Containing ε-particles but No Fission Products. Line (1) is drawn with a slope of 90 mV/decade of current, the slope expected on noble metals [117].

The effect of H₂O₂ on UO₂ corrosion has been extensively studied using both chemical and electrochemical methods [76, 84, 113, 114, 132-140]. The cathodic reduction rate of H₂O₂, being ~200 times greater than that of O₂, can be attributed to the ability of H₂O₂ to create its

own U^{IV}/U^V catalytic DAR surface sites. This reaction is driven by the initial formation of surface $OH\bullet$ radicals [141-143],



rather than relying on the number of pre-existing sites on the fuel surface, as with O_2 . These sites are subsequently reduced by electrons liberated by the anodic reaction under open circuit corrosion conditions,



Under electrochemical conditions, the chemical formation of DAR sites leads to a weak dependence of the cathodic current for reaction 1.13 on applied potential (i.e., large Tafel slopes of 200-400 mV^{-1}) and fractional reaction orders with respect to $[H_2O_2]$ as a consequence of the potential dependent surface coverage by DAR sites [114, 137, 144, 145]. Since the first reaction (reaction 1.12) is a chemical reaction dependent on $[H_2O_2]$ and the second reaction (reaction 1.13) an electrochemical reaction dependent on potential, the reaction rate changes from electrochemical control at high $[H_2O_2]$, when the chemical reaction is rapid, to chemical control when $[H_2O_2]$ is lower and the potential sufficiently negative.

For DGR conditions, when radiolytically produced H_2O_2 concentrations will be many orders of magnitude lower than those used in laboratory experiments, the chemical reaction step would be expected to be rate-controlled. As for O_2 reduction, it is possible that H_2O_2 reduction could be catalyzed on an RE^{III} -doped surface and possibly on ϵ -particles in SIMFUELS.

1.4.10. The Consequences of Hydrogen Peroxide Decomposition

The kinetics of H_2O_2 reactions on UO_2 surfaces are complicated by the ability of H_2O_2 to participate in both the anodic and cathodic reactions. The influence of H_2O_2 on the anodic dissolution of UO_2 will be discussed below. Here, the emphasis is on the decomposition of H_2O_2 on the UO_2 surface. Besides causing corrosion by acting as a cathodic reagent,



H_2O_2 can also undergo oxidation,



leading to its overall decomposition, as illustrated in Figure 1-25.

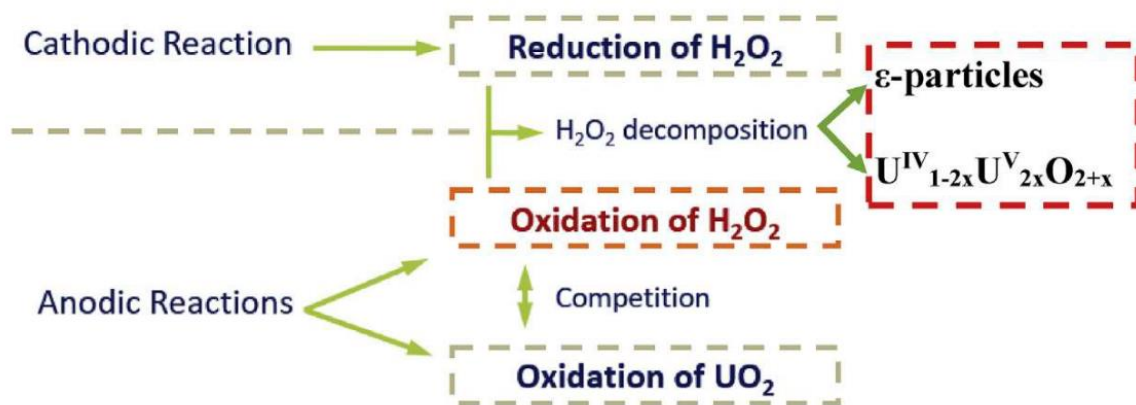


Figure 1-25. Schematic illustration showing that the reduction of H_2O_2 can occur on either the catalytic $\text{U}^{\text{IV}}_{1-2x}\text{U}^{\text{V}}_{2x}\text{O}_{2+x}$ surface or on ϵ -particles and couple to either UO_2 or H_2O_2 oxidation [119].

The decomposition of H_2O_2 has been studied on various metal oxides, with recent studies showing the reaction proceeds via a radical mechanism [125, 126, 128, 141, 146, 147],



with the first electron transfer from adsorbed $\text{OH}\cdot$ being the rate-determining step [123].

The balance between corrosion and decomposition has been studied in some detail and shown to be a complex function of $[\text{H}_2\text{O}_2]$ and $[\text{CO}_3]_{\text{total}}$, the composition of the oxidized surface, and whether or not the oxide is RE^{III} -doped. The role of ϵ -particles in SIMFUELS on H_2O_2 reduction remains ambiguous. In chemical (as opposed to electrochemical) experiments [142], it was observed that consecutive exposures to H_2O_2 led to a decrease in U^{VI} release to solution but no decrease in the amount of H_2O_2 consumed (Figure 1-26). This was taken as evidence of alterations to the chemical state of the surface, which continued to support decomposition but not dissolution. That this was the case was demonstrated in a series of experiments in which both the $[\text{CO}_3]_{\text{total}}$ and $[\text{H}_2\text{O}_2]$ were changed, and the evolution of the surface condition was followed by measuring E_{CORR} , the changes in polarization resistance (R_{p}), and the surface composition using XPS [148], Figure 35 and Figure 36. In both series of experiments, the dominant reaction consuming H_2O_2 was shown to be decomposition, although the balance between corrosion and decomposition was different since one set of experiments was performed on undoped UO_2 and the other on 3 at% SIMFUEL. RE^{III} doping of the matrix (present in SIMFUEL) stabilizes the matrix against corrosion, shifting the balance in favour of decomposition [149].

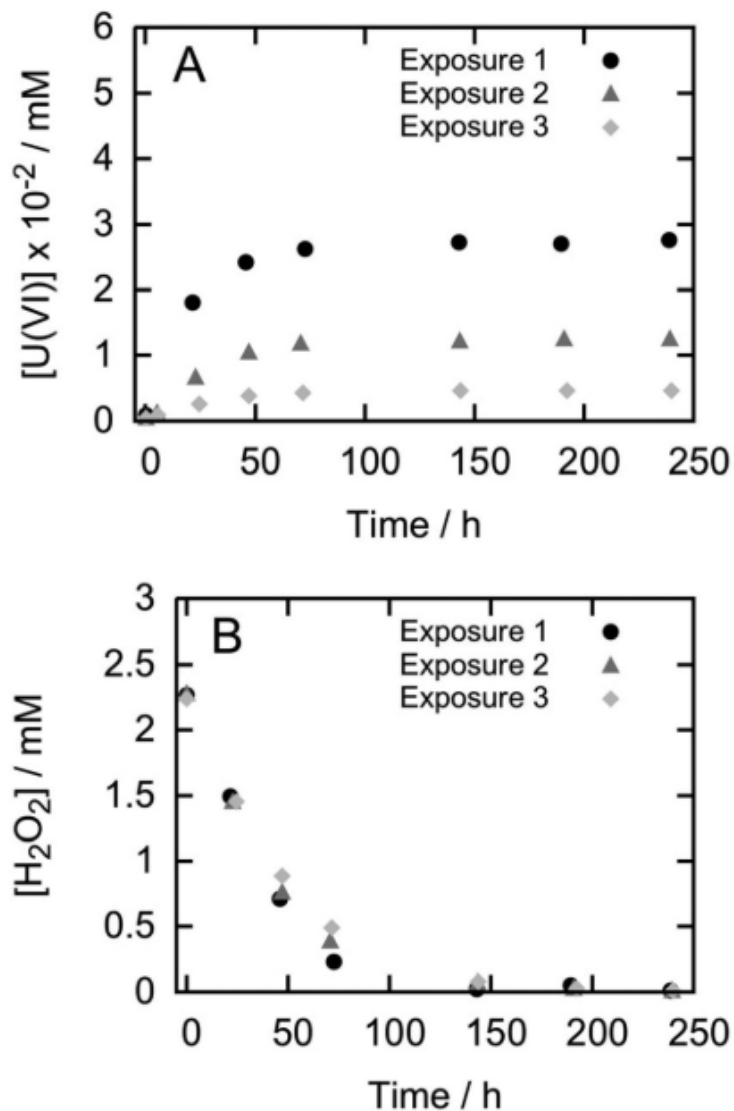


Figure 1-26. Uranium release into solution (A) and H₂O₂ consumption on UO₂ (B) during three consecutive exposures to a deaerated 1 x 10⁻³ mol/L HCO₃⁻ solution [142].

XPS analyses indicate catalysis of the decomposition reaction by a reversible redox transformation occurring on a U^{IV}_{1-2x}U^V_{2x}O_{2+x} surface, Figure 1-27. This catalyzed decomposition process is illustrated schematically by reactions 1.1 and 1.2 in Figure 1-28. Although not shown in the figure, this process proceeds via OH• radical species (reactions 1.16-1.18). For short immersion periods (~5 h), the changes in E_{CORR} and R_P with [H₂O₂]

demonstrate that both the rate of formation of the $U^{IV}_{1-2x}U^{V}_{2x}O_{2+x}$ layer and the rate of decomposition on it increased as $[H_2O_2]$ increased.

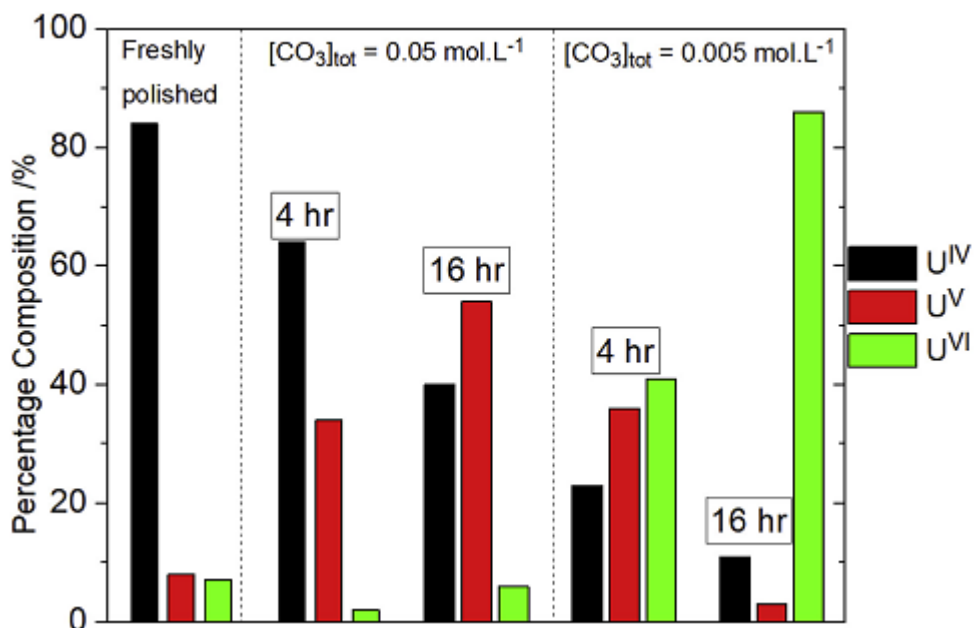


Figure 1-27. Percentage of U oxidation states in a 3 at% SIMFUEL surface after exposure to a 10^{-2} mol/L H_2O_2 solution. Values obtained by deconvolution of the U $4f_{7/2}$ peaks in XPS spectra [148].

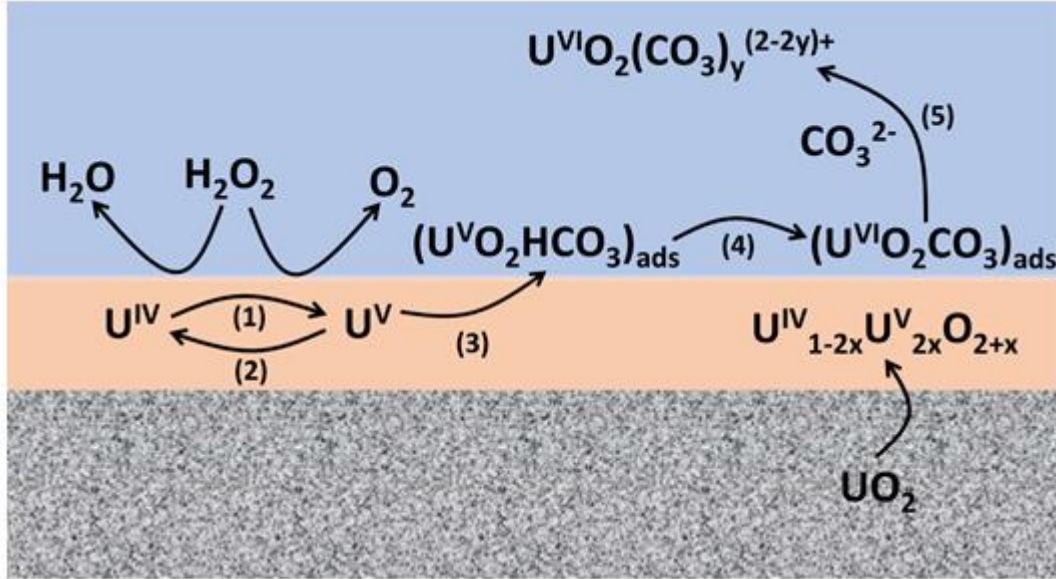


Figure 1-28. Illustration of the H_2O_2 decomposition (reactions 1.1 and 1.2) and UO_2 corrosion reaction (reactions 1.3, 1.4, 1.5) occurring on a $\text{U}^{\text{IV}}_{1-2x}\text{U}^{\text{V}}_{2x}\text{O}_{2+x}$ surface layer on UO_2 [148].

The E_{CORR} values recorded in the presence of H_2O_2 [132, 148, 150, 151] are well above the established value at which the onset of tetragonal distortions in the cubic UO_2 lattice can initiate dissolution. Despite these high values, the surface remains catalytic for H_2O_2 decomposition since the catalytic interconversion of U^{IV} and U^{V} is reversible, preventing the irreversible transition involving the breakdown of the cubic structure, which would lead to dissolution. A positive shift in E_{CORR} , which could disturb reversibility, requires $[\text{H}_2\text{O}_2]$ approaching 10^{-2} mol/L [119, 132, 148], a concentration many orders of magnitude beyond that achievable under DGR conditions. This suggests radiolytically produced H_2O_2 should predominantly undergo decomposition. Additionally, the surface of the fuel is likely to remain catalytic to support radical reactions capable of scavenging radiolytic oxidants such as those induced in the presence of H_2 .

1.5. The Influence of Redox Scavengers on Fuel Corrosion

The two corrosion fronts existing within a failed container, illustrated in Figure 1-29, are interconnected by groundwater diffusion processes. Since the separation in corrosion potentials (E_{CORR}) between the two surfaces is large (Figure 1-13), this introduces the possibility that the products of steel corrosion (Fe^{2+} and H_2) will scavenge the radiolytic oxidants (predominantly H_2O_2) responsible for UO_2 corrosion.

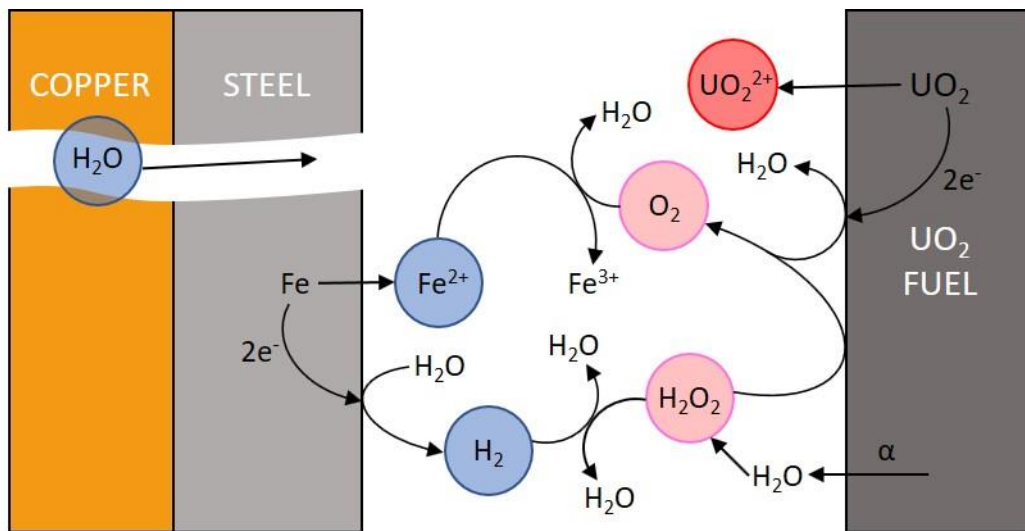


Figure 1-29. Illustration showing the two corrosion fronts within a groundwater-containing failed container [70].

1.5.1. Ferrous Ions

Ferrous ions (Fe^{2+}) are well-known regulators of redox conditions in natural waters, and their reaction with oxidants, in particular O_2 , has been extensively studied [152]. The overall reaction can be written,



where the exact speciation of Fe^{II} and Fe^{III} is determined by groundwater composition, redox conditions, and pH. The redox chemistry of the steel/iron oxide/soluble Fe system and its likely impact on fuel corrosion have been reviewed in detail [153].

The radiolytically produced H₂O₂ will also be consumed by the Fenton reaction [154],



Separating the effects of the two possible redox scavengers (Fe²⁺, H₂) on fuel corrosion is difficult in experiments conducted in the presence of Fe. That H₂ is the dominant steel corrosion product suppressing the corrosion of UO₂ was demonstrated by Puranen, et al. [155].

Direct attempts have been made to determine the influence of Fe²⁺ on UO₂ corrosion [156-158]. Calculations based on the Fenton reaction and experimentally determined rate constants showed the suppression of UO₂ dissolution by a factor of 40 [159]. More recent model calculations show that, as the [Fe²⁺] increases towards its solubility limit for groundwaters in the expected repository pH range, the radiolytically-produced H₂O₂ is scavenged by the Fenton reaction at locations progressively closer to the fuel surface [160]. At the fuel surface itself, where the influence of Fe²⁺ is determined by the relative rates of the Fenton reaction and the interfacial corrosion rate, the influence is relatively minor. When the accumulation of corrosion product deposits is included in model calculations, and access of Fe²⁺ to the UO₂ surface is controlled by limited porosity in the deposit, the influence of Fe²⁺ becomes marginal [161].

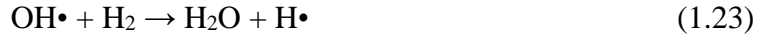
1.5.2. Hydrogen (H₂)

Within a failed container there are two sources of H₂: (i) radiolytic production and (ii) formation by the anoxic corrosion of the inner used fuel container vessel with groundwater. The second will be the major source,



The hydrostatic pressure at a DGR depth of 500 m (~ 5 MPa, or 50 bar) would lead to a dissolved [H₂] of ~ 40 mmol/L. Water radiolysis can produce additional H₂ inside a failed

container. It is clear from previous studies [16, 76, 89, 155, 162-165] that dissolved H₂ can reduce the concentrations of radiolytic oxidants to levels below their analytical detection limit. To act as a reductant, H₂ must be activated by dissociation into reactive H•, which can be achieved by radiolytically formed OH• radicals,



The ability of H₂ to suppress fuel corrosion at [H₂] in the range of 10⁻⁴ and 10⁻⁵ mol/L has been shown by scavenging molecular radiolytic oxidants to below detection limits and consuming small amounts of added H₂O₂ [166]. Given the ability of H₂ to scavenge OH• radicals in bulk solution, the scavenging of surface OH• created by the dominant radiolytic oxidant, H₂O₂, would be the expected first reaction step preventing the onset of UO₂ oxidation, leading eventually to the release of U^{VI}O₂²⁺ to solution or the decomposition of H₂O₂ to O₂ and H₂O (reactions 1.16-1.18). Since U release is completely suppressed and no O₂ is detected in reactions in the presence of γ- or α-radiation, reaction 1.24 would be the dominant reaction pathway.



A second pathway exists for the activation of H₂ on spent nuclear fuel surfaces. Noble metals (ε-particles) are well-known catalysts for oxidation/reduction reactions, especially the H₂/H•/H⁺ reaction, with 3 of the 5 dominant components of ε-particles (Pd, Rh, Ru) possessing high exchange currents in the range of 10⁻⁴ to 10⁻³ A.cm⁻² [167]. Thus, it would be expected that ε-particles, despite their low surface coverage, could act as galvanically coupled anodes (for H₂ oxidation) and cathodes (for H₂O₂/O_s reduction). H₂ activation on ε-particles will produce H• which would be expected to drive the recombination of H₂O₂ and H₂ on ε-particle surfaces by reaction with surface OH• species, reaction 1.24.

The influence of these particles on fuel behaviour in the presence of H₂ has been studied on SIMFUELS [140, 168-172], on UO₂ in the presence of noble metals [173, 174] and on particles extracted from actual spent fuel specimens [175]. On SIMFUEL, the H₂/H•/H⁺ reaction would be reversible, and the UO₂ matrix should be inert, as appears to be the case for spent fuels and

α -doped UO_2 [19, 76, 162, 166]. However, H_2 cannot be activated, or activated only to a minor degree, on SIMFUEL not containing ϵ -particles [176].

Two pathways for protection against oxidation are possible, as illustrated in Figure 1-30: either the recombination reaction on the ϵ -particles (Figure 1-30(a)) or H_2O_2 reduction on UO_2 driven by galvanic coupling to H_2 oxidation on ϵ -particles (Figure 1-30(b)). Since the reaction of H_2O_2 with UO_2 is rapid, the second pathway appears more likely given the much larger available UO_2 surface area. Similar experiments in which H_2O_2 was added to an Ar/H_2 purged solution containing a SIMFUEL with no ϵ -particles [172] generated E_{CORR} transients indicating the same oxidation (by H_2O_2)/reduction (by H_2) coupled reaction. Again, XPS analyses confirmed the reduced state of the surface when the transient was complete. These observations suggest that, while the recombination process may be accelerated by $\text{H}\cdot$ formation on ϵ -particles, it can also occur on the UO_2 surface via the H_2 scavenging of surface $\text{OH}\cdot$ radicals, which would otherwise lead to UO_2 oxidation.

It has been well established that the reactions of H_2O_2 with UO_2 and with H_2 on UO_2 (and on other metal oxides) proceed via surface radical states ($\text{OH}\cdot$). This was recently confirmed on SIMFUEL in D isotope studies by Bauhn, et al. [177] in $\text{NaCl}/\text{HCO}_3^-$ solutions, in which the reaction of surface adsorbed $\text{OH}\cdot$ on SIMFUEL surfaces with dissolved D_2 was demonstrated by the detection of HDO.

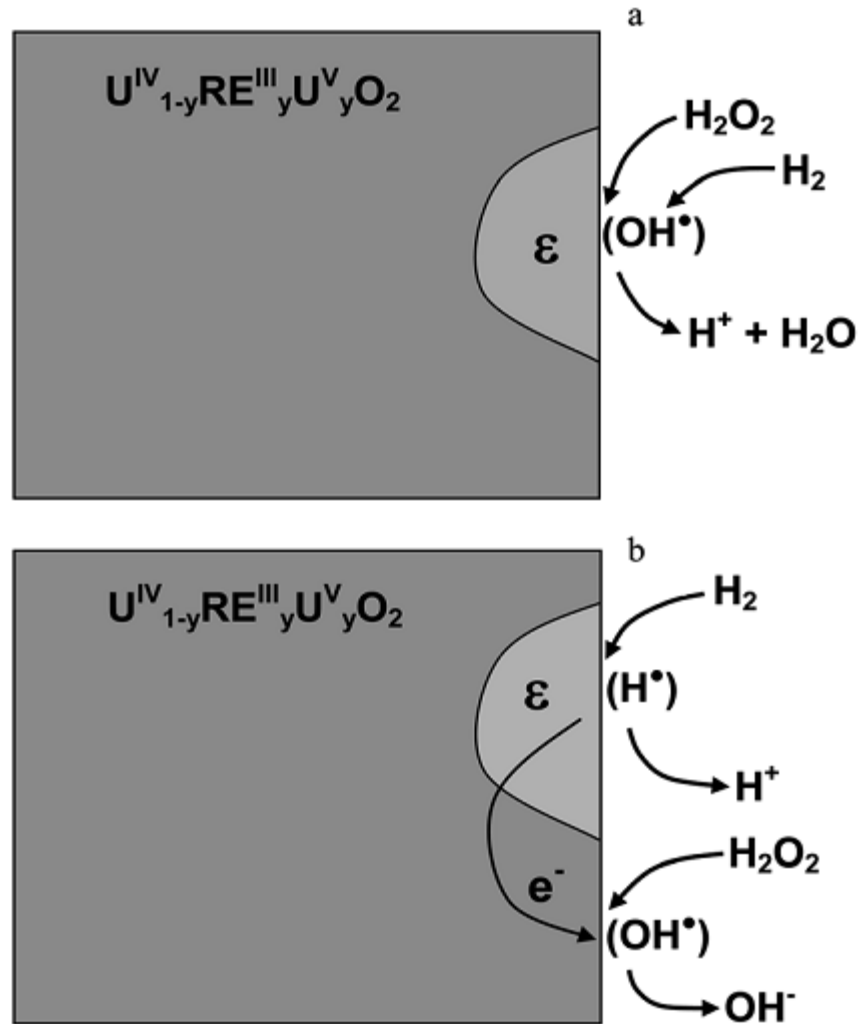


Figure 1-30. Schematic illustrating the possible reaction pathways for the scavenging of H_2O_2 by reaction with H_2 on a 1.5 at% SIMFUEL surface by (a) reaction on ϵ -particles; (b) by H_2 oxidation on ϵ -particles galvanically coupled to the reduction of H_2O_2 on the oxide surface [140].

1.6. Chemical Dissolution Under Anoxic Conditions

When oxidants are scavenged and E_{CORR} is lowered to a value $< (E^\circ)_{\text{UO}_2/\text{U}_4\text{O}_9}$, the fuel will become immune to corrosion and any further degradation leading to radionuclide release can

only proceed by chemical dissolution as U^{IV} . Under these conditions, the UO_2 matrix would be expected to achieve solubility equilibrium, and any further dissolution would require disturbance of this equilibrium and a transition to chemically controlled dissolution. This disturbance could occur by one of two processes: (i) the transport of U^{IV} away from the fuel surface and its adsorption on available surfaces in the vicinity of the fuel (e.g., container corrosion products) and (ii) conversion of UO_2 to the more stable U^{IV} phase, coffinite ($USiO_4$).

A number of measurements of fuel dissolution rates (as opposed to corrosion rates) have been made [19, 178-181] with values ranging from $(6 \pm 2.5) \times 10^{-5}$ mol/m²·a in dynamic flow through experiments [178] to $(4 \text{ to } 35) \times 10^{-8}$ mol/m²·a in static experiments [180]. Generally, experiments conducted under dynamic conditions yielded higher values than those performed under static conditions, which would be consistent with the avoidance of solubility equilibrium under dynamic conditions.

1.7. Thesis Goals and Outline

The goals of this thesis are as follows:

- To characterize natural UO_2 samples manufactured between 1965 and 2017 using a combination of electrochemical and surface analytical techniques.
- To determine the influence of conductivity of UO_2 samples on the kinetics of reactions involving H_2O_2 .
- To investigate the ability of the UO_2 surface in the activation of H_2 to form $(H\bullet)_{ads}$ and its subsequent suppression of reactions involving H_2O_2 .
- To identify whether H_2 can reduce an oxidized $U^{IV}_{1-2x}U^{V}_{2x}O_{2-x}$ surface in the absence of ϵ -particles when H_2O_2 is present.

1.8. References

- [1] Natural Resources Canada, Energy Fact Book 2022-2023, **2023**.
- [2] S. Schlömer, T. Bruckner, L. Fulton, E. Hertwich, A. McKinnon, D. Perczyk, J. Roy, R. Schaeffer, R. Sims, P. Smith, R. Wisser, *2014: Annex III: Technology-specific cost and performance parameters*, in: *Climate Change 2014: Mitigation of Climate Change* [O. Edenhofer, R. Pichs-Madruga, Y. Sokona, E. Farahani, S. Kadner, K. Seyboth, A. Adler, I. Baum, S. Brunner, P. Eickemeier, B. Kriemann, J. Savolainen, S. Schlömer, C. von Stechow, T. Zwickel, J.C. Minx (eds.)], Cambridge University Press, United Kingdom and New York, NY, USA, **2014**, pp. 1329-1356.
- [3] D.W. Shoesmith, *Fuel corrosion processes under waste disposal conditions*, J Nucl Mater. (**2000**). 282 (1), 1-31.
- [4] T. Reilly, Nuclear Fuel Waste Projections in Canada - 2023 Update, Nuclear Waste Management Organization, NWMO-TR-2023-09 R001, Toronto, Canada (**2023**).
- [5] H. He, M. Broczkowski, K. O'Neil, D. Ofori, O. Semenikhin, D. Shoesmith, Corrosion of nuclear fuel (UO₂) inside a failed nuclear waste container, Nuclear Waste Management Organization, NWMO TR-2012-09, Toronto, ON, Canada (**2012**).
- [6] J. Chen, Z. Qin, D. Shoesmith, *Long-term corrosion of copper in a dilute anaerobic sulfide solution*, Electrochim Acta. (**2011**). 56 (23), 7854-7861.
- [7] J. Noronha, Deep geological repository conceptual designs report: crystalline/sedimentary rock environment, Nuclear Waste Management Organization, APM-REP-00440-0015 R001, Toronto, Canada (**2016**).
- [8] Nuclear Waste Management Organization, Ensuring Safety: Multiple-Barrier System, **2021**.
- [9] D.S. Hall, M. Behazin, W.J. Binns, P.G. Keech, *An evaluation of corrosion processes affecting copper-coated nuclear waste containers in a deep geological repository*, Prog Mater Sci. (**2021**). 118, 100766.
- [10] L. Werme, C. Lilja, Fuel and canister process report for the safety assessment SR-Site, Swedish Nuclear Fuel and Waste Management Co., SKB TR-10-46, (**2010**).
- [11] L.H. Johnson, D.W. Shoesmith, *Spent Fuel*, in: *Radioactive Waste Forms for the Future* [W.B. Lutze, R.C. Ewing (eds.)], Elsevier, Amsterdam, Netherlands, **1988**, pp. 635-698.

- [12] L.H. Johnson, D.M. LeNeveu, D.W. Shoesmith, D.W. Oscarson, M.N. Gray, R.J. Lemire, N.C. Garisto, The disposal of Canada's nuclear fuel waste: the vault model for postclosure assessment, Atomic Energy of Canada Ltd, AECL-10714, Canada (1994).
- [13] L.H. Johnson, D.M. LeNeveu, F. King, D.W. Shoesmith, M. Kolar, D.W. Oscarson, S. Sunder, C. Onofrei, J.L. Crosthwaite, The disposal of Canada's nuclear fuel waste: a study of postclosure safety of in-room emplacement of used CANDU fuel in copper containers in permeable plutonic rock Volume 2: vault model, Atomic Energy of Canada Limited, AECL-11494-2, COG-95-552-2, Pinawa, Canada (1996).
- [14] D. Shoesmith, J. Noel, Z. Qin, C. Lee, J. Goldik, B. Santos, M. Broczkowski, Corrosion of nuclear fuel (UO₂) inside a failed nuclear waste container, Ontario Power Generation, 06819-REP-01200-10145-R00, (2005).
- [15] D.W. Shoesmith, J.C. Tait, S. Sunder, W.J. Gray, S.A. Steward, R.E. Russo, J.D. Rudnicki, Factors affecting the differences in reactivity and dissolution rates between UO₂ and spent nuclear fuel, Atomic Energy of Canada Ltd, AECL-11515, Canada (1995).
- [16] B. Grambow, A. Loida, P. Dressler, H. Geckeis, J. Gago, I. Casas, J.d. Pablo, J. Gimenez, M.E. Torrero, Long-term safety of radioactive waste disposal: Chemical reaction of fabricated and high burnup spent UO₂ fuel with saline brines Final report, Forschungszentrum Karlsruhe, FZKA-5702, Germany (1996).
- [17] B. Grambow, K. Lemmens, Y. Minet, C. Poinssot, K. Spahiu, D. Bosbach, C. Cachoir, I. Casas, F. Clarens, B. Christiansen, J. de Pablo, C. Ferry, J. Giménez, S. Gin, J.P. Glatz, J.A. Gago, E. Gonzalez-Robles, N.C. Hyatt, E. Iglesias, B. Kienzler, B. Luckscheiter, A. Martinez-Esparza, V. Metz, A. Ödegaard-Jensen, K. Ollila, J. Quiñones, A. Rey, S. Ribet, V.V. Rondinella, G. Skarnemark, D. Wegen, D. Serrano-Purroy, T. Wiss, NF-PRO RTD Component 1: Dissolution and release from the waste matrix, EUR 23730, Brussels (2008).
- [18] B. Grambow, J. Bruno, L. Duro, J. Merino, A. Tamayo, C. Martin, G. Pepin, S. Schumacker, O. Smidt, C. Ferry, C. Jegou, J. Quiñones, E. Iglesias, N. Rodriguez Villagra, J.M. Nieto, A. Martínez-Esparza, A. Loida, V. Metz, B. Kienzler, G. Bracke, D. Pellegrini, G. Mathieu, V. Wasselin-Trupin, C. Serres, D. Wegen, M. Jonsson, L. Johnson, K. Lemmens, J. Liu, K. Spahiu, E. Ekeröth, I. Casas, J. de Pablo, C. Watson, P. Robinson, D. Hodgkinson, Model uncertainty for the mechanism of dissolution of spent fuel in a nuclear waste repository, EUR 24597 EN, Brussels (2010).
- [19] C. Poinssot, C. Ferry, M. Kelm, B. Grambow, A. Martinez-Esparza, L. Johnson, Z. Andriambololona, J. Bruno, C. Cachoir, J.M. Cavendon, Final report of the European project spent fuel stability under repository conditions, Atomic Energy Commission (CEA), CEA-R-6093, Gif-sur-Yvette, France (2005).

- [20] V.M. Oversby, Rates and mechanisms of radioactive release and retention inside a waste disposal canister - in Can Processes, Swedish Nuclear Fuel and Waste Management Co., NEI-SE-562, Stockholm, Sweden (**2003**).
- [21] B. Kienzler, V. Metz, A. Valls, FIRST-Nuclides: Fast/Instant release of safety relevant radionuclides from spent nuclear fuel, EURATOM FP7 Collaborative Project, FP7-295722; Deliverable 5.13, Luxembourg, Germany (**2015**).
- [22] J. Cunnane, CSNF Waste Form Degradation: Summary Abstraction, prepared by Bechtel SAIC Company, LLC for the U.S. Department of Energy, ANL-EBS-MD-000015 Rev 02, Las Vegas, NV (**2004**).
- [23] K. Lemmens, C. Cachoir, T. Mennecart, Dissolution behaviour of spent nuclear fuel at highly alkaline conditions, SCK CEN, 27622175, ER-0505, Belgium (**2019**).
- [24] D.W. Shoesmith, S. Sunder, W.H. Hocking, *Electrochemistry of UO₂ nuclear fuel*, in: *Electrochemistry of Novel Materials* [J. Lipkowski, P.N. Ross (eds.)], VCH Publishers, New York, NY, **1994**, pp. 297-337.
- [25] L.O. Werme, K. Spahiu, L.H. Johnson, V.M. Oversby, F. King, B. Grambow, D.W. Shoesmith, Spent fuel performance under repository conditions: A model for use in SR-Can, 1404-0344, Sweden (**2004**).
- [26] G.A. Parks, D.C. Pohl, *Hydrothermal solubility of uraninite*, *Geochim Cosmochim Acta.* (**1988**). 52 (4), 863-875.
- [27] I. Grenthe, J. Fuger, R.J. Konings, R.J. Lemire, A.B. Muller, C. Nguyen-Trung, H. Wanner, *Chemical thermodynamics of uranium*, Elsevier, Amsterdam, **1992**.
- [28] J. Fuger, *Problems in the Thermodynamics of the Actinides in Relation with the Back-end of the Nuclear Fuel Cycle*, *J Nucl Mater.* (**1993**). 201, 3-14.
- [29] V. Neck, J. Kim, *Solubility and hydrolysis of tetravalent actinides*, *Radiochim Acta.* (**2001**). 89 (1), 1-16.
- [30] D. Rai, M. Yui, D.A. Moore, *Solubility and Solubility Product at 22°C of UO₂(c) Precipitated from Aqueous U(IV) Solutions*, *J Solution Chem.* (**2003**). 32 (1), 1-17.
- [31] I. Casas, J. de Pablo, J. Giménez, M.E. Torrero, J. Bruno, E. Cera, R.J. Finch, R.C. Ewing, *The role of pe, pH, and carbonate on the solubility of UO₂ and uraninite under nominally reducing conditions*, *Geochim Cosmochim Acta.* (**1998**). 62 (13), 2223-2231.
- [32] T. Yajima, Y. Kawamura, S. Ueta, *Uranium(IV) Solubility and Hydrolysis Constants Under Reduced Conditions*, *MRS Online Proc Lib.* (**1994**). 353, 1137.

- [33] D. Rai, A.R. Felmy, J.L. Ryan, *Uranium(IV) hydrolysis constants and solubility product of $UO_2 \cdot xH_2O(am)$* , Inorg Chem. (1990). 29 (2), 260-264.
- [34] I. Grenthe, X. Gaona, L. Rao, A. Plyasunov, W. Runde, B. Grambow, R. Konings, A. Smith, E. Moore, M.-E. Ragoussi, J.S. Martinez, D. Costa, A. Felmy, K. Spahiu, *Second update on the chemical thermodynamics of uranium, neptunium, plutonium, americium and technetium*, Nuclear Energy Agency of the OECD (NEA), Boulogne-Billancourt, France, 2020.
- [35] R.J. Lemire, F. Garisto, The solubility of U, Np, Pu, Th and Tc in a geological disposal vault for used nuclear fuel, Atomic Energy of Canada Ltd., AECL-10009, Pinawa, Canada (1989).
- [36] R.J. Lemire, P.R. Tremaine, *Uranium and plutonium equilibriums in aqueous solutions to 200°C*, J Chem Eng Data. (1980). 25 (4), 361-370.
- [37] J. Paquette, R.J. Lemire, *A Description of the Chemistry of Aqueous Solutions of Uranium and Plutonium to 200°C Using Potential-pH Diagrams*, Nucl Sci Eng. (1981). 79 (1), 26-48.
- [38] E.L. Mühr-Ebert, F. Wagner, C. Walther, *Speciation of uranium: Compilation of a thermodynamic database and its experimental evaluation using different analytical techniques*, Appl Geochem. (2019). 100, 213-222.
- [39] T. Lampman, Update to fuel burnups and power ratings, Nuclear Waste Management Organization, NWMO-TR-2019-04, Toronto, Canada (2021).
- [40] I. Hastings, Structures in irradiated UO_2 fuel from Canadian reactors, Atomic Energy of Canada Limited, AECL-MISC-249, Chalk River, Canada (1982).
- [41] I.J. Hastings, M.J.F. Notley, D.H. Rose, *Irradiation-induced volume changes in commercial UO_2 fuel: Comparison with model prediction*, J Nucl Mater. (1978). 75 (2), 301-303.
- [42] H. Matzke, *Radiation damage in crystalline insulators, oxides and ceramic nuclear fuels*, Radiat Eff Defects Solids. (1982). 64 (1-4), 3-33.
- [43] M. Badley, D.W. Shoesmith, The corrosion/dissolution of used nuclear fuel in a deep geologic repository, Nuclear Waste Management Organization, NWMO-TR-2022-09, Toronto, Canada (2022).
- [44] D.W. Shoesmith, *Chemistry/Electrochemistry of spent nuclear fuel as a wasteform*, in: *Uranium: Cradle to Grave* [P.C. Burns, G.E. Sigmon (eds.)], Mineralogical Association of Canada, Canada, 2013, pp. 1-32.
- [45] K. Heckman, J. Edward, Radionuclide inventory for reference CANDU fuel bundles, Nuclear Waste Management Organization, NWMO-TR-2020-05, Toronto, Canada (2020).

- [46] H. Kleykamp, *The chemical state of the fission products in oxide fuels*, J Nucl Mater. (1985). 131 (2), 221-246.
- [47] M. Gobien, K. Liberda, C. Medri, Fuel Radiotoxicity and Screening Analysis, Nuclear Waste Management Organization, NWMO-TR-2021-16 R002, Toronto, Canada (2022).
- [48] H. Kleykamp, *The solubility of selected fission products in UO_2 and $(U, Pu)O_2$* , J Nucl Mater. (1993). 206 (1), 82-86.
- [49] H. Kleykamp, *The Chemical State of Fission Products in Oxide Fuels at Different Stages of the Nuclear Fuel Cycle*, Nucl Technol. (1988). 80 (3), 412-422.
- [50] B.D. Hanson, The burnup dependence of light water reactor spent fuel oxidation, Pacific Northwest National Laboratory, PNNL-11929, Richland, WA, USA (1998).
- [51] T.B. Lindemer, T.M. Besmann, *Chemical thermodynamic representation of UO_{2+x}* , J Nucl Mater. (1985). 130, 473-488.
- [52] E.H.P. Cordfunke, R.J.M. Konings, *Chemical interactions in water-cooled nuclear fuel: A thermochemical approach*, J Nucl Mater. (1988). 152 (2), 301-309.
- [53] H. Kleykamp, *Post-irradiation examinations and composition of the residues from nitric acid dissolution experiments of high-burnup LWR fuel*, J Nucl Mater. (1990). 171 (2), 181-188.
- [54] M. Floyd, J. Novak, P. Truant, Fission-gas release in fuel performing to extended burnups in Ontario Hydro nuclear generating stations, Atomic Energy of Canada Ltd., AECL-10636, Chalk River, Canada (1992).
- [55] H. Smith, J. Tait, R. Von Massow, Radioactive decay properties of Bruce "A" CANDU™ UO_2 fuel and fuel recycle waste, Atomic Energy of Canada Ltd., AECL-9072, Pinawa, Manitoba (1987).
- [56] J. McMurry, B. Ikeda, S. Stroes-Gascoyne, D. Dixon, Evolution of a Canadian deep geologic repository, Atomic Energy of Canada Ltd, 06819-REP-01200-10127-R00, Toronto, Canada (2004).
- [57] M.B. Chadwick, M. Herman, P. Obložinský, M.E. Dunn, Y. Danon, A.C. Kahler, D.L. Smith, B. Pritychenko, G. Arbanas, R. Arcilla, R. Brewer, D.A. Brown, R. Capote, A.D. Carlson, Y.S. Cho, H. Derrien, K. Guber, G.M. Hale, S. Hoblit, S. Holloway, T.D. Johnson, T. Kawano, B.C. Kiedrowski, H. Kim, S. Kunieda, N.M. Larson, L. Leal, J.P. Lestone, R.C. Little, E.A. McCutchan, R.E. MacFarlane, M. MacInnes, C.M. Mattoon, R.D. McKnight, S.F. Mughabghab, G.P.A. Nobre, G. Palmiotti, A. Palumbo, M.T. Pigni, V.G. Pronyaev, R.O. Sayer, A.A. Sonzogni, N.C. Summers, P. Talou, I.J. Thompson, A. Trkov, R.L. Vogt, S.C. van der Marck, A. Wallner, M.C. White, D. Wiarda, P.G. Young, *ENDF/B-VII.1 Nuclear Data for Science and Technology: Cross*

Sections, Covariances, Fission Product Yields and Decay Data, Nucl Data Sheets. **(2011)**. 112 (12), 2887-2996.

[58] W.J. Gray, D.M. Strachan, C.N. Wilson, *Gap and Grain-Boundary Inventories of Cs, Tc, and Sr in Spent LWR Fuel*, MRS Online Proc Lib. **(1991)**. 257 (1), 353-360.

[59] D. Roudil, C. Jégou, V. Broudic, B. Muzeau, S. Peugeot, X. Deschanel, *Gap and grain boundaries inventories from pressurized water reactor spent fuels*, J Nucl Mater. **(2007)**. 362 (2), 411-415.

[60] D. Roudil, C. Jegou, V. Broudic, M. Tribet, *Rim Instant Release Radionuclide Inventory From French High Burnup Spent UOX Fuel*, MRS Online Proc Lib. **(2009)**. 1193, 627.

[61] L. Johnson, D. McGinnes, Partitioning of radionuclides in Swiss power reactor fuels, National Cooperative for the Disposal of Radioactive Waste (Nagra), NAGRA NTB 02-07, Wettingen, Switzerland **(2002)**.

[62] S. Stroes-Gascoyne, *Measurements of instant-release source terms for ^{137}Cs , ^{90}Sr , ^{99}Tc , ^{129}I and ^{14}C in used CANDU fuels*, J Nucl Mater. **(1996)**. 238 (2), 264-277.

[63] S. Stroes-Gascoyne, L.H. Johnson, D.M. Sellinger, *The Relationship Between Gap Inventories of Stable Xenon, ^{137}Cs , and ^{129}I in Used CANDU Fuel*, Nucl Technol. **(1987)**. 77 (3), 320-330.

[64] S. Stroes-Gascoyne, J.C. Tait, N.C. Garisto, R.J. Porth, J.P.M. Ross, G.A. Glowa, T.R. Barnsdale, *Instant Release of ^{14}C , ^{99}Tc , ^{90}Sr and ^{137}Cs from Used Candu Fuel at 25°C in Distilled Deionized Water*, MRS Online Proc Lib. **(1991)**. 257 (1), 373-380.

[65] S. Stroes-Gascoyne, L. Johnson, D. Sellinger, D. Wilkin, Release of fission products and actinides from used CANDU fuel fragments under reducing conditions at 100°C, Atomic Energy of Canada Ltd., AECL-10574, COG-92-31, Pinawa, Canada **(1992)**.

[66] S. Stroes-Gascoyne, D. Moir, M. Kolar, R. Porth, J. McConnell, A. Kerr, *Measurement of Gap and Grain-Boundary Inventories of ^{129}I Used in Candu Fuels*, MRS Online Proc Lib. **(1994)**. 353, 625.

[67] M. Gobien, F. Garisto, E. Kremer, C. Medri, Sixth case study: Reference data and codes, Nuclear Waste Mangement Organization, NWMO-TR-2018-10, Toronto, Canada **(2016)**.

[68] L. Johnson, C. Ferry, C. Poinssot, P. Lovera, *Spent fuel radionuclide source-term model for assessing spent fuel performance in geological disposal. Part I: Assessment of the instant release fraction*, J Nucl Mater. **(2005)**. 346 (1), 56-65.

- [69] F. King, D.S. Hall, P.G. Keech, *Nature of the near-field environment in a deep geological repository and the implications for the corrosion behaviour of the container*, Corros Eng Sci Technol. (2017). 52 (sup1), 25-30.
- [70] D.W. Shoesmith, *Used Fuel and Uranium Dioxide Dissolution Studies – A Review*, The University of Western Ontario, NWMO-TR-2007-03, (2007).
- [71] D.W. Shoesmith, M. Kolar, F. King, *A Mixed-Potential Model to Predict Fuel (Uranium Dioxide) Corrosion within a Failed Nuclear Waste Container*, Corros Sci. (2003). 59 (9), 802-816.
- [72] S. Sunder, D.W. Shoesmith, N.H. Miller, *Oxidation and dissolution of nuclear fuel (UO₂) by the products of the alpha radiolysis of water*, J Nucl Mater. (1997). 244 (1), 66-74.
- [73] D. Shoesmith, F. King, *A mixed-potential model for the prediction of the effects of alpha-radiolysis, precipitation and redox processes on the dissolution of used nuclear fuel*, Ontario Hydro, No: 06819-REP-01200-0038-R00, Pinawa, Canada (1998).
- [74] NWMO, *Adaptive Phased Management: Used fuel repository conceptual design and postclosure safety assessment in crystalline rock*, Nuclear Waste Management Organization, NWMO TR-2012-16, Toronto, Ontario (2012).
- [75] E. Ekeröth, O. Roth, M. Jonsson, *The relative impact of radiolysis products in radiation induced oxidative dissolution of UO₂*, J Nucl Mater. (2006). 355 (1), 38-46.
- [76] J.C. Wren, D.W. Shoesmith, S. Sunder, *Corrosion behavior of uranium dioxide in alpha radiolytically decomposed water*, J Electrochem Soc. (2005). 152 (11), B470.
- [77] C.T. Lee, M.S. Odziemkowski, D.W. Shoesmith, *An In Situ Raman-Electrochemical Investigation of Carbon Steel Corrosion in Na₂CO₃/NaHCO₃, Na₂SO₄, and NaCl Solutions*, J Electrochem Soc. (2006). 153 (2), B33.
- [78] C.T. Lee, Z. Qin, M. Odziemkowski, D.W. Shoesmith, *The influence of groundwater anions on the impedance behaviour of carbon steel corroding under anoxic conditions*, Electrochim Acta. (2006). 51 (8), 1558-1568.
- [79] M.D.M. Badley, D.W. Shoesmith, J.J. Noël, *Effect of Hydrogen on the Dissolution of Uranium Dioxide in Peroxide-Containing Environments*, J Electrochem Soc. (2023). 170 (9), 096506.
- [80] B.G. Santos, H.W. Nesbitt, J.J. Noel, D.W. Shoesmith, *X-ray photoelectron spectroscopy study of anodically oxidized SIMFUEL surfaces*, Electrochim Acta. (2004). 49 (11), 1863-1873.
- [81] E.S. Ilton, A. Haiduc, C.L. Cahill, A.R. Felmy, *Mica Surfaces Stabilize Pentavalent Uranium*, Inorg Chem. (2005). 44 (9), 2986-2988.

- [82] E.S. Ilton, J.-F. Boily, P.S. Bagus, *Beam induced reduction of U(VI) during X-ray photoelectron spectroscopy: The utility of the U4f satellite structure for identifying uranium oxidation states in mixed valence uranium oxides*, Surf Sci. (2007). 601 (4), 908-916.
- [83] M. Schindler, F.C. Hawthorne, M.S. Freund, P.C. Burns, *XPS spectra of uranyl minerals and synthetic uranyl compounds. I: The U 4f spectrum*, Geochim Cosmochim Acta. (2009). 73 (9), 2471-2487.
- [84] M. Razdan, D.S. Hall, P.G. Keech, D.W. Shoesmith, *Electrochemical reduction of hydrogen peroxide on SIMFUEL (UO₂) in acidic pH conditions*, Electrochim Acta. (2012). 83, 410-419.
- [85] M.E. Broczkowski, J.J. Noël, D.W. Shoesmith, *The influence of dissolved hydrogen on the surface composition of doped uranium dioxide under aqueous corrosion conditions*, J Electroanal Chem. (2007). 602 (1), 8-16.
- [86] M. Razdan, D.W. Shoesmith, *The electrochemical reactivity of 6.0 wt% Gd-Doped UO₂ in aqueous carbonate/bicarbonate solutions*, J Electrochem Soc. (2014). 161 (4), H225-H234.
- [87] N. Liu, Z. Zhu, J.J. Noël, D.W. Shoesmith, *Corrosion of nuclear fuel inside a failed waste container*, in: *Encyclopedia of Interfacial Chemistry: Surface Science and Electrochemistry* [K. Wandelt (Ed.)] 2018, pp. 172-182.
- [88] V.M. Oversby, V. Konsult, *Uranium dioxide, SIMFUEL, and spent fuel dissolution rates—a review of published data*, Swedish Nuclear Fuel Management Co, TR-99-22, Stockholm, Sweden (1999).
- [89] C. Poinssot, C. Ferry, M. Kelm, J. Cavedon, C. Corbel, C. Jegou, P. Lovera, F. Miserque, A. Poulesquen, B. Grambow, *Spent fuel stability under repository conditions—final report of the European Project*, French Alternative Energies and Atomic Energy Commission, CEA-R-6039, Gif-sur-Yvette, France (2005).
- [90] J.D. Rudnicki, R.E. Russo, D.W. Shoesmith, *Photothermal deflection spectroscopy investigations of uranium dioxide oxidation*, J Electroanal Chem. (1994). 372 (1), 63-74.
- [91] M.J. Nicol, C.R.S. Needes, *The anodic dissolution of uranium dioxide—II. In carbonate solutions*, Electrochim Acta. (1977). 22 (12), 1381-1384.
- [92] D.E. Grandstaff, *A kinetic study of the dissolution of uraninite*, Econ Geol. (1976). 71 (8), 1493-1506.
- [93] J.-P. Crocombette, F. Jollet, L.T. Nga, T. Petit, *Plane-wave pseudopotential study of point defects in uranium dioxide*, Phys Rev B: Condens Matter. (2001). 64 (10), 104107.

- [94] M. Freyss, T. Petit, J.-P. Crocombette, *Point defects in uranium dioxide: Ab initio pseudopotential approach in the generalized gradient approximation*, J Nucl Mater. (2005). 347 (1-2), 44-51.
- [95] F. Gupta, G. Brilliant, A. Pasturel, *Correlation effects and energetics of point defects in uranium dioxide: a first principle investigation*, Philos Mag. (2007). 87 (17), 2561-2569.
- [96] H.Y. Geng, Y. Chen, Y. Kaneta, M. Iwasawa, T. Ohnuma, M. Kinoshita, *Point defects and clustering in uranium dioxide by LSDA+ U calculations*, Phys Rev B: Condens Matter. (2008). 77 (10), 104120.
- [97] P. Nerikar, T. Watanabe, J.S. Tulenko, S.R. Phillpot, S.B. Sinnott, *Energetics of intrinsic point defects in uranium dioxide from electronic-structure calculations*, J Nucl Mater. (2009). 384 (1), 61-69.
- [98] S.D. Conradson, D. Manara, F. Wastin, D.L. Clark, G.H. Lander, L.A. Morales, J. Rebizant, V.V. Rondinella, *Local structure and charge distribution in the UO_2 - U_4O_9 system*, Inorg Chem. (2004). 43 (22), 6922-6935.
- [99] H. He, D.W. Shoesmith, *Raman spectroscopic studies of defect structures and phase transition in hyper-stoichiometric UO_{2+x}* , Phys Chem Chem Phys. (2010). 12 (28), 8109-8118.
- [100] D. Bevan, I. Grey, B. Willis, *The crystal structure of β - U_4O_9* , J Solid State Chem. (1986). 61 (1), 1-7.
- [101] F. Garrido, R.M. Ibberson, L. Nowicki, B.T.M. Willis, *Cuboctahedral oxygen clusters in U_3O_7* , J Nucl Mater. (2003). 322 (1), 87-89.
- [102] J.M. Elorrieta, L.J. Bonales, N. Rodríguez-Villagra, V.G. Baonza, J. Cobos, *A detailed Raman and X-ray study of UO_{2+x} oxides and related structure transitions*, Phys Chem Chem Phys. (2016). 18 (40), 28209-28216.
- [103] N.A. Brincat, M. Molinari, G.C. Allen, M.T. Storr, S.C. Parker, *Density functional theory calculations of defective UO_2 at U_3O_7 stoichiometry*, J Nucl Mater. (2015). 467, 724-729.
- [104] L. Desgranges, G. Baldinozzi, D. Simeone, H.E. Fischer, *Structural Changes in the Local Environment of Uranium Atoms in the Three Phases of U_4O_9* , Inorg Chem. (2016). 55 (15), 7485-7491.
- [105] H. He, Z. Ding, D.W. Shoesmith, *The determination of electrochemical reactivity and sustainability on individual hyper-stoichiometric UO_{2+x} grains by Raman microspectroscopy and scanning electrochemical microscopy*, Electrochem Commun. (2009). 11 (8), 1724-1727.

- [106] H. He, R.K. Zhu, Z. Qin, P. Keech, Z. Ding, D.W. Shoesmith, *Determination of local corrosion kinetics on hyper-stoichiometric UO_{2+x} by scanning electrochemical microscopy*, J Electrochem Soc. (2009). 156 (3), C87-C94.
- [107] H. He, Z. Qin, D.W. Shoesmith, *Characterizing the relationship between hyperstoichiometry, defect structure and local corrosion kinetics of uranium dioxide*, Electrochim Acta. (2010). 56 (1), 53-60.
- [108] H. He, *The influence of non-stoichiometry and rare earth doping on the oxidation and dissolution of uranium dioxide*, Ph.D. Thesis, The University of Western Ontario, London, Canada, 2010.
- [109] N. Liu, H. He, J.J. Noël, D.W. Shoesmith, *The electrochemical study of Dy_2O_3 doped UO_2 in slightly alkaline sodium carbonate/bicarbonate and phosphate solutions*, Electrochim Acta. (2017). 235, 654-663.
- [110] Y. Kumagai, A. Barreiro-Fidalgo, M. Jonsson, *Impact of stoichiometry on the mechanism and kinetics of oxidative dissolution of UO_2 induced by H_2O_2 and gamma-irradiation*, J Phys Chem C. (2019). 123 (15), 9919-9925.
- [111] F. Garisto, Sixth case study: Features, Events and Processes, Nuclear Waste Management Organization, NWMO TR-2017-08, Toronto, Canada (2017).
- [112] M. Nicol, C. Needes, The mechanism of the anodic dissolution of uranium dioxide, Atomic Energy Board, 1973.
- [113] M.M. Hossain, E. Ekeröth, M. Jonsson, *Effects of HCO_3^- on the kinetics of UO_2 oxidation by H_2O_2* , J Nucl Mater. (2006). 358 (2), 202-208.
- [114] J.S. Goldik, J.J. Noël, D.W. Shoesmith, *Surface electrochemistry of UO_2 in dilute alkaline hydrogen peroxide solutions: Part II. Effects of carbonate ions*, Electrochimica Acta. (2006). 51 (16), 3278-3286.
- [115] P.G. Keech, J.S. Goldik, Z. Qin, D.W. Shoesmith, *The anodic dissolution of SIMFUEL (UO_2) in slightly alkaline sodium carbonate/bicarbonate solutions*, Electrochim Acta. (2011). 56 (23), 7923-7930.
- [116] S. Sundin, B. Dahlgren, O. Roth, M. Jonsson, *H_2O_2 and radiation induced dissolution of UO_2 and SIMFUEL in HCO_3^- deficient aqueous solution*, J Nucl Mater. (2013). 443 (1-3), 291-297.
- [117] W.H. Hocking, J.S. Betteridge, D.W. Shoesmith, *The cathodic reduction of oxygen on uranium dioxide in dilute alkaline aqueous solution*, J Electroanal Chem. (1994). 379 (1-2), 339-351.

- [118] D.W. Shoesmith, J.S. Betteridge, W.H. Hocking, *The cathodic reduction of oxygen on n-type UO₂ in dilute alkaline aqueous solution*, J Electroanal Chem. (1996). 406 (1), 69-81.
- [119] Z. Zhu, L. Wu, J.J. Noël, D.W. Shoesmith, *Anodic reactions occurring on simulated spent nuclear fuel (SIMFUEL) in hydrogen peroxide solutions containing bicarbonate/carbonate – The effect of fission products*, Electrochim Acta. (2019). 320.
- [120] S.M. Peper, L.F. Brodnax, S.E. Field, R.A. Zehnder, S.N. Valdez, W.H. Runde, *Kinetic Study of the Oxidative Dissolution of UO₂ in Aqueous Carbonate Media*, Ind Eng Chem Res. (2004). 43 (26), 8188-8193.
- [121] G.S. Goff, L.F. Brodnax, M.R. Cisneros, S.M. Peper, S.E. Field, B.L. Scott, W.H. Runde, *First Identification and Thermodynamic Characterization of the Ternary U(VI) Species, UO₂(O₂)(CO₃)₂⁴⁻, in UO₂-H₂O₂-K₂CO₃ Solutions*, Inorg Chem. (2008). 47 (6), 1984-1990.
- [122] S. Sunder, D.W. Shoesmith, H. Christensen, N.H. Miller, *Oxidation of UO₂ fuel by the products of gamma radiolysis of water*, J Nucl Mater. (1992). 190, 78-86.
- [123] E. Ekeröth, M. Jonsson, *Oxidation of UO₂ by radiolytic oxidants*, J Nucl Mater. (2003). 322 (2-3), 242-248.
- [124] S.-S. Lin, M.D. Gurol, *Catalytic decomposition of hydrogen peroxide on iron oxide: kinetics, mechanism, and implications*, Environ Sci Technol. (1998). 32 (10), 1417-1423.
- [125] D. Fu, X. Zhang, P.G. Keech, D.W. Shoesmith, J.C. Wren, *An electrochemical study of H₂O₂ decomposition on single-phase γ -FeOOH films*, Electrochim Acta. (2010). 55 (11), 3787-3796.
- [126] A. Hiroki, J.A. LaVerne, *Decomposition of hydrogen peroxide at water– ceramic oxide interfaces*, J Phys Chem B. (2005). 109 (8), 3364-3370.
- [127] C.M. Lousada, M. Trummer, M. Jonsson, *Reactivity of H₂O₂ towards different UO₂-based materials: The relative impact of radiolysis products revisited*, J Nucl Mater. (2013). 434 (1-3), 434-439.
- [128] C.M. Lousada, M. Yang, K. Nilsson, M. Jonsson, *Catalytic decomposition of hydrogen peroxide on transition metal and lanthanide oxides*, J Mol Catal A: Chem. (2013). 379, 178-184.
- [129] A. Barreiro-Fidalgo, B. Dahlgren, T. Brinck, M. Jonsson, *Surface reactions of H₂O₂, H₂, and O₂ in aqueous systems containing ZrO₂*, J Phys Chem C. (2016). 120 (3), 1609-1614.
- [130] J.S. Betteridge, N.A.M. Scott, D.W. Shoesmith, L.E. Bahen, W.H. Hocking, P.G. Lucuta, *Effects of hyperstoichiometry and fission products on the electrochemical reactivity of UO₂ nuclear fuel*, Atomic Energy of Canada Limited, AECL-11647, COG-96-331-1, (1997).

- [131] N.A. Anastasijević, Z. Dimitrijević, R.R. Adžić, *Oxygen reduction on a ruthenium electrode in alkaline electrolytes*, J Electroanal Chem. (1986). 199 (2), 351-364.
- [132] S. Sunder, N.H. Miller, D.W. Shoesmith, *Corrosion of uranium dioxide in hydrogen peroxide solutions*, Corros Sci. (2004). 46 (5), 1095-1111.
- [133] R. Brown, *Uranium precipitation with hydrogen peroxide*, Soc Min Eng AIME, 1980, pp. 1836-1840.
- [134] M. Amme, *Contrary effects of the water radiolysis product H₂O₂ upon the dissolution of nuclear fuel in natural ground water and deionized water*, Radiochim Acta. (2002). 90 (7), 399-406.
- [135] M. Amme, B. Renker, B. Schmid, M.P. Feth, H. Bertagnolli, W. Döbelin, *Raman microspectrometric identification of corrosion products formed on UO₂ nuclear fuel during leaching experiments*, J Nucl Mater. (2002). 306 (2-3), 202-212.
- [136] M. Jonsson, E. Ekeröth, O. Roth, *Dissolution of UO₂ by One- and Two-Electron Oxidants*, MRS Online Proc Lib. (2003). 807 (1), 277-282.
- [137] J.S. Goldik, J.J. Noel, D.W. Shoesmith, *The effects of simulated fission products in the reduction of hydrogen peroxide on simulated nuclear fuel electrodes*, J Electrochem Soc. (2006). 153 (9), E151.
- [138] P.G. Keech, J.J. Noël, D.W. Shoesmith, *The electrochemical reduction of hydrogen peroxide on uranium dioxide under intermediate pH to acidic conditions*, Electrochim Acta. (2008). 53 (18), 5675-5683.
- [139] M.E. Broczkowski, D. Zagidulin, D.W. Shoesmith, *The role of dissolved hydrogen on the corrosion/dissolution of spent nuclear fuel*, in: *Nuclear Energy and the Environment*, American Chemical Society, 2010, pp. 349-380.
- [140] M. Razdan, D.W. Shoesmith, *The influence of hydrogen peroxide and hydrogen on the corrosion of simulated spent nuclear fuel*, Faraday Discuss. (2015). 180, 283-299.
- [141] A. Barreiro-Fidalgo, Y. Kumagai, M. Jonsson, *The role of surface-bound hydroxyl radicals in the reaction between H₂O₂ and UO₂*, J Coord Chem. (2018). 71 (11-13), 1799-1807.
- [142] A.C. Maier, P. Kegler, M. Klinkenberg, A. Baena, S. Finkeldei, F. Brandt, M. Jonsson, *On the change in UO₂ redox reactivity as a function of H₂O₂ exposure*, Dalton Trans. (2020). 49 (4), 1241-1248.
- [143] Y. Kumagai, M. Jonsson, *γ -Radiation and H₂O₂ induced oxidative dissolution of uranium(IV) oxide in aqueous solution containing phthalic acid*, Dalton Trans. (2020). 49 (6), 1907-1914.

- [144] J.S. Goldik, H.W. Nesbitt, J.J. Noël, D.W. Shoesmith, *Surface electrochemistry of UO₂ in dilute alkaline hydrogen peroxide solutions*, *Electrochim Acta*. (2004). 49 (11), 1699-1709.
- [145] J.S. Goldik, J.J. Noël, D.W. Shoesmith, *The electrochemical reduction of hydrogen peroxide on uranium dioxide electrodes in alkaline solution*, *J Electroanal Chem*. (2005). 582 (1), 241-248.
- [146] D. Zigah, J. Rodríguez-López, A.J. Bard, *Quantification of photoelectrogenerated hydroxyl radical on TiO₂ by surface interrogation scanning electrochemical microscopy*, *Phys Chem Chem Phys*. (2012). 14 (37), 12764-12772.
- [147] C.M. Lousada, A.J. Johansson, T. Brinck, M. Jonsson, *Reactivity of metal oxide clusters with hydrogen peroxide and water – a DFT study evaluating the performance of different exchange–correlation functionals*, *Phys Chem Chem Phys*. (2013). 15 (15), 5539-5552.
- [148] Z. Zhu, J.J. Noël, D.W. Shoesmith, *Hydrogen peroxide decomposition on simulated nuclear fuel bicarbonate/carbonate solutions*, *Electrochim Acta*. (2020). 340.
- [149] S. Nilsson, M. Jonsson, *H₂O₂ and radiation induced dissolution of UO₂ and SIMFUEL pellets*, *J Nucl Mater*. (2011). 410 (1-3), 89-93.
- [150] L. Wu, D.W. Shoesmith, *An electrochemical study of H₂O₂ oxidation and decomposition on simulated nuclear fuel (SIMFUEL)*, *Electrochim Acta*. (2014). 137, 83-90.
- [151] L. Wu, J.S. Goldik, D.W. Shoesmith, *The anodic reactions on simulated spent fuel (SIMFUEL) in H₂O₂ solutions: Effect of carbonate/bicarbonate*, *J Electrochem Soc*. (2014). 161 (6), C363.
- [152] W. Stumm, J.J. Morgan, *Aquatic chemistry: chemical equilibria and rates in natural waters*, Third Edition, John Wiley & Sons, New York, USA, 2012.
- [153] F. King, S. Stroes-Gascoyne, *An assessment of the long-term corrosion behaviour of C-steel and the impact of the redox conditions inside a nuclear fuel waste disposal container*, Ontario Power Generation, No. 066819-REP-01200-10028-R00, (2000).
- [154] R.G. Zepp, B.C. Faust, J. Hoigne, *Hydroxyl radical formation in aqueous reactions (pH 3-8) of iron(II) with hydrogen peroxide: the photo-Fenton reaction*, *Environ Sci Technol*. (1992). 26 (2), 313-319.
- [155] A. Puranen, A. Barreiro, L.Z. Evins, K. Spahiu, *Spent fuel corrosion and the impact of iron corrosion – The effects of hydrogen generation and formation of iron corrosion products*, *J Nucl Mater*. (2020). 542.
- [156] A. Loida, M. Kelm, B. Kienzler, H. Geckeis, A. Bauer, *The Effect of Nearfield Constraints on the Corrosion Behavior of High Burnup Spent Fuel*, *MRS Online Proc Lib*. (2006). 932, 72.1.

- [157] D. Cui, J. Low, K. Spahiu, *Environmental behaviors of spent nuclear fuel and canister materials*, Energy Environ Sci. (2011). 4 (7), 2537-2545.
- [158] M. Odorowski, C. Jegou, L. De Windt, V. Broudic, G. Jouan, S. Peugeot, C. Martin, *Effect of metallic iron on the oxidative dissolution of UO₂ doped with a radioactive alpha emitter in synthetic Callovian-Oxfordian groundwater*, Geochim Cosmochim Acta. (2017). 219, 1-21.
- [159] M. Jonsson, F. Nielsen, O. Roth, E. Ekeroth, S. Nilsson, M.M. Hossain, *Radiation induced spent nuclear fuel dissolution under deep repository conditions*, Environ Sci Technol. (2007). 41 (20), 7087-7093.
- [160] L.D. Wu, Z. Qin, D.W. Shoesmith, *An improved model for the corrosion of used nuclear fuel inside a failed waste container under permanent disposal conditions*, Corros Sci. (2014). 84, 85-95.
- [161] F. King, M. Kolar, Validation of the mixed-potential model for used fuel dissolution against experimental data, Ontario Power Generation, No. 06819-REP01200-10077-R00, (2002).
- [162] E. Ekeroth, M. Granfors, D. Schild, K. Spahiu, *The effect of temperature and fuel surface area on spent nuclear fuel dissolution kinetics under H₂ atmosphere*, J Nucl Mater. (2020). 531.
- [163] P. Fors, P. Carbol, S. Van Winckel, K. Spahiu, *Corrosion of high burn-up structured UO₂ fuel in presence of dissolved H₂*, J Nucl Mater. (2009). 394 (1), 1-8.
- [164] B. Muzeau, C. Jegou, F. Delaunay, V. Broudic, A. Brevet, H. Catalette, E. Simoni, C. Corbel, *Radiolytic oxidation of UO₂ pellets doped with alpha-emitters (^{238/239}Pu)*, J Alloys Compd. (2009). 467 (1-2), 578-589.
- [165] N.L. Hansson, P.L. Tam, C. Ekberg, K. Spahiu, *XPS study of external α -radiolytic oxidation of UO₂ in the presence of argon or hydrogen*, J Nucl Mater. (2021). 543.
- [166] P. Carbol, J. Cobos-Sabate, J.P. Glatz, B. Grambow, B. Kienzler, A. Loida, A. Martinez Esparza Valiente, V. Metz, J. Quiñones, C. Ronchi, The effect of dissolved hydrogen on the dissolution of ²³³U doped UO₂ (s) high burn-up spent fuel and MOX fuel, Swedish Nuclear Fuel and Waste Management Co., TR-05-09, Stockholm, Sweden (2005).
- [167] J.K. Nørskov, T. Bligaard, A. Logadottir, J. Kitchin, J.G. Chen, S. Pandalov, U. Stimming, *Trends in the exchange current for hydrogen evolution*, J Electrochem Soc. (2005). 152 (3), J23.
- [168] M.E. Broczkowski, R. Zhu, Z. Ding, J.J. Noël, D.W. Shoesmith, *Electrochemical, SECM, and XPS Studies of the Influence of H₂ on UO₂ Nuclear Fuel Corrosion*, Mater Res Soc Symp P. (2006). 932, 449-456.

- [169] M.E. Broczkowski, J.J. Noël, D.W. Shoesmith, *The inhibiting effects of hydrogen on the corrosion of uranium dioxide under nuclear waste disposal conditions*, J Nucl Mater. (2005). 346 (1), 16-23.
- [170] M.E. Broczkowski, J.J. Noel, D.W. Shoesmith, *The influence of temperature on the anodic oxidation/dissolution of uranium dioxide*, Electrochim Acta. (2007). 52 (25), 7386-7395.
- [171] M.E. Broczkowski, P.G. Keech, J.J. Nol, D.W. Shoesmith, *Corrosion of uranium dioxide containing simulated fission products in dilute hydrogen peroxide and dissolved hydrogen*, J Electrochem Soc. (2010). 157 (8), C275-C281.
- [172] M.E. Broczkowski, P.G. Keech, J.J. Noël, D.W. Shoesmith, *The role of dissolved hydrogen on rare earth-doped uranium dioxide corrosion in the presence of hydrogen peroxide*, J Electrochem Soc. (2011). 158 (12), C439-C444.
- [173] S. Nilsson, M. Jonsson, *On the catalytic effects of $UO_2(s)$ and $Pd(s)$ on the reaction between H_2O_2 and H_2 in aqueous solution*, J Nucl Mater. (2008). 372 (2-3), 160-163.
- [174] S. Nilsson, M. Jonsson, *On the catalytic effect of $Pd(s)$ on the reduction of UO_2^{2+} with H_2 in aqueous solution*, J Nucl Mater. (2008). 374 (1), 290-292.
- [175] D. Cui, J. Low, V.V. Rondinella, K. Spahiu, *Hydrogen catalytic effects of nanostructured alloy particles in spent fuel on radionuclide immobilization*, Appl Catal B. (2010). 94 (1), 173-178.
- [176] M.E. Broczkowski, *The effects of hydrogen and temperature on the electrochemistry and corrosion of uranium dioxide*, Ph.D. Thesis, The University of Western Ontario, London, Canada, 2008.
- [177] L. Bauhn, N. Hansson, C. Ekberg, P. Fors, K. Spahiu, *The fate of hydroxyl radicals produced during H_2O_2 decomposition on a SIMFUEL surface in the presence of dissolved hydrogen*, J Nucl Mater. (2018). 507, 38-43.
- [178] J. Bruno, I. Casas, I. Puigdomènech, *The kinetics of dissolution of UO_2 under reducing conditions and the influence of an oxidized surface layer (UO_{2+x}): Application of a continuous flow-through reactor*, Geochim Cosmochim Acta. (1991). 55 (3), 647-658.
- [179] B. Grambow, E. Giffaut, *Coupling of Chemical Processes in the Near Field*, MRS Online Proc Lib. (2006). 932, 119.1.
- [180] K. Ollila, *Dissolution of unirradiated UO_2 and UO_2 doped with ^{233}U in low- and high-ionic-strength NaCl under anoxic and reducing conditions*, Posiva Oy, Working Report 2008-50, Eurajoki, Finland (2008).

[181] S. Salah, C. Cachoir, K. Lemmens, N. Maes, *Static dissolution tests of α -doped UO_2 under repository relevant conditions: Influence of Boom Clay and α -activity on fuel dissolution rates*, MRS Online Proc Lib. (2006). 932, 85.1.

Chapter 2

2. Experimental Techniques and Details

2.1. Experimental Design

The experimental design and techniques used in this project are described in this chapter. Subsequent chapters provide specific experimental parameters.

2.2. UO₂ Material

The UO₂ materials studied in this project are natural UO₂ manufactured between 1965 and 2017 for use in CANDU reactors. The UO₂ pellets were provided by BWX Technologies (BWXT) and Canadian Nuclear Laboratories (CNL) on behalf of Atomic Energy of Canada Limited (AECL). All materials were received in pellet form. Their nominal O/U ratios are unknown but general compositions close to stoichiometric would be expected.

2.3. Electrochemical Experimental Techniques

2.3.1. Electrochemical Cell and Instrumentation

2.3.1.1. Three-Compartment Cell

A standard 1 L, three-compartment cell, Figure 2-1, was used for the electrochemical experiments presented in Chapter 5. The UO₂ working electrode (WE) was attached to a conductive rod and placed in the main compartment. The main compartment was separated from the counter (CE) and reference (RE) electrode compartments using dense glass frits. A Luggin capillary was used to minimize IR drop between the WE and the RE. A saturated calomel (SCE, +0.241 V vs. standard hydrogen electrode (SHE) [1]) reference electrode was used for all experiments performed in the cell. A 1 cm² Pt foil spot-welded to a Pt wire was used as the counter electrode. All experiments were performed in a grounded Faraday cage to minimize interference from external electrical noise. A Solartron model 1287 potentiostat was

used for cyclic voltammetry experiments and CorrWare software (version 3.5d) was used to control the potentiostat and CorrView software (Scribner Associates) was used to analyze the data. Applied potentials and measured current responses for corrosion potential and linear polarization experiments were controlled, recorded, and analyzed using a Solartron Model 1480 Multistat and CorrWare software (Scribner Associates), respectively.

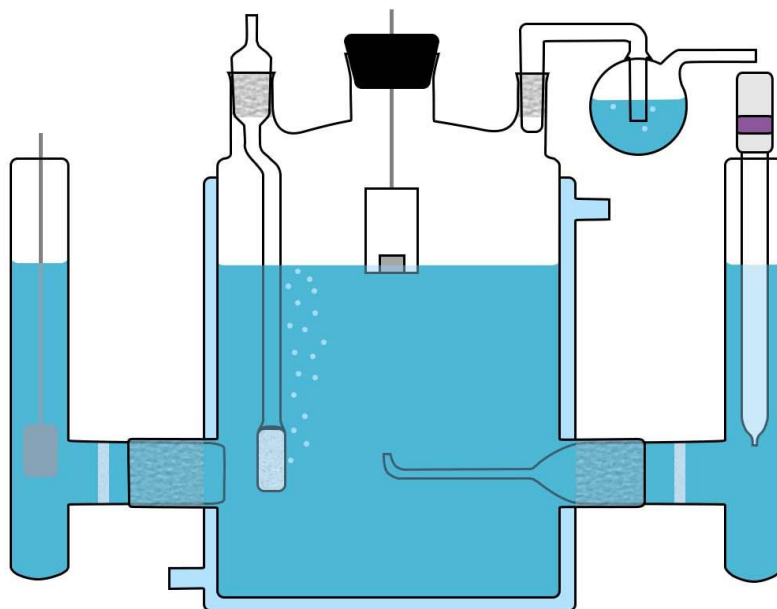


Figure 2-1. Schematic illustrating a 1 L, three-compartment electrochemical cell.

2.3.1.2. Single-Compartment Cell

A 50 mL, single-compartment cell, Figure 2-2, was used for the electrochemical experiments presented in Chapter 4. The CE was a Pt wire were placed in the same compartment as the RE. An Ag/AgCl in saturated KCl (+0.197 V vs. SHE [1]) RE was used for all experiments. The electrochemical cell was housed in a grounded Faraday cage to minimize interference from external electrical noise. Applied potentials and measured current responses were controlled,

recorded, and analyzed using a Solartron Model 1480 Multistat and CorrWare software (Scribner Associates), respectively.

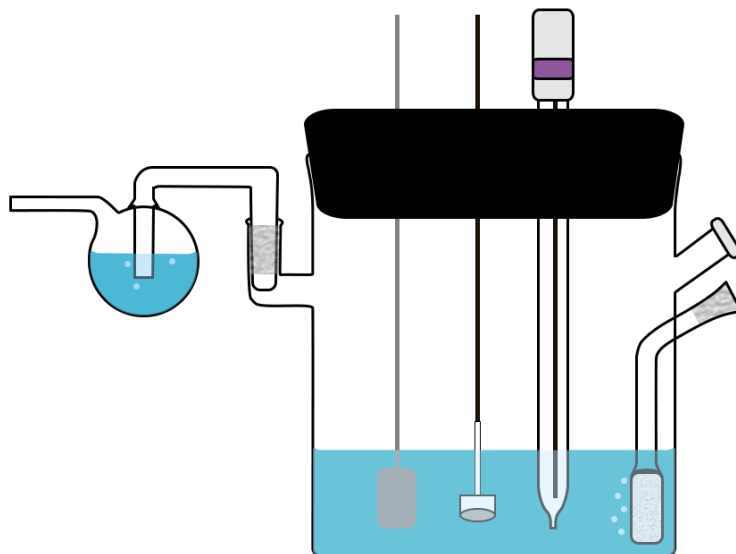


Figure 2-2. Schematic illustration of the 50 mL, small electrochemical cell used in H_2O_2 decomposition experiments.

2.3.2. Electrode Preparation

All UO_2 samples were received as pellets ~20 mm long and ~12 mm in diameter. The pellets were cut into discs 2-3 mm thick using a diamond blade saw. To prevent cracking of the ceramic material during cutting, the pellets were first mounted in a transparent epoxy (Buehler Sampl-Wick liquid and powder at a 1:2 ratio). To create a good electrical contact with external circuitry, one exposed face of the disc was polished and electroplated with a thin layer of Cu. The electroplating procedure is illustrated in Figure 2-3. The disk was secured in place at the end of a rubber tube and immersed in a 0.1 mol/L CuSO_4 and 0.1 M H_2SO_4 mol/L solution. Mercury was carefully poured into the tubing, and a conductive wire inserted to connect the

mercury to the negative terminal of a DC power supply (GPR-30H10D). A polished Cu wire was attached to the positive terminal of the power supply, and a 10 mA current was applied for 5 minutes. The resulting electrodeposited Cu layer was uniformly distributed across the UO_2 surface.

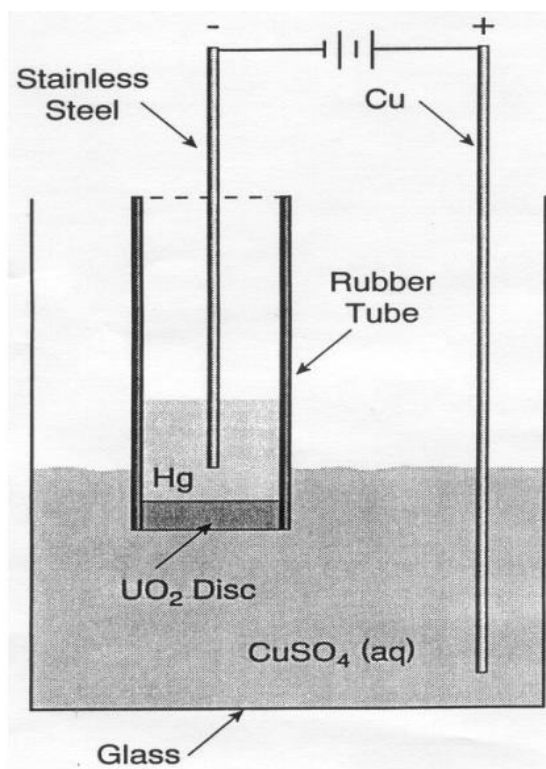


Figure 2-3. Schematic illustration of the experimental setup used to electroplate one side of a UO_2 disk with Cu [2].

A conductive threaded backing is attached to the Cu-electrodeposited face of the UO_2 disk using highly conductive silver epoxy (Hysol KS004). The UO_2 sample is then coated with Amercoat epoxy (90HS, Amercoat Canada), leaving a single face of the disk to be exposed in a solution. Prior to an experiment, the exposed UO_2 surface is polished with 1200 grit SiC

paper, then sonicated for 2 minutes in Type 1 H₂O (resistivity = 18.2 MΩ.cm) to remove polishing debris.

2.3.3. Solution Preparation

All solutions were prepared using Type 1 H₂O (resistivity of 18.2 MΩ.cm) obtained from a Milli-Q[®] Millipore system. All experiments were conducted in a 0.1 mol/L NaCl and 0.05 mol/L NaHCO₃ solution, made using reagent grade NaCl (Fisher Chemical) and NaHCO₃ (EMD Millipore). The pH was adjusted to 9.5 using NaOH. When H₂O₂ was added, a 3% stock solution was diluted to the desired concentration. The solutions were purged with ultra-high purity (UHP) Ar gas or safe gas (95% Ar/5% H₂) for a minimum of 45 minutes in the large electrochemical cell and 20 minutes in the small electrochemical cell before an experiment to ensure anoxic conditions. The solution was continuously sparged with either Ar gas or safe gas during an experiment.

2.4. Electrochemical Techniques

Prior to electrochemical experiments, electrodes were polished using 1200 grit SiC paper and rinsed with Type 1 H₂O. After immersion in solution, the electrode was cathodically cleaned using potentiostatic polarization at -1.2 V vs. SCE for two minutes in the large electrochemical cell and 20 seconds in the small electrochemical cell to remove air-formed oxides.

2.4.1. Corrosion Potential (E_{CORR}) Measurements

The corrosion potential (E_{CORR}) is the potential measured between the working and reference electrodes in the absence of an applied potential. E_{CORR} represents the open circuit potential for a corroding system. For a UO₂ system, this involves the coupling of the anodic oxidation of UO₂ with the cathodic reduction of an available oxidant,



where Ox is the oxidant, and Red is its reduced form.

2.4.2. Linear Polarization Resistance (LPR) Measurements

The polarization resistance (R_p) is a measurement of the corrosion rate. As the current at E_{CORR} is zero,

$$i_{CORR} = \sum i_a = - \sum i_c \quad (2.2)$$

where i_{CORR} is the corrosion current, and i_a and i_c are the currents for the anodic and cathodic half-reactions, respectively. Since the net current measurable in an external circuit is zero at E_{CORR} , the potential is polarized to ± 10 mV, and the current response is recorded. The current-potential relationship over the small potential range results in a linear slope around E_{CORR} that defines R_p , which is inversely proportional to the corrosion rate [3].

2.4.3. Cyclic Voltammetry (CV) Measurements

Cyclic voltammetry (CV) is an electrochemical technique that dynamically polarizes a sample at a constant scan rate between two potential limits, with the current response measured as a function of applied potential. The observed anodic and cathodic currents provide insight into the kinetics and mechanism of surface reactions occurring as a result of heterogeneous electron transfer [4]. The shape and size of the observed anodic and cathodic currents yield information on the oxidation and reduction reactions occurring on the surface and, when coupled with analytical methods, enable the surface electrochemistry/chemistry properties to be elucidated.

2.4.4. Potentiostatic Polarization (PSP) Measurements

Potentiostatic polarization (PSP) is an electrochemical technique that applies a constant potential difference between the WE and RE and records the current response between the WE and the CE as a function of time. By applying a potential more positive or negative than E_{CORR} , the anodic or cathodic reactions can be accelerated, respectively. The measured current at applied potentials more positive than E_{CORR} represents the reaction rate on the WE surface due to oxidation of the surface and possible dissolution. The measured current at applied potentials more negative than E_{CORR} represents the reduction reaction rate on the WE.

2.4.5. Electrochemical Impedance Spectroscopy (EIS)

Electrochemical impedance spectroscopy (EIS) is an in-situ technique used in this study to determine the resistivity of each sample. Using a Solartron Model 1255 Frequency Response Analyser and ZView software (Scribner Associates), the sample was perturbed by a small-amplitude sinusoidal potential of ± 10 mV vs a direct current input potential, and the sinusoidal current response was measured, Figure 2-4. The input signal was applied over a frequency range from 10^5 to 10^{-3} Hz with 11 data points recorded per decade.

Using a modified version of Ohm's Law for an alternating current system, the applied potential ($E(\omega)$) can be related to the current output response ($i(\omega)$), where ω is the angular frequency and $Z(\omega)$ is the impedance, equation 3. In this study, impedance measurements are used to determine the impedance of samples at frequencies when the interface is in phase, when $Z(\omega)$ becomes a resistance.

$$E(\omega) = i(\omega) Z(\omega) \quad (2.3)$$

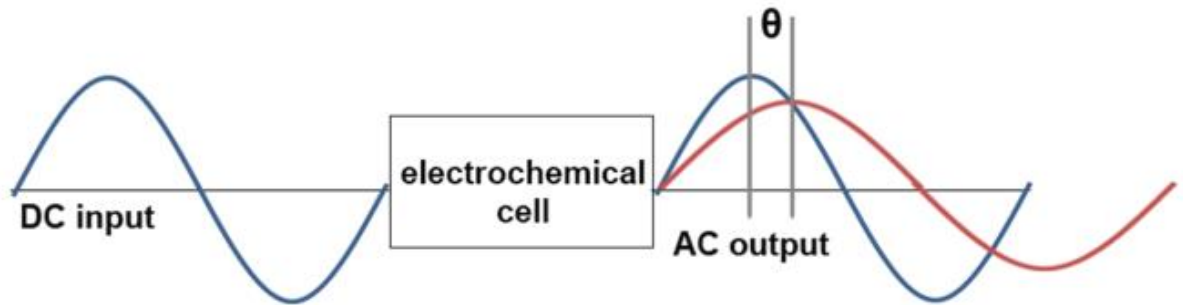


Figure 2-4. Schematic of the potential perturbation applied during an EIS experiment and the resulting AC current response [5]. The change in the phase angle is represented by θ .

The UO_2 disk was secured in the end of a piece of rubber tubing. Using a 20 mL glass vial, mercury (Hg) was used to create an electrical connection to both sides of the UO_2 disk. A conductive wire was placed in the Hg and connected to a potentiostat with a frequency response analyzer, Figure 2-5.

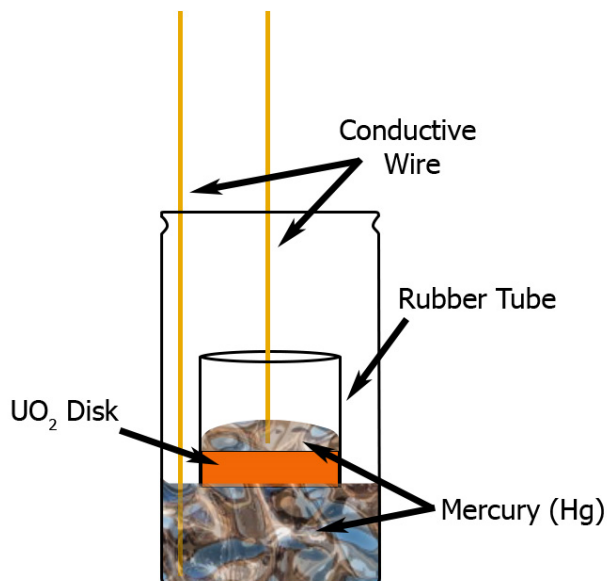


Figure 2-5. Schematic illustration of the experimental setup used to measure the resistivity of a UO_2 disk.

2.5. Surface Analysis Techniques

2.5.1. Raman Spectroscopy

Raman spectroscopy provides information about a sample's molecular vibrations by probing the polarizable species using monochromatic light to measure inelastic photon scattering. Most of the scattered photons are elastically scattered (Rayleigh scattering), but a small portion are inelastically scattered (Raman scattering) with either higher or lower frequencies compared to the incident light frequency, Figure 2-6 [6].

Using a Renishaw InVia Reflex Raman spectrometer and WiRE 4.2 software, the UO_2 lattice was probed to determine the defect structure within the wavenumber range from 156.6 cm^{-1} to 1373 cm^{-1} .

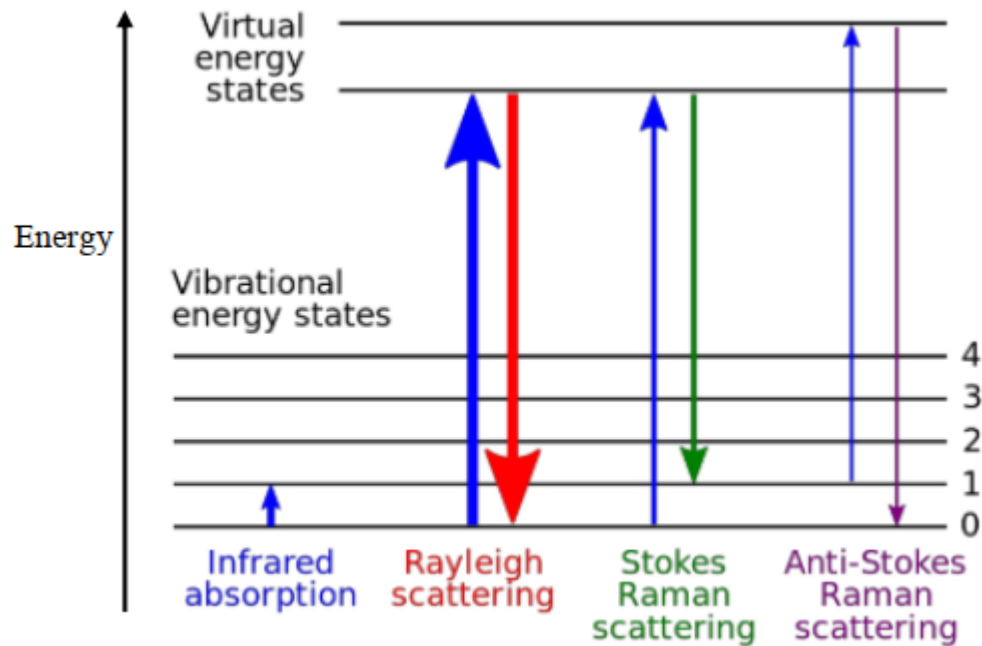


Figure 2-6. Schematic illustrating the energy level diagram of the states involved in a Raman signal. The signal strength from the described energy transitions is qualitatively represented by the line thickness.

2.5.2. Scanning Electron Microscopy

Scanning electron microscopy (SEM) is an analytical technique used to study surface morphology. Using a beam of high-energy electrons (primary electrons), a high-resolution image of a sample surface can be obtained. The primary electron beam is generated from the thermionic emission of electrons from a metal filament, such as tungsten. A set of condenser lenses and an objective lens focus the electron beam to a very small diameter, the diameter of

which is dependent on the primary electron source. The finely focused electron beam is rastered across the sample surface, resulting in various electronic interactions. The most common products from these interactions are secondary electrons, backscattered electrons, Auger electrons, and X-rays, as summarized in Figure 2-7.

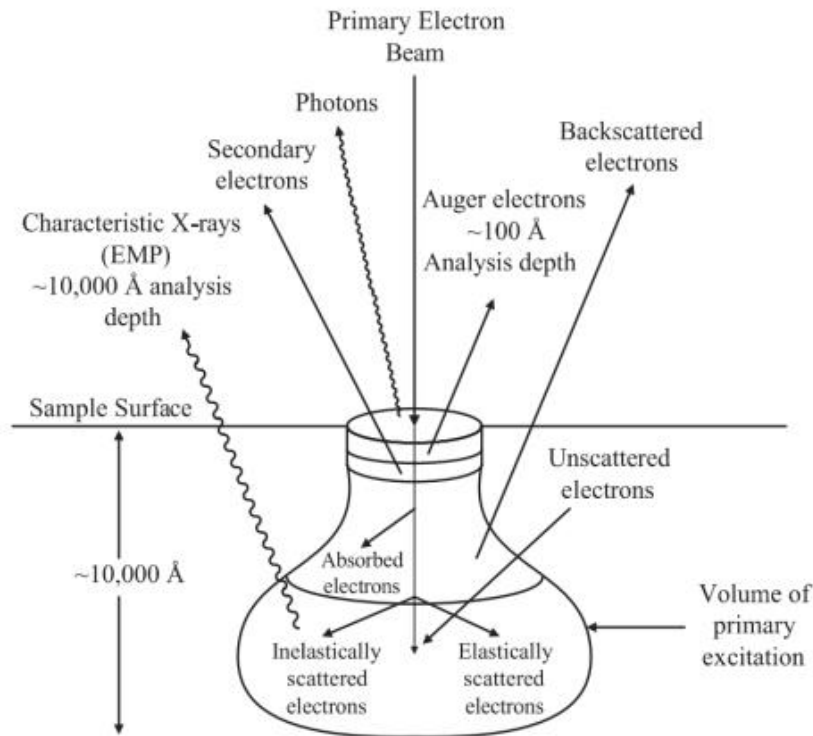


Figure 2-7. Schematic illustration of the possible interactions between a primary electron beam and a sample surface [7].

Secondary electrons are produced due to inelastic interactions between the primary electrons and the sample. The inelastic collisions result in an energy transfer from the primary electrons to electrons in the sample surface. When the transferred energy is greater than the work function of the material, an electron is ejected from the sample. The ejected electron, known as a “secondary” electron, is used to characterize the morphology of a sample surface. The

morphology is determined by the depth at which the secondary electron can escape. Electrons near the surface, with a high probability of reaching the detector without undergoing further inelastic collisions, appear brighter in the SEM image. Electrons from deeper locations have a lower probability of reaching the detector and, thus, appear darker in the image.

2.5.3. X-ray Photoelectron Spectroscopy

X-ray photoelectron spectroscopy (XPS) is an analytical technique based on the photoelectric effect that can be used to quantitatively measure elemental oxidation states in a sample surface. XPS probes the outer 5 to 10 nm of a surface by irradiating it with low-energy X-rays. When an X-ray of a known energy ($h\nu$) interacts with an atom, a photoelectron can be emitted via the photoelectric effect, Figure 2-8. The kinetic energy of the photoelectron (E_K) can then be measured, and the binding energy (E_b) of the photoelectron calculated using the following equation,

$$E_b = h\nu - E_K - \Phi \quad (2.4)$$

where Φ is the work function of the spectrometer.

The measured kinetic energy of a photoelectron is sensitive to the chemical environment of the atom from which it was ejected. The intensity of the peaks provides information on the concentration of the element in the area of analysis, while subtle shifts in the measured kinetic energy provide characteristic information on the atom's oxidation state. These subtle shifts can be observed in high-resolution spectra. Using CasaXPS (version 2.3.19), the peaks were fit to deconvolute the spectra and obtain quantitative information on the surface oxidation states [8].

With paramagnetic states, a shake-up peak will commonly appear near the main peak of an element at a slightly higher binding energy. This occurs due to the excitation of a valence electron by the outgoing photoelectron and the loss of a small amount of kinetic energy. The position of the satellite structure can be used in the assignment of the chemical states of the element in question.

Spectra were collected on a Kratos AXIS Supra spectrometer using a monochromatic Al K_{α} (1486.6 eV, 15 mA, 14kV) source. The instrument work function was calibrated for the Au $4f_{7/2}$ metallic gold binding energy of 83.96 ± 0.025 eV, and the spectrometer dispersion was adjusted to a binding energy (BE) of 932.62 ± 0.025 eV for metallic Cu $2p_{3/2}$. When necessary, surface charging was corrected for by setting the C 1s BE at 284.8 eV. Survey spectra were collected over a BE range from 0 to 1100 eV at a pass energy of 160 eV. High-resolution spectra were collected for O 1s, U 4f, and C 1s at a pass energy of 20 eV. For all measurements, the area of analysis was $\sim 400 \times 700 \mu\text{m}$.

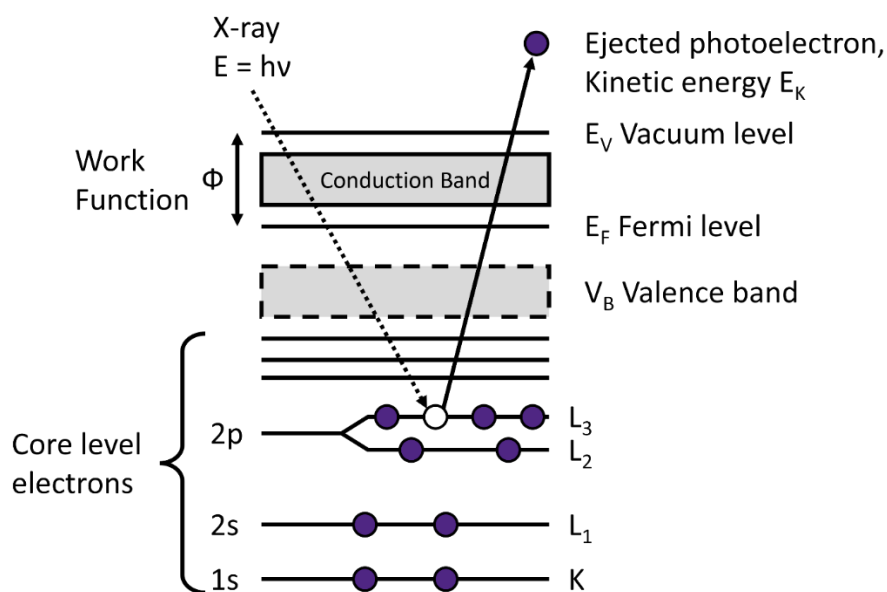


Figure 2-8. Schematic illustration of the excitation of a core level electron by an X-ray beam and the subsequent generation of a photoelectron.

2.6. Solution Analysis Techniques

2.6.1. Inductively Coupled Plasma-Mass Spectrometry

Inductively coupled plasma-mass spectrometry (ICP-MS) is a solution analysis technique used to measure the concentration of solutes. This is done by ionizing a solution into the gas phase using extremely high temperatures (6000-7000 K). The sample is then aerosolized and focused into a quadrupole mass spectrometer using ion lenses. The spectrometer consists of four charged rods that generate a magnetic field by applying a direct current (DC) field and alternating current (AC) of radio frequency on opposite pairs of the four rods. By manipulating the AC/DC ratio on the pairs of rods, ions of a specific mass-charge ratio can be filtered, and the concentration of the desired ion measured [9].

Solutions were analyzed using an Agilent 7700x ICP-MS. Prior to solution analysis, the spectrometer was calibrated with a series of ^{238}U standards. All samples were diluted with 2% HNO_3 before injection to achieve the optimal detection range and to prevent precipitation. ICP-MS was used in this work to determine the concentration of U ions dissolved in solution throughout and after corrosion experiments.

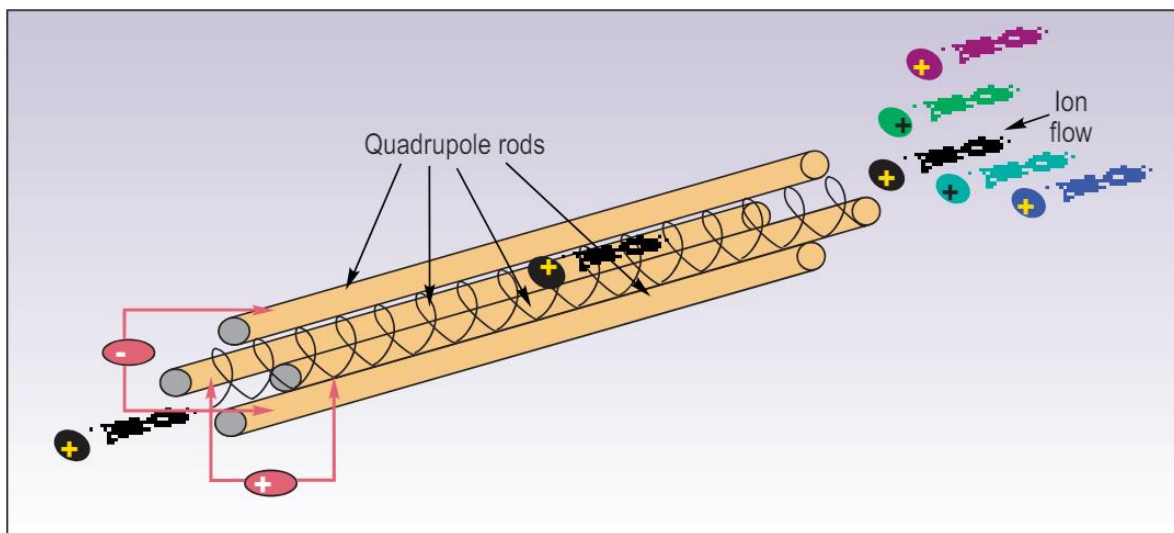


Figure 2-9. Schematic illustration of a quadrupole mass filter [9].

2.6.2. Ultraviolet-Visible Spectroscopy

Ultraviolet-visible (UV-vis) absorption spectroscopy uses electromagnetic radiation with a wavelength between 200 nm and 800 nm, covering the UV (200-400 nm) and visible (400-800 nm) ranges. The solution's absorbance can be calculated by measuring the intensity of a light beam before and after passing through the sample,

$$A = \log I_0/I \quad (2.5)$$

where A is the absorbance of the sample, I_0 is the intensity of the incident beam, and I is the beam's intensity after passing through the sample. Using the measured absorption, a concentration can be calculated using the Beer-Lambert law,

$$A = \epsilon \cdot c \cdot l \quad (2.6)$$

where ϵ is the molar absorption coefficient of the chemical species, c is the concentration of the sample, and l is the optical path length.

UV-vis is based on the ability of a molecule to absorb UV and visible light, causing the excitation of electrons from the highest occupied molecular orbital (HOMO) to the lowest unoccupied molecular orbital (LUMO). The frequency at which the light is absorbed is characteristic of the chemical structure of the absorbing species. An optical spectrometer measures the wavelengths at which absorption occurs and yields a spectrum of absorbance with respect to wavelength.

In this work, UV-vis was performed using a diode array spectrophotometer (BioLogic Science Instruments), Figure 2-10, to measure H_2O_2 concentrations using the Ghormley tri-iodide method in which H_2O_2 oxidizes I^- to I_3^- in the presence of ammonium molybdate [10]. UV-vis analysis was performed immediately after sampling the experimental solution, and the absorbance at 352 nm was used to measure the concentration of H_2O_2 . For all experiments containing H_2O_2 , the electrochemical cells were covered with commercial-grade aluminum foil to avoid photolytic decomposition.

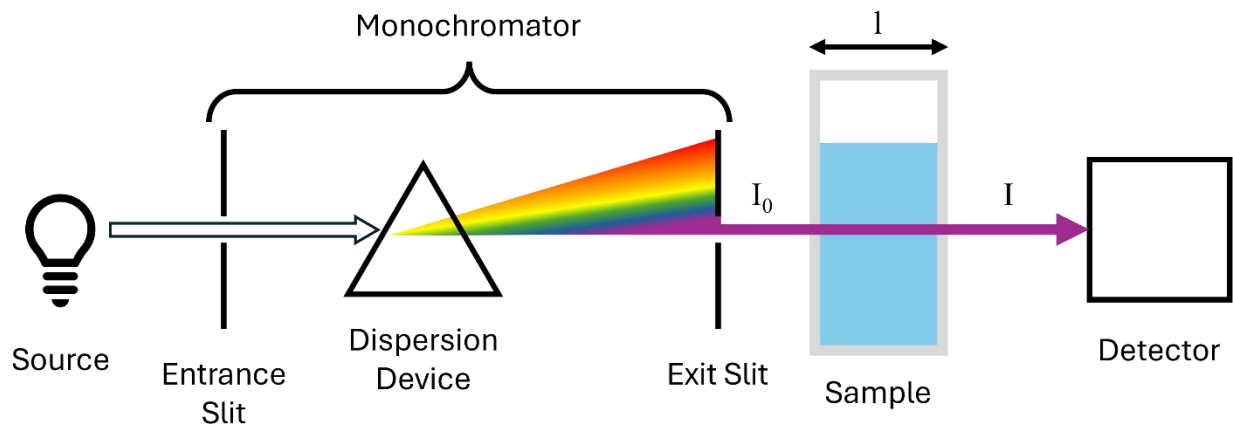


Figure 2-10. Schematic illustration of a diode array UV-vis spectrophotometer.

2.7. References

- [1] C.G. Zoski, *Handbook of electrochemistry*, Elsevier, Amsterdam, **2006**.
- [2] L. Wu, *The Electrochemistry of Hydrogen Peroxide on Uranium Dioxide and the Modelling of Used Nuclear Fuel Corrosion under Permanent Disposal Conditions*, Ph.D. Thesis, The University of Western Ontario, London, Canada, **2014**.
- [3] A.J. Bard, L.R. Faulkner, H.S. White, *Electrochemical methods: fundamentals and applications*, 3rd Edition, John Wiley & Sons, **2022**.
- [4] D.K. Gosser, *Cyclic voltammetry—simulation and analysis of reaction mechanisms*, Wiley VCH, New York, **1993**.
- [5] T. Martino, *Electrochemical and Corrosion Examination of Copper under Deep Geologic Conditions for the Application of Nuclear Waste Containers*, Ph.D. Thesis, University of Western Ontario, London, Canada, **2018**.
- [6] R. Petry, M. Schmitt, J. Popp, *Raman Spectroscopy—A Prospective Tool in the Life Sciences*, ChemPhysChem. (**2003**). 4 (1), 14-30.
- [7] R.P. Gunawardane, C.R. Arumainayagam, *Auger Electron Spectroscopy*, in: *Handbook of Applied Solid State Spectroscopy* [D.R. Vij (Ed.)], Springer US, Boston, MA, **2006**, pp. 451-483.
- [8] M. Razdan, D.S. Hall, P.G. Keech, D.W. Shoesmith, *Electrochemical reduction of hydrogen peroxide on SIMFUEL (UO₂) in acidic pH conditions*, Electrochim Acta. (**2012**). 83, 410-419.
- [9] R. Thomas, *Mass Analyzers: Quadrupole Technology*, in: *Practical Guide to ICP-MS and Other Atomic Spectroscopy Techniques: A Tutorial for Beginners*, CRC Press, **2023**, pp. 47-54.
- [10] I. Štefanić, J.A. LaVerne, *Temperature dependence of the hydrogen peroxide production in the γ -radiolysis of water*, J Phys Chem A. (**2002**). 106 (2), 447-452.

Chapter 3

3. Characterizing Natural Uranium Dioxide Specimens

3.1. Introduction

The primary concern for the release of radionuclides under permanent disposal conditions is the corrosion and dissolution of the UO_2 lattice. One factor controlling the corrosion and dissolution process is the degree of non-stoichiometry. While it does not affect the mechanism of these reactions, it could influence the anodic and cathodic kinetics. For undoped UO_2 , the degree of non-stoichiometry (x in UO_{2+x}) has previously been shown to influence the reactivity by up to two orders of magnitude [1-4].

The degree of non-stoichiometry can be estimated using an array of techniques. These techniques include, but are not limited to, measuring sample conductivity by electrical impedance measurements [5], characterizing changes in the matrix structure by Raman spectroscopy [6], determining the spatial distribution of measured differences in matrix structure using Raman mapping, characterizing the grain morphology of the sample surface [1], and measuring corrosion processes using electrochemical techniques [7].

As discussed in Chapter 1, UO_2 adopts a fluorite lattice structure with interstitial sites that can accommodate additional interstitial oxygen atoms (O_I) to form hyperstoichiometric $\text{U}^{\text{IV}}_{1-2x}\text{U}^{\text{V}}_{2x}\text{O}_{2+x}$. In the stoichiometric form, UO_2 is considered a Mott-Hubbard insulator with a band gap of ~ 5 eV [8-10]. However, the introduction of O_I atoms into the fluorite lattice structure occurs readily as the energy of formation for O_I is negative [11-16]. This leads to an increase in the electrical conductivity as a UO_{2+x} p-type semiconductor with a band gap of ~ 2 eV. Thus, the increase in conductivity (decrease in resistivity) is sensitive to the degree of non-stoichiometry, with the latter having been shown to enhance the reactivity of the oxide and accelerate corrosion [17].

The expected range for the stoichiometry of Canada Deuterium Uranium (CANDU) fuel is 2.001 to 2.007 [18]. However, depending on the efficiency of the reductive sintering process used during fabrication, higher levels of hyper-stoichiometry may occur at localized sites such as grain boundaries. This study investigates a series of CANDU UO_2 samples manufactured between 1965 and 2017 to determine the range of possible reactivities based on their physical and electrochemical properties. A knowledge of these properties is required to support the investigations of corrosion processes on the UO_2 surface.

3.2. Experimental

3.2.1. Electrode Materials and Preparation

Experiments were conducted on un-doped natural UO_2 electrodes cut as 2-3 mm-thick discs from commercial fuel pellets manufactured between 1965 and 2017 for use in CANDU reactors. Electrodes were prepared for three samples manufactured in January 2017, September 1990, and November 1977. The details of electrode preparation have been discussed previously [19]. The surface area of a single face of the disk ranged from 0.89 cm^2 to 1.65 cm^2 , and the thickness of the disk for each sample ranged from 1.5 cm to 6.1 cm. Prior to all experiments, the electrode was polished with 1200 grit SiC paper and then sonicated for 2 minutes in Type 1 H_2O (resistivity = 18.2 $\text{M}\Omega\cdot\text{cm}$) to remove polishing debris.

3.2.2. Resistance Measurements

Electrochemical impedance spectroscopy (EIS) was used to determine the resistance of each sample. The UO_2 disks were secured in the end of a piece of rubber tubing. Using a 20 mL glass vial, mercury (Hg) was used to create an electrical connection to both sides of the UO_2 disk. Conductive wire was placed in the Hg and connected to a potentiostat with a frequency response analyzer. Using a Solartron Model 1255 Frequency Response Analyser and ZView software (Scribner Associates), the sample was perturbed by a small-amplitude sinusoidal potential of ± 10 mV, and the sinusoidal current response was recorded. The input signal was applied to a frequency range of 10^5 to 10^{-3} Hz.

Using a modified version of Ohm's Law for an alternating current system, the applied potential ($E(\omega)$) can be related to the current output response ($i(\omega)$), where ω is the angular frequency and $Z(\omega)$ is the impedance, equation 3.1. In this study, impedance measurements are used to determine the impedance of samples at frequencies when the interface is in phase (1 Hz), and $Z(\omega)$ becomes a resistance, Figure 3-1.

$$E(\omega) = i(\omega) Z(\omega) \quad (3.1)$$

3.2.3. Raman Spectroscopy

Raman spectra were acquired using a Renishaw 2000 confocal Raman spectrometer (Renishaw, UK). Spectra were excited using a 50 mW He-Ne laser with a wavelength of 632.8 nm. The power of the laser beam was reduced to 50% to avoid heating effects. Spectra were recorded over the wavenumber range 150 to 1400 cm^{-1} . A Gaussian-Lorentzian peak model with a Shirley background correction was used to fit spectra. The deconvolution of the broad band between 500 and 700 cm^{-1} was performed as previously described [20, 21].

3.2.4. Scanning Electron Microscopy (SEM)

Images of the sample surface were collected using a Hitachi SU3500 Variable Pressure SEM. The electron beam was accelerated at 5 kV or 10 kV with a working distance of 10 mm to collect high-resolution images. All SEM micrographs were taken at surface locations where the grain structure was visible.

3.2.5. Electrochemical Cell and Equipment

All experiments were conducted using a standard 1 L three-electrode, three-compartment electrochemical cell. All potential measurements were recorded against a commercial saturated calomel reference electrode (SCE; 0.241 V vs. standard hydrogen electrode) [22]. The counter electrode was a 1 cm^2 Pt foil spot-welded to a platinum wire. The electrochemical cell was housed in a grounded Faraday cage to minimize interference from external electrical noise. Applied potentials and measured current responses were controlled,

recorded, and analyzed using a Solartron Model 1287 Multistat and CorrWare software (Scribner Associates), respectively.

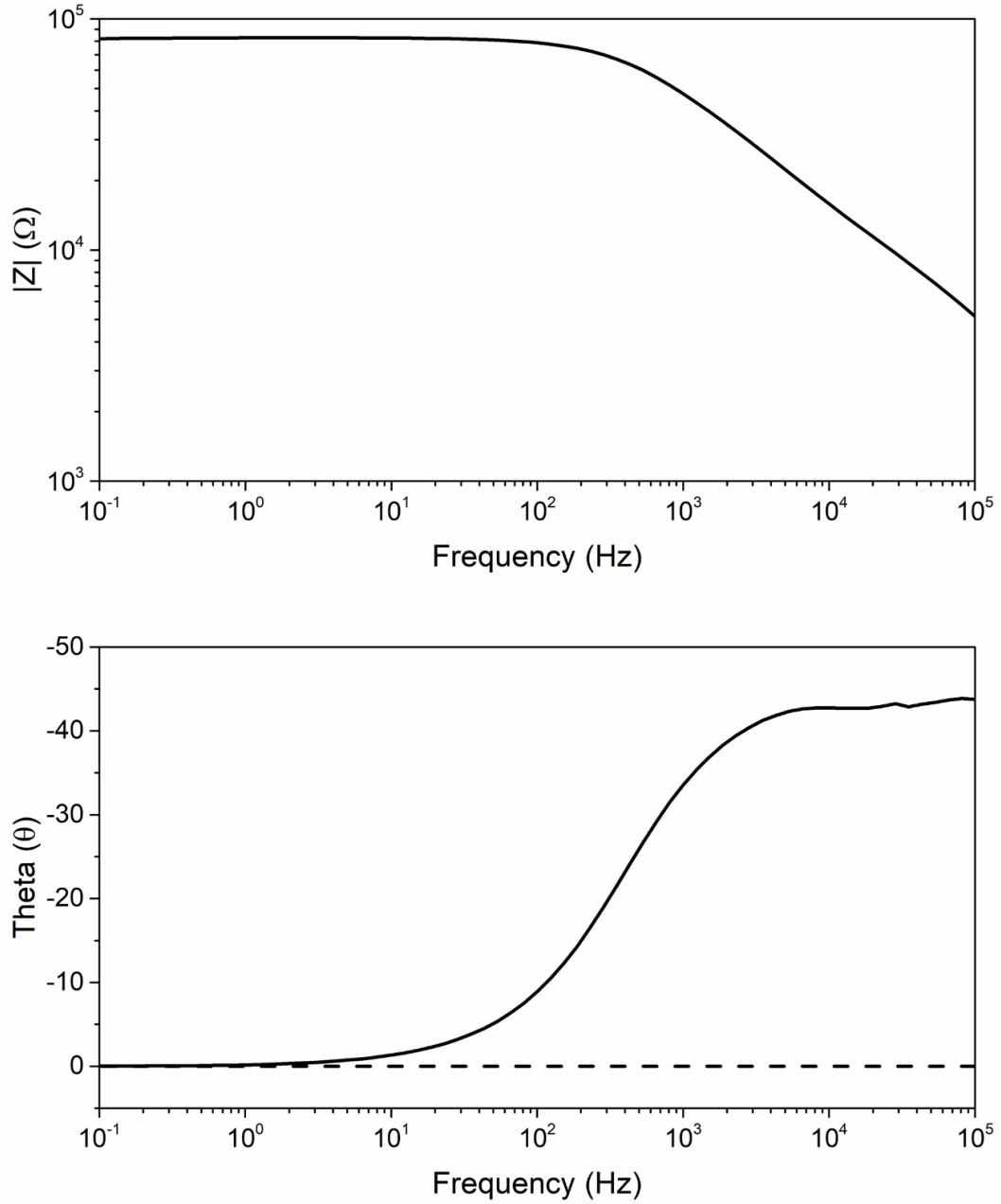


Figure 3-1. Bode plot collected for a UO₂ disk. The dashed line represents a phase angle of 0, where $Z(\omega)$ represents the resistance of the UO₂ disk.

3.2.6. Electrochemical Techniques

Prior to any experiment, the UO_2 electrode was potentiostatically polarized to -1200 mV (vs SCE) for 2 minutes. This procedure removed air-formed oxides from the surface, ensuring each experiment begins with a fresh surface.

Cyclic voltammetry (CV) experiments were performed to observe the electrochemical behaviour of the UO_2 sample. The potential was scanned from -1200 mV (vs SCE) to a positive limit of 250 mV (vs SCE) and back at a scan rate of $10 \text{ mV}\cdot\text{s}^{-1}$. The current interrupt method was used to compensate for electrode resistance.

3.3. Results and Discussion

Figure 3-2 shows the measured resistivity of all the UO_2 slices with respect to the year they were manufactured. The deviations in measured resistivity values were considerably higher for older pellets, suggesting a possible range of reactivities if it is related to the inverse of resistivity (conductivity). This variability could indicate that some pellets may not have been fully sintered to stoichiometric UO_2 during manufacturing. The measured resistivities range over three orders of magnitude for the pellets manufactured in 1991, 1990, 1997 and 1965.

Figure 3-3 shows the resistivities measured on slices taken from UO_2 pellets manufactured in 2017, 1992, 1990, 1977, and 1965, respectively. Given the observed values for a specimen will be that of the path of least resistance, the measured resistivity provides insight into the conductivity and, hence, non-stoichiometry of a sample and, therefore, the potential reactivity under redox conditions. Furthermore, by measuring the resistivity across a pellet, the uniformity of the sintering process can be assessed, and the reactivity at different points through the pellet determined. The pellets manufactured in 2017 and 1992 effectively show a constant resistivity throughout, suggesting the sintering process was consistent throughout the two pellets. The resistivity for the pellet from 2017 was up to, and sometimes over, one order of magnitude greater, indicating that the sample from 2017 was effectively reduced during sintering. The pellets from 1990, 1977, and 1965 show a much greater distribution of resistivities throughout the pellet, in some cases ranging over approximately three orders of

magnitude (1990). Though there is greater variability in the resistivity of the pellet slices, there is no clear trend in the resistivity through the pellet. These variations suggest that the reactivity of these pellets may vary throughout.

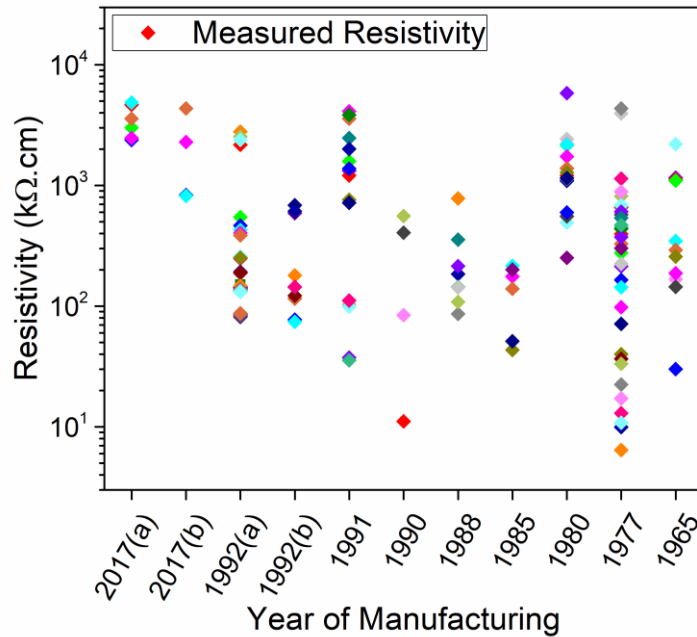


Figure 3-2. Measured resistivities for un-doped UO₂ samples manufactured between 1965 and 2017. Individual resistivity measurements are shown for each sample.

Raman spectroscopy can be used to assess the influence of defects and O_I on the UO₂ matrix [20]. An example of a deconvoluted Raman spectra is shown in Figure 3-4. The peak at 450 cm⁻¹ is attributed to the T_{2g} O-U^{IV} stretching mode and is indicative of the undisturbed fluorite lattice [23], while the broad band between 500 cm⁻¹ and 700 cm⁻¹ includes responses which reflect defect structures within the oxide. In fitting the spectra, the peak at 450 cm⁻¹ was treated as Lorentzian with the contributions to the wide band treated as Gaussian. While the peak at 450 cm⁻¹ is dominant, confirming the fluorite structure, deconvolution of the broad band reveals two additional contributions. The peak at 575 cm⁻¹ has been assigned as

the first-order L-O phonon, with its intensity thought to indicate a loss of translational symmetry at a vacancy site, which could be a self-trapped Frenkel defect and/or an O vacancy [24-28] in a close-to-perfect fluorite lattice [23]. The peak, at 630 cm^{-1} , has been assigned to an A_{1g} stretching mode attributed to the formation of cuboctahedral clusters formed when sufficient O_I are incorporated into the fluorite structure [20, 26, 29], indicating a degree of non-stoichiometry, which would influence the local conductivity and, hence, the local reactivity.

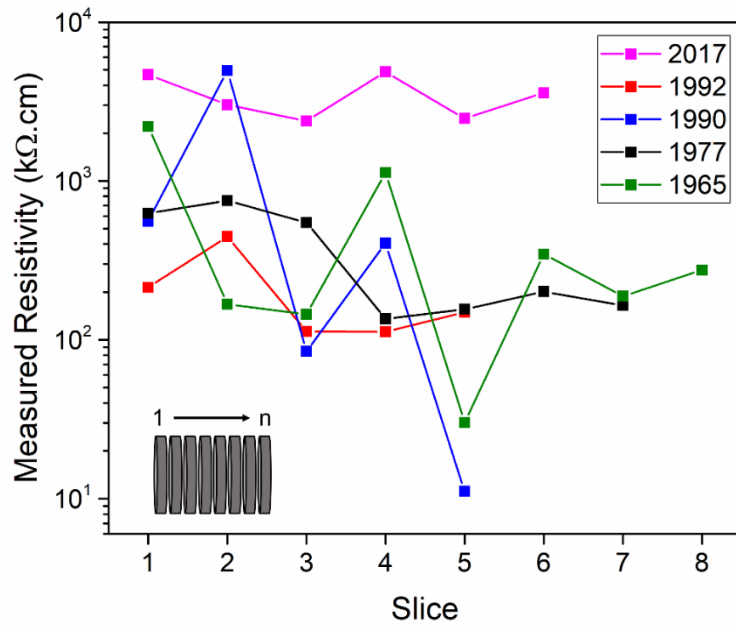


Figure 3-3. Measured resistivities with respect to individual slices from un-doped UO_2 pellets manufactured between 1965 and 2017. The schematic represents the numbering format used for slices from a single pellet.

Figure 3-5 shows a series of Raman spectra collected at regular spacing intervals across the surface of specimens with resistivities ranging over three orders of magnitude. Normalizing the T_{2g} peak allows a qualitative assessment of the bands in the 500 cm^{-1} to 700 cm^{-1} range.

Peaks were observed at both 575 cm^{-1} and 630 cm^{-1} , commonly together, indicating locations with both defects. This suggests a general distribution of localized lattice distortions and areas of non-stoichiometry regardless of resistivity.

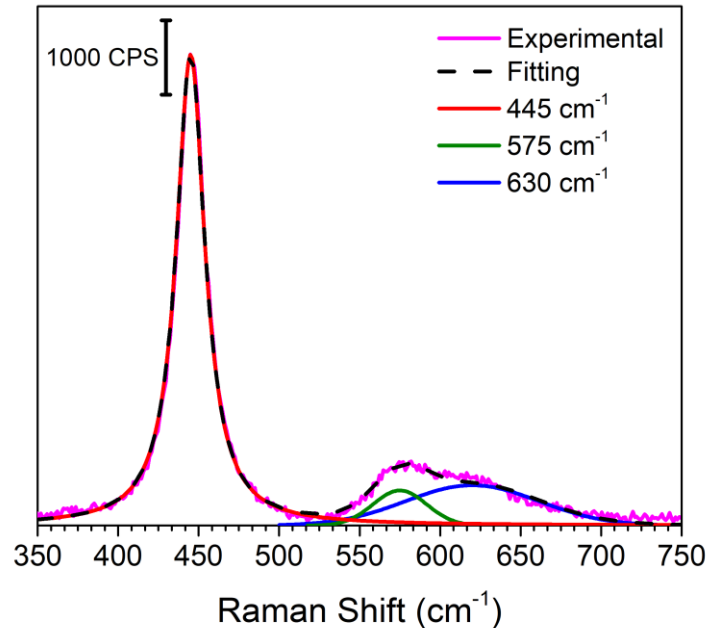


Figure 3-4. The deconvoluted Raman spectrum of an un-doped UO₂ sample demonstrates the peak deconvolution into contributions from bands at $\sim 445\text{ cm}^{-1}$, 575 cm^{-1} , and 630 cm^{-1} .

Since non-stoichiometric locations are expected to be the most reactive, Raman maps were collected for the T_{2g} (450 cm^{-1}) and A_{1g} (630 cm^{-1}) peaks. Maps and the corresponding optical images were recorded on specimens covering the fabrication range from 1965 to 2017. Given the limited surface preparation of the specimens (described in section 3.2.1.) and limitations of the instrument's optical microscope, having the whole of the surfaces shown in focus was not possible. Consequently, a smaller area was selected for Raman mapping, identified by the green boxes in Figure 3-6(a) to (e). Though it is difficult to determine the grain size using optical microscopy, it appears consistent for all samples, as shown in Figure 3-7.

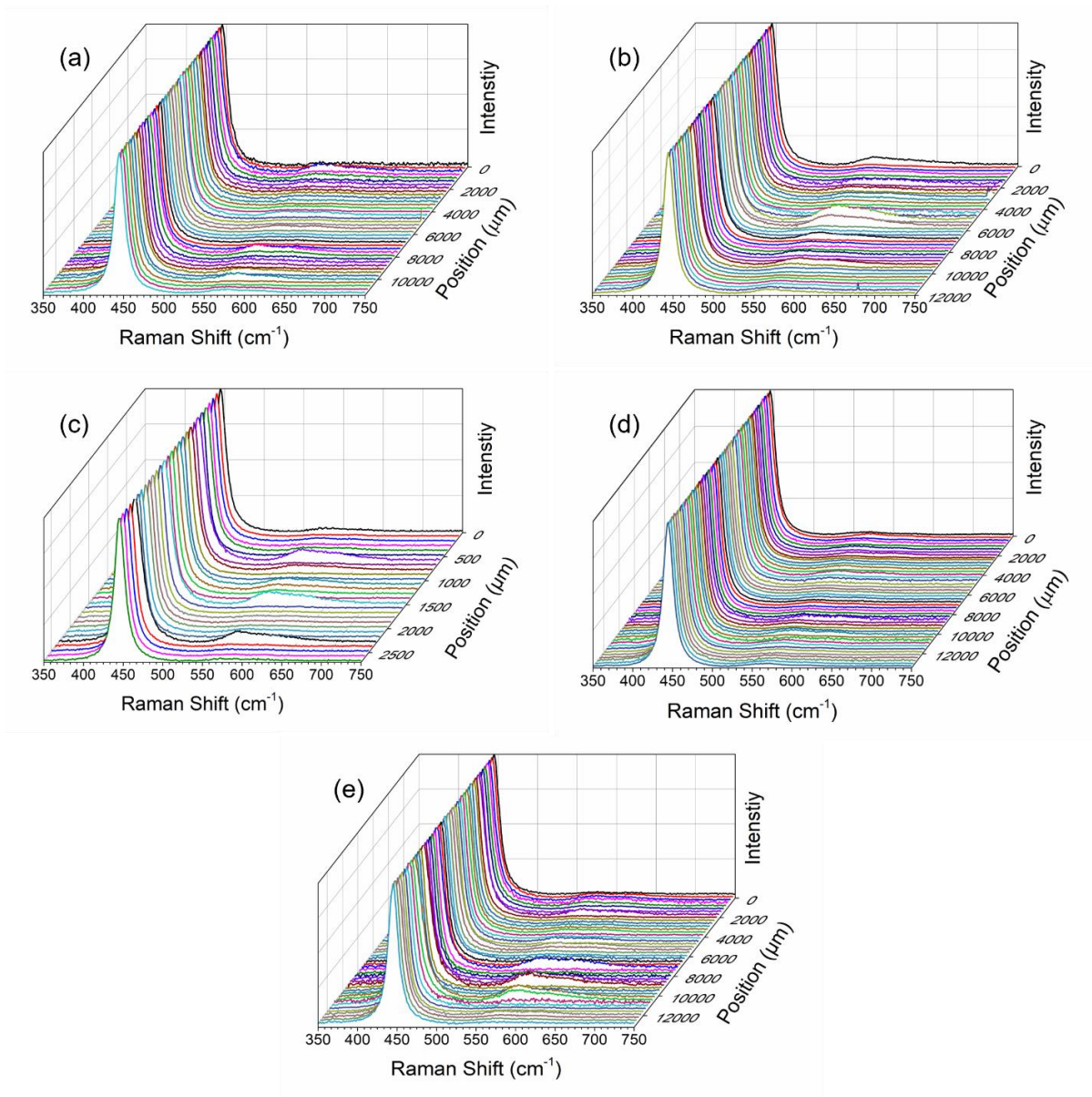


Figure 3-5. Raman spectra, collected across the sample surface, show defect distortion distribution across the sample surfaces. The peak at 445 cm^{-1} was normalized to 1 to compare the intensity of lattice distortions at 630 cm^{-1} . Samples were manufactured in (a) 2017, (b) 1992, (c) 1990, (d) 1977, and (e) 1965.

Figure 3-6(f-j) shows the Raman maps collected from the previously discussed green rectangles, Figure 3-6(a-e). The areas with a strong T_{2g} peak, indicating a stoichiometric lattice structure, are shown in red. In contrast, the areas with a strong A_{1g} peak, indicating a non-stoichiometric location, are shown in blue, with overlapping areas shown in purple. The black regions are out of focus, resulting in an insufficient signal.

For all but one specimen, a separation was observed between the defect-free T_{2g} lattice structure and the non-stoichiometric A_{1g} lattice structure. The exception was the 2017 specimen, for which a clear separation of sites was not observed, Figure 3-6(f). The separation observed for the other specimens suggests the presence of variations in the non-stoichiometry between either individual grains or grain boundaries. Any attempt to further distinguish between these types of sites is thwarted by the lack of resolution of the optical images (Figure 3-6(a) to (e)). Furthermore, the distribution of the T_{2g} and A_{1g} signals observed in the Raman maps suggests that the reactivity could vary from grain to grain. This agrees with previous studies using Raman analysis on hyperstoichiometric UO_2 samples that correlated lattice defects with specific grains [20, 26].

Coupling Raman spectroscopy and SEM, He et al. [1] found a correlation between the Raman spectra and the observed grain structure in SEM micrographs recorded on grains with known degrees of non-stoichiometry. Three distinct correlations were made between the observed grain morphology and the degree of non-stoichiometry [17]:

- Grains with featureless surfaces were near stoichiometric;
- Faceted grains with a shallow, stepped pattern were slightly hyperstoichiometric ($\sim UO_{2.15}$);
- Spiral-like grains with a large, stepped pattern were more hyperstoichiometric ($\sim UO_{2.32}$)

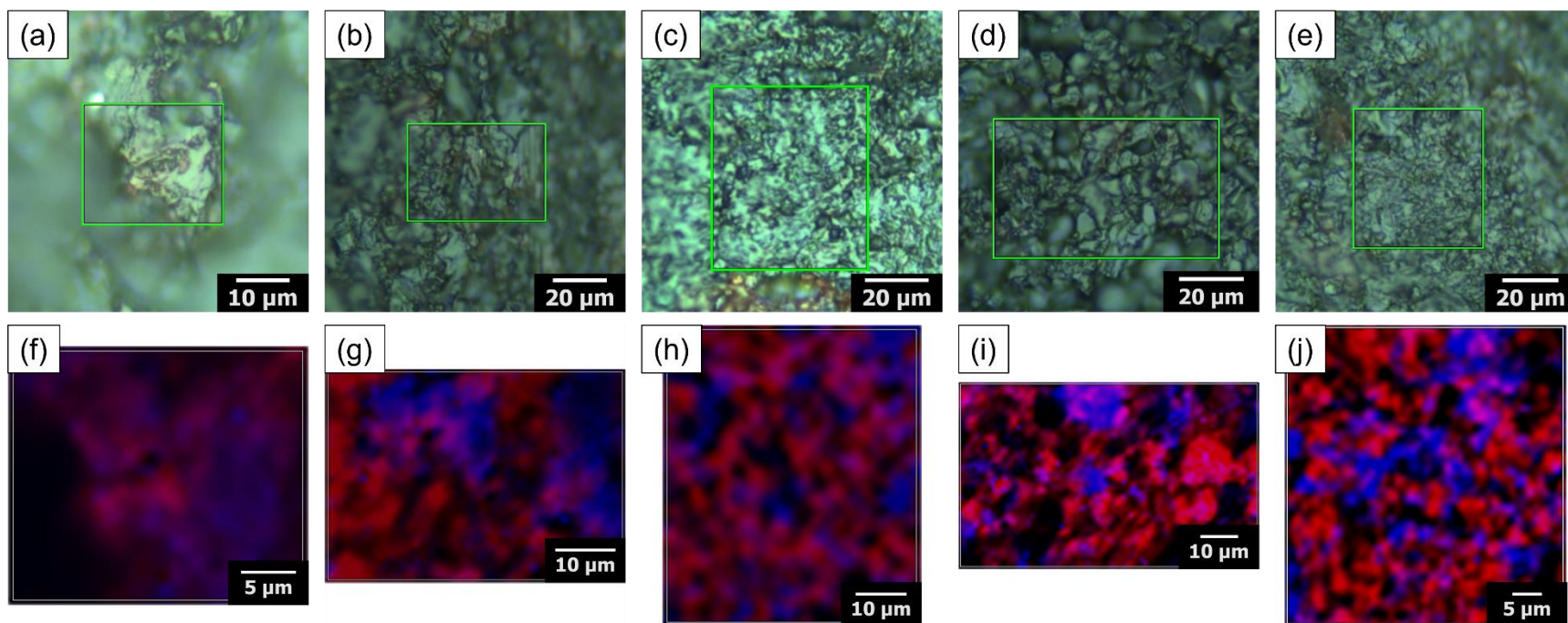
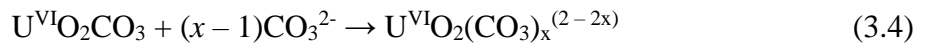
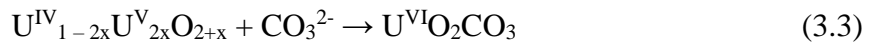


Figure 3-6. Optical images (a) to (e) of the UO₂ surface, with the area of analysis highlighted (green rectangle). Raman mapping (f) to (j) of the UO₂ surface with the overlay of the T_{2g} (red) and A_{1g} (blue) distribution across the sample surface. The samples were manufactured in 2017 (a and f), 1990 (b and g), 1992 (c and h), 1977 (d and i), and 1965 (e and j).

Near stoichiometric, smooth, featureless grains were observed on samples manufactured post-1992, Figure 3-7(a-c), with the most uniform structure observed from the 2017 specimen with the highest and most uniform resistivity, Figure 3-3. The most variable structure with both well-defined grains and nodular clusters, suggesting incomplete sintering, was observed for the 1990 specimen (Figure 3-7c), which also exhibited resistivities that varied by almost three orders of magnitude. The 1977 specimen (Figure 3-7d) exhibited grains with spiral-like patterns, thought to indicate hyperstoichiometry. Although uniform throughout, the resistivity of this specimen is quite low, Figure 3-3. Based on these observations, it is difficult to define any direct correlation between resistivity, the degree of non-stoichiometry (as indicated by the Raman analyses), and the surface morphology of the specimens.

Cyclic voltammetry was used to investigate the influence of resistivity, and hence the degree of non-stoichiometry, on the electrochemical reactivity of specimens. Figure 3-8 to 3-10 show CVs recorded on specimens with measured low (10 k Ω .cm, 2017), medium (50 k Ω .cm, 1977), and high (2500 k Ω .cm, 2017) resistivities with the current interrupt technique used to compensate the bulk resistance of the specimens. In a previous study [7], it has been shown that the oxidation/dissolution of UO₂ in a carbonate-containing solution involves two stages: the oxidation of a thin layer (a few nanometers) of the surface (reaction 3.2) followed by further oxidation to an adsorbed uranyl carbonate layer (reaction 3.3) and the chemical dissolution of the adsorbed species (reaction 3.4).



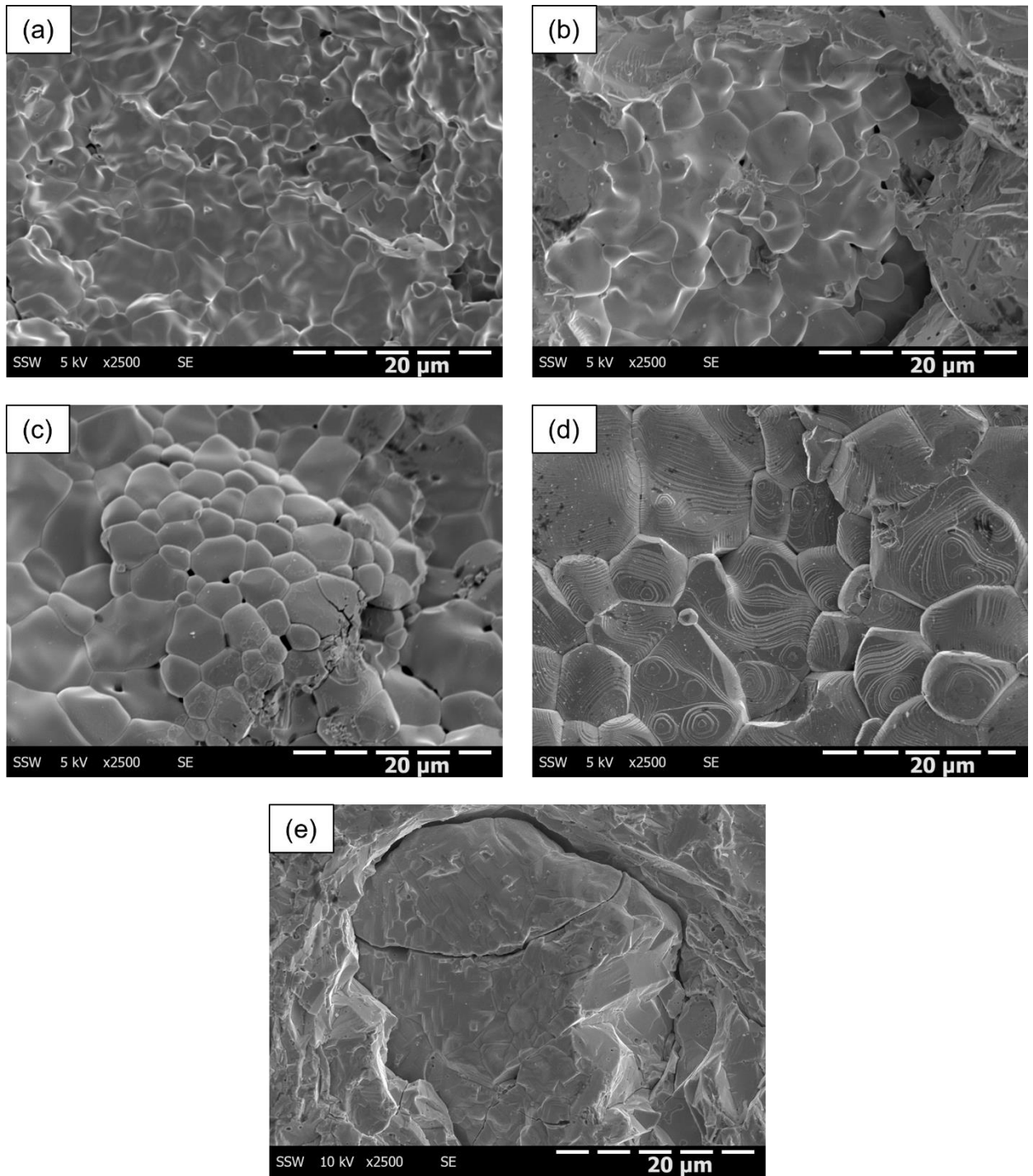


Figure 3-7. SEM micrographs showing different grain morphology of UO_2 samples with varying measured resistivities. Samples were manufactured in (a) 2017, (b) 1992, (c) 1990, (d) 1977, and (e) 1965.

For the low-resistivity specimen, Figure 3-8, a series of oxidation (forward scan) and reduction (reverse scan) processes were observed, confirming that the bulk resistance of the specimen was compensated, enabling observation of the electrochemical and chemical surface processes (reactions 3.2 to 3.4). Three distinct stages of anodic oxidation (Figure 3-8, labelled 1, 2, and 3) were observed on the forward scan and a cathodic reduction process (Figure 3-8, labelled 4) on the reverse scan. These observations are consistent with those previously observed on SIMFUELS [7, 30, 31] and rare earth-doped UO_2 [32-34], a specimen with a known low degree of non-stoichiometry ($\text{UO}_{2.002}$) [33], and on an uncharacterized CANDU fuel pellet [35, 36]. This ability to observe the surface reactions confirmed a conductive pathway exists within the specimen.

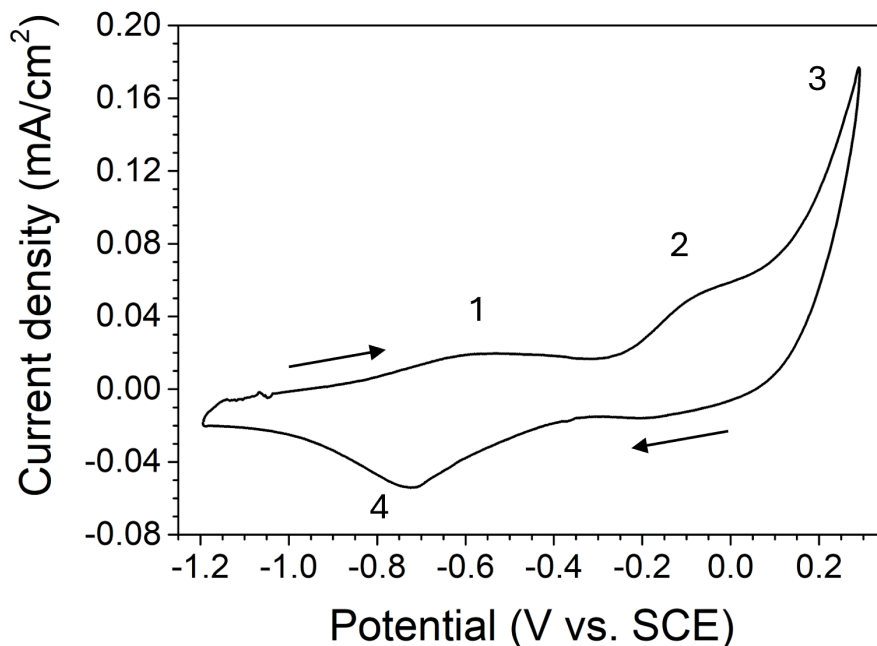


Figure 3-8. Cyclic voltammogram recorded on a UO_2 electrode manufactured in 1990 with a resistivity of $10 \text{ k}\Omega\cdot\text{cm}$, in Ar-purged $0.1 \text{ mol}\cdot\text{L}^{-1} \text{ NaCl} + 0.05 \text{ mol}\cdot\text{L}^{-1} \text{ HCO}_3^-/\text{CO}_3^{2-}$ solution adjusted to pH 9.5. Arrows represent the scan direction.

The observation of a current in potential region 1 (Figure 3-8) can be attributed to the oxidation of hyperstoichiometric surface locations which have been shown to oxidize at potentials below the equilibrium potential for the oxidation of the stoichiometric UO_2 matrix [17]. The shallow, ill-defined peak observed indicates the presence of a range of hyperstoichiometric compositions with different reactivities. It has been suggested, but not demonstrated, that hyperstoichiometry is located within grain boundaries [7, 36].

The current observed in region 2 has been shown to be due to the onset of the oxidation and dissolution of stoichiometric UO_2 , which would be thermodynamically feasible at potentials ≥ -0.4 V (vs SCE) [33], with the plateau in region 2 attributed to coverage by $\text{U}^{\text{VI}}\text{O}_2\text{CO}_3$ before the onset of extensive dissolution in region 3 [37]. Although not particularly relevant to the present study, region 4 is due to the reduction of surface species formed in regions 2 and 3 and the partial reduction of the oxidized sites formed in region 1.

Figure 3-9 shows the CV recorded for the specimen with a medium resistivity (50 $\text{k}\Omega\cdot\text{cm}$, 1977). Although similar anodic and cathodic peaks are observed, suggesting a similar sequence of reactions to those observed on the low-resistivity specimen, they are less well-defined than those observed on the lower-resistivity specimen, Figure 3-8, and the CV is tilted. Therefore, the values are unreliable as the specimen's bulk resistance is not fully compensated for by the potentiostat. Despite this qualitative uncertainty, both the anodic and cathodic currents recorded were significantly larger than observed on the lower resistivity specimen. A comparison of the currents in regions 1 and 2 shows the sub-thermodynamic oxidation of hyperstoichiometric locations (region 1) was more extensive than that of the matrix (region 2). Additionally, the current attributed to oxide reduction (region 4) was considerably larger. Both these features are consistent with the observations of He, et al. [17] and Badley and Shoesmith [38] who attributed the more extensive oxidation to the increased mobility of O_i within the hyperstoichiometric regions compared to within stoichiometric regions of the oxide surface. This would be consistent with the presence of the spiral-like features observed on the specimen surface which were shown to be an indication of hyperstoichiometry [17] and supports the suggestion in the Raman maps (Figure 3-6(d) and (i)) that distinct grain size regions of the surface yield a significant signal at 630 cm^{-1} due to

hyperstoichiometry. That the specimen from 1977 exhibited a larger resistivity despite appearing more hyperstoichiometric than the specimen from 1990 would be consistent with the more localized nature of the hyperstoichiometry as observed by He, et al. [17]. This would lead to a less interlinked conductivity network throughout the specimen and a correspondingly higher resistivity. This separation appeared visible in the Raman maps, where the map for the medium resistivity specimen (1977) exhibited more distinctly red and blue surface locations compared to the low-resistivity specimen (1990), for which purple locations are more prominent.

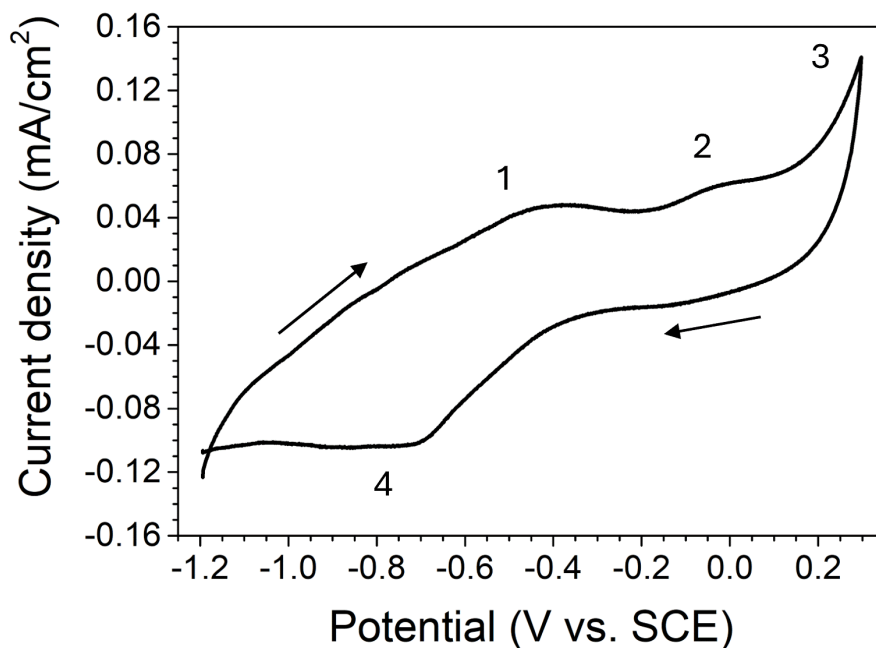


Figure 3-9. Cyclic voltammogram recorded on a UO₂ electrode manufactured in 1977 with a resistivity of 50 kΩ.cm, in Ar-purged 0.1 mol.L⁻¹ NaCl + 0.05 mol.L⁻¹ HCO₃⁻ /CO₃²⁻ solution adjusted to pH 9.5.

For the specimen with the highest resistivity (2500 k Ω .cm, 2017), the current recorded was very low, and the response ohmic, Figure 3-10, confirming the specimen resistance was dominant and uncorrected by the potentiostat. Consequently, any surface reactivity was obscured. The extremely high resistivity confirms the absence of hyperstoichiometric conductive pathways through the oxide.

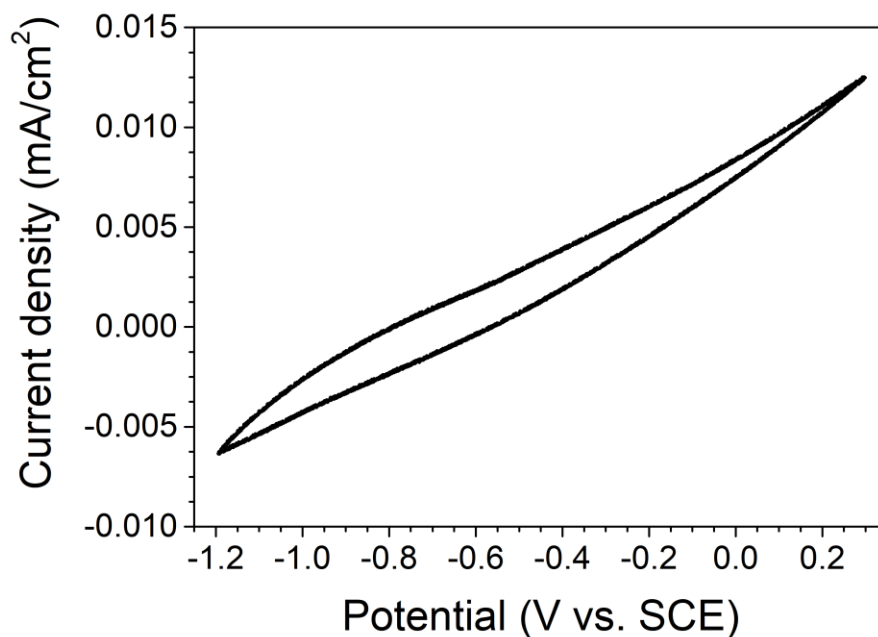


Figure 3-10. Cyclic voltammogram recorded on a UO₂ electrode manufactured in 2017 with a resistivity of 2500 k Ω .cm, in Ar-purged 0.1 mol.L⁻¹ NaCl + 0.05 mol.L⁻¹ HCO₃⁻ /CO₃²⁻ solution adjusted to pH 9.5.

3.4. Summary and Conclusions

The resistivities of a series of CANDU UO₂ pellets manufactured between 1965 and 2017 were measured using impedance spectroscopy, and the locations of residual hyperstoichiometry were investigated using Raman spectroscopy and SEM. Measured

resistivities show variations ranging over two to three orders of magnitude depending on when the fuel pellets were manufactured, indicating significant variations in reductive sintering efficiencies.

Both Raman and SEM analyses indicate the presence of distinct areas of hyperstoichiometry. In some pellets (1990), this correlated with low resistivity values, indicating the presence of a conductive network throughout the pellet. The presence of such a network was confirmed electrochemically. When the bulk resistance of the specimen was compensated, the surface electrochemical/chemical reactions on the oxide surface were distinguishable electrochemically.

For specimens which appeared to exhibit distinctly hyperstoichiometric and stoichiometric grains (1977), detected by Raman spectroscopy and SEM, the resistivity was higher, but the surface reactivity, detected electrochemically, was also higher. This appears to be due to a less interlinked conductivity network throughout the specimen due to the hyperstoichiometry being localized within individual grains rather than distributed along inter-connected grain boundaries.

For the specimen from 2017, which exhibited an extremely high resistivity, the matrix was free of interconnected hyperstoichiometric locations. Consequently, an electrochemical attempt to determine surface reactivity was unsuccessful.

3.5. Acknowledgements

This work was jointly funded by the Natural Sciences and Engineering Research Council of Canada and the Nuclear Waste Management Organization through Alliance Grant ALLRP561193-20. Surface Science Western is acknowledged for the use of their instruments.

3.6. References

- [1] H. He, Z. Qin, D.W. Shoesmith, *Characterizing the relationship between hyperstoichiometry, defect structure and local corrosion kinetics of uranium dioxide*, *Electrochim Acta*. (2010). 56 (1), 53-60.
- [2] J.S. Betteridge, N.A.M. Scott, D.W. Shoesmith, L.E. Bahen, W.H. Hocking, P.G. Lucuta, *Effects of hyperstoichiometry and fission products on the electrochemical reactivity of UO₂ nuclear fuel*, Atomic Energy of Canada Limited, AECL-11647, COG-96-331-1, (1997).
- [3] H. He, Z. Ding, D.W. Shoesmith, *The determination of electrochemical reactivity and sustainability on individual hyper-stoichiometric UO_{2+x} grains by Raman microspectroscopy and scanning electrochemical microscopy*, *Electrochem Commun.* (2009). 11 (8), 1724-1727.
- [4] Y. Kumagai, A. Barreiro-Fidalgo, M. Jonsson, *Impact of stoichiometry on the mechanism and kinetics of oxidative dissolution of UO₂ induced by H₂O₂ and gamma-irradiation*, *J Phys Chem C*. (2019). 123 (15), 9919-9925.
- [5] G.J. Hyland, J. Ralph, *Electronic contributions to the high-temperature thermophysical properties of UO_(2+x): a critical analysis*, *High Temp-High Pressures*. (1983). 15 (2), 179-190.
- [6] H. He, M. Broczkowski, K. O'Neil, D. Ofori, O. Semenikhin, D. Shoesmith, *Corrosion of nuclear fuel (UO₂) inside a failed nuclear waste container*, Nuclear Waste Management Organization, NWMO TR-2012-09, Toronto, ON, Canada (2012).
- [7] B.G. Santos, J.J. Noël, D.W. Shoesmith, *The effect of pH on the anodic dissolution of SIMFUEL (UO₂)*, *J Electroanal Chem.* (2006). 586 (1), 1-11.
- [8] P. Winter, *The electronic transport properties of UO₂*, *J Nucl Mater.* (1989). 161 (1), 38-43.
- [9] S.M. Gilbertson, T. Durakiewicz, G.L. Dakovski, Y. Li, J.-X. Zhu, S.D. Conradson, S.A. Trugman, G. Rodriguez, *Ultrafast Photoemission Spectroscopy of the Uranium Dioxide UO₂ Mott Insulator: Evidence for a Robust Energy Gap Structure*, *Phys Rev Lett.* (2014). 112 (8), 087402.
- [10] L.E. Roy, T. Durakiewicz, R.L. Martin, J.E. Peralta, G.E. Scuseria, C.G. Olson, J.J. Joyce, E. Guziewicz, *Dispersion in the Mott insulator UO₂: A comparison of photoemission spectroscopy and screened hybrid density functional theory*, *J Comput Chem.* (2008). 29 (13), 2288-2294.
- [11] J.-P. Crocombette, F. Jollet, L.T. Nga, T. Petit, *Plane-wave pseudopotential study of point defects in uranium dioxide*, *Phys Rev B: Condens Matter.* (2001). 64 (10), 104107.

- [12] M. Freyss, T. Petit, J.-P. Crocombette, *Point defects in uranium dioxide: Ab initio pseudopotential approach in the generalized gradient approximation*, J Nucl Mater. (2005). 347 (1-2), 44-51.
- [13] H.Y. Geng, Y. Chen, Y. Kaneta, M. Iwasawa, T. Ohnuma, M. Kinoshita, *Point defects and clustering in uranium dioxide by LSDA+ U calculations*, Phys Rev B: Condens Matter. (2008). 77 (10), 104120.
- [14] F. Gupta, G. Brillant, A. Pasturel, *Correlation effects and energetics of point defects in uranium dioxide: a first principle investigation*, Philos Mag. (2007). 87 (17), 2561-2569.
- [15] P. Nerikar, T. Watanabe, J.S. Tulenko, S.R. Phillpot, S.B. Sinnott, *Energetics of intrinsic point defects in uranium dioxide from electronic-structure calculations*, J Nucl Mater. (2009). 384 (1), 61-69.
- [16] R. Ngayam-Happy, M. Krack, A. Pautz, *Effects of stoichiometry on the defect clustering in uranium dioxide*, J Phys-Condens Mat. (2015). 27 (45), 455401.
- [17] H. He, R.K. Zhu, Z. Qin, P. Keech, Z. Ding, D.W. Shoesmith, *Determination of local corrosion kinetics on hyper-stoichiometric UO_{2+x} by scanning electrochemical microscopy*, J Electrochem Soc. (2009). 156 (3), C87-C94.
- [18] H. Smith, J. Tait, R. Von Massow, *Radioactive decay properties of Bruce "A" CANDU™ UO_2 fuel and fuel recycle waste*, Atomic Energy of Canada Ltd., AECL-9072, Pinawa, Manitoba (1987).
- [19] M. Razdan, *Electrochemical and Surface Compositional Studies on Uranium Dioxide*, PhD Thesis, University of Western Ontario, London, Ontario, 2013.
- [20] H. He, D.W. Shoesmith, *Raman spectroscopic studies of defect structures and phase transition in hyper-stoichiometric UO_{2+x}* , Phys Chem Chem Phys. (2010). 12 (28), 8109-8118.
- [21] M. Razdan, D.W. Shoesmith, *Influence of trivalent-dopants on the structural and electrochemical properties of uranium dioxide (UO_2)*, J Electrochem Soc. (2014). 161 (3), H105-H113.
- [22] C.G. Zoski, *Handbook of electrochemistry*, Elsevier, Amsterdam, 2006.
- [23] D. Manara, B. Renker, *Raman spectra of stoichiometric and hyperstoichiometric uranium dioxide*, J Nucl Mater (2003). 321 (2), 233-237.
- [24] P.R. Graves, *Raman Microprobe Spectroscopy of Uranium Dioxide Single Crystals and Ion Implanted Polycrystals*, Appl Spectrosc. (1990). 44 (10), 1665-1667.

- [25] G. Guimbretière, L. Desgranges, A. Canizarès, G. Carlot, R. Caraballo, C. Jégou, F. Duval, N. Raimboux, M.R. Ammar, P. Simon, *Determination of in-depth damaged profile by Raman line scan in a pre-cut He²⁺ irradiated UO₂*, Appl Phys Lett. (2012). 100 (25).
- [26] Z. Talip, T. Wiss, P.E. Raison, J. Paillier, D. Manara, J. Somers, R.J.M. Konings, *Raman and X-ray Studies of Uranium–Lanthanum-Mixed Oxides Before and After Air Oxidation*, J Am Ceram Soc. (2015). 98 (7), 2278-2285.
- [27] L. Desgranges, G. Guimbretière, P. Simon, C. Jégou, R. Caraballo, *A possible new mechanism for defect formation in irradiated UO₂*, Nucl Instrum Methods Phys Res Sect B. (2013). 315, 169-172.
- [28] K. Rickert, T.A. Prusnick, M.M. Kimani, E.A. Moore, C.A. Merriman, J.M. Mann, *Assessing UO₂ sample quality with μ -Raman spectroscopy*, J Nucl Mater. (2019). 514, 1-11.
- [29] L. Desgranges, G. Baldinozzi, P. Simon, G. Guimbretière, A. Canizares, *Raman spectrum of U₄O₉: a new interpretation of damage lines in UO₂*, J Raman Spectrosc. (2012). 43 (3), 455-458.
- [30] L. Wu, D.W. Shoesmith, *An electrochemical study of H₂O₂ oxidation and decomposition on simulated nuclear fuel (SIMFUEL)*, Electrochim Acta. (2014). 137, 83-90.
- [31] Z. Zhu, L. Wu, J.J. Noël, D.W. Shoesmith, *Anodic reactions occurring on simulated spent nuclear fuel (SIMFUEL) in hydrogen peroxide solutions containing bicarbonate/carbonate – The effect of fission products*, Electrochim Acta. (2019). 320.
- [32] M. Razdan, D.W. Shoesmith, *The electrochemical reactivity of 6.0 wt% Gd-Doped UO₂ in aqueous carbonate/bicarbonate solutions*, J Electrochem Soc. (2014). 161 (4), H225-H234.
- [33] N. Liu, H. He, J.J. Noël, D.W. Shoesmith, *The electrochemical study of Dy₂O₃ doped UO₂ in slightly alkaline sodium carbonate/bicarbonate and phosphate solutions*, Electrochim Acta. (2017). 235, 654-663.
- [34] N. Liu, J. Kim, J. Lee, Y.-S. Youn, J.-G. Kim, J.-Y. Kim, J.J. Noël, D.W. Shoesmith, *Influence of Gd Doping on the Structure and Electrochemical Behavior of UO₂*, Electrochim Acta. (2017). 247, 496-504.
- [35] D.W. Shoesmith, *Fuel corrosion processes under waste disposal conditions*, J Nucl Mater. (2000). 282 (1), 1-31.
- [36] B.G. Santos, H.W. Nesbitt, J.J. Noel, D.W. Shoesmith, *X-ray photoelectron spectroscopy study of anodically oxidized SIMFUEL surfaces*, Electrochim Acta. (2004). 49 (11), 1863-1873.

[37] P.G. Keech, J.S. Goldik, Z. Qin, D.W. Shoesmith, *The anodic dissolution of SIMFUEL (UO₂) in slightly alkaline sodium carbonate/bicarbonate solutions*, *Electrochim Acta.* (2011). 56 (23), 7923-7930.

[38] M. Badley, D.W. Shoesmith, *The corrosion/dissolution of used nuclear fuel in a deep geologic repository*, Nuclear Waste Management Organization, NWMO-TR-2022-09, Toronto, Canada (2022).

Chapter 4

4. Influence of Resistivity on the Dissolution of Uranium Dioxide in Peroxide-Containing Environments

4.1. Introduction

The development of disposal procedures for high-level nuclear waste has resulted in the internationally accepted approach of a deep geological repository (DGR). The use of a multiple barrier system will isolate and contain the fuel. The fuel will be sealed within a corrosion-resistant Cu-coated steel container surrounded by a bentonite clay buffer that seals the container within the host rock. Although the container is expected to remain intact until radiation levels decay to natural levels [1, 2], it is necessary to assess the possible consequences of container failure when the spent fuel could come in contact with groundwater. This has led to an extensive international effort to determine the behaviour of spent fuel under a range of possible DGR conditions which could lead to the release of harmful radionuclides [3-9].

The majority of radionuclides are contained within the fuel matrix [10, 11], and their release will be determined by the corrosion or dissolution rates of the uranium dioxide (UO_2) matrix [3]. Since the solubility of U in the U^{VI} state is many orders of magnitude higher than in the U^{IV} state [12], the redox condition of the groundwater in contact with the fuel is important. While any dissolved O_2 originally present in the groundwater will be rapidly consumed by reactions with minerals and organic material in the clay and by corrosion of the copper/steel container [13], the α -radiolysis of water within a failed container can result in the generation of oxidants [14]. Of the oxidants produced, H_2O_2 is dominant with its cathodic reduction in support of the anodic oxidation of the fuel occurring ~ 200 times faster than that of O_2 [15]. While H_2O_2 acts as a cathodic reagent on the UO_2 surface, its behaviour is complicated since it can also rapidly decompose on oxides to produce the slower reacting O_2 [16-18], as illustrated in Figure 4-1.

addition, repeat exposure to H₂O₂ solutions has been shown to dramatically decrease the anodic dissolution of UO₂, while the decomposition of H₂O₂ proceeds unimpeded, regardless of sample doping [29].

In this study, the influence of conductivity of a number of UO₂ specimens on their reactions involving H₂O₂ was investigated using a combination of electrochemical, and solution and surface analytical techniques. The primary goal was to determine whether the resistivity of UO₂ (the inverse of its conductivity) exerted any influence on the kinetics of reactions of H₂O₂, the key radiolytic oxidant likely to drive UO₂ corrosion, and hence radionuclide release under disposal conditions. To this end, experiments were conducted on CANDU fuel specimens with a distribution of resistivities produced over a 40-year period (1977-2017) of fuel pellet production. The behaviour observed was expected to be representative of the variability in fuel reactivity in a Canadian DGR.

4.2. Experimental

4.2.1. Electrode Materials and Preparation

Experiments were conducted on un-doped natural UO₂ electrodes cut as 2mm-thick discs from commercial fuel pellets manufactured in January 2017, September 1990, and November 1977. The details of electrode preparation have been discussed previously [30]. The surface area of the single exposed face of a disc was 0.89 cm², 1.16 cm², and 1.65 cm² respectively. The resistivity of UO₂ is known to be sensitive to the degree of stoichiometry (x in UO_{2+x}) [21, 31-34]. The measured value for the specimens used were approximately 2500 kΩ.cm (2017), 10 kΩ.cm (1990), and 50 kΩ.cm (1977). The large resistivity of the fuel pellet manufactured in 2017 suggests the pellet is stoichiometric, while the lower resistivities of the pellets manufactured in 1990 and 1977 are close to that measured on a UO_{2.002} specimen, suggesting the pellets may have had slight degrees of non-stoichiometry [35]. Prior to an experiment, the electrode was polished with 1200 grit SiC paper and then sonicated for 2 minutes in Type 1 H₂O (resistivity = 18.2 MΩ.cm) to remove polishing debris.

4.2.2. Solution Preparation

Solutions were prepared using Type 1 H₂O obtained from a Millipore Milli-Q direct water purification system and were deaerated using a stream of ultra-high purity Ar gas (Praxair) for a minimum of one hour prior to each experiment. All experiments were conducted in a 100 mM NaCl (Fisher Scientific) solution containing 0.05 mol L⁻¹ NaHCO₃/Na₂CO₃ (EMD Chemicals) and a [H₂O₂] in the range 1 mM to 20 mM achieved by adding the appropriate amount of a diluted 3% W/V solution (Fisher Scientific). The pH was adjusted to 9.5 using 500 mM NaOH.

4.2.3. Electrochemical Cell and Equipment

All experiments were conducted in a 50 mL single-compartment, three-electrode electrochemical cell. Potentials were recorded against a commercial saturated Ag/AgCl electrode (0.197 V vs. standard hydrogen electrode) [36]. A Pt foil spot-welded to a Pt wire was used as the counter electrode. The electrochemical cell was housed in a grounded Faraday cage to minimize interference from external electrical noise and covered with Al foil to avoid photolytic decomposition of the H₂O₂. Applied potentials and measured current responses were controlled, recorded, and analyzed using a Solartron Model 1480 Multistat and CorrWare software (Scribner Associates), respectively.

4.2.4. Electrochemical Techniques

Corrosion potential (E_{CORR}) experiments were performed in solutions purged with UHP Ar (Praxair). After electrochemically reducing the surface at -1200 mV (vs Ag/AgCl) for 20 seconds, E_{CORR} was measured for 24 hours.

Linear polarization resistance (LPR) measurements were performed hourly over the 24-hour duration of an experiment. A potential bias of ± 10 mV vs E_{CORR} was applied at a scan rate of 0.167 mV/s starting at E_{CORR} . The slope from the resulting linear region of the current-potential relationship yields the polarization resistance (R_p) value, which is inversely proportional to the rate of interfacial charge transfer processes. In this study, the R_p value is representative of the sum of the resistances for the two reactions possible on the sample surface, Figure 4-1.

4.2.5. Ultraviolet-Visible Spectroscopy (UV-vis)

Hydrogen peroxide (H_2O_2) concentrations were measured using an Agilent Cary 8454 UV-Vis diode array instrument, with a detection limit for H_2O_2 of 0.003 mM. The absorbance at 352 nm was measured using the Ghormley tri-iodide method [37, 38]. To reduce the effect of H_2O_2 decomposition due to exposure to light, all volumetric flasks were covered with Al foil and analyses were performed immediately after sampling the solution. Additionally, to correct for any contribution of H_2O_2 decomposition in solution, a blank solution with no electrode was prepared for each experiment and analyzed concurrently.

4.2.6. Inductively Coupled Plasma-Mass Spectrometry (ICP-MS)

Dissolved U concentrations were measured using an Agilent 7700x ICP-MS instrument. Prior to analysis, all samples were filtered through a 0.2 μm filter paper and diluted in 2% HNO_3 , with a dilution factor of 100, to minimize matrix effects. The instrument was calibrated using a series of uranium standards, with a detection limit of 1.68×10^{-7} mM.

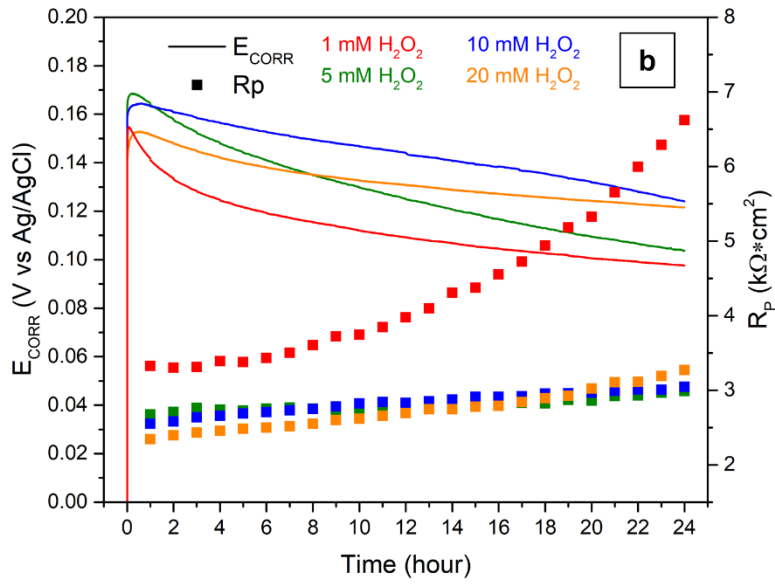
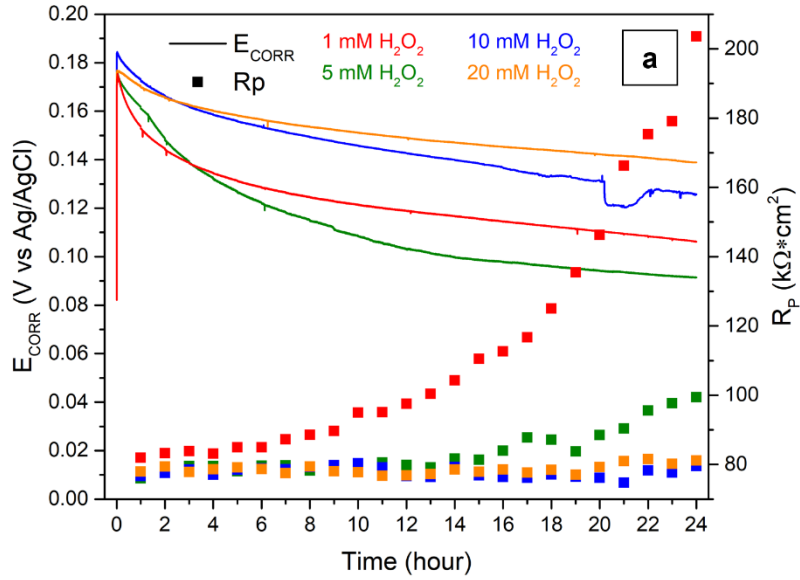
4.2.7. Scanning Electron Microscopy (SEM)

Images of the sample surface were collected using a Hitachi SU3500 Variable Pressure SEM. The electron beam was accelerated at 5 kV with a working distance of 10 mm to collect high-resolution images. All SEM micrographs were taken at surface locations where the grain structure was visible.

4.3. Results and Discussion

Figure 4-2 shows a series of E_{CORR} and R_{P} measurements in solutions containing initial concentrations of H_2O_2 ($[\text{H}_2\text{O}_2]_{\text{i}}$) ranging from 1 mM to 20 mM. The initial E_{CORR} values are in the range 0.16 V to 0.18 V (vs sat. Ag/AgCl) and do not vary significantly with $[\text{H}_2\text{O}_2]_{\text{i}}$. This is consistent with the findings of Wu and Shoosmith [28] in a similar H_2O_2 concentration range. The E_{CORR} decreases with time for all electrodes, yielding final values in the range 0.14 V to 0.10 V (vs sat. Ag/AgCl). At these values of E_{CORR} , it has been shown that the surface is oxidized to a composition of $\text{U}^{\text{IV}}_{0.34}\text{U}^{\text{V}}_{0.66}\text{O}_{2.33}$ [35]. This represents the terminal composition

for the fluorite structure, beyond which dissolution, as opposed to further solid state oxidation, becomes the dominant reaction [35, 39, 40]. As shown by Broczkowski, et al. [41], at these potentials, the surface is irreversibly oxidized.



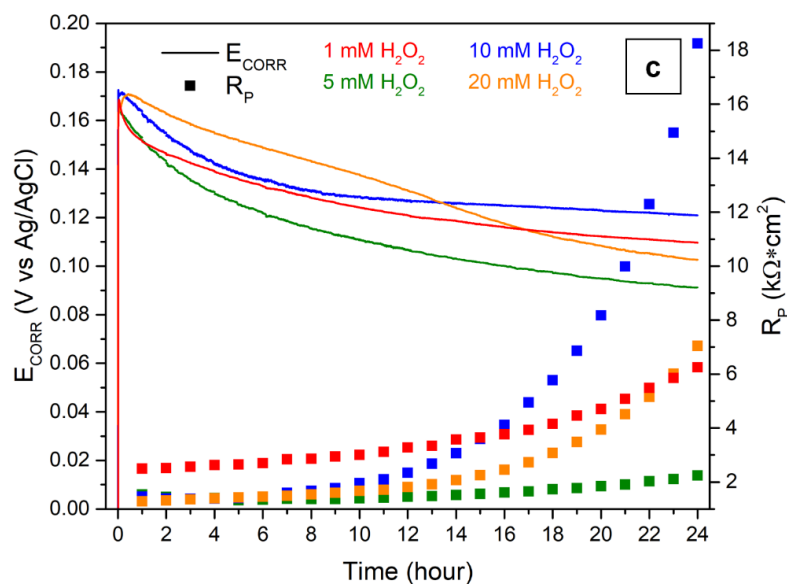


Figure 4-2. E_{CORR} (line) and R_P (squares) measurements as a function of time with various $[H_2O_2]_i$. Recorded on a natural UO_2 electrode with (a) high resistivity, 2500 $k\Omega\cdot cm$, (b) low resistivity, 10 $k\Omega\cdot cm$, or (c) mid resistivity, 50 $k\Omega\cdot cm$, in $0.1\ mol\ L^{-1}\ NaCl + 0.05\ mol\ L^{-1}\ HCO_3^-/CO_3^{2-}$ solution adjusted to pH 9.5.

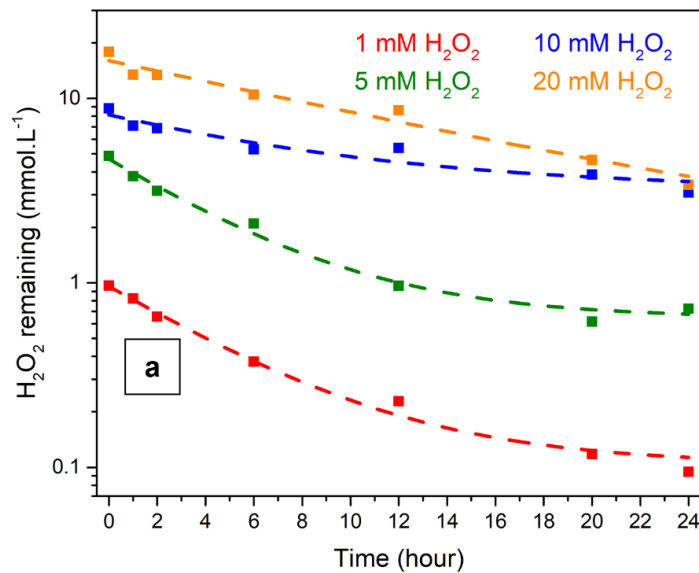
For the electrodes with high and low resistivities, Figure 4-2(a) and (b) respectively, at high $[H_2O_2]_i$, R_P values show little-to-no change over the course of the experiment. This suggests the cathodic reduction of H_2O_2 proceeds on the UO_2 surface, supporting H_2O_2 decomposition and UO_2 corrosion over the full 24 hours, at a constant rate which is not directly dependent on $[H_2O_2]$ and is changing as the experiment proceeds. For $[H_2O_2]_i = 1\ mM$, R_P increases exponentially after ~ 6 hours especially for the high and low resistivity specimens. An increase in R_P with a decrease in E_{CORR} suggests a decrease in rate of the cathodic reaction, likely due to the consumption of H_2O_2 at this low concentration, Figure 4-3. For the electrode with a mid resistivity, Figure 4-2(c), increases in R_P were observed at $[H_2O_2]_i \leq 10\ mM$. For this specimen the R_P value unexpectedly increases more at longer times for $[H_2O_2]_i = 10\ mM$ than at 1 mM. For all electrodes, an increase in R_P was only observed when $[H_2O_2] \leq 1\ mM$, Figure 4-3.

Comparison of the R_P values measured on the three specimens shows the values appear related to the overall resistivities,

$$R_P(2500) \gg R_P(50) > R_P(10)$$

If the measured resistivities are indicative of the degree of non-stoichiometry of the specimens [21], this order suggests a relationship between the rate of the two possible interfacial processes and the stoichiometry of the specimens.

Figure 4-3 shows the remaining concentration of H_2O_2 in solution during the experiments plotted in Figure 4-2 as a function of time. For all electrodes and $[H_2O_2]_i$, the remaining concentration of H_2O_2 in solution decreases as a function of time as observed in other studies [42, 43].



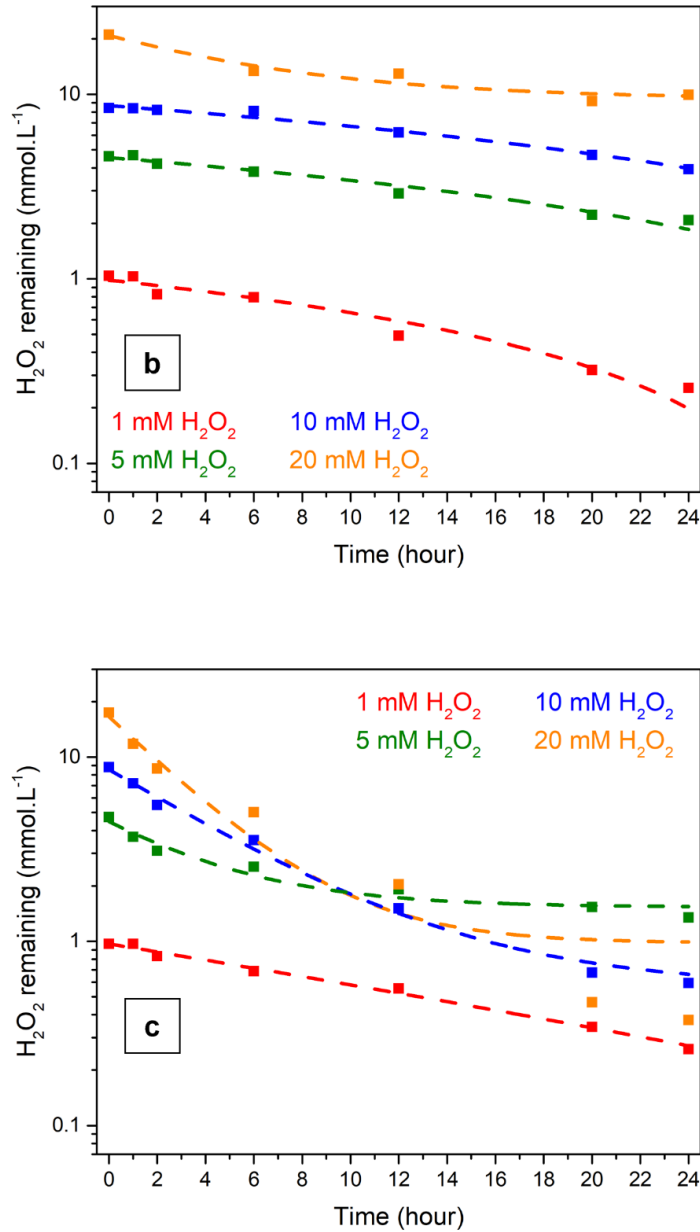


Figure 4-3. Measured $[H_2O_2]$ remaining in solution as a function of time for $[H_2O_2]_i$ ranging from 1-20 $mmol.L^{-1}$. Recorded on a natural UO_2 electrode with high resistivity, 2500 $k\Omega.cm$ (a), low resistivity, 10 $k\Omega.cm$ (b), or mid resistivity, 50 $k\Omega.cm$ (c), in $0.1 mol L^{-1} NaCl + 0.05 mol L^{-1} HCO_3^-/CO_3^{2-}$ solution adjusted to pH 9.5.

Figure 4-4 shows the relationship between the remaining $[H_2O_2]$ as a function of the measured E_{CORR} at the time at which the $[H_2O_2]$ was analyzed over the 24-hour experiments. Apart from the low-resistivity specimen in 20 mM $[H_2O_2]$, E_{CORR} decreases as H_2O_2 was consumed for all specimens. As noted above, once oxidized to the terminal composition of $U^{IV}_{0.34}U^V_{0.66}O_{2.37}$ the surface composition does not decrease as E_{CORR} decreases. Consequently, changes in E_{CORR} reflect the surface $[H_2O_2]$.

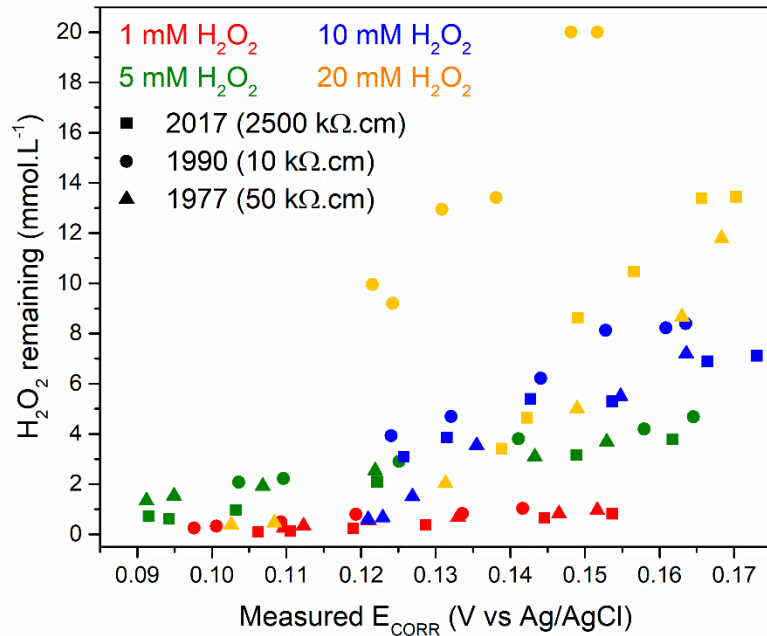


Figure 4-4. The remaining $[H_2O_2]$, taken after 1, 2, 6, 12, 20, and 24 hours of immersion, with respect to measured E_{CORR} . Recorded on a natural UO_2 electrode with high resistivity, 2500 k $\Omega \cdot cm$ (square), low resistivity, 10 k $\Omega \cdot cm$ (circle), or mid resistivity, 50 k $\Omega \cdot cm$ (triangle), in 0.1 mol L^{-1} NaCl + 0.05 mol L^{-1} HCO_3^-/CO_3^{2-} solution adjusted to pH 9.5.

Figure 4-5 shows the amount of H_2O_2 consumed on the UO_2 surface as a function of $[\text{H}_2\text{O}_2]_i$ and time. For all specimens, the amount of H_2O_2 consumed increases with both time and $[\text{H}_2\text{O}_2]_i$, Figure 4-5, which is to be expected. While this behaviour is consistent for all specimens, the total amount of H_2O_2 consumed varies significantly, with the consumption of H_2O_2 decreasing with decreasing sample resistivity. This is at odds with the suggestion that R_P^{-1} is an indication of interfacial rate, and clearly indicates that the reactivity of the UO_2 is not determined by the resistivity of the specimen; i.e., to the degree of non-stoichiometry remaining on completion of the fuel fabrication and sintering process. The amount of H_2O_2 consumed and the measured R_P , using the data for $[\text{H}_2\text{O}_2]_i = 20 \text{ mM}$, where the surface reactions are least likely to be influenced by transport control, the order of increase in both cases is

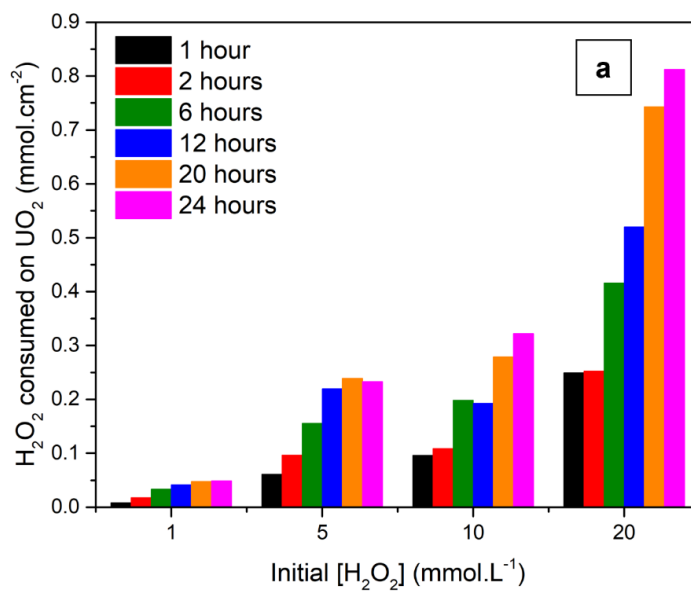
$$2500 \text{ k}\Omega\cdot\text{cm} \gg 50 \text{ k}\Omega\cdot\text{cm} > 10 \text{ k}\Omega\cdot\text{cm}$$

confirming that the R_P value is not a reliable indicator of the surface reactivity. This suggests the R_P values indicate, at least partially if not predominantly, the bulk resistance of the specimens and not the interfacial polarization resistances (which would define the surface reactivity).

For the low and mid resistivity specimens, the amount of H_2O_2 consumed plateaus at longer times regardless of $[\text{H}_2\text{O}_2]_i$. As a substantial $[\text{H}_2\text{O}_2]$ is still present, this cannot be attributed to a lack of H_2O_2 in solution, suggesting that for these two specimens the surface becomes less reactive with time. Possible due to the rate limiting presence of a UO_2CO_3 layer. This trend is observed at low $[\text{H}_2\text{O}_2]_i \leq 5 \text{ mM}$ for the high resistivity sample, however, at higher $[\text{H}_2\text{O}_2]_i \geq 10 \text{ mM}$, the amount of consumed H_2O_2 continues to increase over the whole exposure period.

The electrode with the highest resistivity, Figure 4-5(a), consumes the greatest amount of H_2O_2 of all the specimens. The specimens with low and mid resistivities, Figure 4-5(b) and (c) respectively, consume similar amounts of H_2O_2 , however, the overall H_2O_2 consumed is approximately 50 % less than the high-resistivity sample. As previously stated, R_P is not a reliable indicator of the surface reactivity. Kumagai, et al. [44] observed a similar trend on

UO_{2.0} and UO_{2.3} specimens, expected to have a high and low resistivity, respectively. They found the rate of H₂O₂ consumption on the UO₂ surface was much greater on the stoichiometric UO_{2.0} sample, while the UO_{2.3} underwent a greater amount of dissolution. It is possible that at the [H₂O₂] used, the dependence on degree of non-stoichiometry is overwhelmed by the ability of H₂O₂ to create and utilize its own catalytic sites via reactions 4.7-4.9.



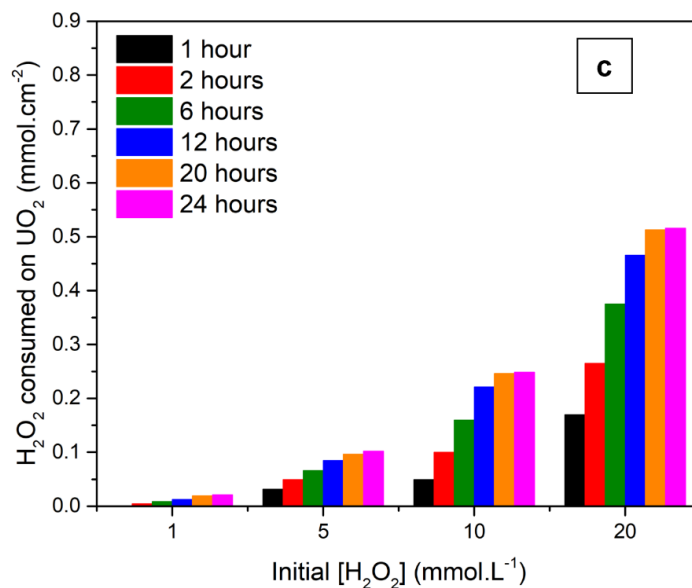
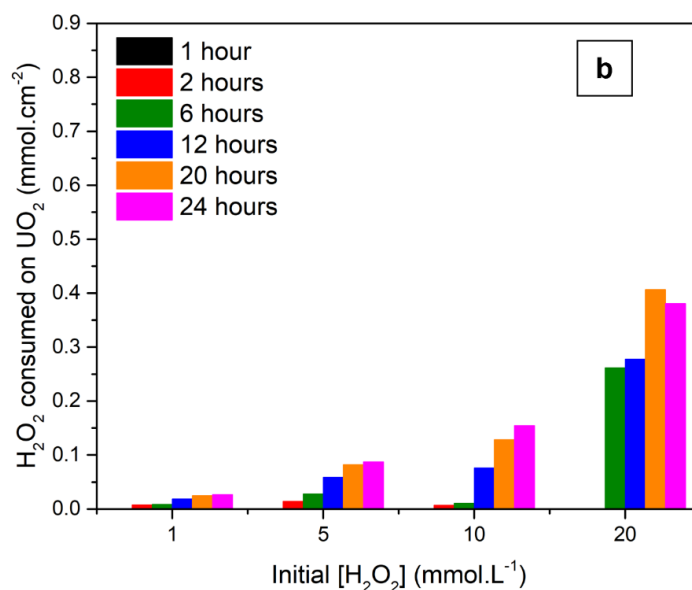
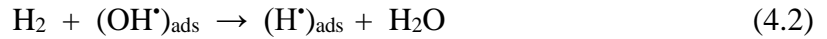
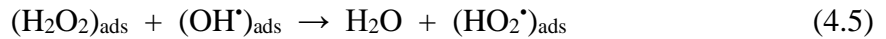


Figure 4-5. Total amount of H₂O₂ consumed at the UO₂ surface over 24 hours as a function [H₂O₂]_i. Recorded on a natural UO₂ electrode with high resistivity, 2500 kΩ.cm (a), low resistivity, 10 kΩ.cm (b), or mid resistivity, 50 kΩ.cm (c), in 0.1 mol L⁻¹ NaCl + 0.05 mol L⁻¹ HCO₃⁻/CO₃²⁻ solution adjusted to pH 9.5.

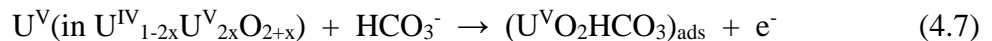


Regardless of $[\text{H}_2\text{O}_2]_i$, the amount of consumed H_2O_2 tends towards a steady state after 20 hours suggesting no more surface oxidation or peroxide decomposition occurs beyond this point. This agrees with Figure 4-3, where the $[\text{H}_2\text{O}_2]$ remaining in solution is shown to reach a steady state after 20 hours regardless of how much H_2O_2 is remaining in solution. Figure 4-8 shows the amount of dissolved uranium for the high and mid resistivity samples reach a similar steady state after 20 hours.

As shown in Figure 4-1, the cathodic reduction of H_2O_2 consumed on the UO_2 surface can couple with one of two possible anodic reactions, the decomposition of H_2O_2 or the dissolution of UO_2 . The decomposition of H_2O_2 has been shown to proceed via a surface radical mechanism, reactions 4.1-4.3 [16, 43, 45-49].



The presence of a thin $\text{U}^{\text{IV}}_{1-2x}\text{U}^{\text{V}}_{2x}\text{O}_{2+x}$ surface layer has been shown to catalyze this process through the formation of $\text{U}^{\text{IV/V}}$ donor-acceptor sites. These sites are accompanied by the incorporation and subsequent release of interstitial O^{2-} at vacant lattice sites within the UO_2 matrix [27]. Reactions 4.4-4.6 illustrate the mechanism by which the U^{V} and U^{VI} states are extracted via complexation as a $\text{HCO}_3^-/\text{CO}_3^{2-}$ complexed with uranyl ion [3].



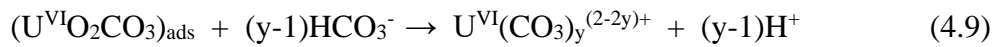


Figure 4-6 shows the amount of dissolved U in solution after 24 hours with respect to $[H_2O_2]_i$ for all three fuel samples. In general, the extent of dissolution increases as the $[H_2O_2]_i$ increases. At the two lowest concentrations, there is little difference between the three specimens in the amount of dissolved U. This is most likely due to the greater likelihood that the interfacial rates of the two possible reactions are at least partially controlled by H_2O_2 transport to the UO_2 surface. At the higher $[H_2O_2]_i$, there is no clear trend between the amount of dissolved U and the specimen resistivities. To better understand what is occurring at the UO_2 -solution interface, we need to consider the dissolution yield; i.e., the fraction of consumed H_2O_2 causing dissolution, Figure 4-7.

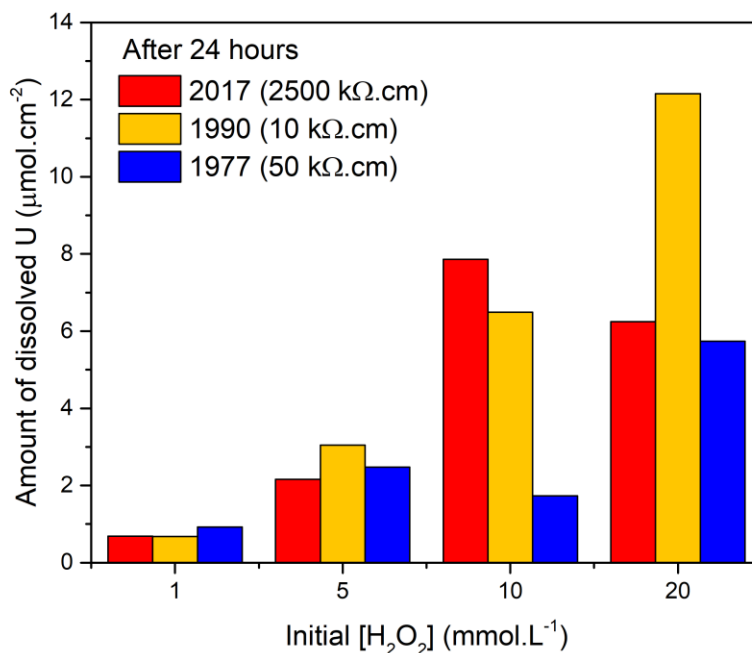


Figure 4-6. Amount of dissolved U in solution with respect to $[H_2O_2]_i$ after 24 hours of immersion.

Dissolution yields after 24 hours with respect to $[\text{H}_2\text{O}_2]_i$ are shown in Figure 4-7. The dissolution yield provides a better indication of the surface's susceptibility to oxidation as a ratio between the dissolution of U and the consumption of H_2O_2 on the sample surface. This dissolution yield shows no consistent trend with $[\text{H}_2\text{O}_2]$, although the slightly lower values for the high-resistivity sample reflect the higher amount of H_2O_2 consumed on this specimen; i.e., the high-resistivity specimen sustains a higher rate of H_2O_2 decomposition, reactions 4.1-4.3. In general, the low-resistivity sample has the greatest dissolution yield. The constant dissolution yield of $\sim 3.4\%$, regardless of $[\text{H}_2\text{O}_2]_i$, suggests U dissolution is concentration dependent. The dissolution yield of the mid-resistivity sample decreases from $\sim 4.5\%$ to $\sim 1\%$ as $[\text{H}_2\text{O}_2]_i$ increases. Though an increase in the $[\text{U}]$ with an increasing $[\text{H}_2\text{O}_2]_i$ is observed in Figure 4-6, this trend suggests the decomposition of H_2O_2 , possibly catalyzed by surface states (reactions 4.7-4.9), occurs more readily than U oxidation and dissolution. The high-resistivity sample shows the least consistent results, though it averages the lowest dissolution yield at $\sim 1.4\%$. This would be expected of a near-stoichiometric sample with slight variances in the local stoichiometry at grain boundaries and from grain to grain that could result in a range of dissolution yields.

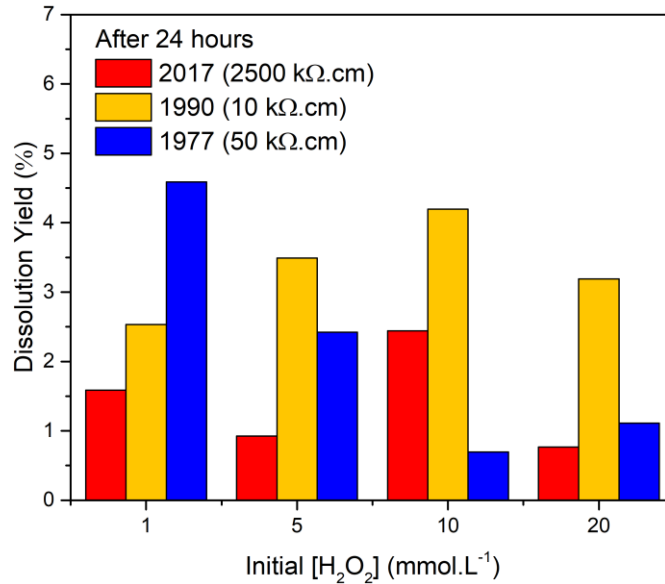


Figure 4-7. Calculated dissolution yield with respect to $[\text{H}_2\text{O}_2]_i$ after 24 hours immersion.

These results confirm that > 95 % of the H₂O₂ consumed on the UO₂ surface is consumed by its own decomposition. However, these results vary from previous findings of Nilsson and Jonsson [26], where the reported dissolution yield for a UO₂ pellet was 14 %. These results are significantly higher than the dissolution yields previously reported on SIMFUEL samples of 0.2 % and 0.76 % [26, 27]. This is expected as the dopants in SIMFUEL stabilize the fuel matrix, decreasing the susceptibility to dissolution. The similarity between these specimens and the behaviour observed on SIMFUEL specimens, on which the R_P values do represent the reactivity of the surface, indicate that the behaviour of the present specimens is controlled by the kinetics of the surface reactions with H₂O₂ [27]. The relatively minor differences in reactivity between specimens and the inability to relate the extent of H₂O₂ consumption to the resistivity of the specimens indicates the reactivity is only loosely connected to the sintering process of the electrodes, if at all.

Figure 4-8 shows the influence of [H₂O₂]_i on the amount of dissolved U for the high and mid resistivity samples over a 24-hour exposure period. Data was not recorded for the low resistivity specimen. At all [H₂O₂]_i, on both specimens, the dissolution yields initially increased with time before approaching a final steady-state after 20 hours. While at a lower [H₂O₂]_i of 1 mM and 5 mM this can be attributed to the depletion of H₂O₂ in the solution, it does not explain the similar trend observed at higher [H₂O₂]_i for which the [H₂O₂] remaining in the solution is significant, as shown in Figure 4-3.

This tendency for an initially more rapid release of U from 1 to 12 hours of immersion followed by a tendency to plateau after 20 hours coincides with the exposure period over which E_{CORR} is rapidly changing as it approaches a steady state value. This trend has been previously observed on a SIMFUEL sample with a resistivity of only 174 ohm.cm [41]. During this early period, it was shown by Zhu, et al. [27] that the fuel surface is oxidized to U^{IV}_{1-2x}U^V_{2x}O_{2+x}, leading to a surface composition which optimized the catalyzed decomposition of H₂O₂ on the oxidized surface and a decrease in the dissolution rate of the UO₂. The establishment of a steady state [U] and [H₂O₂], Figure 4-5, suggests there may be U^{VI} secondary phase deposits partially blocking the surface, preventing further oxidation. For the pH range in this study, the solubility limit ranges from 3.2 μmol.L⁻¹ to 4.5 μmol.L⁻¹ [20, 50, 51]. Further analysis using

X-ray photoelectron spectroscopy would be necessary to confirm the presence of these secondary phases.

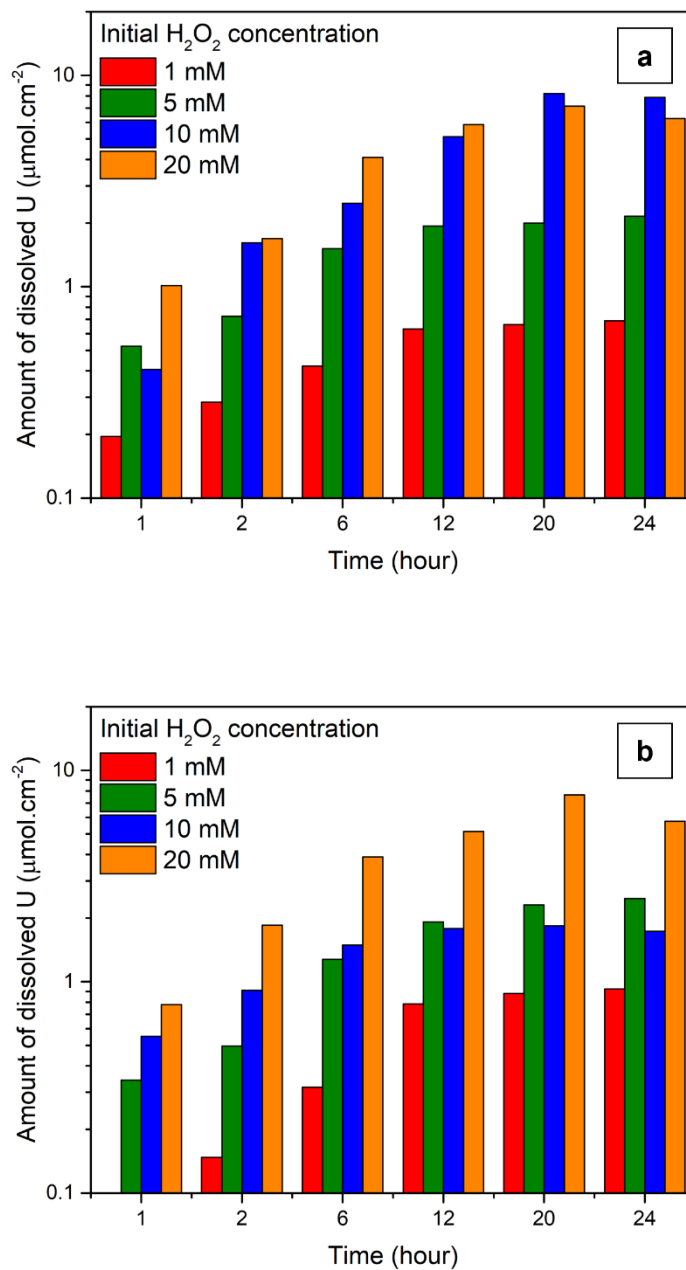


Figure 4-8. Amount of dissolved U in solution with respect to time for electrodes with (a) high resistivity, 2500 kΩ.cm, and (b) mid resistivity, 50 kΩ.cm.

Figure 4-9 shows the influence of $[\text{H}_2\text{O}_2]_i$ on the dissolution yield of U for the high and mid resistivity samples over a 24-hour exposure period. For the high-resistivity sample, the overall extent of dissolution is lower than that of the mid-resistivity sample, despite the greater consumption of H_2O_2 . This suggests the matrix is more stable at the higher resistivity. For the mid-resistivity, the dissolution yield is higher at the lower $[\text{H}_2\text{O}_2]_i$ (1 mM, and especially, 5 mM) at most time points. A possible explanation for this is that the dissolution is first order with respect to $[\text{H}_2\text{O}_2]$ while the decomposition of H_2O_2 is second order. At low $[\text{H}_2\text{O}_2]_i$, the formation of $(\text{OH})_{\text{ads}}^*$, reaction 4.1, occurs, however, diffusion may control the $[\text{H}_2\text{O}_2]$ at the fuel surface, resulting in reaction 4.2 being slow, allowing the extent of dissolution via reactions 4.5 and 4.6 to increase. Under these conditions, dissolution could occur.

Figure 4-10 and Figure 4-11 show a series of SEM micrographs of the sample surface for the high- and mid-resistivity samples pre- and post-immersion in 1 mM, 5 mM, 10 mM, and 20 mM H_2O_2 solutions respectively. The pre-immersion micrographs show a uniform surface for both samples with minor variances in grain morphology, suggesting minor compositional differences, not surface damage. At $[\text{H}_2\text{O}_2]_i \leq 1$ mM, the samples show little-to-no corrosion damage across the sample surface. However, as the $[\text{H}_2\text{O}_2]_i$ increases, both samples begin to undergo localized corrosion events.

The high-resistivity sample, Figure 4-10, shows minimal corrosion damage after immersion in the 1 mM H_2O_2 solution as the grain structure remains clearly visible. At $[\text{H}_2\text{O}_2]_i > 1$ mM, localized dissolution occurs. For 5 mM, 10 mM, and 20 mM, respectively, intergranular corrosion with deep penetration into the sample was observed. Additionally, the micrograph recorded after exposure to the 20 mM solution shows more severe damage at grain boundaries across the sample surface. The non-uniform dissolution suggests the possible establishment of localized chemistries, probably at the grain boundaries where the availability of lattice defects may enhance both anodic and cathodic reactions, reactions 4.4-4.6 and 4.1-4.3, respectively. The alternative that anodic and cathodic sites are physically well separated is unlikely given the high resistivity of this specimen.

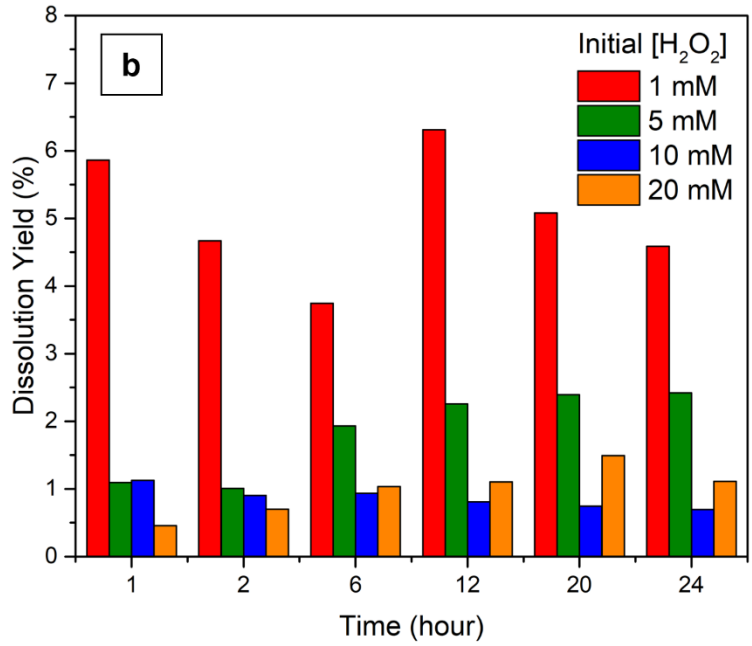
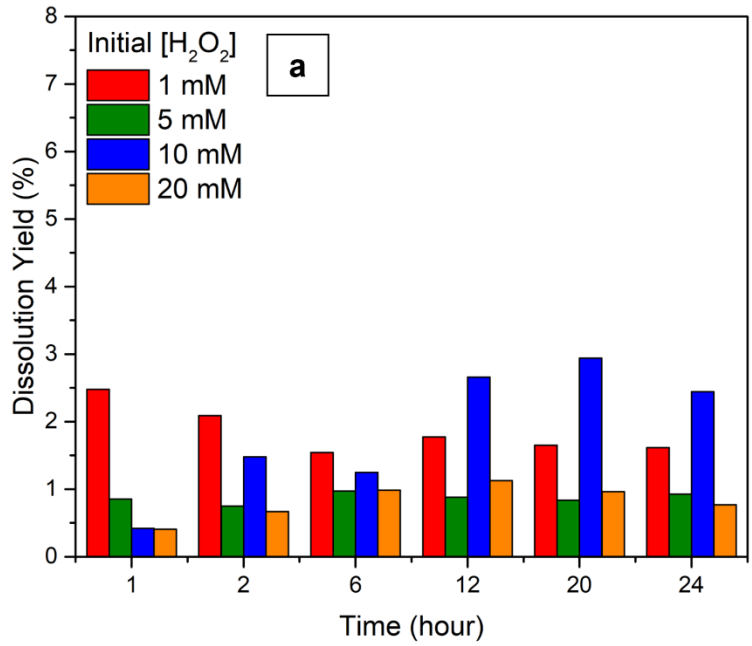


Figure 4-9. Calculated dissolution yield with respect to time for electrodes with (a) high resistivity, 2500 kΩ.cm, and (b) mid resistivity, 50 kΩ.cm.

Given that the localized corrosion damage was observed on the high resistivity specimen but not the medium resistivity specimen, micro-indentations were deliberately made on the low-resistivity specimen to introduce physical surface defects, Figure 4-12(b). Prior to performing any immersion experiments, the general grain structure of the surface was smooth and flat, Figure 4-12(a). Upon completion of all immersion experiments, the general surface of the specimen was only slightly roughed, Figure 4-12(c), consistent with the occurrence of minimal dissolution. By contrast, the locations with the micro-indentations and a natural slight fracture in the surface were considerably more aggressively corroded, Figure 4-12(d). This indicates that dissolution occurs dominantly at physically defective locations. It is also possible, but not unequivocally proven in this study, that the reduction of H_2O_2 is enhanced at these locations.

The mid-resistivity sample, Figure 4-11, shows minimal corrosion damage after immersion in all solutions, consistent with the minimal amounts of dissolved U (Figure 4-6) and the low dissolution yield. No evidence for localized corrosion, as seen for the high resistivity specimen, was observed although there is some evidence for slight grain etching at the highest $[\text{H}_2\text{O}_2]_i$, Figure 4-11e.

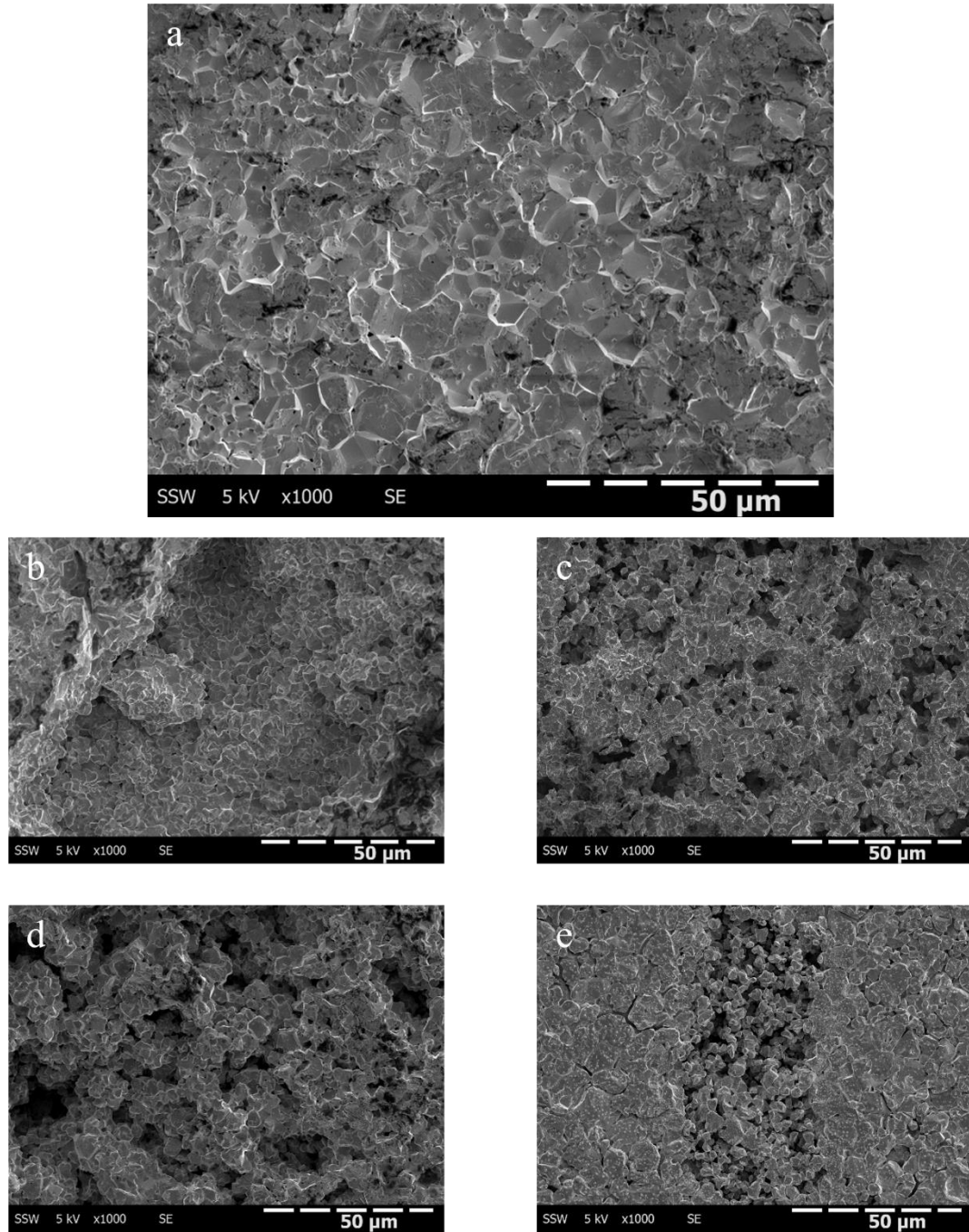


Figure 4-10. SEM of the high-resistivity sample (2017, 2500 k Ω .cm) (a) before immersion, and after 24 hours immersion at various $[H_2O_2]_i$ (b) 1 mM, (c) 5 mM, (d) 10 mM, and (e) 20 mM.

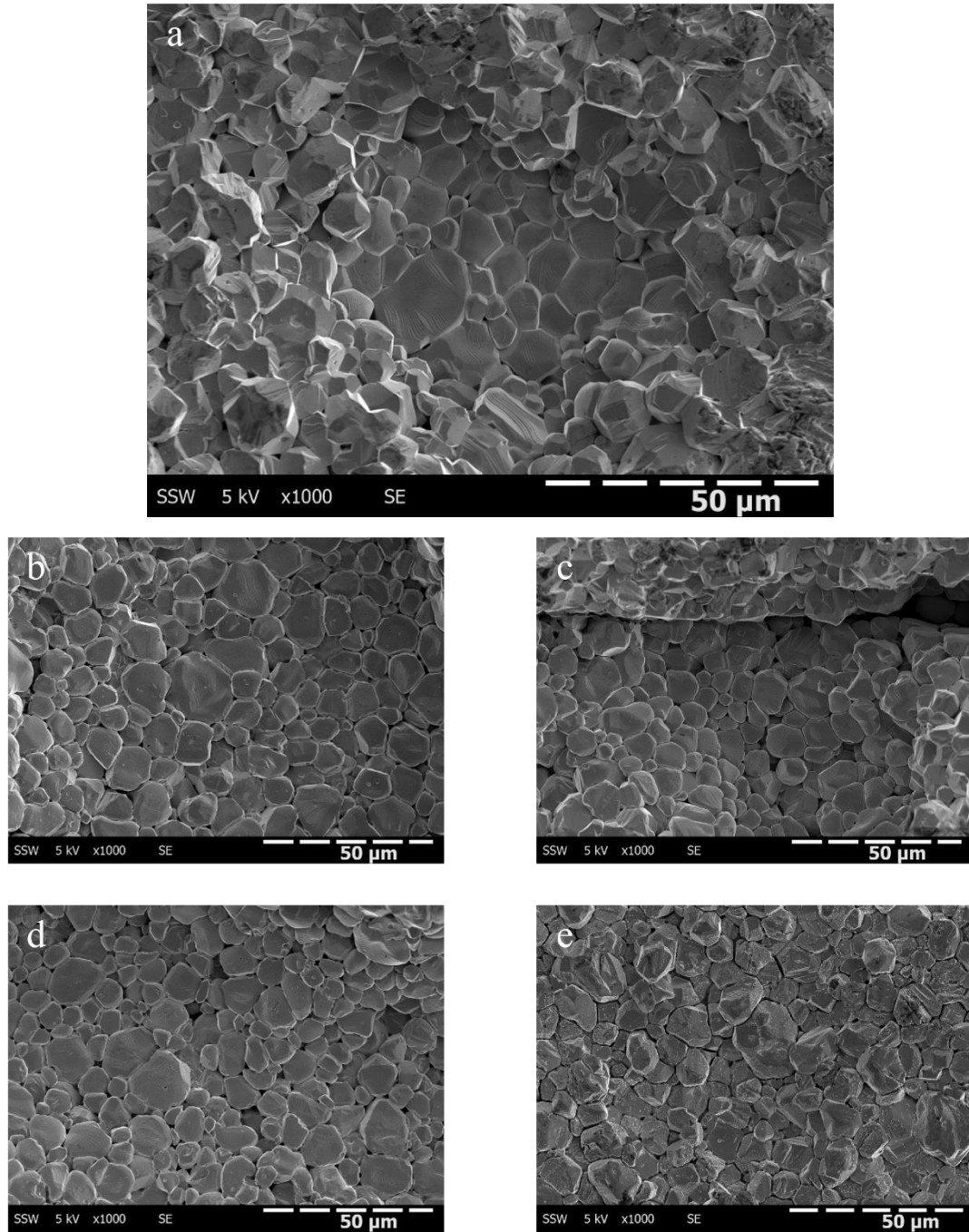


Figure 4-11. SEM of the mid-resistivity sample (1977, 50 kΩ.cm) (a) before immersion, and after 24 hours immersion at various $[H_2O_2]_i$ (b) 1 mM, (c) 5 mM, (d) 10 mM, and (e) 20 mM.

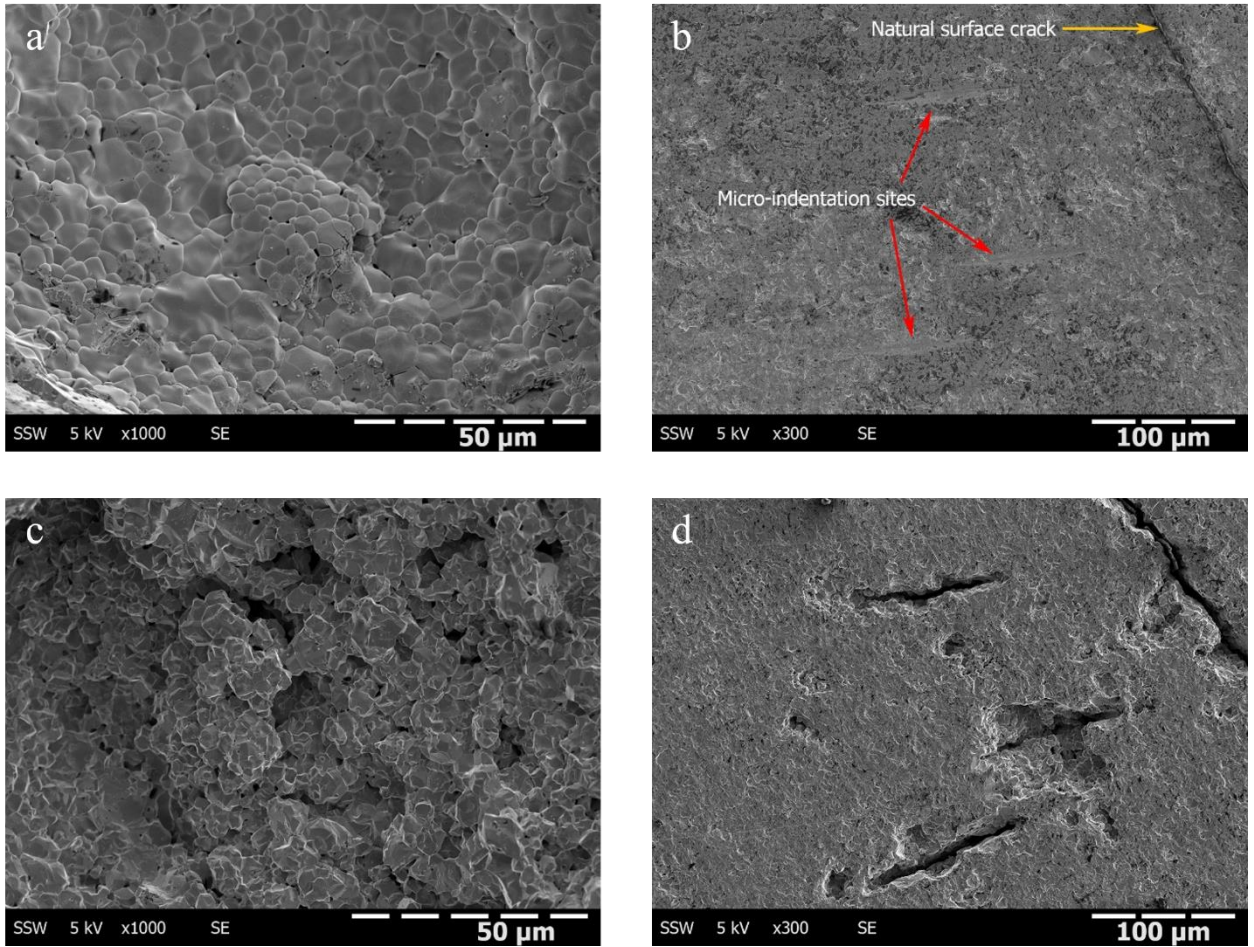


Figure 4-12. SEM of the low-resistivity sample (1990, 10 kΩ.cm) (a) and (b) before immersion, or (c) and (d) after all immersion experiments. Micro-indentations created on the surface are indicated with red arrows and a natural crack along the surface indicated with a yellow arrow.

4.4. Summary and Conclusions

There is clearly a wide distribution in the conductivities for fuels used in CANDU reactors over the > 60 years of operation. The differences in resistivity (inverse of conductivity) suggest significant variability in fuel fabrication over the lifetime of reactors.

Based on these results, we have shown that the reactivity of these un-doped UO_2 specimens is only loosely related to the sintering process. Further, there appears to be no relationship between the measured resistivity of a specimen and its reactivity as the consumption of H_2O_2 does not correlate to the measured R_P .

The majority of H_2O_2 consumed on the UO_2 surface was consumed by H_2O_2 decomposition. Any dissolution that did occur was primarily at physically defective locations, resulting in localized damage. Though the high-resistivity specimen consumed the greatest amount of H_2O_2 in solution, it underwent the least U dissolution of all the specimens, suggesting a more stable matrix than the two lower resistivity specimens.

Additional investigations using X-ray photoelectron spectroscopy would provide surface state information for each specimen and identify the surface composition and degree of oxidation for each experimental set.

4.5. Acknowledgements

This work was jointly funded by the Natural Sciences and Engineering Research Council of Canada and the Nuclear Waste Management Organization through Alliance Grant ALLRP561193-20. Surface Science Western is acknowledged for the use of their instruments.

4.6. References

- [1] D.S. Hall, M. Behazin, W.J. Binns, P.G. Keech, *An evaluation of corrosion processes affecting copper-coated nuclear waste containers in a deep geological repository*, Prog Mater Sci. **(2021)**. 118, 100766.
- [2] I. Ariani, Dose Rate Analysis to Support Radiolysis Assessment of Used CANDU Fuel, Nuclear Waste Management Organization, NWMO-TR-2022-02, Toronto, Canada **(2022)**.
- [3] M. Badley, D.W. Shoesmith, The corrosion/dissolution of used nuclear fuel in a deep geologic repository, Nuclear Waste Management Organization, NWMO-TR-2022-09, Toronto, Canada **(2022)**.
- [4] B. Grambow, K. Lemmens, Y. Minet, C. Poinssot, K. Spahiu, D. Bosbach, C. Cachoir, I. Casas, F. Clarens, B. Christiansen, J. de Pablo, C. Ferry, J. Giménez, S. Gin, J.P. Glatz, J.A. Gago, E. Gonzalez-Robles, N.C. Hyatt, E. Iglesias, B. Kienzler, B. Luckscheiter, A. Martinez-Esparza, V. Metz, A. Ödegaard-Jensen, K. Ollila, J. Quiñones, A. Rey, S. Ribet, V.V. Rondinella, G. Skarnemark, D. Wegen, D. Serrano-Purroy, T. Wiss, NF-PRO RTD Component 1: Dissolution and release from the waste matrix, EUR 23730, Brussels **(2008)**.
- [5] B. Grambow, J. Bruno, L. Duro, J. Merino, A. Tamayo, C. Martin, G. Pepin, S. Schumacker, O. Smidt, C. Ferry, C. Jegou, J. Quiñones, E. Iglesias, N. Rodriguez Villagra, J.M. Nieto, A. Martínez-Esparza, A. Loida, V. Metz, B. Kienzler, G. Bracke, D. Pellegrini, G. Mathieu, V. Wasselin-Trupin, C. Serres, D. Wegen, M. Jonsson, L. Johnson, K. Lemmens, J. Liu, K. Spahiu, E. Ekeröth, I. Casas, J. de Pablo, C. Watson, P. Robinson, D. Hodgkinson, Model uncertainty for the mechanism of dissolution of spent fuel in a nuclear waste repository, EUR 24597 EN, Brussels **(2010)**.
- [6] K. Lemmens, C. Cachoir, T. Mennecart, Dissolution behaviour of spent nuclear fuel at highly alkaline conditions, SCK CEN, 27622175, ER-0505, Belgium **(2019)**.
- [7] V.M. Oversby, Rates and mechanisms of radioactive release and retention inside a waste disposal canister - in Can Processes, Swedish Nuclear Fuel and Waste Management Co., NEI-SE-562, Stockholm, Sweden **(2003)**.
- [8] C. Poinssot, C. Ferry, M. Kelm, B. Grambow, A. Martinez-Esparza, L. Johnson, Z. Andriambololona, J. Bruno, C. Cachoir, J.M. Cavendon, Final report of the European project spent fuel stability under repository conditions, Atomic Energy Commission (CEA), CEA-R-6093, Gif-sur-Yvette, France **(2005)**.
- [9] L. Werme, C. Lilja, Fuel and canister process report for the safety assessment SR-Site, Swedish Nuclear Fuel and Waste Management Co., SKB TR-10-46, **(2010)**.

- [10] E.C. Buck, B.D. Hanson, B.K. McNamara, *The geochemical behaviour of Tc, Np and Pu in spent nuclear fuel in an oxidizing environment*, J Geol Soc London. (2004). 236 (1), 65-88.
- [11] R.C. Ewing, *Long-term storage of spent nuclear fuel*, Nat Mater. (2015). 14 (3), 252-257.
- [12] L.O. Werme, K. Spahiu, L.H. Johnson, V.M. Oversby, F. King, B. Grambow, D.W. Shoesmith, *Spent fuel performance under repository conditions: A model for use in SR-Can*, 1404-0344, Sweden (2004).
- [13] F. King, D.S. Hall, P.G. Keech, *Nature of the near-field environment in a deep geological repository and the implications for the corrosion behaviour of the container*, Corros Eng Sci Technol. (2017). 52 (sup1), 25-30.
- [14] J.C. Wren, D.W. Shoesmith, S. Sunder, *Corrosion behavior of uranium dioxide in alpha radiolytically decomposed water*, J Electrochem Soc. (2005). 152 (11), B470.
- [15] E. Ekeröth, M. Jonsson, *Oxidation of UO₂ by radiolytic oxidants*, J Nucl Mater. (2003). 322 (2-3), 242-248.
- [16] C.M. Lousada, M. Yang, K. Nilsson, M. Jonsson, *Catalytic decomposition of hydrogen peroxide on transition metal and lanthanide oxides*, J Mol Catal A: Chem. (2013). 379, 178-184.
- [17] C.M. Lousada, M. Jonsson, *Kinetics, mechanism, and activation energy of H₂O₂ decomposition on the surface of ZrO₂*, J Phys Chem C. (2010). 114 (25), 11202-11208.
- [18] A. Barreiro-Fidalgo, B. Dahlgren, T. Brinck, M. Jonsson, *Surface reactions of H₂O₂, H₂, and O₂ in aqueous systems containing ZrO₂*, J Phys Chem C. (2016). 120 (3), 1609-1614.
- [19] Z. Zhu, L. Wu, J.J. Noël, D.W. Shoesmith, *Anodic reactions occurring on simulated spent nuclear fuel (SIMFUEL) in hydrogen peroxide solutions containing bicarbonate/carbonate – The effect of fission products*, Electrochim Acta. (2019). 320.
- [20] D.W. Shoesmith, S. Sunder, W.H. Hocking, *Electrochemistry of UO₂ nuclear fuel*, in: *Electrochemistry of Novel Materials* [J. Lipkowsky, P.N. Ross (eds.)], VCH Publishers, New York, NY, 1994, pp. 297-337.
- [21] H. He, R.K. Zhu, Z. Qin, P. Keech, Z. Ding, D.W. Shoesmith, *Determination of local corrosion kinetics on hyper-stoichiometric UO_{2+x} by scanning electrochemical microscopy*, J Electrochem Soc. (2009). 156 (3), C87-C94.
- [22] H. He, Z. Qin, D.W. Shoesmith, *Characterizing the relationship between hyperstoichiometry, defect structure and local corrosion kinetics of uranium dioxide*, Electrochim Acta. (2010). 56 (1), 53-60.

- [23] N. Liu, Z. Zhu, J.J. Noël, D.W. Shoesmith, *Corrosion of nuclear fuel inside a failed waste container*, in: *Encyclopedia of Interfacial Chemistry: Surface Science and Electrochemistry* [K. Wandelt (Ed.)], **2018**, pp. 172-182.
- [24] A.C. Maier, A. Barreiro Fidalgo, M. Jonsson, *Impact of H₂ and consecutive H₂O₂ exposures on the oxidative dissolution of (U_{1-x}Gd_x)O₂ pellets under deep repository conditions for spent nuclear fuel*, *Eur J Inorg Chem.* (**2020**). 2020 (20), 1946-1950.
- [25] A. Barreiro-Fidalgo, M. Jonsson, *Radiation induced dissolution of (U, Gd)O₂ pellets in aqueous solution - A comparison to standard UO₂ pellets*, *J Nucl Mater.* (**2019**). 514, 216-223.
- [26] S. Nilsson, M. Jonsson, *H₂O₂ and radiation induced dissolution of UO₂ and SIMFUEL pellets*, *J Nucl Mater.* (**2011**). 410 (1-3), 89-93.
- [27] Z. Zhu, J.J. Noël, D.W. Shoesmith, *Hydrogen peroxide decomposition on simulated nuclear fuel bicarbonate/carbonate solutions*, *Electrochim Acta.* (**2020**). 340.
- [28] L. Wu, D.W. Shoesmith, *An electrochemical study of H₂O₂ oxidation and decomposition on simulated nuclear fuel (SIMFUEL)*, *Electrochim Acta.* (**2014**). 137, 83-90.
- [29] A.C. Maier, P. Kegler, M. Klinkenberg, A. Baena, S. Finkeldei, F. Brandt, M. Jonsson, *On the change in UO₂ redox reactivity as a function of H₂O₂ exposure*, *Dalton Trans.* (**2020**). 49 (4), 1241-1248.
- [30] M. Razdan, *Electrochemical and Surface Compositional Studies on Uranium Dioxide*, PhD Thesis, University of Western Ontario, London, Ontario, **2013**.
- [31] N. Dudney, R. Coble, H. Tuller, *Electrical Conductivity of Pure and Yttria-Doped Uranium Dioxide*, *J Am Ceram Soc.* (**1981**). 64 (11), 627-631.
- [32] L. Collier, R. Hampton, G. Saunders, A. Stoneham, *Electrical conductivity of polycrystalline uranium dioxide*, *J Nucl Mater.* (**1989**). 168 (3), 268-279.
- [33] G.J. Hyland, J. Ralph, *Electronic contributions to the high-temperature thermophysical properties of UO_(2+x): a critical analysis*, *High Temp-High Pressures.* (**1983**). 15 (2), 179-190.
- [34] P. Winter, *The electronic transport properties of UO₂*, *J Nucl Mater.* (**1989**). 161 (1), 38-43.
- [35] N. Liu, F. King, J.J. Noël, D.W. Shoesmith, *An electrochemical and radiolytic study of the effects of H₂ on the corrosion of UO₂-based materials*, *Corros Sci.* (**2021**). 192, 109776.
- [36] C.G. Zoski, *Handbook of electrochemistry*, Elsevier, Amsterdam, **2006**.

- [37] I. Štefanić, J.A. LaVerne, *Temperature dependence of the hydrogen peroxide production in the γ -radiolysis of water*, J Phys Chem A. (2002). 106 (2), 447-452.
- [38] C.J. Hochanadel, *Effects of Cobalt γ -Radiation on Water and Aqueous Solutions*, J Phys Chem. (1952). 56 (5), 587-594.
- [39] M. Razdan, D.W. Shoesmith, *The electrochemical reactivity of 6.0 wt% Gd-Doped UO_2 in aqueous carbonate/bicarbonate solutions*, J Electrochem Soc. (2014). 161 (4), H225-H234.
- [40] M. Razdan, D.W. Shoesmith, *The influence of hydrogen peroxide and hydrogen on the corrosion of simulated spent nuclear fuel*, Faraday Discuss. (2015). 180, 283-299.
- [41] M.E. Broczkowski, P.G. Keech, J.J. Noël, D.W. Shoesmith, *The role of dissolved hydrogen on rare earth-doped uranium dioxide corrosion in the presence of hydrogen peroxide*, J Electrochem Soc. (2011). 158 (12), C439-C444.
- [42] S. Sundin, B. Dahlgren, O. Roth, M. Jonsson, *H_2O_2 and radiation induced dissolution of UO_2 and SIMFUEL in HCO_3^- deficient aqueous solution*, J Nucl Mater. (2013). 443 (1-3), 291-297.
- [43] C.M. Lousada, M. Trummer, M. Jonsson, *Reactivity of H_2O_2 towards different UO_2 -based materials: The relative impact of radiolysis products revisited*, J Nucl Mater. (2013). 434 (1-3), 434-439.
- [44] Y. Kumagai, A. Barreiro-Fidalgo, M. Jonsson, *Impact of stoichiometry on the mechanism and kinetics of oxidative dissolution of UO_2 induced by H_2O_2 and gamma-irradiation*, J Phys Chem C. (2019). 123 (15), 9919-9925.
- [45] A. Barreiro-Fidalgo, Y. Kumagai, M. Jonsson, *The role of surface-bound hydroxyl radicals in the reaction between H_2O_2 and UO_2* , J Coord Chem. (2018). 71 (11-13), 1799-1807.
- [46] S.-S. Lin, M.D. Gurol, *Catalytic decomposition of hydrogen peroxide on iron oxide: kinetics, mechanism, and implications*, Environ Sci Technol. (1998). 32 (10), 1417-1423.
- [47] D. Fu, X. Zhang, P.G. Keech, D.W. Shoesmith, J.C. Wren, *An electrochemical study of H_2O_2 decomposition on single-phase γ - $FeOOH$ films*, Electrochim Acta. (2010). 55 (11), 3787-3796.
- [48] A. Hiroki, J.A. LaVerne, *Decomposition of hydrogen peroxide at water– ceramic oxide interfaces*, J Phys Chem B. (2005). 109 (8), 3364-3370.
- [49] D. Zigah, J. Rodríguez-López, A.J. Bard, *Quantification of photoelectrogenerated hydroxyl radical on TiO_2 by surface interrogation scanning electrochemical microscopy*, Phys Chem Chem Phys. (2012). 14 (37), 12764-12772.

[50] M. Altmaier, E. Yalçıntaş, X. Gaona, V. Neck, R. Müller, M. Schlieker, T. Fanghänel, *Solubility of U(VI) in chloride solutions. I. The stable oxides/hydroxides in NaCl systems, solubility products, hydrolysis constants and SIT coefficients*, J Chem Thermodyn. (2017). 114, 2-13.

[51] I. Grenthe, X. Gaona, L. Rao, A. Plyasunov, W. Runde, B. Grambow, R. Konings, A. Smith, E. Moore, M.-E. Ragoussi, J.S. Martinez, D. Costa, A. Felmy, K. Spahiu, *Second update on the chemical thermodynamics of uranium, neptunium, plutonium, americium and technetium*, Nuclear Energy Agency of the OECD (NEA), Boulogne-Billancourt, France, 2020.

Chapter 5

5. Effect of Hydrogen on the Dissolution of Uranium Dioxide in Peroxide-Containing Environments

5.1. Introduction

The internationally accepted approach for the disposal of high-level nuclear waste is to isolate and contain it within a deep geologic repository (DGR). Canada's design to ensure the containment of used nuclear fuel is to seal it in a corrosion-resistant Cu-coated steel container isolated within a multiple barrier system composed of the fuel waste form, the container, bentonite clay buffer and seals around the container and the surrounding host rock. While the container will provide long-term containment,¹ it is necessary to evaluate the potential consequences of its failure when the fuel waste form could come in contact with groundwater. An extensive international effort has been expended on determining fuel behaviour and the possible release from the fuel of radionuclides under a range of DGR conditions.²⁻¹³

The groundwater entering the failed container will be anoxic, the dissolved O₂ in the vicinity of the container having been consumed by reactions with organic matter, oxidizable minerals in the clay buffer and the host rock and container corrosion processes. Consequently, the radiolysis of the groundwater will be the only source of oxidants within the container. Since U solubility increases by many orders of magnitude when oxidized to U^{VI} (as UO₂²⁺),¹⁴ radiolytic oxidants, in particular, H₂O₂ will lead to fuel corrosion and radionuclide release.¹⁵ However, the radiolysis of H₂O and the corrosion of the carbon steel container will produce the oxidant scavengers H₂ and Fe²⁺, which will suppress oxidizing conditions at the UO₂ surface by both homogeneous and heterogeneous reactions.¹⁶⁻¹⁸ Of these two potential reducing agents, H₂ has been shown to be dominant in suppressing the corrosion rate.^{16, 17, 19} Consequently, the influence of H₂ on fuel corrosion has been extensively studied as summarized by Badley and Shoesmith, and references therein.¹³

For dissolved H_2 to act as a reductant, it must be activated, i.e., dissociated into reactive H^\bullet radicals. This has been shown to occur on the surfaces of simulated spent nuclear fuels (SIMFUEL), catalyzed by noble metal (ϵ) particles composed of metals known to catalyze H_2 dissociation [Rh, Pd, Ru, Mo].²⁰ These particles are galvanically coupled to the UO_2 matrix and act as anodes which catalyze H^\bullet oxidation to H^+ , forcing the matrix to adopt a corrosion potential (E_{CORR}) too low for the oxidation/dissolution of UO_2 . In the absence of such particles, galvanic protection does not occur, with experiments indicating minimal activation of H_2 on the UO_2 surface.¹⁹ Activation can also be achieved in the presence of radiation (both α and γ) with the radiolytically-produced H^\bullet on the UO_2 surface acting as a scavenger for radiolytic oxidants, a process shown to suppress their reaction with UO_2 .^{19, 21-28}

Since the noble metals in the ϵ -particles are catalytic for both the reduction of oxidants, such as H_2O_2 , as well as the oxidation of H_2 , it is not surprising that UO_2 oxidation in H_2O_2 solutions containing H_2 can be suppressed when they are present either as particles in the UO_2 surface or as separated powder in the solution.^{19, 29-31} However, experiments in which H_2O_2 was added to Ar/ H_2 -purged solutions in the presence of a SIMFUEL containing no ϵ -particles suggested but did not clearly demonstrate that H_2 scavenging could also occur directly on the UO_2 surface. This would not be surprising since H_2O_2 reactions (particularly its decomposition to O_2 and H_2O) have been shown to proceed via the formation of surface OH^\bullet radicals introducing the possibility they could be scavenged by reactions with soluble H_2 on the UO_2 surface in the absence of radiation and ϵ -particles.³²⁻³⁸

In this study, the role of the UO_2 surface in reactions involving H_2O_2 and H_2 is investigated using a combination of electrochemical and surface analytical techniques.

5.2. Experimental

5.2.1. Electrode Materials and Preparation

Experiments were conducted on an un-doped natural UO_2 electrode cut as a 2mm-thick disc from a commercial fuel pellet manufactured by Zircotec Precision Industries (Now Cameco Fuel Manufacturing, Port Hope, Ontario) in September 1990. The details of electrode

preparation have been discussed previously.³⁹ The surface area of the single exposed face of the disc was 1.16 cm². The resistivity of UO₂ is known to be sensitive to the degree of stoichiometry (x in UO_{2+x}).⁴⁰⁻⁴⁴ The measured value for the specimen used was 10 kΩ.cm. This is close to that measured on a UO_{2.002} specimen,⁴⁵ suggesting the pellet may have had a slight residual excess O within the matrix. Before an experiment, the electrode was polished with 1200 grit SiC paper, then sonicated for 2 minutes in Type 1 H₂O (resistivity = 18.2 MΩ.cm) to remove polishing debris.

5.2.2. Solution Preparation

Solutions were prepared using Type 1 H₂O from a Millipore Milli-Q direct water purification system and deaerated using either Ar or 5% H₂/95% Ar gas (Praxair) for one hour prior to each experiment. All experiments were conducted in a 0.1 mol.L⁻¹ NaCl (Fisher Scientific) and 0.05 mol.L⁻¹ NaHCO₃/Na₂CO₃ (EMD Chemicals) solution, with the pH adjusted to 9.5 using 0.5 mol.L⁻¹ NaOH. H₂O₂ was added by diluting a 3% W/V solution (Fisher Scientific).

5.2.3. Electrochemical Cell and Equipment

All experiments were conducted using a standard 1 L three-electrode, three-compartment electrochemical cell. All potential measurements were recorded against a commercial saturated calomel electrode (SCE; 0.241 V vs. standard hydrogen electrode).⁴⁶ A 1 cm² Pt foil spot-welded to a platinum wire was used as the counter electrode. The electrochemical cell was housed in a grounded Faraday cage to minimize interference from external electrical noise. Applied potentials and measured current responses were controlled, recorded, and analyzed using a Solartron Model 1480 Multistat and CorrWare software (Scribner Associates), respectively.

5.2.4. Electrochemical Techniques

Prior to experiments, the UO₂ specimen was potentiostatically polarized to -1200 mV (vs SCE) for 2 minutes. This process removes any air-formed oxides on the surface to ensure each experiment begins with a fresh surface.

Cyclic voltammetry (CV) experiments were performed to confirm the electrochemical viability of the UO₂ specimen. A potential scan was performed from -1200 mV (vs SCE) to a positive limit of 250 mV (vs SCE) and back at a scan rate of 10 mV.s⁻¹. The current interrupt method was used to compensate for electrode resistance.

Open circuit experiments were performed in solutions purged with either UHP Ar (Praxair) or UHP 5% H₂/95% Ar (Praxair) (dissolved [H₂] ~ 10⁻⁴ M). After electrochemically reducing the surface at -1200 mV (vs SCE) for 2 minutes, E_{CORR} was allowed to stabilize for 1-2 days before H₂O₂ additions.

Potentiostatic polarization (PSP) experiments were performed with UHP 5% H₂/95% Ar. After 1 day, to allow the system to reach a steady state, the UO₂ electrode was polarized to 0.1 V (vs SCE) or -0.1 V (vs SCE), with E_{CORR} being monitored both before and after polarization.

5.2.5. X-ray Photoelectron Spectroscopy

X-ray photoelectron spectroscopy (XPS) was used to measure the surface composition of the electrode on completion of some experiments. Samples were transferred between the electrochemical cell and XPS instrument using a vacuum-sealed desiccator. Analyses were performed using a Kratos AXIS Supra Spectrometer with a monochromatic Al K α (15 mA, 14 kV) radiation source ($h\nu = 1486.6$ eV). The instrument work function was calibrated for the Au 4f_{7/2} metallic gold binding energy of 83.96 ± 0.025 eV, and the spectrometer dispersion was adjusted to a binding energy (BE) of 932.62 ± 0.025 eV for metallic Cu 2p_{3/2}. When necessary, surface charging was corrected by setting the C 1s BE at 284.8 eV. Survey spectra were collected over a BE range from 0 to 1100 eV at a pass energy of 160 eV. High-resolution spectra were collected for O 1s, U 4f, and C 1s at a pass energy of 20 eV. For all measurements, the area of analysis was ~ 400 x 700 μ m. All spectra were analyzed using CasaXPS software (version 2.3.19) with the fitting parameters used described elsewhere.⁴⁷

5.2.6. Raman Analyses

Raman spectra were acquired using a Renishaw 2000 confocal Raman spectrometer (Renishaw, UK). Spectra were excited using a 50 mW He-Ne laser with a wavelength of 632.8

nm. The power of the laser beam was reduced to 50% to avoid heating effects. Spectra were recorded over the wavenumber range 150 to 1400 cm^{-1} . A Gaussian-Lorentzian peak model with a Shirley background correction was used to fit spectra. The deconvolution of the broad band between 500 and 700 cm^{-1} was performed as previously described.^{48, 49}

5.3. Results and Discussion

Figure 5-1 shows a CV recorded from -1200 mV (vs SCE) to +250 mV (vs SCE) with the vertical line at ~ -400 mV (vs SCE), indicating the thermodynamic threshold for oxidation of stoichiometric UO_2 . By confining the negative potential limit to -1200 mV (vs SCE), the possibility of reducing any oxidized states (U^{V}) pre-existing in the UO_2 specimen was avoided, as demonstrated previously.⁴⁵ Consequently, the shallow sub-thermodynamic oxidation current observed on the forward scan (from ~ -800 mV to -400 mV) can be attributed to the oxidation of pre-existing non-stoichiometric locations within the UO_2 matrix. This sub-thermodynamic oxidation at such sites is thought to be associated with grain boundaries,^{50, 51} and has been observed previously and characterized in detail.^{44, 50, 52, 53} The current plateau observed when the scan is extended to more positive potentials can be attributed to the anodic oxidation of the surface of the $\text{U}^{\text{IV}}\text{O}_2$ matrix to a thin layer (a few nm) of $\text{U}^{\text{IV}}_{1-2x}\text{U}^{\text{V}}_{2x}\text{O}_{2+x}$. The final rise in current, as the positive potential limit is approached, is attributable to the further oxidation of this layer to soluble uranyl carbonate complexes $(\text{U}^{\text{VI}}\text{O}_2(\text{CO}_3)_x)^{(2-2x)+}$.⁵³ The cathodic peak observed on the reverse scan has been shown to be due to the partial reduction of the surface layer.⁵³

A series of Raman spectroscopic analyses yielded mainly spectra exhibiting only a single peak located at 445 cm^{-1} , assigned to the symmetric O- U^{IV} stretching mode in an undisturbed stoichiometric lattice. However, a number of locations exhibited both this peak and a broad shallow band located between 500 and 700 cm^{-1} , Figure 5-2, indicative of a disturbed lattice. Deconvolution of this band yielded a peak at 575 cm^{-1} , assigned to a first-order LO phonon and a second peak at 630 cm^{-1} .⁴⁸ This last peak can be attributed to distortion of the anion sublattice involving the formation of clusters of interstitial O atoms and is a signature of a degree of non-stoichiometry consistent with the voltammetric observation, Figure 5-1.^{54, 55}

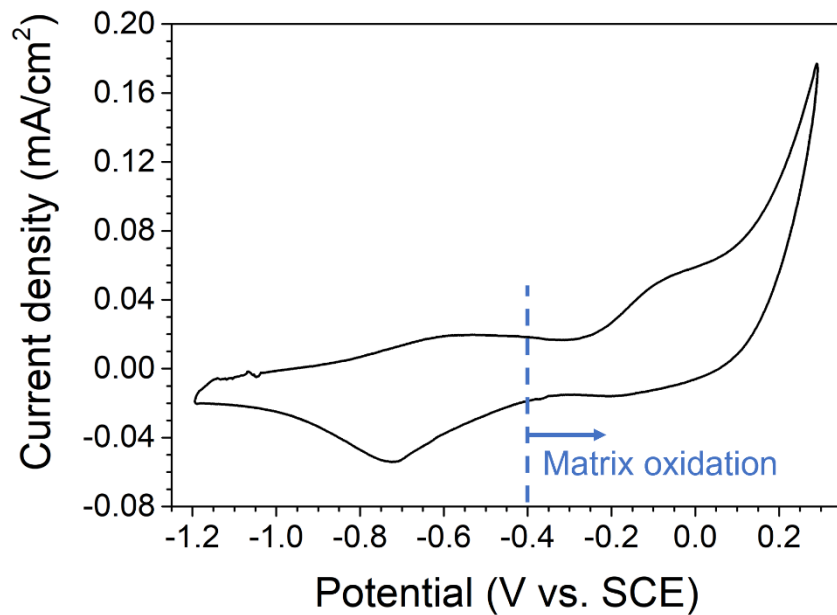


Figure 5-1. Cyclic voltammogram recorded on a UO₂ electrode in Ar-purged 0.1 mol.L⁻¹ NaCl + 0.05 mol.L⁻¹ HCO₃⁻/CO₃²⁻ solution adjusted to pH 9.5. The vertical dashed line at ~ -400 mV (vs SCE) indicates the thermodynamic threshold for matrix oxidation.

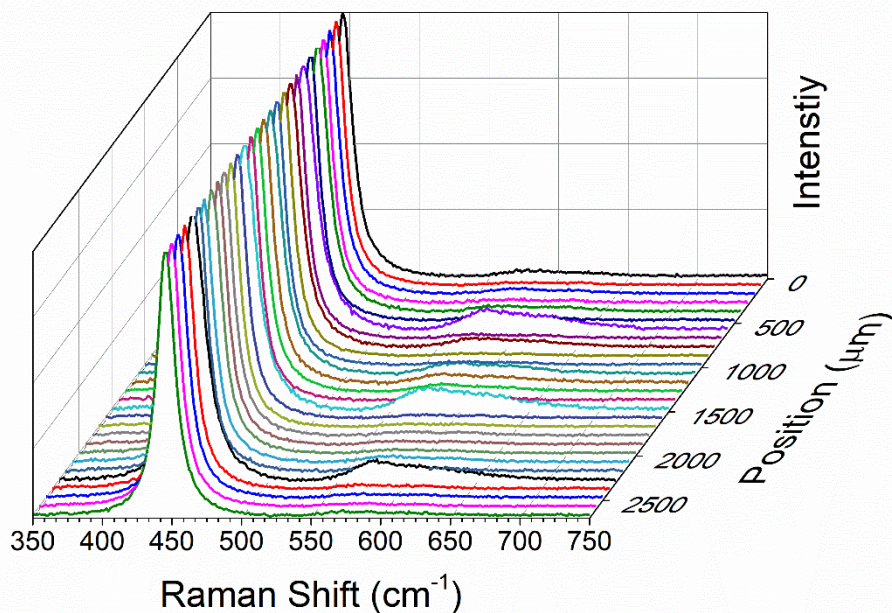


Figure 5-2. Raman spectra recorded across the surface of an unoxidized UO₂ specimen.

Figure 5-3 shows a series of E_{CORR} measurements in solutions purged with either Ar (Figure 5-3a) or 5% H_2 /95% Ar (Figure 5-3b). Prior to the first H_2O_2 addition, E_{CORR} was allowed to approach a steady state. Irrespective of the purge gas, E_{CORR} increased to a value between -150 mV (vs SCE) and -100 mV (vs SCE). Since the thermodynamic threshold for the oxidation of stoichiometric UO_2 is ~ -400 mV (vs SCE) for the conditions employed in these experiments, Figure 5-1, these values suggest a slight oxidation of the UO_2 surface, probably by traces of dissolved O_2 .

In the absence of H_2 , Figure 5-3a, each H_2O_2 addition led to a small increase in E_{CORR} to a new steady state value, up to a $[\text{H}_2\text{O}_2] = 10^{-6}$ M. For $[\text{H}_2\text{O}_2] = 5 \times 10^{-6}$ M, a very marked increase in E_{CORR} occurred, with subsequent increases in $[\text{H}_2\text{O}_2]$ leading to only minor further increases, with the potential stabilizing around ~ 60 mV (vs SCE). When H_2 was present (in the present case at $\sim 10^{-4}$ M), Figure 5-3b, increases in $[\text{H}_2\text{O}_2]$ up to 10^{-6} M led to similar small increases in E_{CORR} . However, when $[\text{H}_2\text{O}_2]$ was increased to $> 10^{-6}$ M, a rapid initial increase was eventually reversed. A similar initial increase/subsequent decrease was observed for $[\text{H}_2\text{O}_2] = 10^{-5}$ M. However, at 5×10^{-5} M, the eventual decrease was arrested as E_{CORR} decreased only slightly and approached a steady state value of ~ 60 mV (vs SCE). This indicates an insensitivity to H_2 for $[\text{H}_2\text{O}_2] \geq 5 \times 10^{-5}$ M on the time scale of this experiment. Similar E_{CORR} behaviour has been consistently observed on SIMFUELS which contain rare earth dopants and ϵ -particles or rare earth dopants only.^{22, 29} While the general form of the transients (in the absence and presence of H_2) are reproducible the actual values recorded can vary as observed in this study and previously.

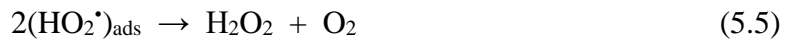
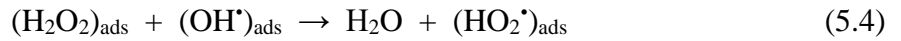
Figure 5-4 shows the final measured values of E_{CORR} , from Figure 5-3, as a function of the total $[\text{H}_2\text{O}_2]$ added to solution. While the values for $[\text{H}_2\text{O}_2] < 10^{-6}$ M may reflect the influence of traces of dissolved O_2 , which could be present at a concentration \geq that of the added H_2O_2 , there is a clear separation in the values measured in the presence and absence of H_2 in the $[\text{H}_2\text{O}_2]$ range indicated approximately by the horizontal arrow. At the highest $[\text{H}_2\text{O}_2]$ (5×10^{-5} M), there is no difference in the two values, indicating an insensitivity to H_2 in this range. This clearly demonstrates that H_2 (at a concentration of $\sim 10^{-4}$ M) can interfere with the reactions of H_2O_2 on the UO_2 surface when $[\text{H}_2\text{O}_2]$ is in the concentration range between approximately

10^{-6} M and 10^{-5} M. It is likely that this interference extends to lower $[\text{H}_2\text{O}_2]$ but is undetectable in these measurements.

A similar insensitivity of E_{CORR} to $[\text{H}_2\text{O}_2] \geq 10^{-5}$ M has been observed previously on undoped UO_2 and attributed to the redox buffering of the H_2O_2 decomposition reaction. Under these conditions, the equilibrium potentials for the two half-reactions involved, reactions 5.1 and 5.2, exhibit identical dependencies on $[\text{H}_2\text{O}_2]$, which are opposite in sign. Providing both reactions are rapid and equally influenced by $[\text{H}_2\text{O}_2]$, a change in $[\text{H}_2\text{O}_2]$ would change the decomposition rate without influencing E_{CORR} .



The decomposition of H_2O_2 proceeds on the surface of various metal oxides via a radical mechanism.³²⁻³⁸



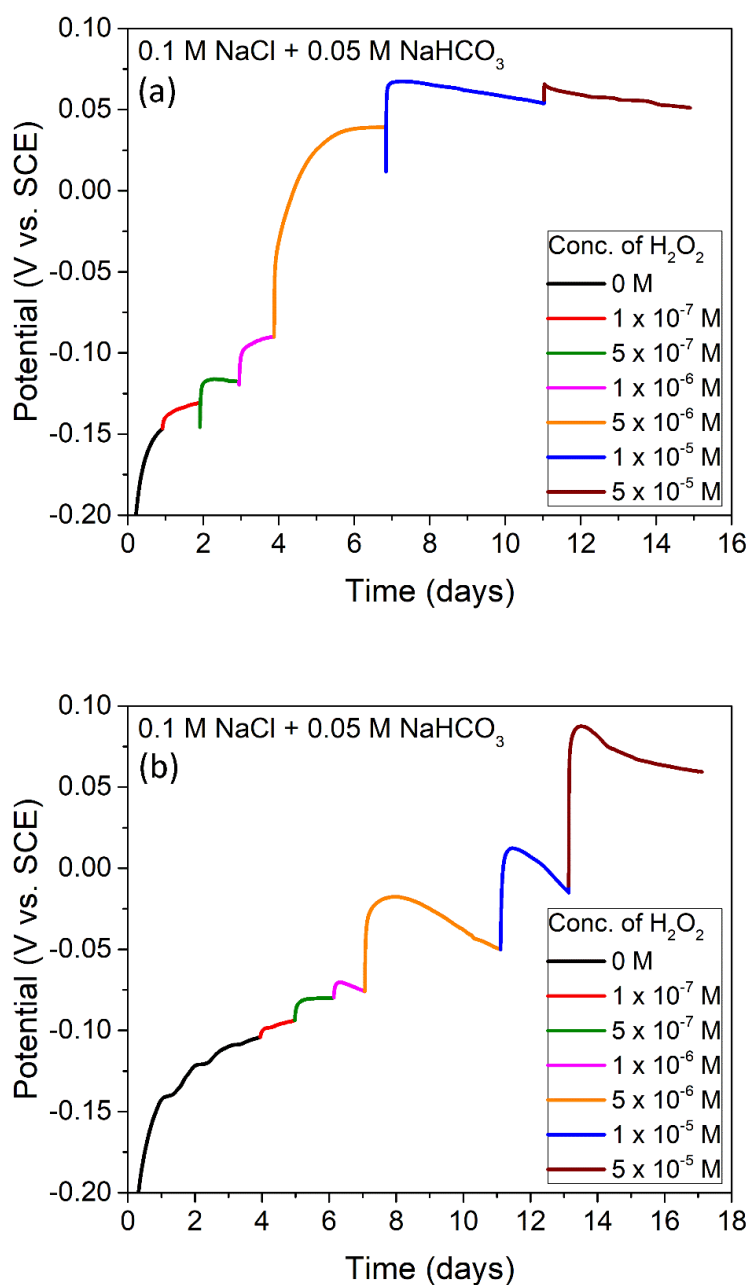
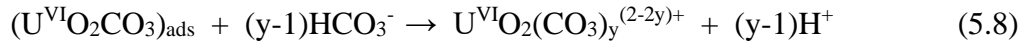
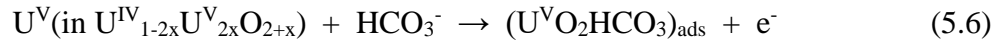


Figure 5-3. E_{CORR} as a function of time with sequential additions of $[H_2O_2]$, recorded on a natural UO_2 electrode in $0.1 \text{ mol.L}^{-1} \text{ NaCl} + 0.05 \text{ mol.L}^{-1} \text{ HCO}_3^-/\text{CO}_3^{2-}$ solution adjusted to pH 9.5 with (a) Ar, or (b) 5% $H_2/95\%$ Ar purge gas. The values show the actual concentration of H_2O_2 during that measurement period.

On UO_2 , this process has been shown to be catalyzed by the presence of a thin $\text{U}^{\text{IV}}_{1-2x}\text{U}^{\text{V}}_{2x}\text{O}_{2+x}$ surface layer; i.e., by the formation and destruction of U^{V} surface sites accompanied by the incorporation and release of O^{2-} at vacant interstitial sites readily available in the UO_2 cubic lattice.⁵⁶ This peroxide decomposition process occurs in competition with the oxidative dissolution (corrosion) of the UO_2 surface via the extraction of the U^{V} state (from the $\text{U}^{\text{IV}}_{1-2x}\text{U}^{\text{V}}_{2x}\text{O}_{2+x}$ surface layer) and its further oxidation to U^{VI} and release to solution as a $\text{HCO}_3^-/\text{CO}_3^{2-}$ complexed uranyl ion¹³



with the electrons consumed by the reduction of $(\text{OH}^*)_{\text{ads}}$.

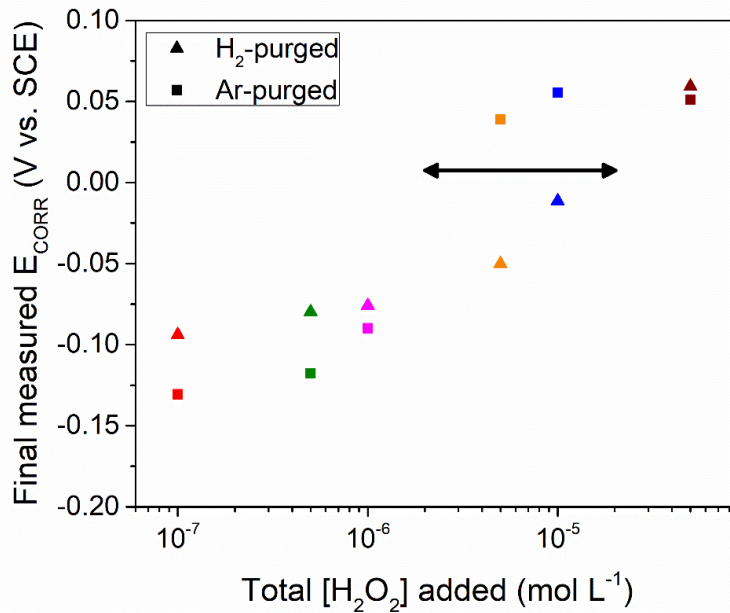


Figure 5-4. Final E_{CORR} values from Figure 5-3, as a function of total $[\text{H}_2\text{O}_2]$. The horizontal arrow indicates the range in which E_{CORR} is sensitive to the presence of H_2 .

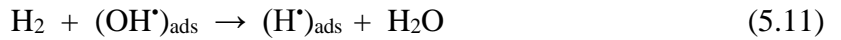
The balance between H_2O_2 decomposition and UO_2 dissolution depends not only on the $[\text{H}_2\text{O}_2]$ and $[\text{CO}_3]_{\text{tot}}$ ($[\text{HCO}_3^-] + [\text{CO}_3^{2-}]$) but also on the composition of the $\text{U}^{\text{IV}}_{1-2x}\text{U}^{\text{V}}_{2x}\text{O}_{2+x}$ surface layer. It also depends on whether or not the oxide matrix is stabilized by rare earth (RE^{III}) doping, with $\sim 14\%$ of the H_2O_2 consumed by dissolution on undoped UO_2 but $< 4\%$ on RE^{III} -doped UO_2 .^{56, 57}

It should be noted that Cl^- and $\text{HCO}_3^-/\text{CO}_3^{2-}$ ions in solution can also react with hydroxyl radicals on the UO_2 surface.⁵⁸ However, all solutions used for immersion experiments had constant $[\text{NaCl}]$ and $[\text{NaHCO}_3/\text{Na}_2\text{CO}_3]$, resulting in a consistent influence on the surface reactions. The effect of these ions is therefore not considered in this article.

Figure 5-5 shows a series of individual E_{CORR} measurements at different single $[\text{H}_2\text{O}_2]$ values. As observed in Figure 5-3, E_{CORR} increased prior to the addition of H_2O_2 in both the absence (Figure 5-5a) and presence (Figure 5-5b) of H_2 towards a steady state value between -160 mV (vs SCE) and -200 mV (vs SCE). The increases are attributed to slight surface oxidation due to trace dissolved O_2 . This occurs independently of the presence of H_2 , confirming there is no detectable influence of H_2 in the absence of H_2O_2 . The values recorded after H_2O_2 addition do not show the same consistent behaviour as in the first set of experiments (Figure 5-3). However, the tendency to more readily generate a peak in the presence of H_2 is observed. As discussed below, this is not surprising given the competition between surface oxidation and oxidant scavenging in the presence of surface radical species. While the results collected in this study were based on single experiments, the behaviour observed (with and without H_2) is consistent with our previous observations.^{22, 29}

After the individual H_2O_2 addition experiments, the extent of surface oxidation was determined by XPS, Figure 5-6. The percentage of reduced (U^{IV}) and oxidized (U^{V} and U^{VI}) states are plotted as a function of the final E_{CORR} value recorded. Although the individual fractions of U^{V} and U^{VI} are determined when deconvoluting the XPS spectra, as described elsewhere,²⁹ the extent of air oxidation from U^{V} to U^{VI} is difficult to control, making the relative analyzed contributions of U^{V} and U^{VI} somewhat variable. This makes the sum of the two states ($\text{U}^{\text{V}} + \text{U}^{\text{VI}}$) a more reliable indication of the extent of oxidation.

Figure 5-6 shows that, despite the absence of a clear relationship between E_{CORR} and $[\text{H}_2\text{O}_2]$, Figure 5-5, the surface composition is dependent on the final measured value of E_{CORR} . The data shows that the extent of oxidation increases as E_{CORR} becomes more positive in both Ar and Ar/ H_2 purged solutions. A similar analysis of the oxidation state of the surface after each incremental addition of H_2O_2 (Figure 5-3) was not possible. This introduces the possibility that the transient behaviour in E_{CORR} observed in these experiments when H_2 is present, Figure 5-3b, can be attributed to a rapid initial oxidation of the surface when H_2O_2 is first added, followed by a subsequent reduction of the temporarily oxidized UO_2 surface. These results suggest that the anticipated scavenging of the surface OH^\bullet radicals, created by reaction 5.3, by dissolved H_2 could involve catalysis by the $\text{U}^{\text{IV}}/\text{U}^{\text{V}}$ states in the UO_2 surface.



The ability of H^\bullet radicals to reduce U^{V} states in a UO_2 surface has been demonstrated in gamma radiolysis experiments.⁴⁵

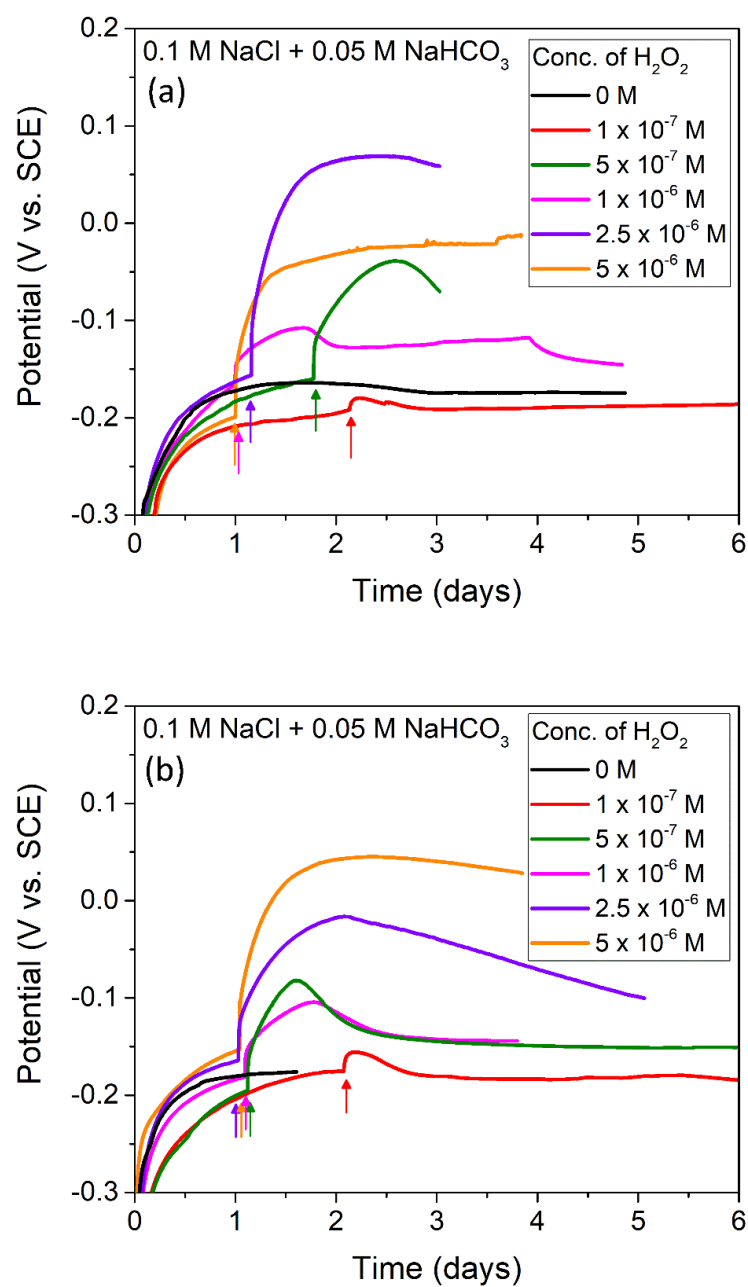


Figure 5-5. E_{CORR} as a function of time before and after individual additions of H_2O_2 (indicated by arrows) prior to XPS analyses. The purge gas was either (a) Ar or (b) 5% H_2 /95% Ar.

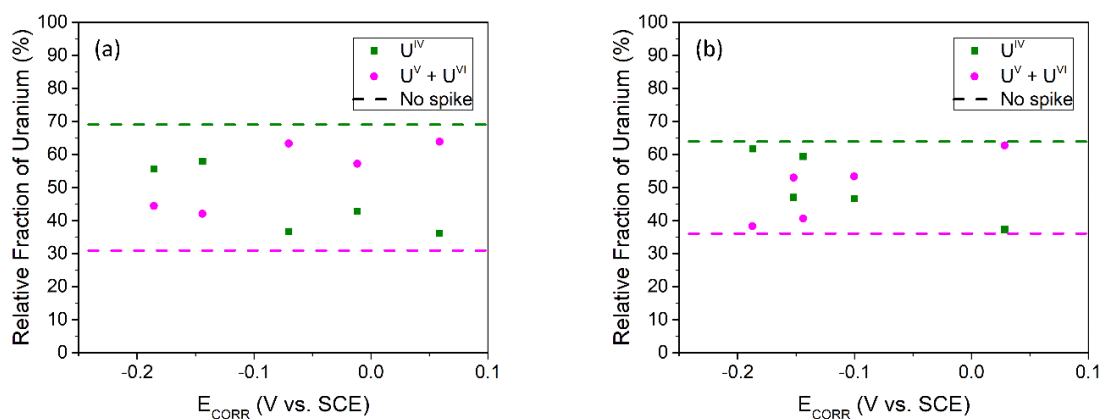


Figure 5-6. Surface compositions recorded on a natural UO_2 electrode as a function of the final measured E_{CORR} in a solution purged with either (a) Ar or (b) 5% $H_2/95\%$ Ar (from Figure 5-5). The horizontal dashed line refers to the composition of U^{IV} (green) and $U^V + U^{VI}$ (magenta) after experiments with no H_2O_2 added.

Figure 5-7 shows the relationship between the final measured E_{CORR} values (from Figure 5-4) and the surface composition expressed as a fraction of surface oxidized states ($(U^V + U^{VI})/U_{tot}$). The surface oxidized states are compared to the composition of a Gd-doped UO_2 surface after electrochemical treatment at a series of applied potentials for 1 hour in a solution with the same composition as that used in the experiments in this paper.^{45, 49} The increase in oxidized surface states with potential is considerably steeper for the undoped UO_2 from this study when compared to that observed for the Gd-doped UO_2 . The enhanced stability of RE^{III} -doped UO_2 to oxidation has been shown to be due to the formation of RE^{III} -oxygen vacancy (O_V) clusters. These clusters limit the available number of O_V , which are required to accommodate interstitial oxygen (O_i) ions as UO_2 is oxidized to $U^{IV}_{1-2x}U^{V}_{2x}O_{2+x}$.⁴⁹

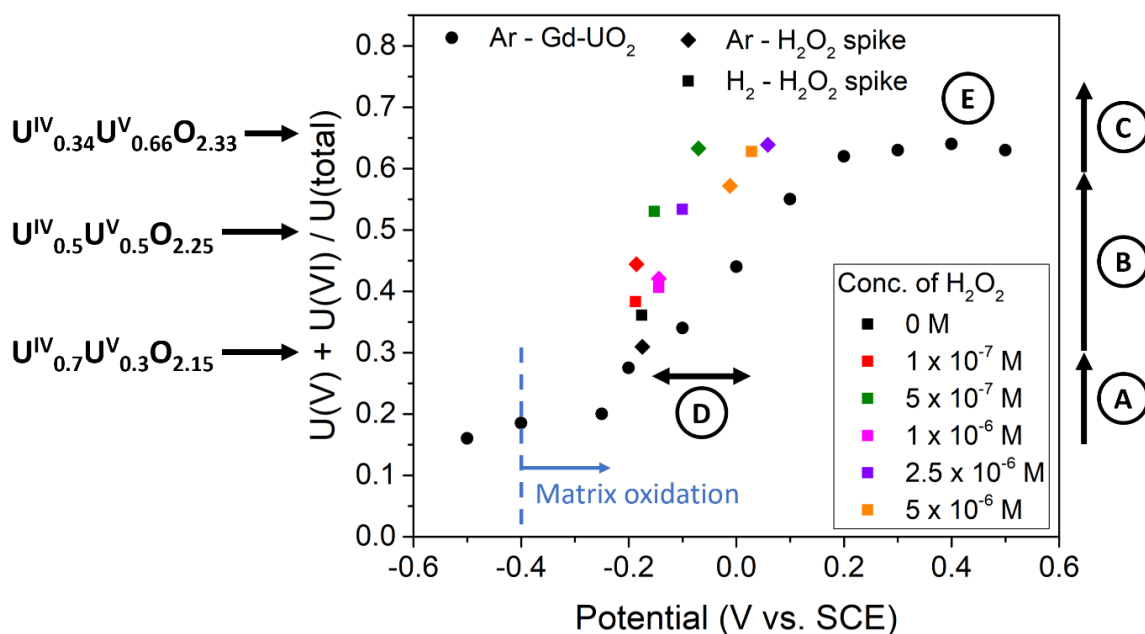


Figure 5-7. Comparison of $(U^V + U^{VI})/U_{total}$ ratio as a function of potential. The solid circles were measured on a Gd- UO_2 electrode in Ar-purged $0.1 \text{ mol.L}^{-1} \text{ NaCl} + 0.05 \text{ mol.L}^{-1} \text{ HCO}_3^-/\text{CO}_3^{2-}$ solution⁶⁰.

Several regions (A to D) are noted in Figure 5-7, in addition to several compositions for specific fractions of oxidized surface states. These regions denote specific ranges of composition and lattice structure determined by He and Shoosmith using Raman spectroscopy.⁴⁸ For relatively low degrees of non-stoichiometry (region A), excess oxygen is randomly distributed within the oxidized surface with an increase in x (in $U^{IV}_{1-2x}U^V_{2x}O_{2+x}$), leading to the association of O_i ions into clusters. For a sufficiently high degree of non-stoichiometry ($x \geq 0.15$) (region B), the generation of large cuboctahedral clusters leads to a significant loss of cubic symmetry, resulting in the onset of a cubic to tetragonal structural transition and the initiation of dissolution.⁵³ In region C, the UO_2 achieves a terminal irreversible composition for the fluorite structure ($U^{IV}_{0.34}U^V_{0.66}O_{2.33}$). Region D, indicated by the horizontal arrow, shows the potential range (and, hence, the range of surface compositions) over which the sequence of reactions 5.10 to 5.12 can be sustained, allowing H_2 to scavenge OH^\bullet radicals and possibly control the surface composition. It is likely that H_2 scavenging of

OH[•] radicals and, hence, a suppression of surface oxidation, the first essential step in the dissolution process (reactions 5.6 to 5.8), is possible at lower [H₂O₂] (and, hence, lower E_{CORR}) but is not detectable in these experiments. Although the potential region over which (H[•])_{ads} appear able to suppress or reverse surface oxidation is narrow (region D) and the change in composition is significant, leading to some uncertainty, these results suggest an ability of the U^{IV}_{1-2x}U^V_{2x}O_{2+x} layer to act catalytically via the reaction sequence 5.10 to 5.12. Once the surface reaches the terminal composition (region E), OH[•] radical scavenging is kinetically more difficult, as indicated by the only minor reversibility of E_{CORR} when [H₂O₂] ≥ 10⁻⁵ M (Figure 5-3). At sufficiently high [H₂O₂] and E_{CORR}, within region E, the dominant reaction is H₂O₂ decomposition (reactions 5.3 to 5.5) accompanied by some dissolution (reactions 5.6 to 5.8). Whether or not OH[•] radical scavenging would compete with these reactions at higher [H₂] remains to be investigated.

To demonstrate that H₂ is only active on the surface at compositions less oxidized than the terminal composition (U^{IV}_{0.34}U^V_{0.66}O_{2.33}) in the presence of OH[•] radicals, a set of potentiostatic polarization experiments were performed in a H₂-purged solution. After reaching a steady state E_{CORR}, the electrode was electrochemically oxidized at -100 mV (vs SCE) or 100 mV (vs SCE) for one hour and immediately analyzed by XPS. In an additional experiment, the electrode was electrochemically oxidized, then E_{CORR} was measured for 4 days before XPS analysis was repeated. The E_{CORR}-time curves and the oxidized fractions ((U^V + U^{VI})/U_{tot}) are shown in Figure 5-8 and Figure 5-9, respectively. Despite the applied overpotential, E_{CORR} rapidly recovered to steady-state values measured prior to polarization. For both applied overpotentials, there is little difference between the surface composition recorded immediately after polarization and after 4 days at E_{CORR}. This is unsurprising for the -100 mV overpotential, as the steady state E_{CORR} is only slightly lower than the applied overpotential. When compared to Figure 5-7, the compositions are in reasonable agreement. However, even though E_{CORR} rapidly recovered to those values measured prior to applying the 100 mV overpotential, the surface composition remained close to the terminal composition (U^{IV}_{0.34}U^V_{0.66}O_{2.33}). While U^{VI}O₂²⁺ formed at this potential would be expected to dissolve as U^{VI}O₂(CO₃)_y^{(2-2y)+} via reaction 5.8, this result demonstrates that H₂ alone cannot reduce the extensively oxidized surface on the time scale of this experiment.

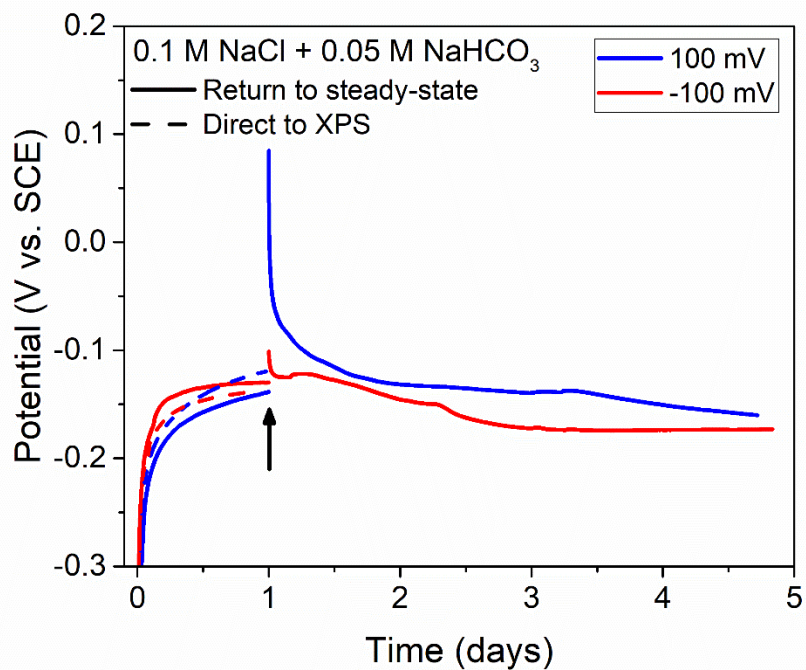


Figure 5-8. E_{CORR} as a function of time in a solution purged with 5% H₂/95% Ar. The arrow indicates the time at which the electrode was potentiostatically polarized to either 100 mV (blue) or -100 mV (red). XPS was performed immediately after polarization (dashed) or after 4 days of allowing the system to return to a steady state (solid).

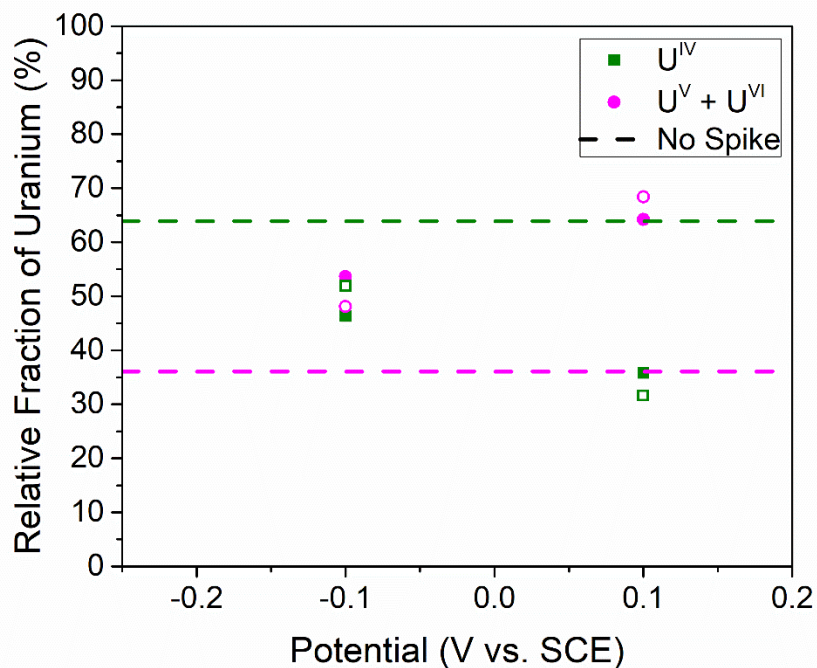


Figure 5-9. Surface compositions recorded as a function of the polarization potential from Figure 5-8. XPS was performed immediately after polarization (open points) or after 4 days of allowing the system to return to a steady state (solid points). The horizontal dashed line refers to the composition of U^{IV} (green) and U^V + U^{VI} (magenta) after experiments with no H₂O₂ added.

To further investigate the ability of H₂ to reduce a partially oxidized UO₂ surface in H₂O₂ containing solutions, experiments from Figure 5-5 were repeated for a [H₂O₂] of 5 x 10⁻⁷ M and 10⁻⁶ M under a H₂ purged environment. In all experiments, the system was left for 24 hours to establish a steady state E_{CORR} before adding H₂O₂, indicated by the vertical arrows. After adding H₂O₂, the system was either left to return to a steady state (solid line) or terminated before E_{CORR} could begin to recover from the initial increase (dashed line), Figure 5-10. Following each experiment, the sample was taken for XPS analysis to determine the fraction of surface oxidized states, Figure 5-11. The reproducibility of the initial increase in E_{CORR} allowed for reliable termination at the maximum E_{CORR} value of ~ -50 mV (vs SCE). When

left to return to a steady state, E_{CORR} decreases to a value lower than the pre-addition value. The surface oxidation ratio for all experiments was approximately 0.66, regardless of the initial $[\text{H}_2\text{O}_2]$ or final measured E_{CORR} . While H_2 was shown to reduce the UO_2 surface for the same concentration range in previous experiments, Figure 5-7, this was not observed for these experiments. This confirms that once the UO_2 surface reaches the terminal composition of $\text{U}^{\text{IV}}_{0.34}\text{U}^{\text{V}}_{0.66}\text{O}_{2.33}$, the formation of cuboctahedral defect clusters occurs.⁵³ When such lattice defects form, H_2 is unable to reduce the surface regardless of the presence of H_2O_2 or the value of E_{CORR} . The transient observed in E_{CORR} is therefore more likely due to the continued consumption of H_2O_2 rather than the reduction of the UO_2 surface.

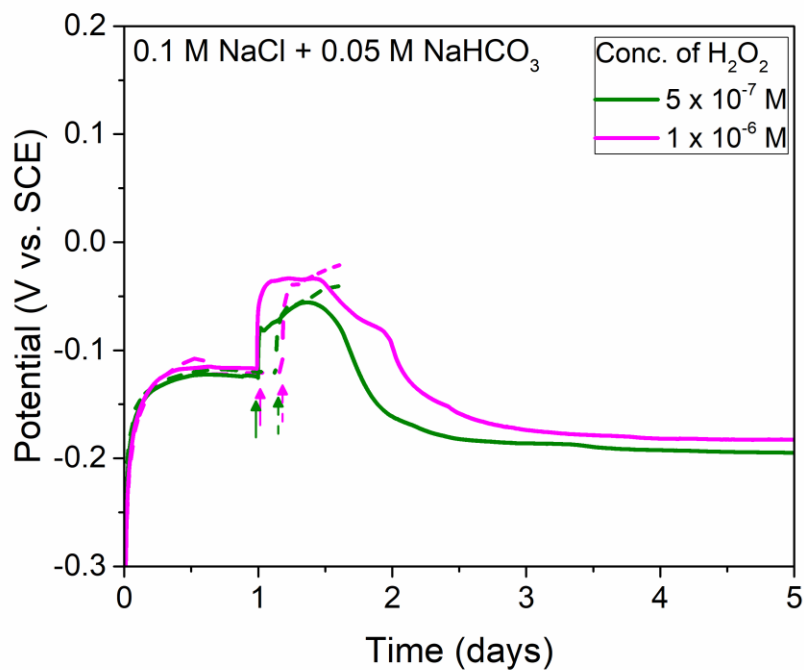


Figure 5-10. E_{CORR} as a function of time in a solution purged with 5% $\text{H}_2/95\%$ Ar. The arrows indicate the time at which H_2O_2 was added. Electrodes were removed for XPS analysis at either the peak potential (dashed lines) or after the eventual achievement of a steady state (solid lines).

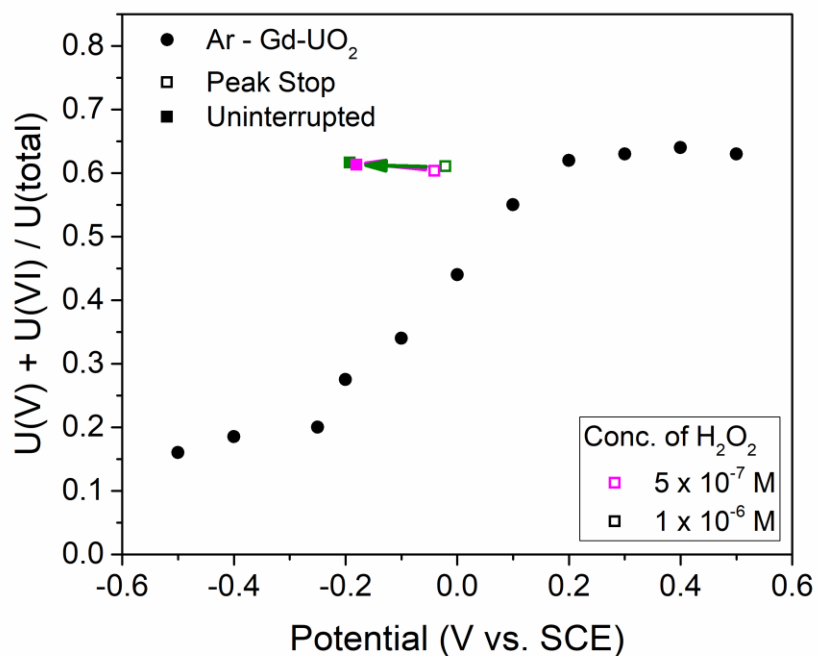


Figure 5-11. Comparison of $(U^V + U^{VI})/U_{total}$ ratio as a function of potential. XPS analysis was performed after the immersion experiment (Figure 5-10) at peak potential (open points) or after returning to a steady state (solid points).

5.4. Summary and Conclusions

Based on these results, it can be claimed that the presence of H_2 can scavenge $(OH^*)_{ads}$, which would otherwise oxidize the UO_2 surface, catalyze the decomposition of H_2O_2 , and stimulate a small amount of dissolution. These results are consistent with recently published model predictions.⁵⁹ Whether or not the H_2 , as $(H^*)_{ads}$, is involved in changing the surface composition is not clear.

The results in Figure 7 and Figure 5-11 suggest H_2 may reduce U^V states on the surface, providing the extent of surface oxidation by $(OH^*)_{ads}$ is limited, and x in $U^{IV}_{1-2x}U^{V}_{2x}O_{2+x}$ remains < 0.25 ; i.e., within the composition range where O_i remain randomly distributed

allowing surface oxidation to be reversed. At higher values of x , when O_i are dominantly located within defect clusters, reversibility of the surface composition does not appear to occur, and H_2O_2 decomposition is the dominant reaction. Whether $(H^*)_{ads}$ produced by the scavenging of $(OH^*)_{ads}$ have an influence in re-reducing the $U^{IV}_{1-2x}U^{V}_{2x}O_{2+x}$ surface layer remains to be demonstrated. This is likely to require experiments at higher H_2 concentrations.

5.5. Acknowledgements

This work was jointly funded by the Natural Sciences and Engineering Research Council of Canada and the Nuclear Waste Management Organization through Alliance Grant ALLRP561193-20. Surface Science Western is acknowledged for the use of their instruments.

Surface Science Western is acknowledged for the use of their instruments.

5.6. References

1. D. S. Hall, M. Behazin, W. J. Binns, and P. G. Keech, *Prog Mater Sci*, **118** 100766 (2021).
2. L. Werme and C. Lilja, Swedish Nuclear Fuel and Waste Management Co., SKB TR-10-46, (2010).
3. L. H. Johnson and D. W. Shoesmith, *Spent Fuel in Radioactive Waste Forms for the Future*, W. B. Lutze and R. C. Ewing, eds., Vol. 20, p. 635-698, Elsevier, Amsterdam, Netherlands (1988).
4. L. H. Johnson, D. M. LeNeveu, D. W. Shoesmith, D. W. Oscarson, M. N. Gray, R. J. Lemire, and N. C. Garisto, Atomic Energy of Canada Ltd, AECL-10714, Canada (1994).
5. D. W. Shoesmith, J. C. Tait, S. Sunder, W. J. Gray, S. A. Steward, R. E. Russo, and J. D. Rudnicki, Atomic Energy of Canada Ltd, AECL-11515, Canada (1995).
6. B. Grambow, A. Loida, P. Dressler, H. Geckeis, J. Gago, I. Casas, J. d. Pablo, J. Gimenez, and M. E. Torrero, Forschungszentrum Karlsruhe, FZKA-5702, Germany (1996).
7. B. Grambow, K. Lemmens, Y. Minet, C. Poinssot, K. Spahiu, D. Bosbach, C. Cachoir, I. Casas, F. Clarens, B. Christiansen, J. de Pablo, C. Ferry, J. Giménez, S. Gin, J. P. Glatz, J. A. Gago, E. Gonzalez-Robles, N. C. Hyatt, E. Iglesias, B. Kienzler, B. Luckscheiter, A. Martinez-Esparza, V. Metz, A. Ödegaard-Jensen, K. Ollila, J. Quiñones, A. Rey, S. Ribet, V. V. Rondinella, G. Skarnemark, D. Wegen, D. Serrano-Purroy, and T. Wiss, EUR 23730, Brussels (2008).
8. B. Grambow, J. Bruno, L. Duro, J. Merino, A. Tamayo, C. Martin, G. Pepin, S. Schumacker, O. Smidt, C. Ferry, C. Jegou, J. Quiñones, E. Iglesias, N. Rodriguez Villagra, J. M. Nieto, A. Martínez-Esparza, A. Loida, V. Metz, B. Kienzler, G. Bracke, D. Pellegrini, G. Mathieu, V. Wasselin-Trupin, C. Serres, D. Wegen, M. Jonsson, L. Johnson, K. Lemmens, J. Liu, K. Spahiu, E. Ekeröth, I. Casas, J. de Pablo, C. Watson, P. Robinson, and D. Hodgkinson, EUR 24597 EN, Brussels (2010).
9. C. Poinssot, C. Ferry, M. Kelm, B. Grambow, A. Martinez-Esparza, L. Johnson, Z. Andriambololona, J. Bruno, C. Cachoir, and J. M. Cavendon, Atomic Energy Commission (CEA), CEA-R-6093, Gif-sur-Yvette, France (2005).
10. V. M. Oversby, Swedish Nuclear Fuel and Waste Management Co., NEI-SE-562, Stockholm, Sweden (2003).
11. B. Kienzler, V. Metz, and A. Valls, EURATOM FP7 Collaborative Project, FP7-295722; Deliverable 5.13, Luxembourg, Germany (2015).

12. K. Lemmens, C. Cachoir, and T. Mennecart, SCK CEN, 27622175, ER-0505, Belgium (2019).
13. M. Badley and D. W. Shoesmith, Nuclear Waste Management Organization, NWMO-TR-2022-09, Toronto, Canada (2022).
14. I. Grenthe, J. Fuger, R. J. Konings, R. J. Lemire, A. B. Muller, C. Nguyen-Trung, and H. Wanner, *Chemical thermodynamics of uranium*, Elsevier, Amsterdam (1992).
15. E. Ekeröth, O. Roth, and M. Jonsson, *J Nucl Mater*, **355** (1), 38-46 (2006).
16. N. Z. Liu, L. D. Wu, Z. Qin, and D. W. Shoesmith, *Environ Sci Technol*, **50** (22), 12348-12355 (2016).
17. L. D. Wu, Z. Qin, and D. W. Shoesmith, *Corros Sci*, **84** 85-95 (2014).
18. T. E. Eriksen, D. W. Shoesmith, and M. Jonsson, *J Nucl Mater*, **420** (1-3), 409-423 (2012).
19. M. E. Broczkowski, D. Zagidulin, and D. W. Shoesmith, The role of dissolved hydrogen on the corrosion/dissolution of spent nuclear fuel in *Nuclear Energy and the Environment*, Vol. 1046, p. 349-380, American Chemical Society (2010).
20. J. K. Nørskov, T. Bligaard, A. Logadottir, J. Kitchin, J. G. Chen, S. Pandalov, and U. Stimming, *J Electrochem Soc*, **152** (3), J23 (2005).
21. J. C. Wren, D. W. Shoesmith, and S. Sunder, *J Electrochem Soc*, **152** (11), B470 (2005).
22. M. E. Broczkowski, P. G. Keech, J. J. Noël, and D. W. Shoesmith, *J Electrochem Soc*, **158** (12), C439-C444 (2011).
23. M. E. Broczkowski, J. J. Noël, and D. W. Shoesmith, *J Nucl Mater*, **346** (1), 16-23 (2005).
24. M. E. Broczkowski, P. G. Keech, J. J. Nol, and D. W. Shoesmith, *J Electrochem Soc*, **157** (8), C275-C281 (2010).
25. P. Carbol, J. Cobos-Sabate, J. P. Glatz, B. Grambow, B. Kienzler, A. Loida, A. Martinez Esparza Valiente, V. Metz, J. Quiñones, and C. Ronchi, Swedish Nuclear Fuel and Waste Management Co., TR-05-09, Stockholm, Sweden (2005).
26. T. Eriksen and M. Jonsson, Swedish Nuclear Fuel and Waste Management Co., TR-07-06, Stockholm, Sweden (2007).
27. D. W. Shoesmith, Nuclear Waste Management Organization, NWMO-TR-2008-19, Ontario, Canada (2008).

28. M. E. Broczkowski, J. J. Noël, and D. W. Shoesmith, *J Electroanal Chem*, **602** (1), 8-16 (2007).
29. M. Razdan and D. W. Shoesmith, *Faraday Discuss*, **180** 283-299 (2015).
30. L. Bauhn, N. Hansson, C. Ekberg, P. Fors, and K. Spahiu, *J Nucl Mater*, **507** 38-43 (2018).
31. S. Nilsson and M. Jonsson, *J Nucl Mater*, **372** (2-3), 160-163 (2008).
32. C. M. Lousada, M. Yang, K. Nilsson, and M. Jonsson, *J Mol Catal A: Chem*, **379** 178-184 (2013).
33. A. Barreiro-Fidalgo, Y. Kumagai, and M. Jonsson, *J Coord Chem*, **71** (11-13), 1799-1807 (2018).
34. S.-S. Lin and M. D. Gurol, *Environ Sci Technol*, **32** (10), 1417-1423 (1998).
35. D. Fu, X. Zhang, P. G. Keech, D. W. Shoesmith, and J. C. Wren, *Electrochim Acta*, **55** (11), 3787-3796 (2010).
36. A. Hiroki and J. A. LaVerne, *J Phys Chem B*, **109** (8), 3364-3370 (2005).
37. D. Zigah, J. Rodríguez-López, and A. J. Bard, *Phys Chem Chem Phys*, **14** (37), 12764-12772 (2012).
38. C. M. Lousada, M. Trummer, and M. Jonsson, *J Nucl Mater*, **434** (1-3), 434-439 (2013).
39. M. Razdan, *Electrochemical and Surface Compositional Studies on Uranium Dioxide* (PhD dissertation), University of Western Ontario, London, Ontario (2013).
40. N. Dudney, R. Coble, and H. Tuller, *J Am Ceram Soc*, **64** (11), 627-631 (1981).
41. L. Collier, R. Hampton, G. Saunders, and A. Stoneham, *J Nucl Mater*, **168** (3), 268-279 (1989).
42. G. J. Hyland and J. Ralph, *High Temp-High Pressures*, **15** (2), 179-190 (1983).
43. P. Winter, *J Nucl Mater*, **161** (1), 38-43 (1989).
44. H. He, R. K. Zhu, Z. Qin, P. Keech, Z. Ding, and D. W. Shoesmith, *J Electrochem Soc*, **156** (3), C87-C94 (2009).
45. N. Liu, F. King, J. J. Noël, and D. W. Shoesmith, *Corros Sci*, **192** 109776 (2021).
46. C. G. Zoski, *Handbook of electrochemistry*, Elsevier, Amsterdam (2006).

47. M. Razdan, D. S. Hall, P. G. Keech, and D. W. Shoesmith, *Electrochim Acta*, **83** 410-419 (2012).
48. H. He and D. W. Shoesmith, *Phys Chem Chem Phys*, **12** (28), 8109-8118 (2010).
49. M. Razdan and D. W. Shoesmith, *J Electrochem Soc*, **161** (3), H105-H113 (2014).
50. D. W. Shoesmith, *J Nucl Mater*, **282** (1), 1-31 (2000).
51. T. Livneh and E. Sterer, *Phys Rev B: Condens Matter*, **73** (8), 085118 (2006).
52. H. He, Z. Qin, and D. W. Shoesmith, *Electrochim Acta*, **56** (1), 53-60 (2010).
53. N. Liu, H. He, J. J. Noël, and D. W. Shoesmith, *Electrochim Acta*, **235** 654-663 (2017).
54. J. M. Elorrieta, L. J. Bonales, N. Rodríguez-Villagra, V. G. Baonza, and J. Cobos, *Phys Chem Chem Phys*, **18** (40), 28209-28216 (2016).
55. L. Desgranges, G. Baldinozzi, P. Simon, G. Guimbretière, and A. Canizares, *J Raman Spectrosc*, **43** (3), 455-458 (2012).
56. Z. Zhu, J. J. Noël, and D. W. Shoesmith, *Electrochim Acta*, **340** (2020).
57. S. Nilsson and M. Jonsson, *J Nucl Mater*, **410** (1-3), 89-93 (2011).
58. D. E. Richardson, H. Yao, K. M. Frank, and D. A. Bennett, *J Am Chem Soc*, **122** (8), 1729-1739 (2000).
59. N. L. Hansson and M. Jonsson, *Radiat Phys Chem*, **210** 111055 (2023).
60. M. Razdan and D. W. Shoesmith, *J Electrochem Soc*, **161** (4), H225-H234 (2014).

Chapter 6

6. Conclusions and Future Work

6.1. Conclusions

The primary goals of this research were, (i) to characterize natural UO_2 samples manufactured between 1965 and 2017 using a combination of electrochemical and surface analytical techniques to determine an estimated reactivity under long-term disposal conditions; and (ii) to investigate the possible reaction mechanisms between a $\text{U}^{\text{IV}}_{1-2x}\text{U}^{\text{V}}_{2x}\text{O}_{2+x}$ surface and radiolytically produced oxidants both in the presence and absence of H_2 , an oxidant scavenger produced by the corrosion of the steel container and by radiolysis of groundwater inside a failed container.

The quality of UO_2 pellets manufactured over four decades of the Canadian nuclear program was characterized to determine qualitatively a range of possible reactivities under DGR conditions. The range of resistivities was over three orders of magnitude, with most of the pellets being highly resistive, suggesting a near-stoichiometric composition. Using Raman spectroscopy, the non-stoichiometric features were found to be grain-specific, and possibly within grain boundaries rather than uniform across the sample. Additionally, SEM showed that variations in the surface morphology partially correlated to the measured resistivity of the samples. Preliminary electrochemical analyses confirmed that only low-resistivity samples were sufficiently conductive to allow compensation of the physical resistance, thereby allowing the surface electrochemical processes to be observed.

Dissolution experiments in solutions containing a range of H_2O_2 concentrations (the key oxidant anticipated due to radiolysis of groundwater after container failure) showed that the reactivity of the natural UO_2 samples investigated in this study was only loosely related to the sintering process. During the immersion experiments, the majority of the H_2O_2 in the solution was consumed by decomposition to O_2 and H_2O over a 24-hour period. The observed dissolution of the UO_2 matrix was localized at natural or manually created physical defects in the sample surface, such as cracks or micro-indentations. Measurements of the amount of U

dissolved showed the sample with the highest resistivity underwent the least U dissolution while consuming the greatest amount of H₂O₂ in the solution, regardless of the initial concentration of H₂O₂. While this observation suggests the resistivity (which is related to the degree of hyperstoichiometry) may have an influence on matrix stability, there does not appear to be a significant correlation between the measured resistivities and R_P values, the latter being a measure of surface reactivity.

With the introduction of H₂ into the system, it was clear that even in the absence of ε-particles, H₂ is capable of scavenging (OH[•])_{ads}. However, the role of (H[•])_{ads} in the changing surface composition is unclear from these experiments. It appears that H₂ can reduce a partially oxidized U^{IV}_{1-2x}U^V_{2x}O_{2+x} surface, provided the degree of surface oxidation has not exceeded $x > 0.25$. Beyond values of $x > 0.25$, the clustering of interstitial oxygen within defect clusters appears to remove the reversibility of the surface composition by H₂. At sufficiently oxidized surface compositions, the decomposition of H₂O₂ becomes the dominant reaction.

6.2. Future Work

In this study, an attempt was made to further understand the corrosion properties of natural UO₂ under long-term disposal conditions. This work specifically looked at the influence of H₂O₂, the primary oxidant of concern, and H₂, the primary oxidant scavenger, on the corrosion mechanism of UO₂ specimens with varying expected degrees of reactivity. However, there are unresolved issues that should be addressed with further research considerations:

- While the characterization of these samples yielded preliminary results, additional SEM and Raman spectroscopy analysis could provide greater confidence in the correlation between surface morphology and lattice defect structures.
- The characterization techniques used in this work could be complemented by scanning electrochemical microscopy (SECM) or scanning electrochemical cell microscopy (SECCM) to probe the reactivity of specific grains using a probe approach curve analysis. Furthermore, given the lack of knowledge surrounding the history of the specimens in this work, thermogravimetric analysis would provide quantitative results

for the degree of non-stoichiometry for the specimens to correlate with previous characterization techniques.

- Performing in-situ analysis of H_2O_2 and U concentrations using atomic emission spectroelectrochemistry (AESEC), a technique that utilizes a flow cell coupled with ICP-MS or inductively coupled plasma-optical emission spectroscopy (ICP-OES), that would provide more accurate results to elucidate the dissolution mechanism of UO_2 .
- Preliminary investigations on the influence of H_2 on the scavenging of oxidants and the reduction of the UO_2 surface were performed in this work. Using pressure cells to increase the dissolved concentration of H_2 would further our understanding of the role of $(\text{H}^*)_{\text{ads}}$ in the re-reducing of the $\text{U}^{\text{IV}}_{1-2x}\text{U}^{\text{V}}_{2x}\text{O}_{2+x}$ surface.
- Repeating the experiments presented in this work using site-specific groundwaters relevant to the NWMO's DGR (CR-10 or SR-290) is essential to confirm the safety case for the disposal of spent nuclear fuel.

Appendix A

Copyrights

Chapter 5 Copyright information.

Journal of The Electrochemical Society



OPEN ACCESS

Effect of Hydrogen on the Dissolution of Uranium Dioxide in Peroxide-Containing Environments

Martin D. M. Badley¹ , David W. Shoesmith^{1,2} and James J. Noël^{1,2} 

Published 20 September 2023 • © 2023 The Author(s). Published on behalf of The Electrochemical Society by IOP

Publishing Limited

[Journal of The Electrochemical Society, Volume 170, Number 9](#)

Citation Martin D. M. Badley et al 2023 *J. Electrochem. Soc.* **170** 096506

DOI 10.1149/1945-7111/acf52b



Figures ▾ References ▾

Article metrics

191 Total downloads

Share this article



You may also like

JOURNAL ARTICLES

[Effects of stoichiometry on the defect clustering in uranium dioxide](#)

[High Potential-Applied Catalyst Behavior of a Mononuclear Ruthenium\(II\) Complex on a Mesoporous ITO Electrode for Water Oxidation](#)

[Understanding Chlorite and Chlorate Formation Associated with Hypochlorite Generation at Boron Doped Diamond Film Anodes](#)

Appendix B

Curriculum Vitae

Education

- Ph.D., Physical & Analytical Chemistry, Faculty of Science
(September 2017 – April 2024)
 - The University of Western Ontario, London, Ontario
 - Research Thesis:
 - Thesis Supervisor: Dr. James J. Noël
- B.Sc., Specialization in Chemistry, Faculty of Science
(September 2013 – April 2017)
 - The University of Western Ontario, London, Ontario
- Minor, French Studies, Faculty of Arts
(September 2013 – April 2017)
 - The University of Western Ontario, London, Ontario

Honours and Awards

- Chemistry Society of Canada Travel Award, 2022
- Canadian Nuclear Association Conference Travel Award, 2022 and 2019
- Roy G Post Foundation Scholarship, 2022
- Centre for Advanced Materials and Biomaterials Research Trainee Travel Award, 2021
- Natural Sciences and Engineering Research Council of Canada Science Exposed Finalist, 2021 and 2020
- Materials Research Society Science as Art Finalist, 2020

- Surface & Interface Analysis Top Downloaded Article, 2018

Publications

1. **Badley, M.**, D.W. Shoesmith and J.J. Noël. 2023. Effect of Hydrogen on the Dissolution of Uranium Dioxide in Peroxide-Containing Environments. *J Electrochem Soc* 170: 096506. (DOI: 10.1149/1945-7111/acf52b)
2. **Badley, M.** and Shoesmith. 2022. The Corrosion/Dissolution of Used Nuclear Fuel in a Deep Geologic Repository. Nuclear Waste Management Organization, NWMO-TR-2022-09. Toronto, Canada. (<https://www.nwmo.ca>)
3. Kobe, B., **M. Badley**, J.D. Henderson, S. Anderson, M.C. Biesinger and D.W. Shoesmith. 2017. Application of Quantitative X-ray Photoelectron Spectroscopy (XPS) Imaging: Investigation of Ni-Cr-Mo Alloys Exposed to Crevice Corrosion Solution. *Surf Interface Anal* 49 (13): 1345-1350. (DOI: 10.1002/sia.6325)

Presentations

1. **Badley M.**; Shoesmith D. W.; Noël J. J., Effect of Hydrogen on the Corrosion of Pre-oxidized and Naturally Corroding Uranium Dioxide. *Annual Workshop on the Environmental Impact of Engineered Materials Degradation in Porous Consolidated Media*, Toronto, ON, Canada. November 3-4, 2022. (Oral Presentation)
2. **Badley M.**; Shoesmith D. W.; Noël J. J., Effect of Hydrogen on the Corrosion of Uranium Dioxide. *Annual Workshop on the Environmental Impact of Engineered Materials Degradation in Porous Consolidated Media*, Toronto, ON, Canada. November 3-4, 2022. (Poster Presentation)
3. **Badley M.**; Shoesmith D. W.; Noël J. J., Effect of Hydrogen on the Corrosion of Pre-oxidized and Naturally Corroding Uranium Dioxide. *Spent Fuel Workshop*, Barcelona, Spain. October 19-21, 2022. (Oral Presentation)
4. **Badley M.**; Shoesmith D. W.; Noël J. J., Effect of Hydrogen on the Corrosion of Uranium Dioxide. *NACE SOSS Symposium*, Kingston, ON, Canada. August 4-5, 2022. (Oral & Poster Presentation)

5. **Badley M.**; Shoesmith D. W.; Noël J. J., Effect of Hydrogen on the Corrosion of Uranium Dioxide. *Aqueous Corrosion Gordon Research Seminar and Conference*, New London, NH, United States. July 9-15, 2022. (Poster Presentation)
6. **Badley M.**; Noël J. J.; Shoesmith D. W., Effect of Hydrogen on the Corrosion of Uranium Dioxide. *Waste Management Symposia*, Phoenix, AZ, United States. March 6-10, 2022. (Invited Poster Presentation – Withdrawn due to COVID)
7. **Badley M.**; Noël J. J.; Shoesmith D. W., Investigating the Influence of Hydrogen Peroxide and Hydrogen on the Corrosion of Uranium Dioxide. *Materials Research Society Spring/Fall Meeting & Exhibit*, Virtual. November 27 – December 4, 2020. (Oral Presentation)
8. **Badley M.**; Noël J. J.; Shoesmith D. W., Investigating the Corrosion of UO₂ by Radiolytically Produced H₂O₂. *Canadian Nuclear Laboratories (CNL)*, Chalk River, ON, Canada. February 25, 2020. (Invited Oral Presentation)
9. **Badley M.**; Shoesmith D. W.; Noël J. J., Investigating the Effect of H₂O₂ on the Reactivity of UO₂ Specimens. *University Network of Excellence in Nuclear Engineering (UNENE)*, Toronto, ON, Canada. December 16-17, 2019. (Poster Presentation)
10. **Badley M.**; Noël J. J.; Shoesmith D. W., The Influence of Composition and Structure on the Reactivity of UO₂. *ECS Student Symposium*, London, ON, Canada. December 9, 2019. (Oral Presentation)
11. **Badley M.**; Noël J. J.; Shoesmith D. W., The Influence of Composition and Structure on the Reactivity of UO₂. *Spent Fuel Workshop*, Gent, Belgium. November 14-15, 2019. (Oral Presentation)
12. **Badley M.**; Shoesmith D. W.; Noël J. J., The Influence of Stoichiometry on the Reactivity of UO₂. *NACE SOSS Symposium*, London, ON, Canada. July 25-26, 2019. (Poster Presentation)
13. **Badley M.**; Shoesmith D. W.; Noël J. J., The Influence of Stoichiometry on the Reactivity of UO₂. *Canadian Chemistry Conference and Exhibition*, Québec City, QC, Canada. June 3-7, 2019. (Poster Presentation)
14. **Badley M.**; Shoesmith D. W.; Noël J. J., The Influence of Microstructure and Composition on the Reactivity of UO₂. *ECS Student Symposium*, London, ON, Canada. December 12, 2018. (Oral Presentation)
15. **Badley M.**; Henderson J. D.; Almusned B.; Kobe B. A.; Biesinger M. C.; Shoesmith D. W.; Noël J. J., Analysis of Ni-Cr-Mo Super Alloys Using X-ray Photoelectron Spectroscopic Imaging. *NACE SOSS Symposium*, Toronto, ON, Canada. July 26-27, 2018. (Poster Presentation)

16. **Badley M.**; Henderson J. D.; Almusned B.; Kobe B. A.; Biesinger M. C.; Shoesmith D. W.; Noël J. J., Analysis of Ni-Cr-Mo Super Alloys Using X-ray Photoelectron Spectroscopic Imaging. *Aqueous Corrosion Gordon Research Conference*, New London, NH, United States. July 7-13, 2018. (Poster Presentation)
17. **Badley M.**; Biesinger M. C.; Kobe B. A; Shoesmith D. W., Development of Quantitative X-ray Photoelectron Spectroscopy (XPS) Imaging. *Southern Ontario Undergraduate Student Chemistry Conference*, Toronto, ON, Canada. March 18, 2017. (Oral Presentation)

Teaching Experience

- Graduate Teaching Assistant
(2017 – 2020) The University of Western Ontario
 - CHEM 1301 – Discovering Chemical Structure
 - CHEM 3372 – Instrumental Analytical Chemistry